№3, 2025

ISSN 2706-977X

MATERIAL AND MECHANICAL ENGINEERING TECHNOLOGY

Material and Mechanical Engineering Technology | MMET

Editorial board of the journal

Content

DOI 10.52209/2706-977X_2025_3_3 IRSTI 81.09.03 UDC 669.71

Optimization of the Aluminum Alloy Phase Composition Based on Si-0.6% Mn-0.5% with Changing the Iron Content

Sultanbek T.Zh.*, Dostayeva A.M., Zhalel A.T.
Abylkas Saginov Karaganda Technical University, Karaganda, Kazakhstan
*corresponding author

Abstract. The article investigates the effect of iron content on the phase composition, microstructure, mechanical properties and electrical conductivity of the Si-0.6% Mn-0.5% aluminum alloy. Experimental alloys with iron content ranging from 0.1% to 2.0% were studied using X-ray diffraction analysis (XRD), optical and scanning electron microscopy, hardness and tensile strength testing, as well as eddy-current conductivity measurements. It was established that an iron content of 0.8% provides the most optimal balance of properties: hardness - 60 HB, tensile strength - 170 MPa, ductility - 16%, and electrical resistivity - 33 μΩ·m. With further increase of iron concentration, hardness and strength increase but electrical conductivity decreases significantly due to the formation of AlFeSi and Al_3Fe phases. The obtained results demonstrate that controlling the iron content allows optimization of aluminum alloys for application in electrical engineering, construction and automotive industries, where both high mechanical strength and stable conductivity are required.

Keywords: aluminum alloy, iron, phase composition, hardness, electrical conductivity, phase diagram, microstructure, heat treatment.

Introduction

Aluminum alloys are among the most demanded structural materials due to their low density, high corrosion resistance, and technological flexibility. They are widely applied in the aerospace, automotive, construction, and electrical industries [1]. However, achieving a balance between mechanical properties and electrical conductivity remains a challenging task for alloy developers.

One of the key factors influencing the performance of aluminum alloys is the presence of iron impurities. Iron is an unavoidable element in most aluminum alloys, and depending on its content it can either improve strength or significantly deteriorate ductility and conductivity [2]. Previous studies have shown that excessive iron leads to the formation of intermetallic compounds such as Al_3Fe and AlFeSi, which cause embrittlement and reduce the electrical conductivity of alloys. At the same time, controlled addition of iron in limited amounts may improve hardness and tensile strength.

Despite the large body of research, most works have focused on Al-Si, Al-Mn or Al-Zr alloys separately, whereas systematic studies of the Si-0.6% Mn-0.5% system with varying Fe content are limited. The scientific gap lies in the absence of quantitative data on how gradual changes in iron concentration affect the phase composition, microstructure, mechanical strength and electrical conductivity in this particular system.

The purpose of this research is to determine the optimal iron content in the Si-0.6% Mn-0.5% aluminum alloy that ensures the best combination of strength, ductility, and electrical conductivity [3]. It is expected that the experimental results will identify a specific Fe concentration that balances these properties, thus contributing to the development of new high-performance aluminum alloys for engineering and electrical applications.

Materials and methods

Samples of Si-0.6% Mn-0.5% alloy with different Fe contents were prepared for testing. The samples were obtained by casting into a metal mold followed by heat treatment at 550 °C within 4 hours.

Aluminum alloys with different iron contents in the range from 0.1% to 2% were used for testing. The alloys were prepared by melting and chill casting, and then subjected to the thermal analysis.

The chemical composition was determined using a Vanta Element-S metal analyzer (Table 1).

Table 1. Chemical composition of experimental aluminum alloys of the Al-Si-Mn-Fe system (wt. %)

No.	Name	Si	Mn	Fe	Al (the rest)
1	Alloy 1	0.6	0.5	0.1	The rest
2	Alloy 2	0.6	0.5	0.3	The rest
3	Alloy 3	0.6	0.5	0.5	The rest
4	Alloy 4	0.6	0.5	0.8	The rest
5	Alloy 5	0.6	0.5	1	The rest
6	Alloy 6	0.6	0.5	1.5	The rest
7	Alloy 7	0.6	0.5	2	The rest

The X-ray diffraction analysis (XRD) was used to identify the phases and their volume fractions. The X-ray phase analysis was performed on an EMPYREAN diffractometer with CuKα radiation, which ensured high accuracy of phase identification. X-ray diffraction showed that with increasing the iron content, in the alloy new phases were formed. With the iron content of up to 0.8%, α-Al and Si remain the main phases; and the AlFeSi phase also appears. With increasing the iron content to 2%, the phase components AlFeSi and Al_3Fe begin to predominate, which leads to significant changes in the microstructure [4]. The TTAL8 database of the ThermoCalc software package was used for the study. It includes the information of the phases formed in aluminum alloys. Figure 1 shows the polythermal sections of the Al-Fe-Si alloy at 450 °C and 600 °C.

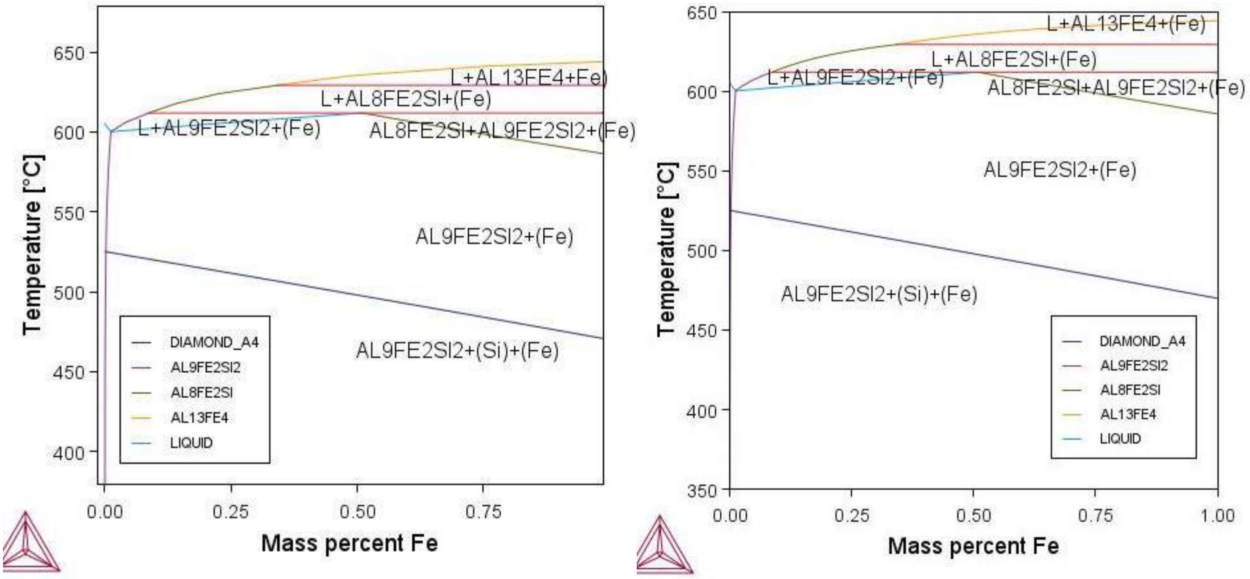

a) b)

Fig.1. - Polythermal sections of the phase diagram of the Al-Fe-Si system at 450 °C (a) and 600 °C (b)

The microstructure was studied using optical (Magus Metal VD700 BD LCD) and scanning electron microscopy (TESCAN VEGA 3) [5-6].

According to the literature data, metallographic studies using a scanning electron microscope showed that with increasing the iron content in the alloy, aggregation of the AlFeSi and Al_3Fe phases occurs, which leads to a coarser structure with increasing the grain size. Alloys with the iron content of 0.8% have the most optimal microstructure with the uniform distribution of phases and smaller grain sizes (Figure 2).

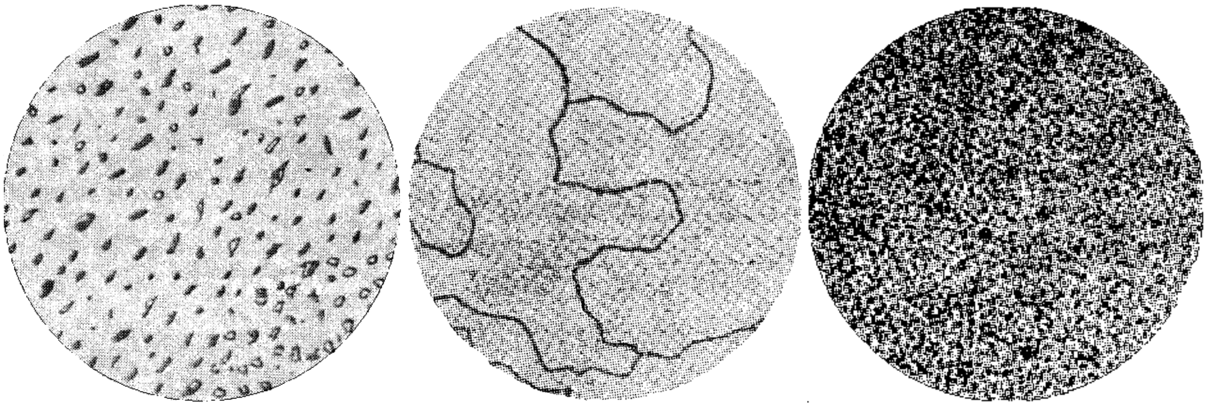

a b c

a) after annealing; b) after quenching from 530°C; c) after quenching and artificial aging at 250°C

Fig.2. - Microstructure of the aluminum alloy of the Al-Fe-Si system under different heat treatment conditions (x250) [7]

Figure 3 shows the microstructure of Al-Si-Mn-Fe alloys with variable iron contents obtained using a scanning microscope. Micrograph 3a shows the formation of primary aluminum grains (designated as (Al)) and precipitation of the intermetallic phase Al_6Fe. These phases are formed along the grain boundaries of aluminum. Micrograph 3b shows a further change in the microstructure. In addition to aluminum grains (Al), there are precipitates of the intermetallic phase Al_3Fe [8-10]. Their size and distribution indicate increasing the iron content of the alloy, which contributes to changing the phase composition. Micrograph 3c shows that with increasing the iron content in the alloy, intermetallic compounds of a more complex composition are formed, such as Al_3Fe_2Si. The phase is distributed along the grain boundaries, which indicates a significant effect of iron on the microstructure of the alloy. Micrograph 3g shows the microstructure characterized by the formation of large intermetallic phases of Al_3Fe_2.

These changes in the microstructure demonstrate how the iron content of aluminum alloys affects the phase composition. Increasing the iron concentration promotes the formation of more complex intermetallic compounds, which in turn affects the mechanical properties and electrical conductivity of the alloy.

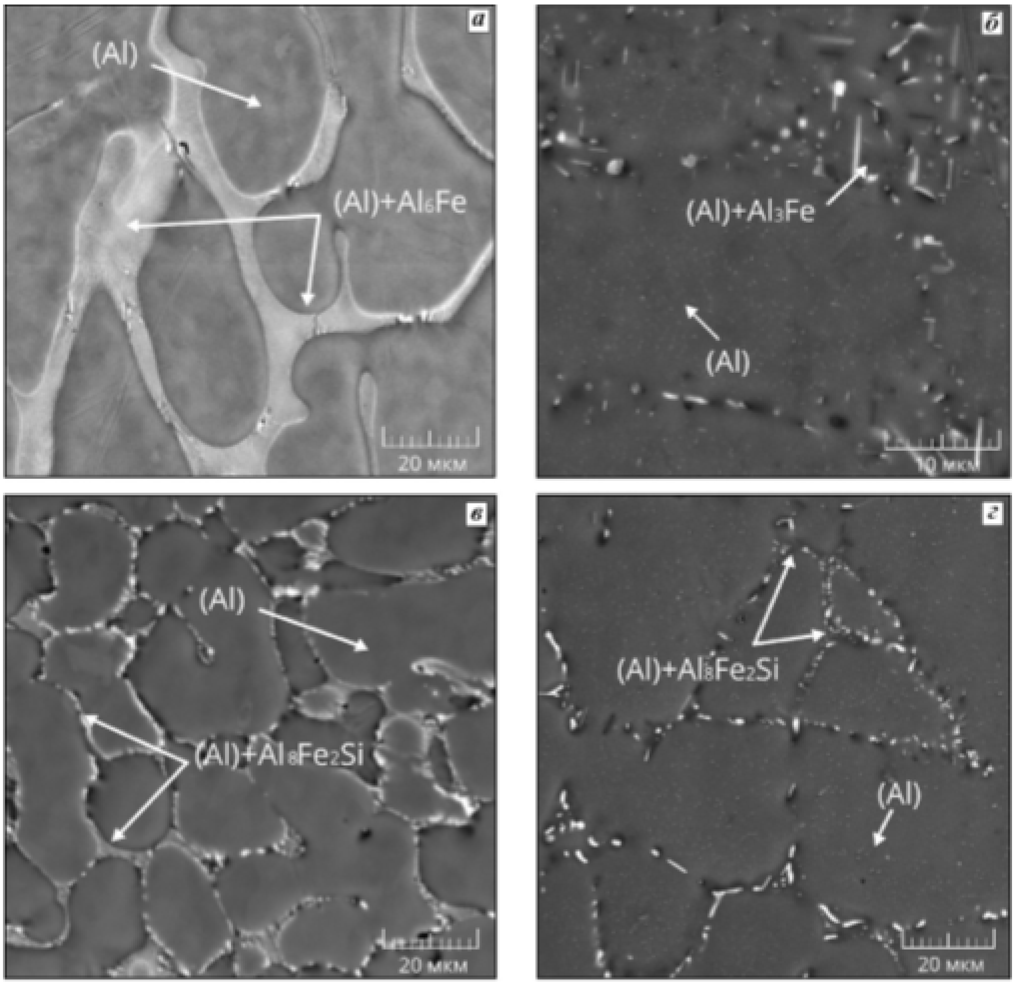

Fig.3. - Detailed microstructure of Al-Si-Mn-Fe alloys with variable iron contents

Vickers hardness was determined using a Willson 1150 hardness tester with the following parameters: the load 50 N, the holding time 15 s.

To determine tensile strength, an Instron universal testing machine with the 100 kN load frame was used. The tests were carried out using standard cylindrical samples in accordance with the ASTM E8/E8M standard [11-13]. The setup was equipped with highly sensitive sensors that ensured the measurement accuracy and reproducibility of results.

The measured values of hardness and strength show that increasing the iron content leads to increasing the alloy hardness but reduces its ductility. The most optimal mechanical properties are observed in the alloys with the iron content of 0.8%, which is caused by the balance between strength and ductility.

Table 2. The iron content effect on the mechanical properties of aluminum alloys of the Al-Si-Mn system

No.	Fe content, %	Hardness, HB	Tensile strength, MPa	Plasticity, %
1	0,1	45	120	20
2	0,3	55	140	19
3	0,5	58	160	18
4	0,8	60	170	16
5	1,0	70	180	15
6	1,5	80	210	12
7	2,0	90	220	10

For each alloy, specific electrical conductivity was measured using the eddy current method on a VE-26NP device, and then converted into specific electrical resistance [14-16].

Electrical conductivity measurements (Table 3) showed that with increasing the iron content, electrical conductivity of the alloy decreased significantly. This was due to the formation of the AlFeSi and Al_3Fe phases that affected the movement of electrons and reduced the overall conductivity of the material. For alloys with the iron content of 0.8%, the minimal decrease in electrical conductivity was observed, which made them optimal for use where good conductivity was important.

Table 3. Changing electrical conductivity of aluminum alloys of the Al–Si–Mn system depending on the iron content

No.	Fe content, %	Electrical conductivity (μΩ·m)	Basic phases
1	0.1	38	α-Al, Si
2	0.3	37	α-Al, Si
3	0.5	35	α-Al, Si, AlFeSi
4	0.8	33	α-Al, Si, AlFeSi
5	1.0	30	α-Al, Si, AlFeSi, Al_3Fe
6	1.5	25	α-Al, Si, AlFeSi, Al_3Fe
7	2.0	20	α-Al, Si, Al_3Fe

Discussion

Optimization of the phase composition of aluminum alloy Si–0.6% Mn–0.5% by changing the iron content reveales patterns that can be used to improve the mechanical properties and electrical conductivity of materials. The greatest improvement in strength characteristics and the minimum decrease in electrical conductivity are observed at the iron content of 0.8%, which makes this composition optimal for various technical applications requiring good mechanical properties and electrical conductivity comparison.

The diagram provided shows the key indicators for various alloys. For alloy 3 (0.8% Fe), the following important aspects can be noted (Figure 4).

The electrical conductivity value is slightly lower than that of alloys with a lower iron content but high enough to remain acceptable for engineering applications. Alloy 3 has the optimal hardness (about 60 HB), which provides sufficient strength for most engineering tasks. Strength reaches the maximum level (about 170 MPa), while maintaining a balance between strength and ductility. Although ductility is slightly lower than that of alloys with a lower Fe content, it remains acceptable (about 16%), which makes the alloy suitable for structural materials.

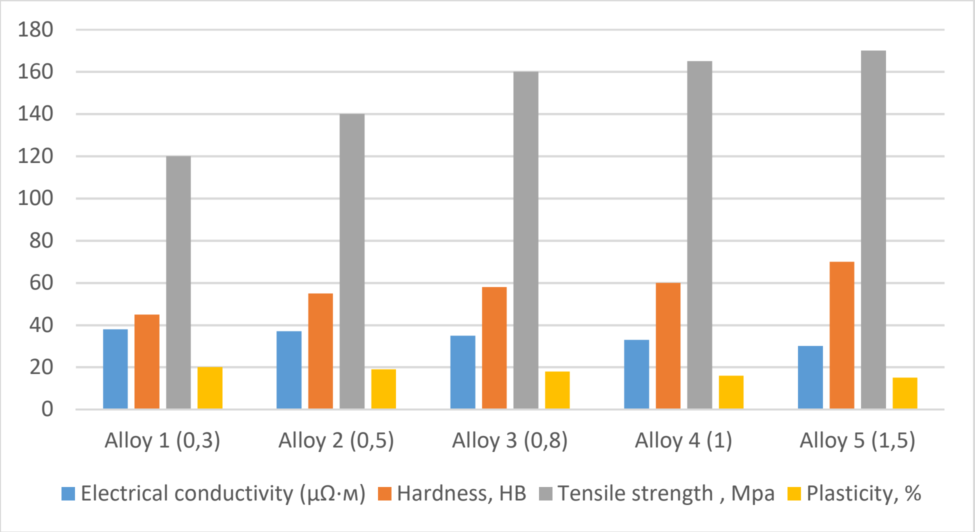

Fig.4. - Results of studying the iron content effect on the properties of aluminum alloys

Alloy 3 (0.8% Fe) exhibits the most optimal combination of properties, including high strength, good hardness and sufficient electrical conductivity. This makes it an ideal choice for industrial applications where it is important to ensure a balance between mechanical properties and electrical conductivity.

Conclusion

Changing the iron content in Si–0.6% Mn–0.5% aluminum alloys has a significant effect on their phase composition, microstructure, mechanical properties and electrical conductivity. The optimal iron content is recognized to be 0.8%, which provides a combination of high strength, ductility and electrical conductivity. This makes this alloy promising for a wide range of engineering tasks.

This alloy is especially suitable for use in structures that require high strength and stable conductivity, such as in the aviation, automotive and construction industries, as well as for electrical components. In addition, the study shows that the iron content of 0.8% contributes to increased corrosion resistance, which expands the scope of its application in aggressive environments.

Optimization of the phase composition and microstructure of this alloy opens up opportunities for further studies aimed at improving performance characteristics. Adjusting the iron content is the key tool for developing materials with specified properties that meet present day industrial requirements.

Thus, the developed aluminum alloy with the optimal iron content of 0.8% can become the basis for developing new materials with improved characteristics. This opens up prospects for its application in the production of electronics, energy equipment and high-tech structures.

References

[1] Ivanov A.A., Petrov B.B. The influence of iron on the properties of aluminum alloys // Metallovedenie. 2020. Vol. 45, P. 123-130.
[2] Johnson M., Smith R. High-temperature properties of Al-Zr alloys // Journal of Materials Science, 2019, Vol. 54., P. 4567–4576.
[3] Smirnov A.A., Ivanov V.V. The influence of manganese on the properties of aluminum alloys // Metallovedenie, 2021, Vol. 46, P. 134-140.
[4] Brown T., Smith J. Influence of Fe on Al-Mn alloys // Journal of Materials Science, 2020, Vol. 55, P. 5678–5685.
[5] Deng Y., Yin Zh., Pan Q., Xu G., Duan Yu., Wang Y. Na-no-structure evolution of secondary Al3(Sc1–xZrx) particles during superplastic deformation and their effects on deformation mechanism in Al—Zn—Mg alloys //J. Alloys and Compnd, 2017, No. 695, P. 142—153.
[6] Gao T., Ceguerra A., Breen A., Liu X., Wu Y., Ringer S. Precipitation behaviors of cubic and tetragonal Zr-rich phase in Al—(Si—) Zr alloys //J. Alloys and Compounds, 2016, No. 674, P. 125—130.
[7] Anisovich A. G. Microstructures of ferrous and non–ferrous metals. – Minsk: Belorusskaya nauka, 2015. – 131 p. - ISBN 978-985-08-1883-6.
[5] Toleuova, A.R., Dostayeva, A.M., Zharkevich, O.M., Adilkanovva, M.A. Calculating and experimental studying phase transformations in the al-zr-fe-si system alloys //Metalurgija, 2020, 59(4), страницы 543–546.
[6] Kulikov, V.Y., Aubakirov, D.R., Kvon, S.S., Dostaeva, A.M., Shcherbakova, E.P. Use of Wear-Resistant Materials in the Kazakhstani Metallurgical Industry Metallurgist, 2019, 62(9-10), страницы 1068–1072.
[7] Batessova F., Omirbay R., Sattarova G., Zholmagambetov N., Zholmagambetov S., Dostayeva A., Suleimenov, N., Medeubayev, N. Reducing industrial noise by the use of damping alloys when manufacturing mining equipment parts //Heliyon, 2023, 9(6), e17152.
[8] Aubakirov D.R., Issagulov A.Z., Akberdin A.A., Kvon Sv.S., Kulikov V.Yu., Arinova S.K., Dostaeva A.M., Chsherbakova Ye.P., Sarkenov B.B., Narembekova A.K. Influence of boron- and barium-containing modifiers on the structure of low-chromium cast iron // Heliyon, 2022, 8(11), e11496.
[9] Dostayeva A.M., Erahtina I.I., N.R. Zholmagambetov N.R., Medeubayev N.A., Zholmagambetov S.R. Investigation of aluminum-titanium alloys production and labor safety in metal smelting process // Metalurgija, 2021, 60(3-4), P. 403–406,
[11] Kovalyova T., Eremin E., Arinova S., Medvedeva I., Dostayeva A. Enhancing surface roughness of castings when sand-resin mold casting //Metalurgija, 2017, 56(1-2).
[12] Belov N. A., Dostaeva A.M., Shurkin P. K., Korotkova N. O., Yakovlev A. A. The effect of annealing on the electrical resistance and hardness of hot-rolled aluminum alloy sheets containing up to 0.5% Zr //Izvestiya vuzov non-ferrous Metallurgy, 2016, No. 3, P.48-55.
[13] Kowalski P., Nowak M., Zielinska A. Effect of Fe content on the mechanical properties and electrical conductivity of Al–Si alloys // Archives of Metallurgy and Materials, 2020, Vol. 65, No. 3, P. 987–994.
[14] Kim S., Lee J., Park H. Effect of iron content on the structure and properties of Al–Si–Mn alloys subjected to severe plastic deformation //Materials Science and Engineering A, 2024, Vol. 891, P. 145–157.
[15] Suleyev B., Issagulov A., Dostayeva A., Aubakirov D., Sultanbek T. Silicon and Manganese Effect on the Phase Composition of an Al-Fe Alloy and the Use of the ThermoCalc Software Complex for Thermodynamic Analysis //Alloys, 2025, 4, 10. https://doi.org/10.3390/alloys4020010
[16] Brown T., Chen Y., Gupta A. Aluminum alloys for electrical engineering: a review // Journal of Materials Science, 2024, Vol. 59, P. 11234–11250.

Information of the authors

Sultanbek Togzhan, doctoral student, Abylkas Saginov Karaganda Technical University
e-mail: togzhan-sultanbek@mail.ru

Dostayeva Ardak Mukhamediyevna, PhD, professor, Abylkas Saginov Karaganda Technical University
e-mail: a.dostayeva@ktu.edu.kz

Zhalel Aigerim, doctoral student, Abylkas Saginov Karaganda Technical University
e-mail: a.zhalel@kstu.kz

DOI 10.52209/2706-977X_2025_3_8 **IRSTI 55.29.33** **UDC 621.7**

The Influence of Nonlinearity System of the Hydro-volume Vibration Mechanism on its Dynamic Characteristics

Moyzes B.*, Kuvshinov K., Plotnikova I., Vavilova G., Vtorushina A.
National Research Tomsk Polytechnic University, Tomsk, Russia
*corresponding author

Abstract. This work is the result of continuation of the research in the context of vibration parameters studying while the generation of an amplitude-frequency modulated signal of a shock-vibration seismic installation. The testing bench simulates the operation of the installation. There are two circuits – low-frequency and high-frequency oscillations in the testing bench. The article presents the results of research on separate operation of high-frequency and low-frequency generators. The main resonant frequencies during generators operation were determined in the study. These frequencies can be adjusted by changing the average pressure in the elastic shells. It is possible to reduce the nonlinearity of the vibration system of the experimental stand by increasing the average pressure in the hydraulic system. The system behaves in the same way with an insignificant difference in the resonant frequencies and amplitude values of the main resonant peak, with separate excitation of oscillations from high-frequency and low-frequency generators. The frequency of additional resonance is determined. This frequency is explained by several degrees of freedom of the vibration mechanism mechanical system. Possible modes of loading the system by oscillation generators are determined.

Keywords: vibration parameters, hydro-volume vibration mechanism, nonlinearity of the system, dynamic characteristics

Introduction

The issues of studying the parameters of vibration that accompanies the operation of various equipment [1-6] or is generated by technical systems [7-10] are always of great importance.

One of the areas of scientific research is vibration seismic exploration [11-15].

This research is a continuation of scientific articles [14, 15]. The purpose of the articles is to generalize the achieved results concerning the development of a shock-vibration source of seismic signals that generates an amplitude-frequency modulated signal.

It is proposed in the research [14] a design scheme of a seismic source with a vibration system and an impact mechanism. A hypothesis is put forward about the validity of replacing the fall of the load on its swinging-oscillatory motion in the research [15].

This motion is formed by the second oscillatory circuit, thus the hydro-volume mechanism consists of

- an oscillatory system with two circuits – low-frequency and high-frequency;
- a system for forming the initial pressure p_0;
- a load that presses the mechanism to the ground.

Experimental studies were first conducted with one generator – high-frequency, then – low-frequency.

The frequency change range is $\omega_1=0\div40$ Hz and $\omega_2=0\div40$ Hz.

The scheme for conducting experimental studies of dynamic characteristics is shown in Figure 1.

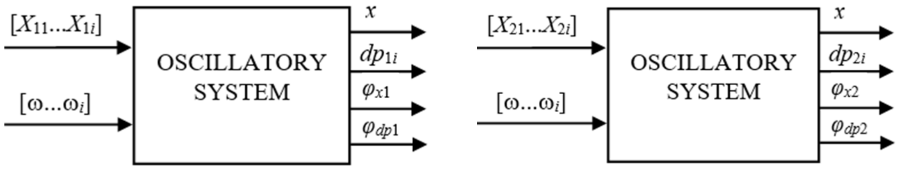

a) *b)*

a) high-frequency; b*)* low-frequency x is the output signal; $dp_{1(2)}$ are the pressure drop; $\varphi_{x1(2)}$ and $\varphi_{dp1(2)}$ are the phase shift angles

Fig. 1. – The scheme of conducting of the experimental studies with excitation by generators:\

To analyze the obtained results, dependency diagrams were constructed (Fig. 2, 3):

- natural frequency ω_0 from the values of inputs $X_1$and X_2, and average pressure p_0;
- coefficient of the ratio of the resonant amplitude of oscillation x_{res} from the values of inputs X_1 and X_2

$$K_{\text{res}} = \frac{x_{\text{res}}}{X_{1(2)}}. \tag{1}$$

Modeling according to the system (2) [14], supplemented by formulas

$$V(t) = \frac{1}{m}\int_{0}^{t} dF(t)dt\,; \tag{2}$$

$$x(t) = \int_{0}^{t} V(t)dt\,; \tag{3}$$

was carried out with the initial pressure value p_0=1 MPa.

Let us recall [14] that the following notations are used in formulas (2, 3):

- *m* is the weight of the load;
- *V* is the movement speed of the movable body of the actuator;
- *x* is the current movement of the moving body.

The rationale for choosing the mean value will be studied in the next paper.

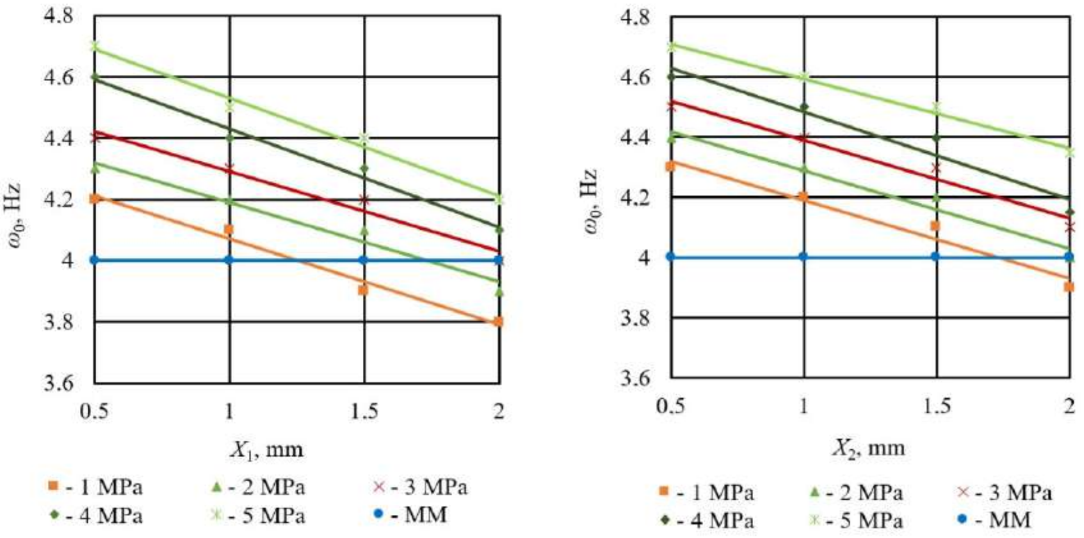

a *b*

Fig. 2. – Dependences of the natural frequency ω_0 on the values of the average pressure p_0 and inputs and X_1 and X_2: *a* – X_1; *b* – X_2; MM – mathematical model

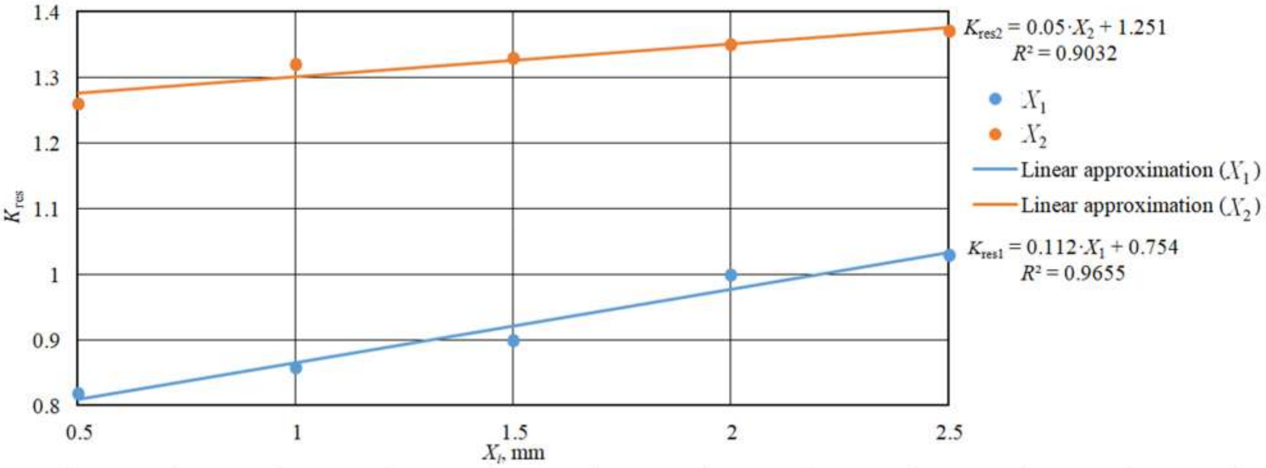

Fig. 3. – Dependence of the coefficient of the ratio of the resonant amplitude of oscillation K_{res} on the value of the inputs X_1 and X_2 at p_0=2 MPa

The results of the studies (Fig. 4, 5) [15] showed that the dynamic system of the vibration mechanism has (according to average values):

- the main resonance along the *x* coordinate and the pressure drop *dp* at the frequency

$$\omega_0 = \omega_x = \omega_{dp} \approx 4 \text{ Hz};$$

- additional resonance along the x coordinate

$$\omega_x' \approx 15.5 \text{ ▯z};$$

- additional resonance along the pressure drop *dp*

$$\omega'_{dp} \approx 3.5 \text{ ▯z.}$$

When comparing the obtained data (Fig. 4, 5) [15], we can conclude that:

• the obtained model, in the first approximation, describes the dynamic characteristics of the system relatively well;

• with different excitation options (from one or the other generator), there is a slight difference in the resonant frequencies of the first ω_{01} and second generators ω_{02}

$$\Delta\omega_0 = \omega_{0(X1)} - \omega_{0(X2)} \approx 0.1 \text{ ▯z,}$$

i.e. the oscillatory system of the vibration mechanism behaves almost identically when exposed to the generators.

At the same time, the linear model does not explain the presence of:

- additional resonance along the *x* coordinate at a frequency of ~15.5 Hz;
- a decrease in resonant frequencies with an increase in the $X_{1(2)}$ input (Fig. 2);
- a change in the value of the coefficients (Fig. 3).

1 Theoretical and Experimental Research

To assess the applicability of the developed linear mathematical model of the vibration mechanism, we will use the results of experimental studies [16-22]. It was found that a loop characteristic is observed between the change in volume dW and the pressure drop dp (Fig. 4, 5). This indicates the existing phase mismatch between dW and dp. Moreover, the direction of the loop indicates the accumulative properties of the shells.

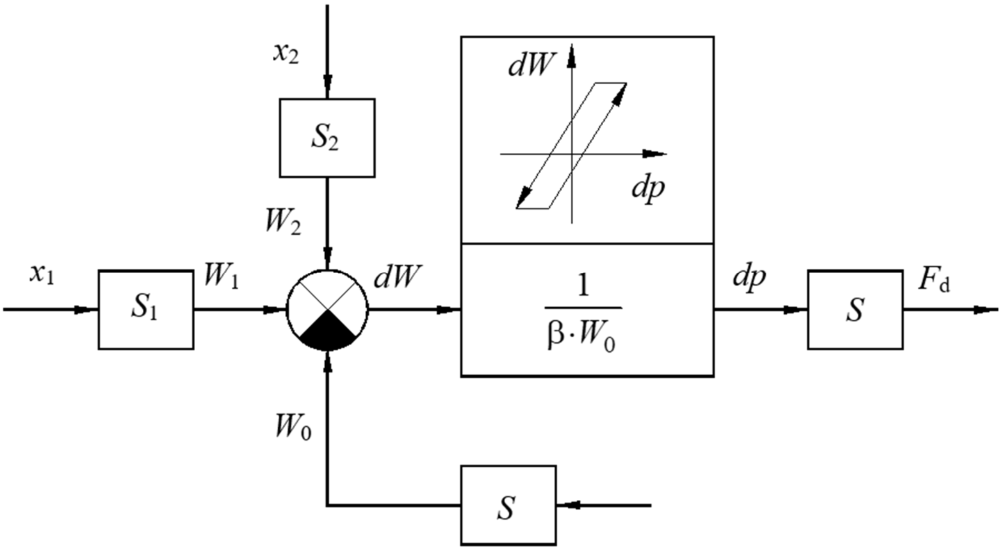

x_1, x_2 are the coordinates of the plungers moving; S_1, S_2 are the area of the generators plungers; S is the operating area of the actuator; $k_{S1}=S_1/S$ and $k_{S2}=S_2/S$ are the area ratio coefficients; W_1, W_2 are liquid volumes supplied by high and low frequency generators to the HPH; W_0, dW is the initial fluid volume in the shells and its change; β is the coefficient of elasticity of the liquid в HPH; dp is the pressure drop in operating cavities; F_d is the driving force

Fig. 4. – Segment of structural diagrams of a hydrovolume vibration mechanism

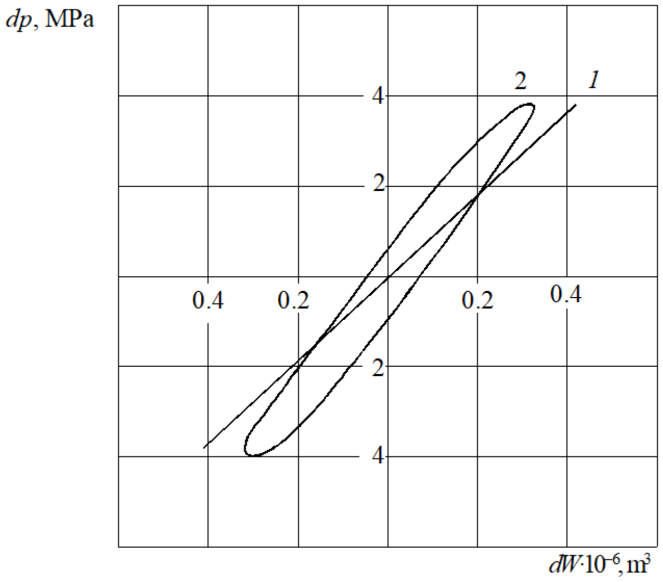

Fig 5. – Experimental characteristics of volumetric elasticity of HPH at $W_1=0.44\cdot10^{-6}$ m^3, $p_0=4$ MPa, $\omega_1=40$ Hz

Other factors influencing the nonlinearity of the system are:

- variable initial pressure p_0;
- variable compression area of elastic shells S.

In the research [14], was shown a nonlinear relationship between the strain force of the HPH F and the amount of their deformation x. In this case, a typical dependency is subject to analysis:

$$F_{\mathrm{d}} = C_p(x)\cdot dx,$$

where F_{d} are the force transmitted through the HPH to the «ground», the driving force;

C_p is the hydraulic stiffness due to volumetric deformation;

dx – deformation of HPH.

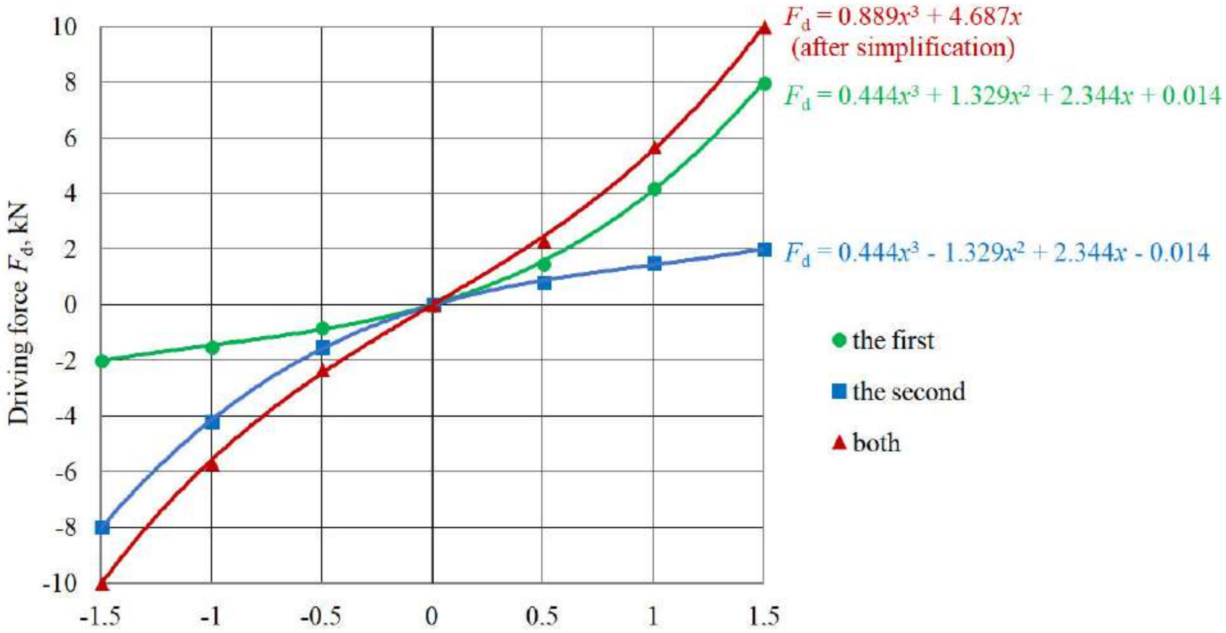

Fig 5. – Hydraulic stiffness of shells (polynomial approximation)

Thus, the system of equations (2) [15] can be rewritten as follows

$$\begin{gathered} dx = x_1' + x_2' - x; \\ F_d = C_p(x)\cdot \mathrm{d}x; \\ F_V = \alpha\cdot V; \\ F_x = C_0\cdot x; \\ dF = F_d - F_V - F_x; \end{gathered} \qquad (2)$$

$$V(t) = \frac{1}{m}\int_0^t dFdt;$$

$$x(t) = \int_0^t dV(t)dt.$$

where α is the coefficient of viscous losses in the oscillatory circuit;

C_0 is the stiffness of the main elastic bonds;

dF, F_x, F_V are the force from the current deformation of the HPH, the force of the viscous internal resistance.

The final structural diagram of the hydrovolume vibration mechanism is shown in Figure 6 [23].

The non-constancy of the average pressure leads to a change in the stiffness of the shells C_p and the total stiffness of the system C_Σ. With an increase in the average pressure, the stiffness (slope of the characteristic) increases (Fig. 6) and the nonlinearity of the system decreases.

In this case, with separate excitation from each generator, symmetrical high-frequency and low-frequency, the link $C_p(x)$ is described by different equations:

$$F_\text{d} = 0.889 \cdot x^3 + 4.687 \cdot x \text{ (after simplification)}$$

and

$$F_\text{d} = 0.444 \cdot x^3 + 1.329 \cdot x^2 + 2.344 \cdot x.$$

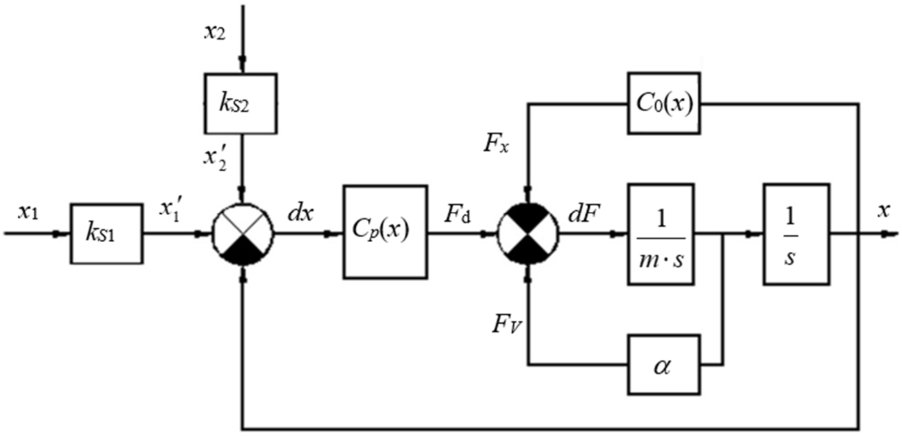

Fig 6. – Detailed structural diagram of a hydrovolume vibration mechanism with nonlinear connections

The presence of additional resonance can be explained by the fact that the system has at least three degrees of freedom, and not one along the vertical axis, designated and considered as the x coordinate (Fig. 7) [24,25].

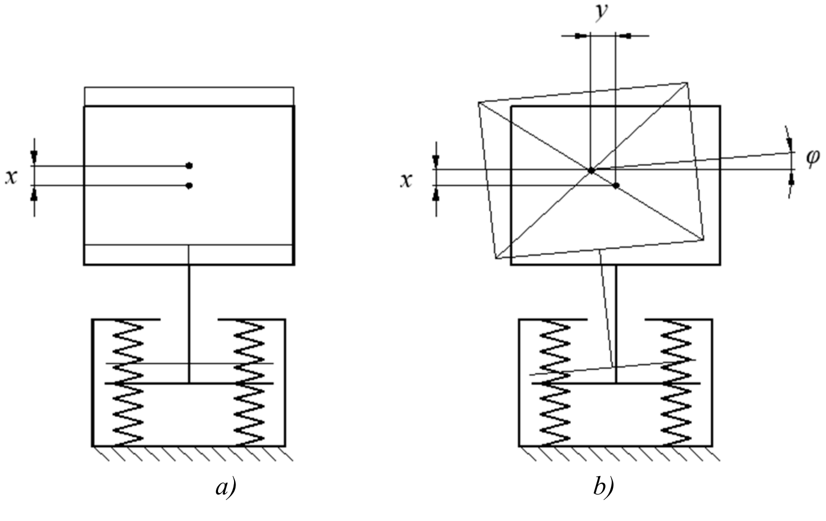

a) b)

a) considered (with one degree of freedom); b) real (with three)

Fig 7. – Mechanical system of the vibration mechanism

Since during the oscillation process the energy of oscillations along the main coordinate x is pumped into the energy of oscillations along the coordinate y and φ [24]. In a real machine, which uses the energy of a load periodically falling in a certain guide housing, which has one degree of freedom in the vertical plane, there are no such phenomena. Therefore, side resonances are not considered in detail in this work.

Based on the experimental data obtained on the vibration stand, it is possible to:

- draw a conclusion about the degree of influence of a particular generator on the amplitude of the movement of the «output link» (Fig. 8);
- propose loading modes of the oscillatory system for further research into the possibility of exciting a combined signal with the simultaneous operation of two generators.

In this case, loading modes are understood as the ratio of the value of the input of one generator to the input of the other.

Based on the obtained equations, a system of equations was compiled:

$$\begin{cases} X_1 = 0.745 \cdot x + 0.179 \\ X_2 = 0{,}597 \cdot x + 0.185 \end{cases}.$$

The calculation carried out in the Mathcad program demonstrated the following result (Fig. 9): the generators load the oscillatory system (x=0.7 mm) almost equally with the input values X_1=0.603≈0.6 mm and X_2=0.701≈0.7 mm.

We accept the ratio of the inputs

$$\frac{X_1}{X_2} = \frac{0.6}{0.7}. \tag{1}$$

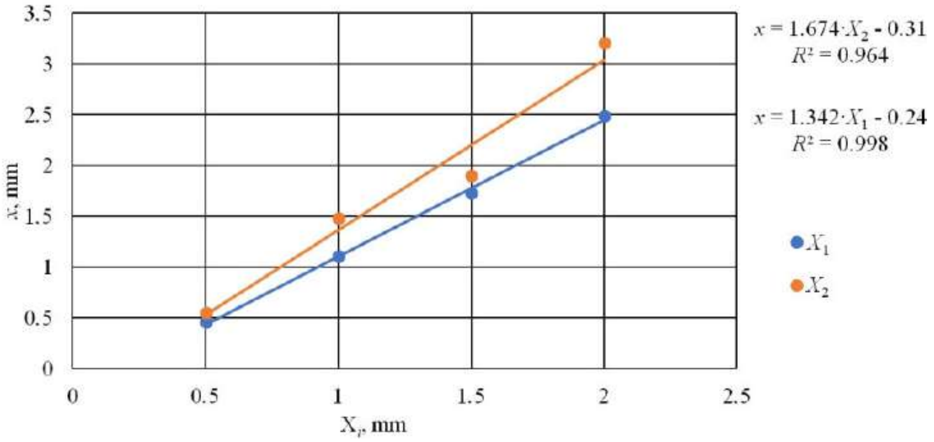

Fig. 8. – Dependence of the amplitude of the oscillation of the «output link» on the input X_1 and X_2

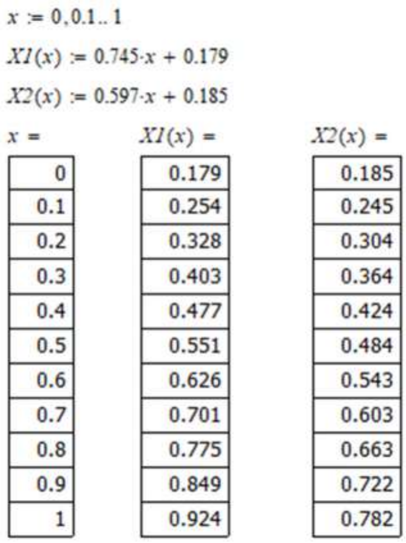

$x := 0, 0.1 .. 1$

$X1(x) := 0.745 \cdot x + 0.179$

$X2(x) := 0.597 \cdot x + 0.185$

x =	X1(x) =	X2(x) =
0	0.179	0.185
0.1	0.254	0.245
0.2	0.328	0.304
0.3	0.403	0.364
0.4	0.477	0.424
0.5	0.551	0.484
0.6	0.626	0.543
0.7	0.701	0.603
0.8	0.775	0.663
0.9	0.849	0.722
1	0.924	0.782

Fig. 9. – Calculation results

Let us derive the relation (1) theoretically. The condition that determines the same disturbing effect on the movement of the "output link" x

$$W_1 = W_2$$

or

$$X_2 = X_1 \frac{S_1}{S_2}, \tag{2}$$

where S_1 is the working area of the high-frequency generator, which has four plungers with a diameter of d_1=7 mm.

Liquid is pumped into the HPH by two pistons:

$$S_1 = 2\frac{\pi \cdot d_1^2}{4} = 76.996\ \text{mm}^2, \tag{3}$$

where S_2 is the working area of the low-frequency generator with a plunger diameter d_2=9 mm

$$S_2 = \frac{\pi \cdot d_2^2}{4} = 63.617\ \text{mm}^2, \tag{4}$$

Based on the values of areas (3, 4), given the value X_1=0.6 mm, using formula (2) we obtain

$$X_{2\text{t}} = 0.6 \cdot \frac{76.97}{63.62} = 0{,}725\ \text{mm}, \tag{5}$$

The error will be

$$\Delta X_2 = \frac{X_{2\text{t}} - X_2}{X_{2\text{t}}} = \frac{0.725 - 0.7}{0.725} \cdot 100\% = 3.44\ \%. \tag{6}$$

From (6) we conclude that the experimentally found ratio X_1/X_2 (1) can be accepted for operation.

In further studies we will accept the loading modes (1:1, 1:2, 1:3):

$$\frac{X_1}{X_2} = \frac{1.2}{1.4} = \frac{1.2}{2.8} = \frac{1.2}{3.2}. \tag{7}$$

Conclusion

The working resonance frequency of the low-frequency generator has been found, which can be adjusted by changing the average pressure p_0.

With an increase in the average pressure, the stiffness of the system increases, thereby reducing its nonlinearity.

The system "responds" equally to the disturbing effect of one or another generator. There is insignificant difference in resonance frequencies and amplitude values of resonance peaks.

The presence of additional resonance at frequency ω''_* is explained by several degrees of freedom of the mechanical system of the vibration mechanism.

It has been established that both generators can be adjusted to the same disturbing effect of the mechanical system.

References

[1] Akhmediev S.K., Filippova T.S., Oryntayeva G.Zh., Tazhenova G.D., Mikhailov V.F. Free and Forced Vibrations of the Carrier Beam of the Vehicle Chassis //Material and Mechanical Engineering Technology, 2023, Vol. 4. – P. 32-41. doi: 10.52209/2706-977X_2023_4_32.

[2] Kvon Sv.S., Kulikov V.Yu., Abylkairova M.M. Study of the Structure and Properties of 30CrMnNiMo Steel Subjected to Vibration and Heat Treatment // Material and Mechanical Engineering Technology, 2023, Vol. 2. – P. 3-9. doi: 10.52209/2706-977X_2023_2_3.

[3] Gavrilin A., Moyzes B., Zharkevich O. Constructive and processing methods of reducing vibration level of the metalworking machinery elements //Journal of Vibroengineering, 2015, Vol. 17, no 7. – P. 3495-3504

[4] Gavrilin A.N., Moyzes B.B., Kuvshinov K.A., Vedyashkin M.V., Surzhikova O.A. Determination of optimal milling modes by means of shock-vibration load reduction on tool and peak-factor equipment //Materials Science Forum, 2019, Vol. 942. – P. 87-96. doi: 10.4028/www.scientific.net/MSF.942.87.

[5] Sikhimbaev M.R., Sherov K.T., Zharkevich O.M., Sherov A.K., Tkachyova Y.O. Experimental studies of stabilization of boring cutter form – building top oscillation //Journal of Vibroengineering, 2012, Vol. 14, no 2. – P. 661-670.

[6] Plotnikova I., Vedyashkin M., Mustafina R., Plotnikov I., Tchaikovskaya O., Bastida J., Verpeta M. Optimization of the Stabilization System for Electromagnetic Suspension in Active Vibration Isolation Devices // MATEC Web of Conferences, 2016, Vol. 79. – 01019. https://doi.org/10.1051/matecconf/20167901019.

[7] Nizhegorodov A.I., Gavrilin A.N., Moyzes B.B., Kuvshinov K.A. Hydraulic drive of vibration stand for testing the robotic systems units by random vibration method // IOP Conference Series: Materials Science and Engineering, 2019, Vol. 516(1). – 012031. doi: 10.1088/1757-899X/516/1/012031

[8] Nizhegorodov A I, Gavrilin A N, Moyzes B B, Cherkasov A I, Zharkevich O M, Zhetessova G S, Savelyeva N A. Radial-piston pump for drive of test machines // IOP Conf. Series: Materials Science and Engineering, 2018, Vol. 289 (1). – 012014. doi:10.1088/1757-899X/289/1/012014.

[9]. Moyzes B., Gavrilin A., Kuvshinov K., Smyshlyaev A., Koksharova I. Using the Vibration Recorder Mobile Diagnostic Complex for Studying Vibration Processes //Material and Mechanical Engineering Technology, 2022, Vol. 3. – P. 50 – 57. doi: 10.52209/2706-977X_2022_3_50.

[10] Gavrilin A., Moyzes B., Cherkasov A., Mel'nov K., Zhang X. 2016 Mobile Complex for Rapid Diagnosis of the Technological System Elements //MATEC Web of Conferences, 2016, Vol. 79. – 01078 doi: 10.1051/matecconf/20167901078.

[11] Duan H., Zhu P., Peng S. Characteristic and processing method of SH-wave data generated by vibroseis source // Journal of Applied Geophysics, 2023, Vol. 214. – 105052. doi: https://doi.org/10.1016/j.jappgeo.2023.105052.

[12] Huang Zh., Shuai J., Hao L., et al. Investigation of radiative characteristics in the near field for shear, vertical and torsional vibroseis source //Soil Dynamics and Earthquake Engineering, 2024, Vol. 180. – 108628. doi: https://doi.org/10.1016/j.soildyn.2024.108628.
[13] Gao J., Xing X., Zhou X. Maximum deviation sliding search based stepped frequency synthesis method for marine vibroseis research //Measurement, 2022, Vol. 202. – 111799. doi: https://doi.org/10.1016/j.measurement.2022.111799.
[14] Moyzes B.B., Nizhegorodov A.I. The Study of the Parameters of Amplitude-Modulated Sweep Signal of the Shock Vibration Source of Seismic Signals // Engineering Materials, 2023, Part F1222. – P. 91-128. doi: https://doi.org/10.1007/978-3-031-38964-1_7.
[15] Moyzes B.B., Kuvshinov K.A., Nizhegorodov A.I., Vavilova G.V., Vtorushina A.N. The Study of the Dynamic Characteristics of the Hydro-volume Vibration Mechanism // Material and Mechanical Engineering Technology, 2024, Vol. 4. – P. 120-126. doi: 10.52209/2706-977X_2024_4_120.
[16] Lepetov V.A. Raschety i konstruirovanie rezino-tekhnicheskih izdelij [Calculations and construction of rubber products] / V.A. Lepetov, L.N. Yurcev. – Leningrad: Himiya, 1977. – 407 p.
[17] Lysenko E.N., Surzhikov A.P., Vlasov V.A. and et al. Synthesis of substituted lithium ferrites under the pulsed and continuous electron beam heating //Nuclear Instruments and Methods in Physics Research, Section B: Beam Interactions with Materials and Atoms, 2017, Vol. 392. – P.1-7.
[18] Lysenko E. N., Surzhikov A. P., Vlasov V. A. Malyshev A. V. and et al. Thermal analysis study of solid-phase synthesis of zinc- and titanium-substituted lithium ferrites from mechanically activated reagents Journal of Thermal Analysis and Calorimetry, 2015, № 3. – p. 1347-1353.
[19] Spivakovskij A.O. Vibracionnye konvejery, pitateli i vspomogatel'nye ustrojstva: nauchnoe izdanie [Vibrating conveyors, feeders and auxiliary devices: scientific publication] / A. O. Spivakovskij, I. F. Goncharevich. – Moscow: Mashinostroenie, 1972. – 327 p.
[20] Tarko L.M. Perekhodnye processy v gidravlicheskih mekhanizmah [Transients in hydraulic mechanisms] / L.M. Tarko. – Moscow: Mashinostroenie, 1973. – 167 p.
[21] Huang Zh., Xu H., Wang X., et al. Self-mixing interference signal analysis based on Lissajous figure convergence algorithm for vibration measurement //Measurement, 2024, Vol. 229. – 114407. doi: https://doi.org/10.1016/j.measurement.2024.114407.
[22] Zhang L., Xiao W., Fang W. A PGC demodulation scheme based on the Lissajous ellipse fitting for homodyne interferometer without using second harmonic carrier signal //Applied Acoustics, 2024, Vol. 221. – 109993. doi: https://doi.org/10.1016/j.apacoust.2024.109993.
[23] Moyzes B.B., Kuvshinov K.A., Nizhegorodov A.I., Vavilova G.V., Vtorushina A.N. //Material and Mechanical Engineering Technology, 2024, №4. – p. 120-126.
[24] Moyzes B.B., Krauin'sh P.Ya. Razrabotka vibroimpul'snogo mekhanizma s razdel'nym upravleniem vibracionnoj i impul'snoj sostavlyayushchimi [Development of a vibration pulse mechanism with separate control of vibration and pulse components] //Proceedings of the III Regional Scientific and practical Conference of students, postgraduates and young scientists "Modern technology and technology". – Tomsk: Publishing office ofTomsk Polytechnic University, 1997. – P.113-114.
[25] Prokop'ev V.N. Dinamika gidroprivoda [Hydraulic drive dynamics]. – M., Mashinostroenie, 1972 – 228 p.

Information of the authors

Moyzes Boris Borisovich, c.t.s., associate professor, National Research Tomsk Polytechnic University
e-mail: mbb@tpu.ru

Kuvshinov Kirill Aleksandrovich, senior lector, National Research Tomsk Polytechnic University
e-mail: kuvshinov@tpu.ru

Plotnikova Inna Vasilevna, c.t.s., associate professor, National Research Tomsk Polytechnic University
e-mail: inna@tpu.ru

Vavilova Galina Vasilevna, c.t.s., associate professor, National Research Tomsk Polytechnic University
e-mail: wgw@tpu.ru

Vtorushina Anna Nikolaevna, c.c.s., associate professor, National Research Tomsk Polytechnic University
e-mail: anl@tpu.ru

DOI 10.52209/2706-977X_2025_3_16 **IRSTI 55.16.99** **UDC 621.98.04**

Investigation of the Design of a Busbar Punching Tool Restored by Replacement of the Working Part with a Carbon Steel Insert

Mussayev M.[1]*, Kassymbabina D.[1], Sherov K.[2]
[1]Abylkas Saginov Karaganda Technical University, Karaganda, Kazakhstan
[2]S.Seifullin Kazakh Agrotechnical Research University, Astana, Kazakhstan
*corresponding author

Abstract. The aim of this study is to conduct a comprehensive comparative analysis of the stress-strain state of a restored busbar punching tool in order to improve its durability and performance. An overview of existing industrial methods for restoring punches and dies was carried out, including surfacing, welding, hard-facing, and thermal treatment approaches. The analysis showed that although these methods are widely used, each of them has inherent advantages and limitations related to cost, technological complexity, and the resulting service life of the tool. To overcome these challenges, a novel restoration technique is proposed, which involves replacing the worn working part of the busbar punching tool with a carbon steel insert. Numerical modeling of the stress-strain state of the restored tool was performed using the ANSYS software suite. The finite element simulations allowed for a detailed investigation of stress distribution, deformation patterns, and contact force distribution in the critical working zones of the tool under operational loads. The obtained results made it possible to identify the most heavily loaded regions of the structure, to compare them with the original tool design, and to assess the effectiveness of the proposed restoration method. The study demonstrated that the use of a carbon steel insert not only reduces localized stress concentrations but also contributes to extending the operational reliability and service life of the busbar punching tool. The findings of this research provide a practical contribution to the modernization and repair of punching tools, offering an economically viable and technically effective alternative to full tool replacement.

Keywords: busbar punching tool, mold, restoration, wear resistance, stress-strain state.

Introduction

In modern mechanical engineering, up to 70–80% of parts are manufactured using cutting operations, which ensures high productivity at relatively low production costs. In the design of technological processes and die tooling, the durability of the working tool becomes particularly important, especially in the case of busbar punching tools that are subjected to high contact loads and impact forces [1].

The main factors limiting the service life of cutting dies include abrasive and adhesive wear, chipping of cutting edges, tempering of the surface layer, and local thermal damage. These types of wear directly affect the accuracy, quality, and dimensional stability of the manufactured parts. Wear of the working elements can increase the labor intensity of the cutting process by up to 40% and the cutting resistance by up to 20%, compared to tools with sharp edges. In addition to improving the wear resistance of new tools, an important direction is the restoration of worn working elements, including busbar punching tools. These measures help extend the service life of expensive tooling, reduce the cost of purchasing new equipment, and minimize production downtime.

Research aimed at determining the applicability of punching operations, the extent and nature of wear, and tool consumption was carried out at several industrial enterprises in Kazakhstan. In particular, practical analysis and data collection were conducted at the following production facilities: Karaganda Zharyk LLP, Astana Electromechanical Plant LLP, Almaty Electromechanical Plant LLP, Asia Trafo LLP, and Kentau Transformer Plant JSC [1, 2].

The results of the research conducted under industrial conditions confirm the high degree of wear experienced by busbar punching tools during operation. It was found that the punches and dies comprising these tools are subject to intensive abrasive wear, edge chipping, and fragmentation of the working surfaces. Due to the nature of their operation, punching tools are classified as heavily loaded, since they come into direct contact with the pressed metal under conditions of high temperature, significant specific pressure, and intense friction. One of the most critical factors contributing to reduced tool life is overheating, which leads to a decrease in the strength properties of the tool material. This results in reduced hardness, plastic deformation, and in some cases, failure of the working elements. Exceeding the tempering temperature of the die material during pressing is especially critical, as it can cause deformation, loss of shape, and tool failure.

Operating conditions are also characterized by sudden dynamic loads caused by uneven distribution of pressing forces. These impact loads require a combination of high hardness and sufficient impact toughness in the tool, which is difficult to achieve with conventional tool steels and alloys. In most cases, the contradiction between hardness and toughness becomes the decisive factor in tool failure under sudden load changes. Moreover, uncontrolled release of pressure at the end of the operation can lead to microcracks and subsequent tool breakage.

Figure 1 shows photographs of broken or worn-out busbar punching tools.

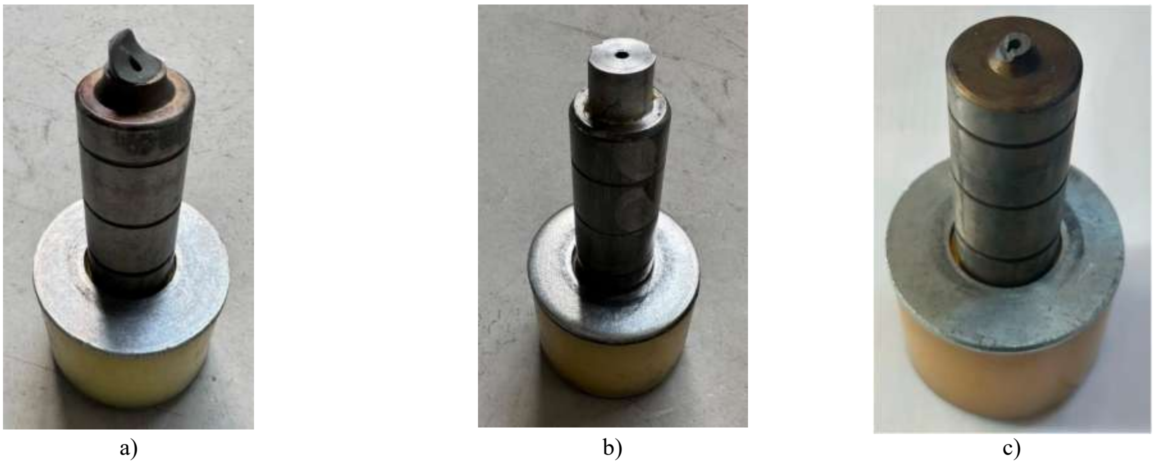
a) b) c)

Fig. 1. - Broken or worn-out busbar punching tools

Given the high wear rate, busbar punching tools are most often designed as replaceable components. This design choice necessitates their regular replacement or restoration. In this regard, the task of improving the design and manufacturing technologies of such tools becomes highly relevant, aiming to enhance their operational durability, reduce maintenance and replacement costs, and increase the overall efficiency of pressing operations. Key directions in ensuring the reliability and longevity of busbar punching tools include the development of new design solutions, the application of modern wear-resistant materials and coatings, and the optimization of equipment operating modes.

Thus, the comprehensive development of methods for enhancing the wear resistance and restoration of stamping tools is a crucial step toward improving the reliability of technological tooling, increasing product quality, and reducing production costs. The conducted studies have shown that various methods and approaches are used to restore tools and technological equipment. One of the most effective restoration approaches is surfacing the working surface with wear-resistant material.

Work [3] describes the plasma surfacing method as an effective means of restoring and improving the wear resistance of stamping tool surfaces that frequently fail. The process uses a high-temperature plasma jet (up to 15,000°C, formed using argon and helium) to melt the filler material and apply it to the surface of the part. Special attention is given to the selection of material, application technology, and optimization of surfacing parameters (current strength, torch distance, powder feed rate) to ensure high-quality coating. Recommended parameters include a current of 55–60 A, a distance of 10–12 mm, 3–4 passes with intermediate cooling, and the necessity of powder drying and sieving. The main drawback of the method is its high sensitivity to process parameters and the need for careful preparation of powder materials, as failure to comply with the technology may result in coating defects and damage to the part.

The study in work [4] focuses on restoration methods for bending dies that wear out during the production of parts such as brackets. Based on analysis of material properties and wear characteristics, the authors proposed and tested three methods: brazing of hard alloy plates, surfacing with welding electrodes, and laser surfacing with powder materials. Testing on samples made of U10A and Kh12M steels-including microstructural analysis and hardness measurements-demonstrated that the most effective methods for restoring strong and wear-resistant surfaces are welding with OZh-3 electrodes and laser powder surfacing. The application of these methods, as well as the potential replacement of die material with Kh12M steel, can significantly increase the service life of the dies and improve production performance.

In conclusion, the analysis of existing restoration methods shows that each method has its own advantages and limitations, and effectiveness largely depends on the type of damage, accuracy requirements, and available resources. Modern technologies offer high precision and minimal thermal deformation but are associated with high costs for equipment and personnel training. Traditional methods remain relevant for restoring large surface areas, although they require careful control and subsequent processing. The most rational approach appears to be the integration of different methods based on the specific task, which allows for optimizing the repair process, extending tool life, and reducing production costs.

As part of these efforts, the Department of Technological Equipment, Mechanical Engineering, and Standardization is carrying out a scientific project. The project focuses on the restoration and enhancement of the wear resistance of busbar punching tools. Particular attention is given to identifying design and technological solutions capable of addressing the shortcomings identified in the literature. As a result of the conducted research, a new tool design has been proposed, offering improved strength characteristics, maintainability, and operational durability. The aim of this study is therefore to conduct a comprehensive comparative analysis of the stress-strain state of a restored busbar punching tool in order to improve its durability and performance.

1. Methods and materials

As a result of the scientific research, a new tool design has been proposed, featuring improved strength, maintainability, and operational durability. This design is based on a composite concept that allows for the replacement of the most wear-prone working element without the need to discard the entire tool body. Such an approach not only enhances service life but also provides significant economic benefits by reducing repair costs and downtime in production. Figure 2a presents a sketch of the working part of the composite tool, illustrating its key design features.

The present research, carried out in the laboratories of the Department of Technological Equipment, Mechanical Engineering and Standardization and the Welding Institute of Abylkas Saginov Karaganda Technical University, continues earlier work aimed at increasing the durability and wear resistance of tooling equipment. Within the framework of this study, both worn-out tools retrieved from production lines and newly manufactured components intended for the assembly of composite tools were investigated. This made it possible to combine practical observations with controlled experimental analysis.

At the initial stage, a thorough examination of the actual condition of the worn working part of the tool was performed (Fig. 1). According to earlier studies and experimental data, this component is subjected to severe operational loads, including high contact pressures, cyclic thermal stresses, and abrasive wear. As a result, it often exhibits surface damage such as intensive wear, chipping, and the formation of micro- and macro-cracks. These defects critically affect the accuracy of busbar punching operations and can ultimately lead to premature tool failure. The detailed assessment carried out at this stage provided a basis for evaluating the extent of material degradation and determining the necessity and scope of restorative measures.

In the preparation stage, the worn working part of the tool was carefully removed by mechanical processing (Fig. 2b). This ensured that the remaining body of the tool could be preserved and reused without compromising its structural integrity. At the same time, new working inserts of different diameters were manufactured in order to carry out comparative testing and validation of the proposed composite design (Fig. 2c). The inserts were produced from carbon tool steel U10A, a material widely recognized for its favorable balance of hardness, wear resistance, and machinability. Its selection was substantiated in earlier phases of the research [5], where U10A demonstrated stable performance under cyclic mechanical loads and suitability for subsequent heat treatment aimed at enhancing strength and toughness.

By integrating these preparatory steps, the foundation was laid for a systematic evaluation of the composite tool's stress–strain state, enabling the subsequent modeling and experimental verification phases of the study.

a) b) c)

Fig. 2. - Sketch of the composite tool design (a), the prepared guiding part of the tool (b), and new working parts of various diameters (c)

The working parts made of U10A steel underwent heat treatment in an SNOL 3/1100 laboratory muffle furnace at the International Materials Science Center of Abylkas Saginov Karaganda Technical University (Fig.3a). This operation is critically important for forming the required microstructure and achieving the necessary physical and mechanical properties, which are essential for the tool's durability.

For carbon steels, typical heat treatment regimes include: normalization – heating to temperatures above the critical points (approximately 800-850°C), followed by holding and air cooling; quenching – heating above the critical temperatures with holding and rapid cooling in water, oil, or salt solutions; tempering – heating the quenched steel to a temperature below the critical point, holding it, and then cooling to achieve the desired toughness.

After heat treatment, the assembly of the composite tool was carried out. The working part was inserted into the guiding part for subsequent permanent joining (Fig.3b).

a) b)

Fig. 3. - Heat treatment in the SNOL 3/1100 muffle furnace (a) and the tool assembly process (b)

The wear of the working surface of the busbar punching tool is largely determined by its stress–strain state in the deformation zone. Given the multi-stage nature of the punching processes, it is advisable to use mathematical modeling, which enables an unlimited number of virtual experiments with minimal labor costs [6].

To study the stress–strain state of the busbar punching tool, a numerical simulation method was employed using the ANSYS software package. In particular, the Explicit Dynamics module was utilized for effectively tracking the propagation of shock waves, analyzing large deformations, and predicting material failure.

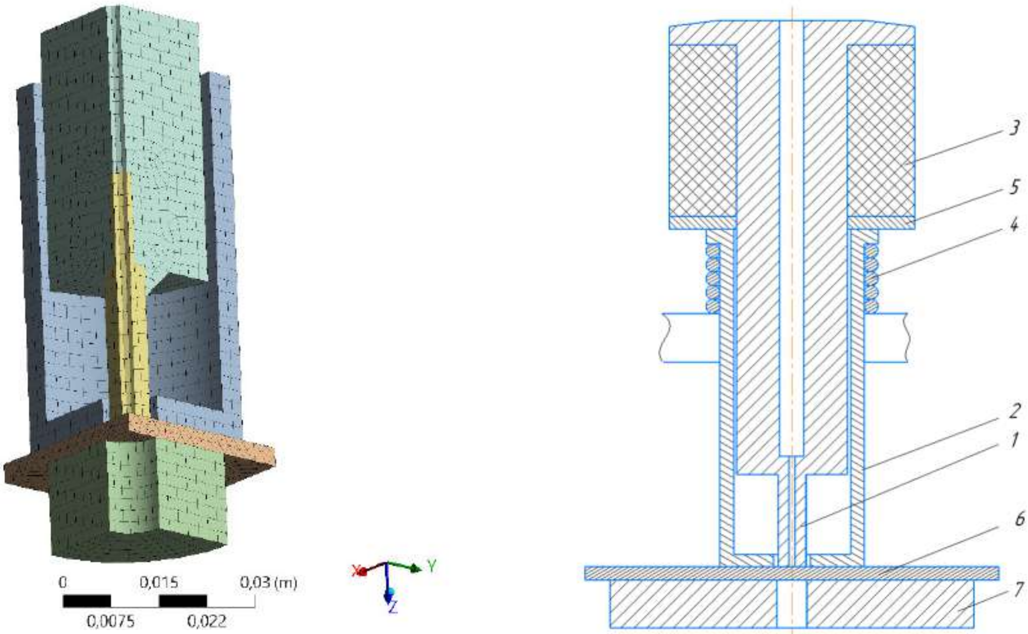

a) b)

Fig. 4. - Finite element model of the tool (a) and punching scheme (b): 1 – punch; 2 – punch holder; 3 – buffer; 4 – spring; 5 – washer; 6 – workpiece; 7 – die

2. Results and discussion

A finite element model of the studied object was developed within the simulation environment. To improve computational efficiency and reduce calculation time, a symmetric quarter-section of the full model was used for simulation (Fig.4a).

At each stage of the modeling process, the stresses, deformations, and distribution of contact forces in the working zones of the tool were determined. The obtained results made it possible to identify the critically loaded areas of the structure and assess the effectiveness of the proposed restoration and modernization methods.

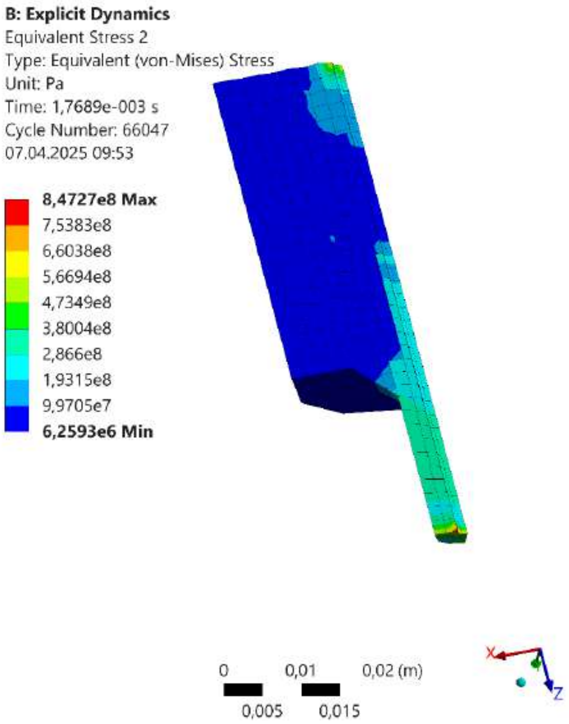

Fig. 5. – Stress-strain state of the composite tool

The highest stresses, indicated in red on the color scale, are concentrated exclusively at the cutting edge of the tool. As the distance from the cutting edge increases into the body of the tool, the stress values drop sharply, transitioning from maximum to significantly lower levels.

For the working part of the tool made from carbon tool steel, the value of 847.27 MPa is considered significant. Carbon tool steels (e.g., grades U8, U10, U12), after proper heat treatment (quenching and tempering), typically exhibit a yield strength in the range of 600-1000 MPa and an ultimate tensile strength of 1000-1200 MPa or higher. Therefore, the obtained maximum stress may fall within the acceptable strength limits of high-strength carbon tool steel.

This indicates that, under the given loading conditions, the cutting edge of the tool is unlikely to experience immediate failure and is capable of withstanding such stresses without significant plastic deformation or brittle fracture.

Funding. This work was carried out within the framework of a scientific project funded by the Committee of Science of the Ministry of Science and Higher Education of the Republic of Kazakhstan (grant No. AP19578884).

Conclusions

The conducted research revealed the issue of premature wear of busbar punching tools, as well as difficulties in their restoration due to the lack of an established technological process for repair and recovery. To address this problem, a restoration method was proposed involving the replacement of the tool's working part with a carbon steel insert.

An experimental prototype of the restored tool was manufactured in the department's laboratory facilities.

Using numerical simulation with the ANSYS software package, the stress-strain state of the busbar punching tools was analyzed. The simulation focused on determining the stresses occurring in the tool's working zones, deformations, and the distribution of contact forces.

In the simulation of the busbar punching tool restored by replacing the working part with a carbon steel insert, it was found that the maximum stress in the working area reaches 847.27 MPa, which falls within the acceptable strength limits for high-strength carbon tool steel.

The results of the computer simulation confirmed the applicability of the proposed restoration method for busbar punching tools. Further research should include experimental testing of tools restored by surfacing and by replacement of the working part with a carbon steel insert, both under laboratory and industrial conditions.

Acknowledgment. This research was conducted as part of a project funded by the Committee of Science of the Ministry of Science and Higher Education of the Republic of Kazakhstan (grant No. AP19578884).

References

[1] Mussayev M., Sherov K., Kassymbabina D., Abdugaliyeva G., Donenbayev B., Kardassinov S., Karsakova N., Tussupova S. Research of wear and increasing wear resistance of the working part of busbar punching tools by surfacing method // Journal of Applied Engineering Science, Vol. 3, 2024, pp. 654-664 https://doi.org/10.5937/jaes0-51175

[2] Mussayev M.M., Donenbaev B.S., Sherov K.T., Kasymbabina D.S., Aman I.M. Shinateskish bildekterdin quraldary`ny`n tozu

sipaty`n zertteu zhane taldau [Analysis and investigation of the wear nature of tools of busbar punching machines] // Nauka i texnika Kazahstana, – Pavlodar: Izd-vo «Toraighyrov University», №2, 2023 – pp. 48-56 https://doi.org/10.48081/RJUO1188
[3] Shtempel O.P., Pilipenko S.V., Fruczkij V.A. Vosstanovlenie shtampovoj osnastki plazmennoj naplavkoj [Restoration of die tooling by plasma surfacing] //Proc. Int. Sci.-Tech. Conf. Energy Saving in the Agro-Industrial Complex: Minsk, 2019. - pp. 195-198.
[4] Galimov E.R., Abdullin I.A., Belyaev A.V., Sirotkina L.V. Methods of restoring worn elements of dies // Vestnik Kazanskogo Tekhnologicheskogo Universiteta, №23(17), 2014, pp. 68-69
[5] Mussayev M.M., Kassymbabina D.S., Abdugalieva G.B., Bobeev A.B. Metallographic study of samples from busbar punching tool material surfaced with ESAB OK Tubrodur 35GM wire // Nauka i Tekhnika Kazakhstana, no. 3, 2024, pp. 52–65, https://doi.org/10.48081/PLNE2708
[6] Kokorin V.N., Podmarev D.R., Khromov M.A., Mishov N.V., Shiller N.V. Study of the stress-strain state of billet material under loading with a wedge-shaped tool // Uprochnyayushchie Tekhnologii i Pokrytiya, (7), 2020, pp.13.
[7] Navas C., Conde A., Fernández B., Zubiri F., de Damborenea J. Laser coatings to improve wear resistance of mould steel //Surface and Coatings Technology, 2025, vol. 194, no. 1, 136-142, DOI: 10.1016/j.surfcoat.2004.05.002
[8] Aliev S.B., Suleev B.D. Study and calculation of the disk-milling tool //Ugol', (11), 2018, pp. 32-34 http://dx.doi.org/10.18796/0041-5790-2018-11-32-34
[9] Jhavar S., Paul C., Jain N. Causes of failure and repairing options for dies and molds: A review //Engineering Failure Analysis, 2013, vol. 34, 519-535 DOI: 10.1016/j.engfailanal.2013.09.006
[10] Pleterski M., Tušek J., Kosec L., Muhič M., Muhič T. Laser Repair welding of molds with various pulse shapes. //Metalurgija, 2010, vol.49, 41-44
[11] Suslov A., Inyutin V., Fyodorov V. Technological increase of cutting-out punch life with laser alloying //Science intensive technologies in mechanical engineering, 2021, vol.3, 36-42 DOI: 10.30987/2223-4608-2021-3-36-42
[12] Choi S-W., Kim Y-S., Yum Y-J., Yang S-Y. A Study on Strengthening Mechanical Properties of a Punch Mold for Cutting by Using an HWS Powder Material and a DED Semi-AM Method of Metal 3D Printing. Journal of Manufacturing and Materials Processing, 2020, vol. 4(4), 98. DOI: 10.3390/jmmp4040098
[13] Kuanov I., Sherov K., Usserbayev M., Mussayev M., Abdugaliyeva G., Ainabekova S., Yessirkepova A., Alipbayev Z. Experimental Study and Computer Modelling of Thermal Friction Treatment Process of the HARDOX 450 Steel // International Review of Mechanical Engineering, vol. 17, no. 7, 2023, pp. 305-312 https://doi.org/10.15866/ireme.v17i7.23773

Information of the authors

Mussayev Medgat, PhD, ass. professor, Abylkas Saginov Karaganda Technical University
e-mail: m.mussayev@ktu.edu

Kassymbabina Dana, PhD student, Abylkas Saginov Karaganda Technical University
e-mail: d.kasymbabina@ktu.edu.kz

Sherov Karibek, d.t.s., professor, S.Seifullin Kazakh Agrotechnical Research University
e-mail: shkt1965@mail.ru

DOI 10.52209/2706-977X_2025_3_22 **IRSTI 81.09.03** **UDC 691.5**

Study of Magnesite Binders' Resistance in Liquid Aggressive Environments

Miryuk O.A.*
Rudny Industrial University, Rudny, Kostanay Region, Kazakhstan
*corresponding author

Abstract. The study presents the results of operational properties of magnesia binders. The research objective is to determine the nature of aggressive liquid media impact on magnesia binders of various compositions. Comparative tests of strength properties of caustic magnesite and a combined magnesia-slag binder were carried out. Diffractometric analysis was used to study binders' composition. Binders' microstructure was studied by electron microscopy. The nature of impact of water, chloride and sulfate solutions on binders' strength was estimated by a resistance coefficient. Effectiveness of combination of caustic magnesite and metallurgical slag was proven. Activating effect of the magnesia binder allows latent compounds of metallurgical slag to be involved in the hydrate formation processes. Expediency of using a complex grout containing solutions of magnesium chloride and sulfate for magnesia binders is shown. Aggressive effect of water and salt solutions on the strength properties of magnesite binders was studied. Information on the change in strength of binders after various periods of exposure to aggressive liquids was provided. The causes of destructive processes occurring in the magnesite binders were identified. Magnesium pentahydroxychloride's decisive role in the formation of durability of magnesite stone was confirmed. The nature of impact of aggressive salt environments on durability of binders of various compositions was established. Technological methods for increasing durability of magnesite binders in the liquid environments were proposed, consisting in the rational minimization of magnesium pentahydroxychloride due to the use of a combined binder and (or) complex salt grouting fluids.

Key words: caustic magnesite, metallurgical slag, combined binders, salt aggression, water resistance.

Introduction

Concrete is a common composite material, its quality largely determines the efficiency of construction. Technological and operational properties of concrete are determined by a binder, which acts as a matrix in the composite material. Cement concretes dominance is due to their high construction and technical indicators and durability. High resource intensity of cement production, accompanied by large CO_2 emissions [1] – [2] predetermines the need for active distribution of low-energy binders with a small carbon footprint.

Caustic magnesite is a type of magnesite binder obtained by firing magnesite rock at a temperature not exceeding 800°C. Comparative characteristics of Portland cement and caustic magnesite allow you to evaluate advantages and identify problems of each binder.

Portland cement is based on calcium silicates, a binder also contains calcium aluminates and aluminoferrites. To obtain a plastic mass (dough), cement is mixed with water. When cement phases interact with water, the hydrated compounds of various compositions are formed, mainly of a weakly crystallized structure. Heat and moisture treatment is used at a temperature of 80 – 95°C to accelerate hardening of cement concrete.

Caustic magnesite consists mainly of magnesium oxide. Caustic magnesite is mixed with solutions of magnesium chloride or sulfate to ensure active magnesium oxide hydration. Preference for magnesium chloride solution is due to binder's intensive hardening and high strength. Main hydrated formations of caustic magnesite mixed with magnesium chloride solution are crystalline compounds of neutral composition – magnesium hydroxychlorides. Compared to Portland cement, the caustic magnesite does not require a humid environment for hardening, it is characterized by intensive increase in early strength, which makes it possible to exclude heat treatment for accelerated hardening of a binder. Design strength values of caustic magnesite are not inferior to similar indicators of high-grade Portland cement. Magnesia binders are favourably distinguished by increased adhesion to various types of filler; this contributes to creation of a wide range of composite materials [3] – [7]. Crystalline base of the hardened magnesite stone ensures durability of a highly porous structure of cellular concrete [8] – [10]. Due to significant amount of chemically bound water, magnesite materials are fire-resistant and suitable for biological protection. Activating ability of the mixture of magnesium oxide and chloride in relation to various substances allows even latent materials to be involved in the processes of structure formation and hardening. This principle underlies the resource-saving technology of combined (mixed) magnesite binders, in which up to 30 – 50% of caustic magnesite is replaced by natural and man-made origin materials [11] – [14].

Low water resistance of magnesite binders prevents the widespread use of caustic magnesite despite its unique properties. When exposed to a humid environment, the main hydrates are destroyed, and binder's strength is significantly reduced. A number of technological solutions were proposed to solve the urgent problem of increasing water resistance of magnesite binders. The first group of measures involves introduction of additives that help increase the resistance of magnesite hydrates by changing their structure [15] – [17]. The second group of solutions is based on the use of sulfate salt solutions instead of magnesium chloride solution, which ensures formation of magnesium hydroxy sulfates that are more resistant to water [18] – [21]. The third group of measures is associated with replacement of caustic magnesite with the combined binders containing mineral components of various compositions [22] – [25]. Increased water resistance of combined magnesite binders is achieved by forming new, water-resistant compounds based on the mineral components.

Along with the aquatic environment, during their operation concretes are exposed to aggressive effects of salt solutions, for example, sodium and magnesium sulfates in the groundwater, sodium and magnesium chloride present in the seawater.

A mechanism and consequences of destructive salt effects on the cement stone are known [26].

Information on the effect of salt solutions on magnesite materials' performance properties is very limited [27] – [28].

The research objective is to study the effect of aggressive liquid environments on durability of magnesite binders of various compositions.

1. Methods and materials

The object of the study was a combined magnesite-slag binder consisting of caustic magnesite grade PMK-75 and metallurgical granulated slag. The main phase of caustic magnesite is magnesium oxide. The phase composition of metallurgical slag includes calcium and magnesium silicates (rankinite $3CaO{\cdot}2SiO_2$, okermanite $2CaO{\cdot}MgO{\cdot}2SiO_2$), calcium aluminosilicates (gehlenite $2CaO{\cdot}Al_2O_3{\cdot}SiO_2$), amorphous phases (Figure 1a). Chemical composition of the binder components is given in Table 1. Properties of caustic magnesite, studied during experiments were adopted for comparison of binders with different compositions.

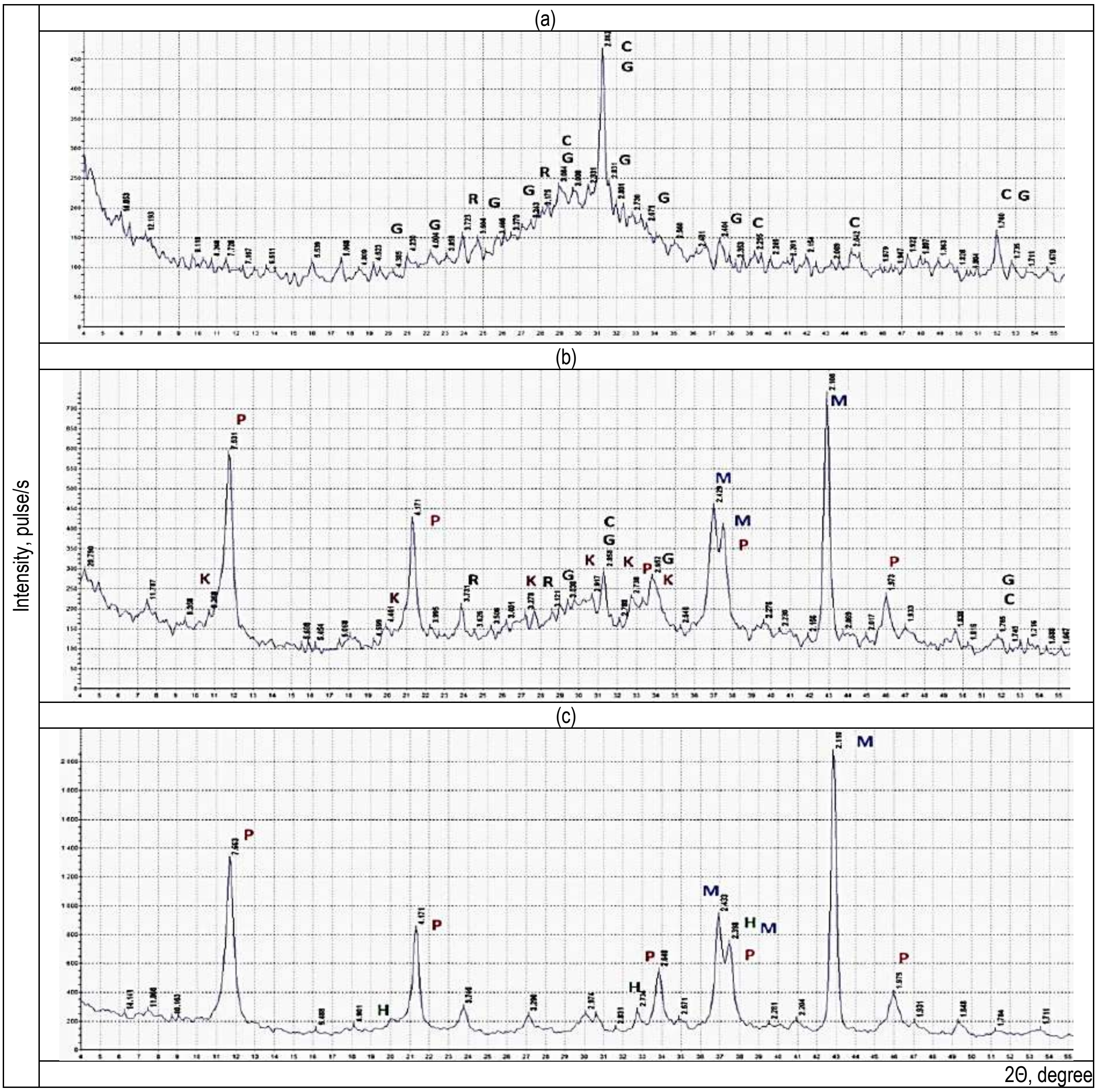

C – okermanite, G – gehlenite, R – rankinite, M – magnesium oxide, H – brucite, P – magnesium pentahydroxychloride, K – hydrates based on slag compounds

Fig.1. – Diffraction patterns of metallurgical slag (a), hardened magnesia-slag binder (b) and hardened caustic magnesite (c)

Table 1. Chemical components of magnesite binder

Material name	SiO_2	Al_2O_3	Fe_2O_3	CaO	MgO	SO_3	Others	Loss on ignition
Caustic magnesite	1.1	0.5	2.3	2.7	87.5	0.1	0.2	5.6
Metallurgical slag	44.0	14.1	0.7	32.7	5.1	2.1	1.3	–

Magnesia-slag binder was obtained by joint grinding of components in the «E-max» vibration mill. Magnesia binders were mixed with magnesium chloride and magnesium sulfate solutions and their combinations. Density of salt solutions was determined with a hydrometer.

Strength properties of a binder were determined on 20x20x20 mm samples by testing on PGM-1000MG4 hydraulic press after a specified curing period. Resistance of the hardened binder to aggressive liquids was estimated by the resistance coefficient taking into account the samples strength after exposure to an aggressive environment for a specified period and samples strength before immersion into a liquid medium. Phase composition of the binders was determined using DRON-3M diffractometer with BSV-24 X – ray tube with CuK α-radiation. Microstructure of the hardened stone was examined using a JSM-649OLV scanning electron microscope.

2. Results and discussion

Addition of 10 – 50% metallurgical slag to the caustic magnesite results in a 5 – 25% decrease in consumption of salt solution to obtain plastic dough (Figure 2). Magnesia-slag binders are characterized by slow hardening during the first three days; with increase in the slag content, the early strength of binders decreases by 4 – 22% (Figure 2). With subsequent hardening, strength properties of the combined binders increase. At the age of 28 days, strength of the binders increases as the technogenic component's content increases. Strength of the combined binder containing 50% slag is 46% higher than the strength of caustic magnesite. The increased strength properties of the magnesia-slag binder are due to changes in the hydrates composition. Features of hydrate formation of the combined magnesia binder are: increased activity of MgO, minimization of brucite $Mg(OH)_2$ content due to its binding into the magnesium pentahydroxychloride $5Mg(OH)_2 \cdot MgCl_2 \cdot 8H_2O$ (5 – form) and the hydrates based on slag compounds (Figure 1b). According to diffractometric analysis, a phase composition basis of magnesia-slag binder's stone is represented by magnesium pentahydroxychloride, characteristic of caustic magnesite. Moreover, the amount of 5 – form is proportional to the share of caustic magnesite in the binder (Figure 1b). The presence of free unhydrated magnesium oxide indicates incomplete implementation of the binding properties of caustic magnesite (Figure 1c).

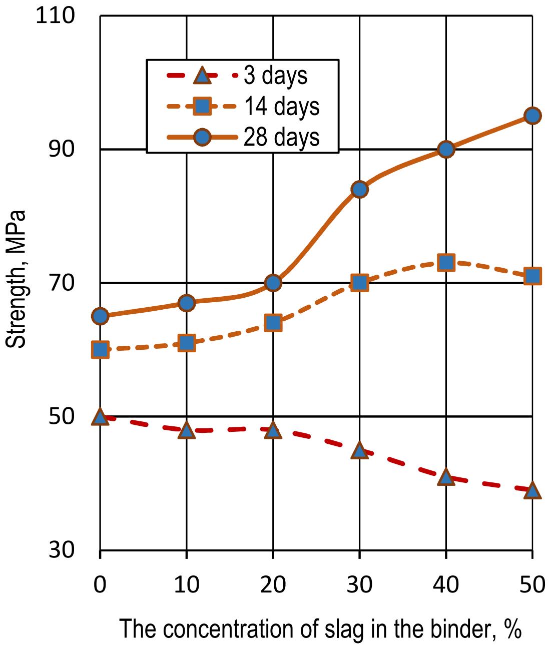

Fig. 2. – Effect of metallurgical slag content on the strength of air-cured magnesia binders

Preference for magnesium chloride solution for mixing magnesite binders is due to significant hardening rate and high strength of the hardened stone. To increase binder's resistance to water, it is recommended to use the solutions of sulfate salts [18] – [21]. However, replacing a magnesium chloride solution with magnesium sulfate or iron sulfate solutions is accompanied by a decrease in strength of caustic magnesite [18] – [21]. Possibility of using combined salt solutions consisting of magnesium chloride solution (density is 1250 kg/m^3) and magnesium sulfate (density is 1210 kg/m^3) for mixing caustic magnesite was studied (Figure 3). Samples of hardened binder aged 7 days were immersed into aggressive environments (water, magnesium chloride and sodium sulfate solutions with a density of 1050 kg/m^3). Binders were tested at the age of 28 days from the moment of mixing.

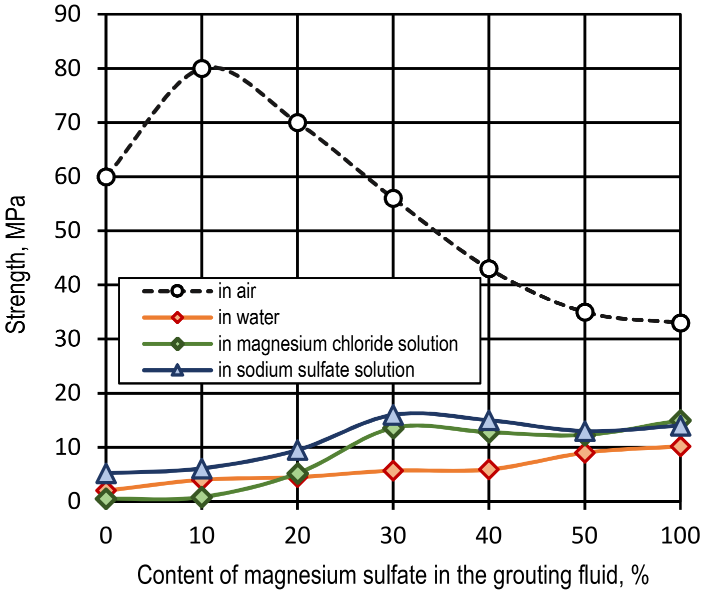

Fig. 3. – Effect of combined grouting fluid on strength of caustic magnesite under various conditions

Presence of 10 – 20% magnesium sulfate in the setting solution increases the strength of the air-hardening binder by 17 – 33%, while with a content of 30 – 50% magnesium sulfate, the strength of the binder decreases by 7 – 42%. With a content of 50% or more magnesium sulfate in the setting solution, the effect of this salt on hardening of caustic magnesite dominates. Presence of samples in liquid media is accompanied by a decrease in strength compared to samples hardened in air. The greatest decrease in strength is observed for binders for which combined solutions containing 0 – 20% magnesium sulfate were used for mixing. Analysis of the test results shows that when using a combined sulfate-chloride sealer containing 20 to 40% magnesium sulfate, it is possible to achieve increased resistance to aggressive environments while ensuring the strength of the air-hardening binder comparable to the strength of caustic magnesite based on magnesium chloride.

Comparative studies of the performance properties of caustic magnesite and magnesia-slag binder containing 50% of the technogenic component were conducted. A magnesium chloride solution (density 1250 kg/m^3) and a sulfate-chloride solution containing 50% magnesium chloride (density 1250 kg/m^3) and 50% magnesium sulfate (density 1210 kg/m^3) were used to mix the binders. For easy description of binders, the following abbreviations were introduced: MX – caustic magnesite mixed with magnesium chloride solution; MC – caustic magnesite mixed with sulfate-chloride solution; SX – magnesia-slag binder mixed with magnesium chloride solution; SC – magnesia-slag binder mixed with sulfate-chloride solution. After 7 days of air hardening, binder samples were placed into the liquids of various compositions (water, magnesium chloride and magnesium sulfate solutions with a density of 1100 kg/m^3). The choice of composition of aggressive salt solutions is determined not only by t distribution of the salts in the operational environment of concrete, but also by participation of salts in the structure formation of the binders under study.

Figure 4 shows the data on the change in strength of binder samples under different conditions. The age of samples is indicated from the moment of mixing, therefore duration of the samples' stay in liquid media is 7 days less than the indicated age. To compare binders’ strength, the indicators of caustic magnesite mixed with magnesium chloride solution and hardened in air are taken as a standard. Along with the assessment of the strength indicators of binders in liquid media, it is very important to compare the values of a resistance coefficient of these substances at the final stage of testing (Figure 5).

Analysis of air-curing binders strength indices. Replacement of 50% caustic magnesite with metallurgical slag promotes an increase in the strength of magnesia-slag binder, mixed with magnesium chloride solution, by 16% in the early stages and by 54% at the age of 28 days. When using a sulfate-chloride solution, the strength indices of caustic magnesite MC and magnesia-slag binder SC are comparable, and compared to the standard, they decrease by 1.3 – 1.6 times. It is noteworthy that the strength at the early stages of hardening is more sensitive to a decrease in magnesium chloride in the salt solution. A stable increase in the strength of all binders indicates ongoing structure formation processes over time. A comparative analysis of the strength properties of air-hardening binders revealed the highest strength values for magnesia-slag binder SX, mixed with magnesium chloride solution. This is due to the favorable combination of crystalline magnesium pentahydroxychloride and weakly crystallized hydrates based on slag phases (Figure 1b).

Analysis of the influence of the aqueous environment on the strength of binders. The effect of water on all magnesia binders is accompanied by a decrease in strength. This fact is explained [29] – [30] by decomposition of magnesium pentahydroxychloride with the formation of magnesium hydroxide. The nature of change in the strength of the binders under study corresponds to known scientific concepts.

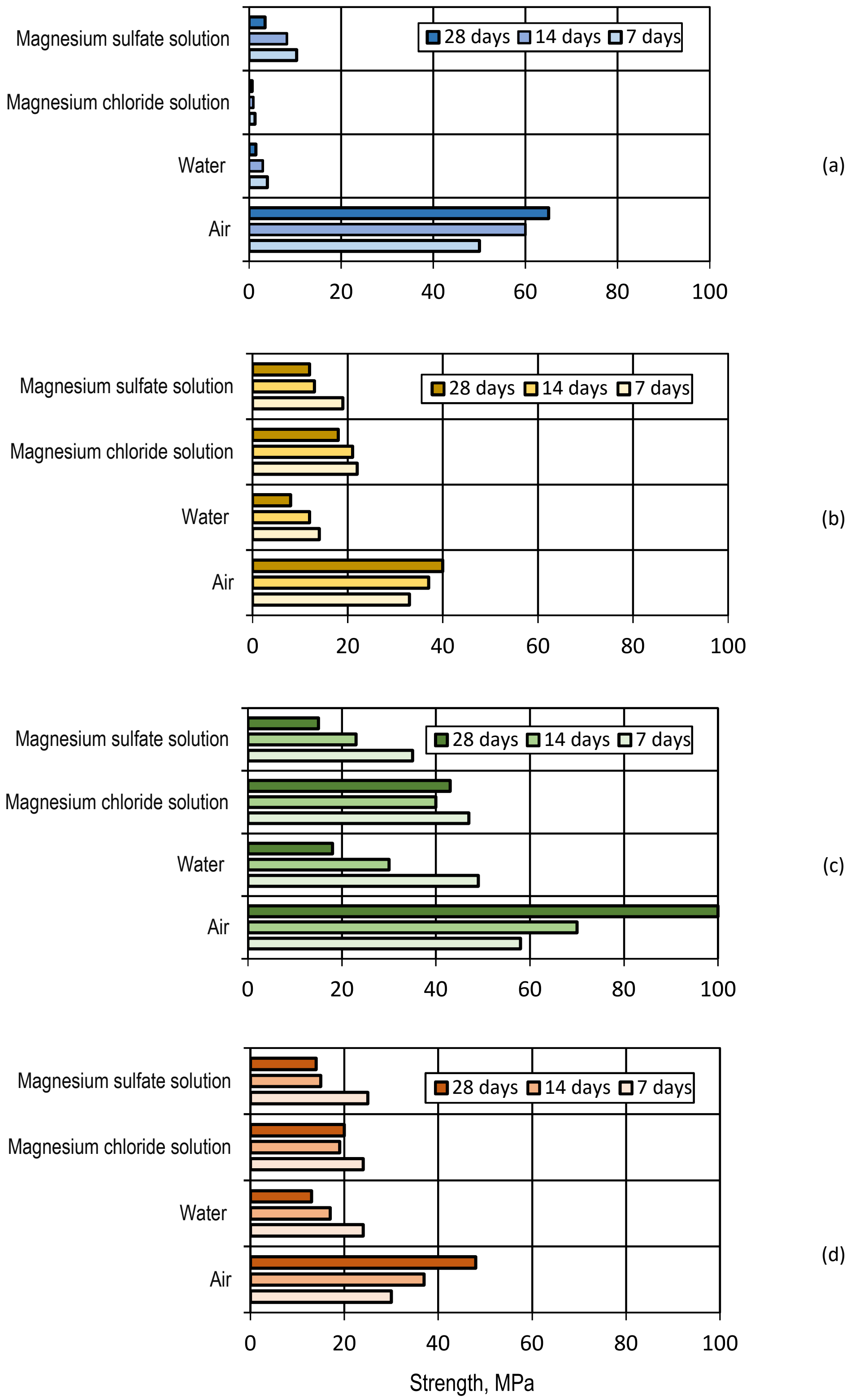

(a) – MX; (b) – MC; (c) – SX; (d) – SC

Fig. 4. – Influence of the hardening environment on strength of magnesia binders of various compositions

The most intense rates of strength decline were noted for caustic magnesite of oxychloride hardening MX, which has the highest content of unstable magnesium pentahydroxychloride. MX samples differ from samples of other binders by the presence of a crack network (Figures 6a, 6c, 6e). Cracks, along with decomposition of the structure-forming phase $5Mg(OH)_2 \cdot MgCl_2 \cdot 8H_2O$, contributed to a decrease in the strength of the MX binder.

The crack network in the structure of magnesia stone is a consequence of the formation of $Mg(OH)_2$ both due to decomposition of magnesium pentahydroxychloride and due to hydration of free magnesium oxide. Magnesia slag binder of oxychloride hardening SX is characterized by a water resistance coefficient of 0.85 after 3 days of continuous exposure to water (Figure 4c). As time passes, the water resistance coefficient decreases on SX.

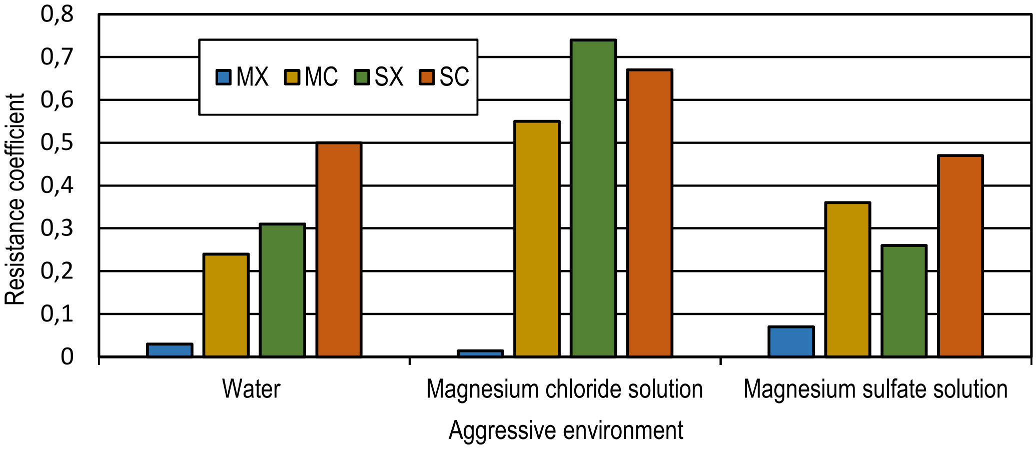

Fig. 5. – Resistance coefficient of binders after 21 days of testing in aggressive environments

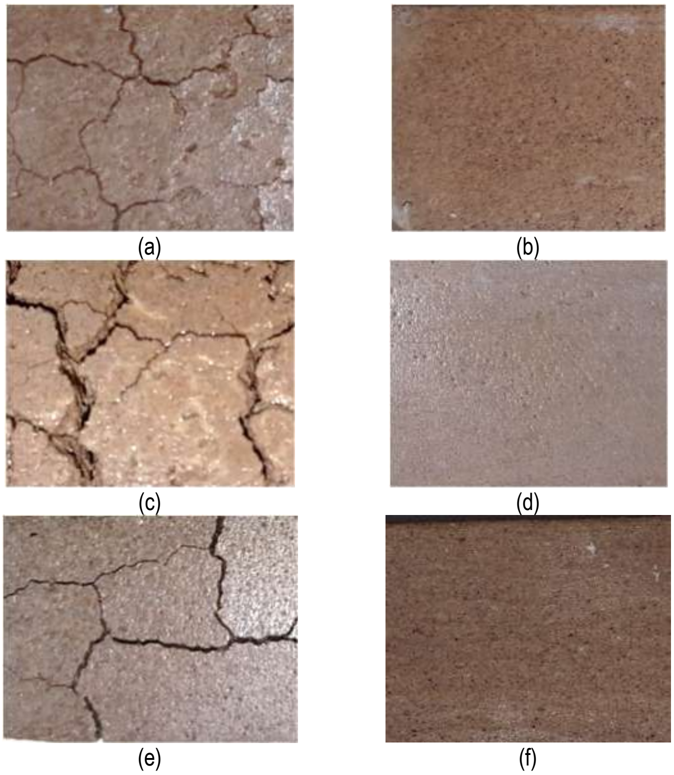

a) – MX (water); b) – SX (water); c) – MX (magnesium chloride solution); d) – SX (magnesium chloride solution); e) – MX (magnesium sulfate solution); f) – SX (magnesium sulfate solution)

Fig. 6. – Appearance of samples after exposure to aggressive environments:

Binders MC and SC, mixed with a sulfate-chloride solution, demonstrated increased water resistance compared to caustic magnesite of oxychloride hardening. After the first 3 days of exposure to water, the water resistance coefficient of binder MC was 0.42 (Figure 4b), and that of binder SC was 0.80 (Figure 4d). During subsequent testing, binders mixed with a sulfate-chloride solution demonstrated decreased sensitivity to the effect of water, as evidenced by a tendency to stabilize strength indicators.

The highest water resistance coefficient was achieved for binder SC (Figure 5). Increased water resistance of magnesia-slag binder is provided by the features of the microstructure (Figures 7c, 7d), the basis of which is made up of lamellar crystals of magnesium pentahydroxychloride formed in the environment of slag compounds that form weakly crystalline hydrates. Needle-shaped crystals of magnesium pentahydroxychloride, forming the structure of the MX binder, are less resistant to the effects of a liquid medium (Figures 7a, 7b).

Analysis of the strength indices of binders exposed to magnesium chloride solution. For oxychloride-hardened caustic magnesite MX, exposure to $MgCl_2$·solution turned out to be the most destructive both in comparison with other test conditions and in comparison with other binders (Figures 4 and 5). Cracks appeared on the MX samples, indicating an intense effect of expansive phases (Figure 6c).

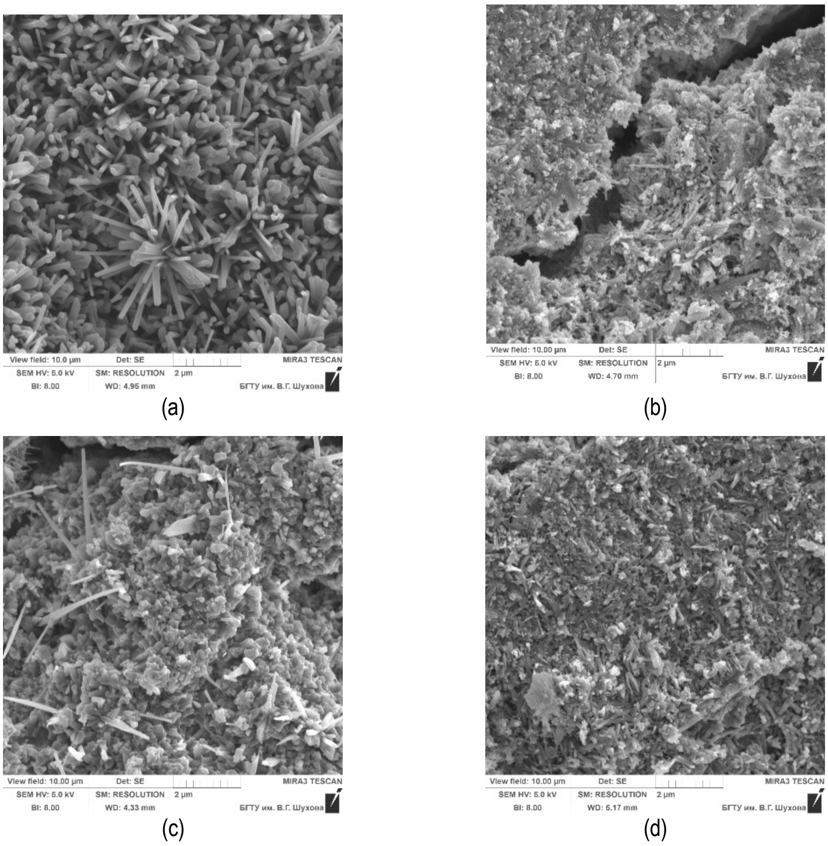

(a) – MX (after 7 days of air hardening); (b) – MX (after 3 days of exposure to water);
(c) –SX (after 7 days of air hardening); (d) – SX (after 3 days of exposure to water)

Fig.7. – Microstructure of magnesite binder stone:

The dominant expansive effect is exerted by secondary magnesium pentahydroxychloride, which is formed during the interaction of an aggressive $MgCl_2$ solution with magnesium oxide and hydroxide, including that formed during the decomposition of the 5 – form. The resistance coefficient of caustic magnesite MC, mixed with a sulfate-chloride solution, equal to 0.55 – 0.67, exceeds the similar indicator of this binder in other liquid media. The integrity of the structure of the MC samples is due to the limited content of unstable magnesium pentahydroxychloride and the presence of magnesium hydroxysulphates.

The aggressive effect of the $MgCl_2$ solution on the oxychloride magnesia-slag binder SX is insignificant: the resistance coefficient at different test periods was 0.74 – 0.81. The strength values of the SX binder exposed to the $MgCl_2$ solution are comparable to or exceed the strength indicators of other binders that hardened in air (Figure 4). Under the influence of magnesium chloride solution, the hydraulic activity of latent slag compounds is activated, which contributes to the formation of an additional amount of hydrates that compact the structure of the SX stone.

Analysis of strength indices of samples exposed to magnesium sulfate solution. Compared with other liquid media, magnesium sulfate solution has a less aggressive effect on oxychloride-hardened caustic magnesite MX: the resistance coefficient at different test times is 0.07 – 0.20. Cracks in the MX stone structure are caused by magnesium hydroxide formed both during MgO hydration and during the decomposition of the 5 – form (Figure 6e). When mixing caustic magnesite with a sulfate-chloride solution, the resistance coefficient of the MC binder increases and is 0.36 – 0.61. Oxychloride magnesite-slag binder SX in a magnesium sulfate solution is characterized by a resistance coefficient of 0.26 – 0.60. For magnesia-slag binder SC, mixed with sulfate-chloride solution, the resistance at different test times is estimated by a coefficient of 0.18 – 0.68. Binder SC is characterized by the highest coefficient of resistance to the aggressive impact of magnesium sulfate solution (Figure 5).

Summarizing the results of studies, it should be noted that a significant content of magnesium pentahydroxychloride under absence or limited amount of weakly crystallized and amorphous hydrate formations increases the vulnerability of crystalline structure of magnesite stone to the effect of aggressive liquids.

Conclusions

There was studied the influence of aggressive liquid environments on durability of magnesite binders of various compositions. The study results expand understanding of causes in destructive processes and contribute to technological methods development for increasing magnesite materials' operational durability.

It is shown that a destructive effect of water is resisted by measures that ensure minimization of unstable magnesium pentahydroxychloride while maintaining the specified strength indices of magnesite binders. This is achieved by reducing the proportion of magnesium oxide in the binder by replacing caustic magnesite with metallurgical slag, as well as by using a sulfate-chloride solution as grouting fluid.

The effect of salt solutions on the durability of magnesia binders of various material compositions was studied for the first time. It was established that an aggressive salt environment creates conditions for hydrate formation and participates in hydrate phase's formation.

Formation of a significant amount of secondary magnesium pentahydroxychloride in a stone surrounded by aggressive $MgCl_2$ solution is facilitated by the presence of $Mg(OH)_2$ in the binder. Expansion of a newly formed crystalline 5 – form destroys the binder stone.

To prevent the expansive action of secondary hydrates, combined binders, such as magnesia-slag binders are preferable. The salt environment initiates hydrate formation with the participation of latent slag compounds, which helps to maintain integrity and strength of a stone structure. Reducing the proportion of magnesium chloride in the composition of the grout also prevents the formation of dangerous quantities of secondary hydrates.

The revealed behavioral features of magnesite binders of various compositions in aggressive salt environments can serve as a basis for substantiating the area of application of magnesite materials in construction.

The research results indicate the possibility of using magnesia-slag binder in composite materials operated in conditions of high humidity and exposure to solutions of chloride and magnesium sulfate.

Caustic magnesite of hydroxychloride hardening should not be exposed to water and salt solutions.

Funding. This research has been/was/is funded by the Science Committee of the Ministry of Science and Higher Education of the Republic of Kazakhstan (Grant No. AP26199493).

References

[1] Benhelal E., Shamsaei E., Rashid M. I. Challenges against CO_2 abatement strategies in cement industry: A review //Journal of Environmental Sciences, Vol. 104, 2021. – p. 84 – 101.

[2] Tang Y., Qiu J. CO_2-sequestering ability of lightweight concrete based on reactive magnesia cement and high-dosage biochar aggregate // Journal of Cleaner Production, Vol. 451, 2024. – Article ID 141922.

[3] Tan Y.,Wu C.,Yu H., Li Y., Wen J. Review of reactive magnesia-based cementitious materials: Current developments and potential applicability// Journal of Building Engineering, Vol. 40, 2021. – Article ID 102342.

[4] Barbieri V., Gualtieri M. L., Manfredini T., Siligardi C. Lightweight concretes based on wheat husk and hemp hurd as bio-aggregates and modified magnesium oxysulfate binder: Microstructure and technological performances // Construction and Building Materials, Vol. 284, 2021. – Article ID 122751.

[5] Kandeel A.M., El-Mahllawy M.S., Hassan H.A., Sufe W.H., Zeedan S.R. Effect of type of mixing water and sand on the physico-mechanical properties of magnesia cement masonry units // HBRC Journal, Vol. 8, 2012. – p. 8 – 13.

[6] Yu K., Guo Y., Zhang Y.X., Soe K. Magnesium oxychloride cement-based strain-hardening cementitious composite: Mechanical property and water resistance // Construction and Building Materials, Vol. 261, 2020. – Article ID 119970.

[7] Miryuk O. Magnesia Composites Formation as a Result of Furniture Production Wood Waste Processing // Environmental and Climate Technologies, Vol. 26, Issue 1, 2022. – p. 836 – 847.

[8] Hao Y., LiY. Study on preparation and properties of modified magnesium oxychloride cement foam concrete // Construction and Building Materials, Vol. 282, 2021. – Article ID 122708.

[9] Miryuk O. Porous Magnesia Compositions with Various Fillers // Lecture Notes in Civil Engineering, Vol. 147, 2021. – p. 344 – 350.

[10] Temiz H., Tandirci E. Investigation of mechanical and insulation properties of Sorel cement binding light concrete // Construction and Building Materials, Vol. 379, 2023. – Article ID 131270.

[11] Guan B., Di W., Wu J., Wang F., Zhang S., He Z. Influence of Mineral Admixtureson the Properties of Magnesium Oxychloride Cement Lean Concrete // Hindawi. Advances in Materials Science and Engineering, Vol. 9, 2023. – Article ID 2817469.

[12] Zhang N., Yu H., Gong W., Liu T., Wang N., Tan Y., Wu C. Effects of low- and high-calcium fly ash on the water resistance of magnesium oxysulfate cement // Construction and Building Materials, Vol. 230, 2020. – Article ID 116951.

[13] Miryuk O., Liseitsev Y., Fediuk R. Influence of Iron-Containing Components on the Curing and Hardening Properties of Magnesium Oxychloride Binders // Journal of Materials in Civil Engineering, Vol. 36, Issue12, 2024. – Article No. 04024413.

[14] Ustinova Y.V., Nikiforova T.P. Effect of various additives on the mechanical properties of magnesia binder based materials // Procedia Engineering, Vol. 111, 2015. – p. 807 – 814.

[15] Xu M., Chen X., Han L. Effect of tartaric acid on the early hydration process and water resistance of magnesium oxychloride cement // Journal of Building Engineering, Vol. 66, 2023. – Article ID 105838.

[16] Huang X., Wang S., Wu Y., Wang J., Zuo Y. Preparation and characterization of high-strength and water-resistant waterborne epoxy resin/magnesium oxychloride composite based on cross-linked network structure // Construction and Building Materials, Vol. 285, 2021. – Article ID 122902.

[17] Xu K., Xi J., Guo Y., Dong S. Effects of a new modifier on the water-resistance of magnesite cement tiles // Solid State Sciences, Vol. 14, 2012. –p. 10 – 14.

[18] Li Y., Li Z., Pei H.,Yu H. The influence of $FeSO_4$ and KH_2PO_4 on the performance of magnesium oxychloride cement // Construction and Building Materials, Vol. 102, 2016. – p. 233 – 238.

[19] Sheng G., Zheng L., Li P., Sun B., Li X., Zuo Y. The water resistance and mechanism of $FeSO_4$ enhancing bamboo scraps/magnesium oxychloride cement composite // Construction and Building Materials, Vol. 317, 2022. – Article ID 125942.

[20] Du H., Li J., Ni W., Hou C., Liu W. The hydration mechanism of magnesium oxysulfate cement prepared by magnesium desulfurization byproducts // Journal of materials research and technology, Vol. 17, 2022. – p. 1211 – 1220.

[21] Tang S., Wei C., Cai R., Huang J., Chen E., Yuan J. In situ monitoring of pore structure of magnesium oxysulfate cement paste: Effect of $MgSO_4/H_2O$ ratio // Journal of Industrial and Engineering Chemistry, Vol. 83, 2019. – p. 387 – 400.

[22] Erdman S.V., Gapparova K.M., Khudyakova T.M., Tomshina A.V. Magnesia binder preparation from local natural and technogenic raw materials // Procedia Chemistry, Vol. 10, 2014. – p. 310 – 313.

[23] Zhang N., Yu H., Gong W., Liu T., Wang N., Tan Y., Wu C. Effects of low- and high-calcium fly ash on the water resistance of magnesium oxysulfate cement // Construction and Building Materials, Vol. 230, 2020. – Article ID 116951.
[24] Gu K., Chen B., Yu H., Zhang N., Bi W., Guan Y. Characterization of magnesium-calcium oxysulfate cement prepared by replacing $MgSO_4$ in magnesium oxysulfate cement with untreated desulfurization gypsum // Cement and Concrete Composites, Vol. 121, 2021. – Article ID 104091.
[25] He P., Poon C. S., Tsang D.C.W. Comparison of glass powder and pulverized fuel ash for improving the water resistance of magnesium oxychloride cement // Cement and Concrete Composites, Vol. 86, 2018. – p. 98 – 109.
[26] Qiu X., Chen W., Yuan J., Zhang Z., Wu G. Study on seawater corrosion resistance of calcium sulfoaluminate cement-based novel grouting materials // Materials Letters, Vol. 366, 2024. –Article ID136509.
[27] Motaleb A.K.Z.M., Pranta A.D., Repon Md. R., Karim F.E. Preparation and characterization of MgO-based composites: Analysis of moisture, corrosion, and fungal resistance, and mechanical properties // Construction and Building Materials, Vol. 447, 2024. – Article ID137926.
[28] Yu C., Wu Q., Ma, H., Yang N., Darkwah K.K., Akbar M. Study On Corrosion Resistance of Magnesium Phosphate Cement-based Coating Modified by Metakaolin // KSCE Journal of Civil Engineering, Vol. 28, Issue 1, 2024. – p. 302 – 314.
[29] Zhao J., Xu J., Cui C., Yu C., Chang J., Hu Z., Bi W. Stability and phase transition of 5·1·7 phase in alkaline solutions // Construction and Building Materials, Vol. 258, 2020. – Article ID 119683.
[30] Zhang X., Ge S., Wang H., Chen R. Effect of 5-phase seed crystal on the mechanical properties and microstructure of magnesium oxychloride cement //Construction and Building Materials, Vol. 150. 2017. – p. 409 – 417.

Information of the author

Miryuk Olga Aleksandrovna, doctor of technical sciences, professor, Rudny Industrial University
e-mail: psm58@mail.ru

DOI 10.52209/2706-977X_2025_3_31 IRSTI 55.01.11 UDC 621.9:658.512

Development of Software for Automated Selection of Machining Parameters

Nurzhanova O.A.[1], Berg A.S.*[1], Berg A.A.[1], Bakenov A.A.[2], Semerenko I.A.[1]
[1]Abylkas Saginov Karaganda Technical University, Karaganda, Kazakhstan
[2]«Maker» LLP, Karaganda, Kazakhstan
*corresponding author

Abstract. This paper describes in detail the research methodology, including the use of a local SQLite database to store information about drawings, materials, processing methods, and formulas. The need for dynamic generation of input fields, real-time calculations, and display of drawing thumbnails is emphasized. Particular attention is paid to the fault tolerance of the system, including exception handling (division by zero, missing variables, incorrect data entry) and ensuring stable operation without abnormal termination. The application architecture is organized according to the modular principle (interface, database, computational engine), which simplifies support and extension. The use of the eval() function in a strictly limited context for safe execution of formulas is noted. The application is developed in Python using PyQt5 and can operate autonomously, without access to the Internet or external servers. The presented work demonstrates a solution to the current problem of automation in mechanical engineering, offering a flexible, reliable and convenient tool for engineers and technologists.

Keywords: machining, software, SQL, Python, data

Introduction

Mechanical processing of workpieces is a key link in the production cycle in mechanical engineering [1]. It is at this stage that the geometric parameters and physical properties of parts are formed, ensuring their compliance with design specifications, tolerances and technical regulations [2]. Given the active introduction of digital technologies in recent years, the task of moving from manual and semi-automatic selection of processing modes to their full automation has become increasingly relevant [3]. This is especially important in the manufacture of products of complex configuration, where even a minimal error can cause defects, a decrease in the operational reliability of units or non-compliance with the requirements [4].

In the conditions of classical production, the process engineer is forced to spend a significant amount of time selecting parameters, based on regulatory reference books, design documentation and his own experience [5]. Such an approach is not only labor-intensive, but also prone to human error, especially when it is necessary to promptly recalculate parameters for several process scenarios. For example, changing just one initial parameter, such as the workpiece material, may require recalculating dozens of dependent quantities [6], which entails multiple revisions of all related calculations and reference data [7].

The use of software solutions in which formulas and input data are stored centrally and automatically updated allows for significantly faster calculations and increased accuracy [8]. This approach is of particular importance when working with new or non-standard design developments, when there are no ready-made process charts and the calculation of modes must be carried out “from scratch”.

An analysis of the current situation at machine-building enterprises allows us to identify a number of typical problems [9–11]:

- use of outdated tables of design parameters that do not take into account new materials and technological processes;
- lack of a centralized repository of formulas and reference data;
- high dependence on the level of qualification of a particular specialist;
- insufficient variability in the choice of parameters, especially when it is necessary to model several designs;
- low visibility of calculation results and their visual presentation.

The problem of integrating heterogeneous types of data deserves special attention: digital models, graphic representations of drawings, reference information, user variables and calculation formulas [12]. When processed manually, this information is usually distributed among disparate sources - Excel files, paper albums, oral instructions or the accumulated experience of individual employees.

Modern production conditions require software systems to be not only accurate in calculations and correct in operation, but also easy to use. Since the end users of such systems are often operators and technologists without deep knowledge in the field of programming, an intuitive interface, visual transparency, and minimization of actions required to obtain a result come to the fore [13].

Currently, the market offers various CAD (computer-aided design) and CAM (Computer-Aided Manufacturing) solutions that include modules for calculating processing parameters [14]. The most popular are Siemens NX, Autodesk Fusion 360, SolidCAM, Mastercam, SprutCAM, etc. These software products are primarily aimed at high-tech enterprises with a developed IT infrastructure, extensive equipment libraries, and a high degree of integration with production management systems (ERP, MES, PLM) [15, 16]. However, their functionality does not always fully meet the specific tasks solved within the framework of this study.

Firstly, most of the listed systems require significant financial investments in licensing, setup and personnel training. This limits their use in small enterprises or individual production units. For example, an annual license for

Fusion 360 costs hundreds of dollars per user, and the implementation of Siemens NX requires the involvement of qualified specialists and lengthy setup [17].

Secondly, complex engineering calculations, such as selection of cutting modes taking into account the features of the part installation and the number of technological passes, are either absent in these systems or are performed separately by the technologist. In most cases, CAM solutions are focused on constructing tool paths, simulating the processing process and generating control programs for CNC, but not on deep local analysis of calculated data adapted to specific production conditions [18].

Thirdly, the flexibility of editing built-in reference books, adding custom formulas, introducing new variables and adjusting algorithms is often limited. Changing even one calculation dependency, such as feed rate, often requires working with closed source code, specialized macros or complex XML templates, which hinders rapid adaptation to changing production tasks [19].

As an alternative to large complex systems, enterprises often use internal developments in the form of Excel files with formulas, macros and connected databases [20].

The analysis shows that there is a significant gap between industrial CAM systems and such home-made solutions [21, 22]: at one extreme are expensive, powerful, but overloaded and inflexible systems, at the other – simple, but unsafe and unstructured tables. It is in this niche that autonomous, customizable and easy-to-use applications are in demand, which can be installed on local workstations without the need for expensive licensing, server capacity and complex IT support.

Among the few suitable solutions, we can mention open engineering platforms such as FreeCAD with support for Python scripts, as well as Node-RED or Qt-based projects focused on visual programming [23]. However, they usually do not contain ready-made calculation algorithms or structured reference data, playing the role of designers for creating applications rather than ready-made technological tools.

There are also attempts by individual organizations to develop their own utilities based on Access, Delphi or Java [24–26]. Such programs are most often developed within the enterprise, have weak documentation, are not distributed beyond its borders and often do not meet modern interface and scalability standards.

Thus, the aim of this work is to create software for automated selection of mechanical processing parameters, providing the presence of a centralized data storage, the possibility of multi-user work, flexible updating of algorithms and protection from incorrect input.

The system was developed taking into account a set of technological processes for processing parts, including the selection and calculation of parameters that affect accuracy. These parameters include cutting depth, feed rate, spindle speed and other characteristics that determine the tool operating modes and surface quality.

All the indicated values are calculated taking into account a number of factors:

- configuration of the part (the presence of complex internal contours or sharp transitions);
- workpiece material (steel, aluminum, copper, etc.);
- processing method (turning, milling, grinding, etc.);
- the supports and basing elements used (for example, methods for fixing a part during multi-axis processing);
- number of technological passes (rough, finishing);
- reference standards and calculation formulas in force in the organization.

As a result, the designed system must ensure operation with a wide range of input parameters and be able to adapt to various technological scenarios. The totality of these requirements determines the complexity of the subject area and the impossibility of its effective coverage without automated means.

1. Research Methodology

The system being developed provides for loading data from a local SQLite database, which stores information about drawings, materials used, processing methods, support types, calculation formulas, and reference variables. The relationships between these elements are shown in Figure 1.

The user should be able to select from drop-down lists:

- the required drawing (including a sketch of the part);
- support type (basing);
- material;
- processing method (e.g. rough milling, grinding, etc.);
- iteration number (for multi-pass processing).

Depending on the selected configuration, the system must extract the values of the variables from the Variables_dependent_on_material_processing_type table that correspond to the combination "material type - processing method - iteration - tooling" (Figure 1).

Based on the loaded formulas, the system automatically generates input fields for all parameters involved in the calculations. The user has the ability to change the values of variables manually, and the recalculation results are displayed instantly.

All calculations are performed in real time when input data changes. Formulas are stored in the Formulas table as strings and are processed in a secure mode using a limited context (math module, eval function).

The output values of formulas are displayed directly below the corresponding variables as numeric labels, which are updated with each recalculation.

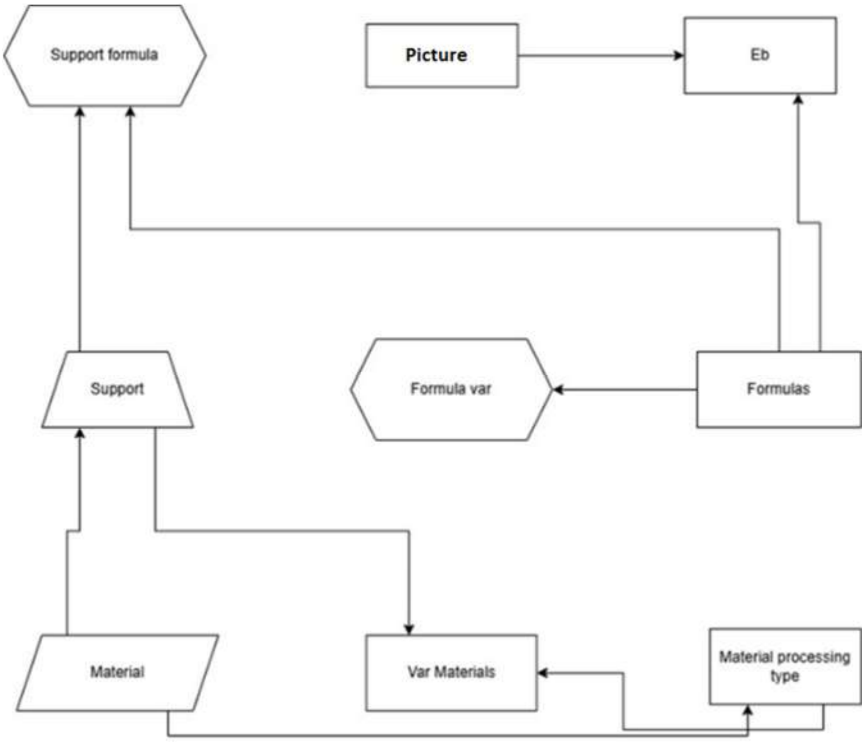

Fig. 1. – Relationships between tables

When a specific drawing is selected, its sketch is loaded, the path to which is specified in the Drawing table.

Formulas may include division operations, logarithm calculations, and other mathematical operations. The program must correctly handle exceptional situations - for example, division by zero, the absence of a variable value, etc. - by returning a neutral value (for example, 0.0) to ensure the robustness of the interface.

The system must be able to dynamically rebuild the set of active formulas with each change in the initial parameters: the selected drawing (Eb-function), the type of support (Support-function) or the processing method (dependent variables). This approach allows the calculation algorithm to be adapted to a specific technological scenario.

Before starting calculations, the application substitutes values from the Reference_data table if the user has not specified them manually.

It is possible to export the database in SQL format or create a backup copy of the file for recovery in case of failure (the function can be implemented by an external script).

The program operates in a completely autonomous mode, without the need for an Internet connection or external servers. All data, including images and formulas, are stored locally.

The system's performance ensures that calculations are completed in less than 0.2 s, even with a large number of formulas and variables.

To protect against input errors, such as entering text instead of a numeric value or incorrect formulas, a system for handling all exceptions has been implemented, preventing abnormal termination of work.

The user interface is designed with an emphasis on simplicity, compactness and scalability. All elements - input fields, lists, labels - automatically adjust to changing window sizes.

The system allows for the addition of new formulas, variables, materials and processing methods solely by updating the database, without interfering with the source code.

The architectural structure of the application is modular and includes three key components: interface (ui), database module (db) and computing module (engine). This simplifies further maintenance and expansion of functionality.

The eval() function works in a closed context that does not have access to the file system, system modules, and environment variables. The software is compatible with major operating systems (Windows/Linux/Mac) with Python and PyQt5 installed. The final build can be performed as executable files .exe or .app.

The application code is provided with comments and logging mechanisms, which simplifies debugging. In case of errors in formulas or at the initialization stage, the program outputs a message to the console or log file.

Only standard and proven libraries are used (for example, math, sqlite3, PyQt5), which minimizes dependence on external components.

Thus, the requirements formed cover all stages of the system life cycle - from data loading to visualization of results and fault tolerance. The following sections provide the rationale for the choice of technologies, the database structure, architectural solutions and a description of the interface.

The development of an application for automated selection of machining parameters was carried out in the Python environment.

2. Results and discussion

2.1 Project structure and code organization

At the logical level, the project structure is divided into three functional blocks:

- Initialization and startup block (main) - is responsible for creating the application object (QApplication), initializing the main window (MachineCalculationApp), setting the size and position on the screen, displaying the user interface and handling the shutdown (app.exec()).;
- User interface block (GUI) — implemented as the main class MachineCalculationApp, inheriting QMainWindow. Within this class, interface elements are created and managed: drop-down lists, text labels, input fields, scroll bars and graphic images.;
- Logic and data processing block — includes functions responsible for receiving information from the database (load_drawings(), load_materials()), forming a set of variables and input fields (create_input_fields()), collecting and calculating data (calculate_all()), safely executing formulas (safe_formula()), and handling events (on_drawing_change(), on_material_change(), etc.).

The class architecture is built with a clear division of function responsibilities, which facilitates the search, modification, and reuse of individual modules. The data exchange diagram between modules is shown in Figure 2.

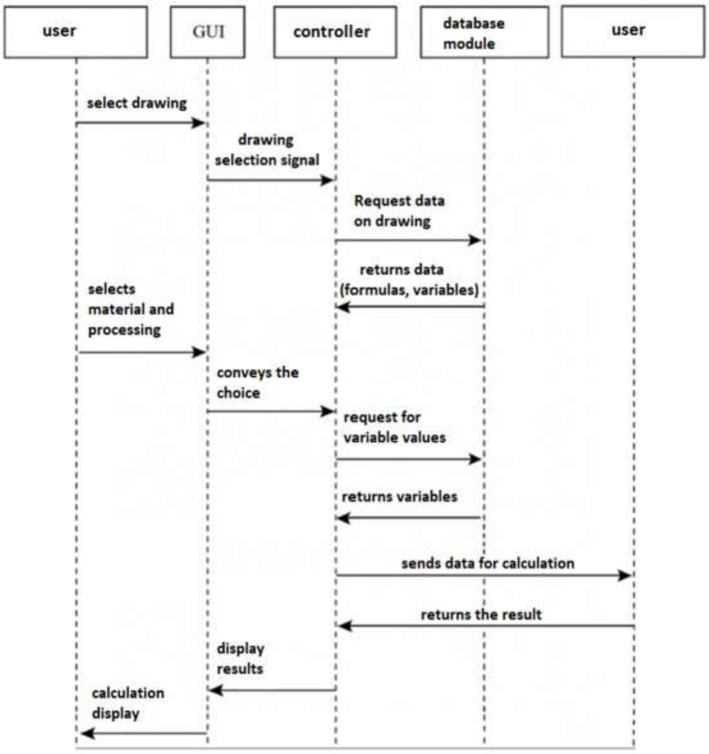

Fig. 2. – Sequence diagram: performing calculation of processing parameters

The project organization follows the principles of modularity: all code is grouped by purpose, structured and provided with comments. The use of a single centralized controller is justified for the current scale of development, and the presence of functions with a clearly defined purpose ensures predictability of the program's operation.

2.2 Implementation of the user interface

The main window of the application is formed on the basis of the QMainWindow class with a central QWidget widget, divided into two zones using a horizontal QHBoxLayout container:

Left panel– a control area that includes drop-down lists for selecting processing parameters (drawing, support, material, method, iteration) and a drawing preview area.;

Right panel– a scrollable area for displaying variables corresponding to the current configuration, their input values and calculated results.

This layout clearly divides the interface into a block for selecting conditions and a block for displaying calculations, which reduces the cognitive load on the user and increases the logicality of interaction.

Interface elements are created dynamically: after the user selects the material and processing method, the system generates a list of necessary variables and displays lines with their name, input field, and result label. When the configuration is changed, irrelevant elements are deleted.

The program implements a reactive operating principle (Figure 3): any change in input data immediately causes a recalculation of values and an update of the interface, which eliminates the need for additional confirmation buttons and speeds up the interaction process.

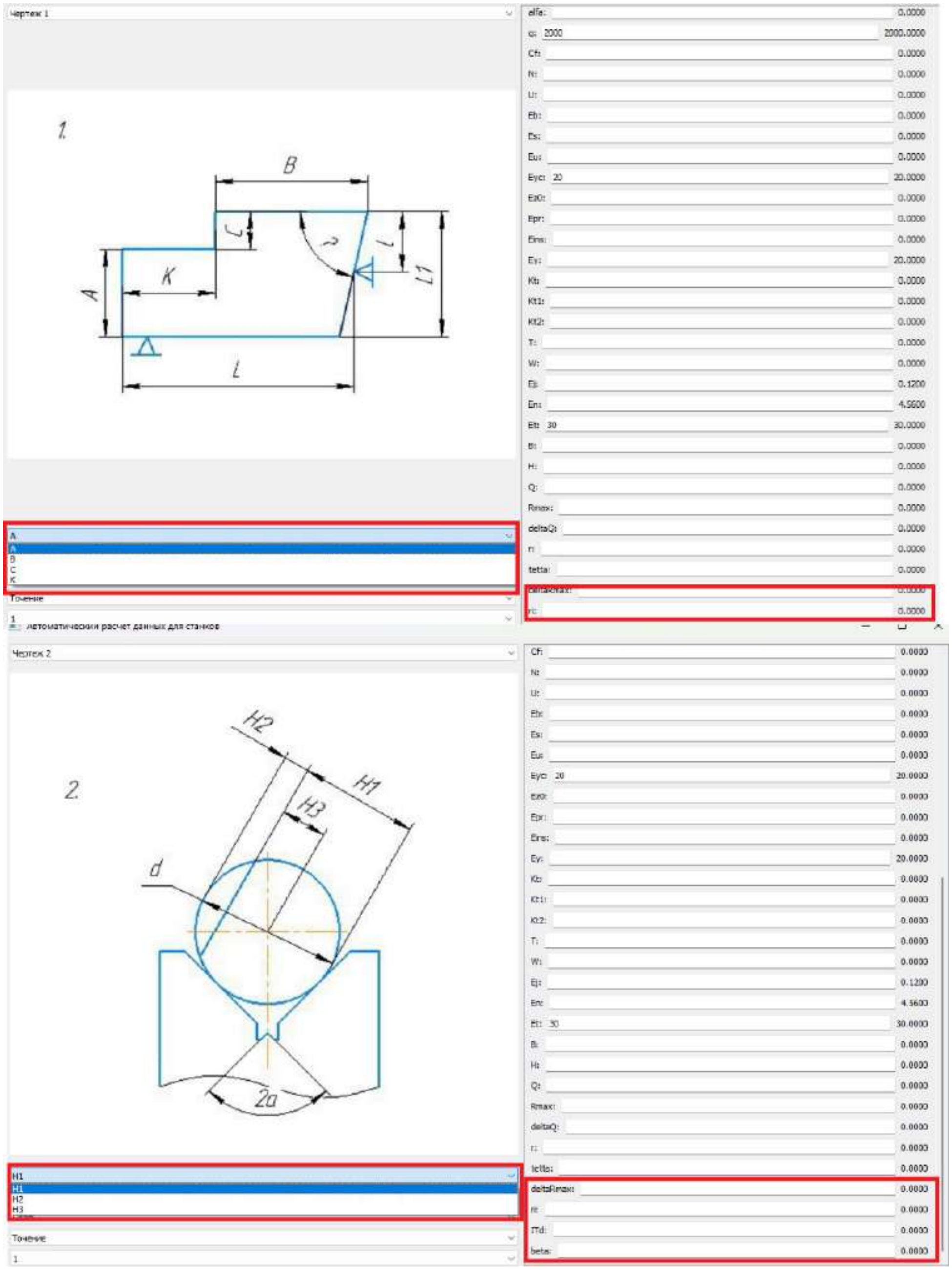

Чертеж 1

alfa: 0.0000
q: 2000 2000.0000
Cf: 0.0000
N: 0.0000
U: 0.0000
Eb: 0.0000
Es: 0.0000
Eu: 0.0000
Eyc: 20 20.0000
Ez0: 0.0000
Epr: 0.0000
Ems: 0.0000
Ey: 20.0000
Kt: 0.0000
Kt1: 0.0000
Kt2: 0.0000
T: 0.0000
W: 0.0000
Ej: 0.1200
En: 4.5600
Et: 30 30.0000
B: 0.0000
H: 0.0000
Q: 0.0000
Rmax: 0.0000
deltaQ: 0.0000
r: 0.0000
tetta: 0.0000
deltaRmax: 0.0000
rc: 0.0000

A
A
B
C
K

Точение
1

Автоматический расчет данных для станков

Чертеж 2

Cf: 0.0000
N: 0.0000
U: 0.0000
Eb: 0.0000
Es: 0.0000
Eu: 0.0000
Eyc: 20 20.0000
Ez0: 0.0000
Epr: 0.0000
Ems: 0.0000
Ey: 20.0000
Kt: 0.0000
Kt1: 0.0000
Kt2: 0.0000
T: 0.0000
W: 0.0000
Ej: 0.1200
En: 4.5600
Et: 30 30.0000
B: 0.0000
H: 0.0000
Q: 0.0000
Rmax: 0.0000
deltaQ: 0.0000
r: 0.0000
tetta: 0.0000
deltaRmax: 0.0000
rc: 0.0000
ITd: 0.0000
beta: 0.0000

H1
H1
H2
H3

Точение
1

Fig. 3. – Interface of the developed program

Thus, after each change of value or selection, the user instantly sees the recalculated results. This eliminates the need for intermediate buttons and makes interaction with the program faster.

2.3 Processing drawings and loading parameters

Each drawing is stored in the database as a record with a unique identifier, name, and path to the image. The Drawing table has the following structure (Figure 4).

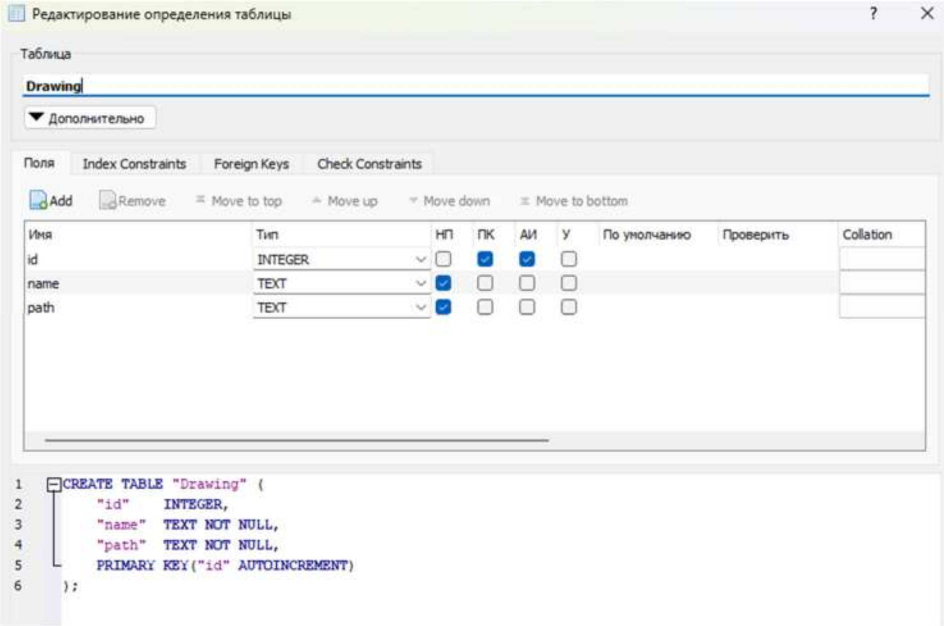

Таблица: Drawing

Имя	Тип	НП	ПК	АИ	У	По умолчанию	Проверить	Collation
id	INTEGER	☐	☑	☑	☐			
name	TEXT	☑	☐	☐	☐			
path	TEXT	☑	☐	☐	☐			

```sql
CREATE TABLE "Drawing" (
    "id"    INTEGER,
    "name"  TEXT NOT NULL,
    "path"  TEXT NOT NULL,
    PRIMARY KEY("id" AUTOINCREMENT)
);
```

Fig. 4. – Structure of the Drawing table

When the program starts, a query is made to all Drawing records, after which the drawing names are added to the interface drop-down list.

Drawings are linked to the base elements (Eb), for which calculation formulas are defined. The Eb table contains foreign keys linking records to the Drawing and Formulas tables, which ensures logical data integrity (Figure 5).

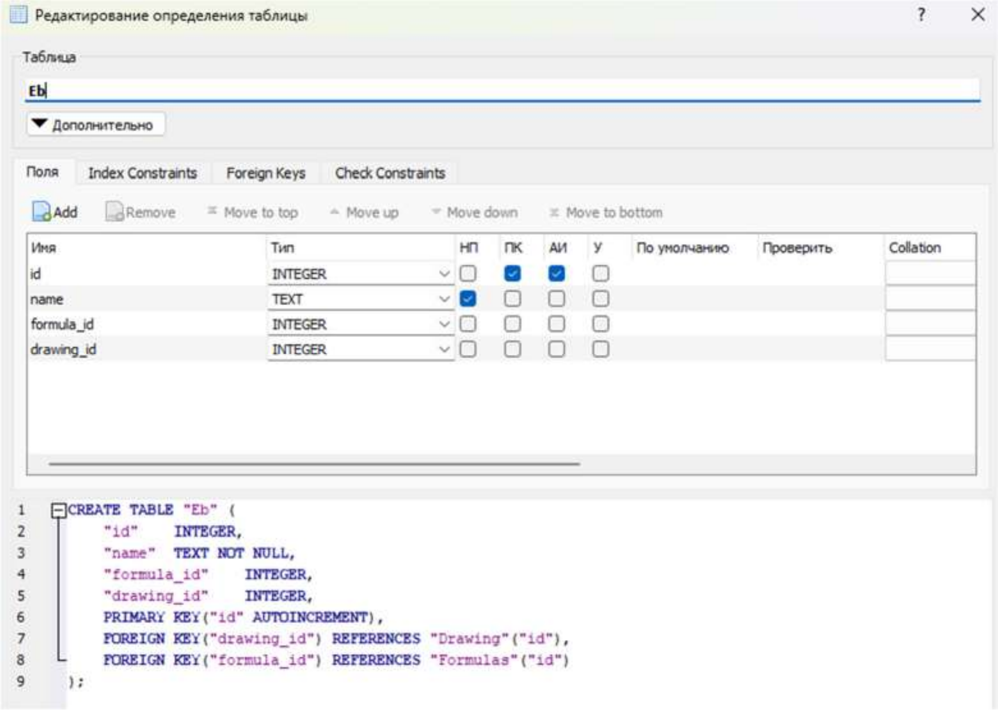

Таблица: Eb

Имя	Тип	НП	ПК	АИ	У	По умолчанию	Проверить	Collation
id	INTEGER	☐	☑	☑	☐			
name	TEXT	☑	☐	☐	☐			
formula_id	INTEGER	☐	☐	☐	☐			
drawing_id	INTEGER	☐	☐	☐	☐			

```sql
CREATE TABLE "Eb" (
    "id"    INTEGER,
    "name"  TEXT NOT NULL,
    "formula_id"    INTEGER,
    "drawing_id"    INTEGER,
    PRIMARY KEY("id" AUTOINCREMENT),
    FOREIGN KEY("drawing_id") REFERENCES "Drawing"("id"),
    FOREIGN KEY("formula_id") REFERENCES "Formulas"("id")
);
```

Fig. 5. – Structure of the Eb table

After selecting a drawing, the application generates a selection from the Eb table, defining a set of formulas related to this image. These formulas are included in the active list of calculations. Thus, the interface is adjusted to a specific drawing and uses the corresponding dependencies.

Formulas can be linked not only to the drawing, but also to the selected equipment (Support) and processing conditions. The program generates a final list of calculations, combining mandatory formulas (mandatory_formula = 1), formulas for the drawing and formulas for the support.

After selecting a drawing, the user specifies the material, processing method, support and iteration, which determines the choice of variables. Their values are stored in Variables_dependent_on_material_processing_type and are specified by four keys: method, iteration, material, tooling.

2.4 Implementation of business logic: formulas and calculations

In the project under development, formulas are stored in the Formulas table as string expressions. Each entry in this table contains:

- uniqueid;
- output variable name (target_value);
- the expression text in Python syntax (formula);
- flag of obligationmandatory_formula, which determines whether the formula should always be applied;
- binding to the support (Support_formula_id) if necessary.

Example of a formula line (Figure 6).

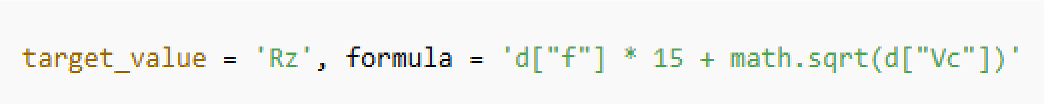

```
target_value = 'Rz', formula = 'd["f"] * 15 + math.sqrt(d["Vc"])'
```

Fig.6. – Example of a formula line

This means that the parameter Rz is calculated based on the current values of the variables f and Vc stored in the dictionary d. When substituting data, the formula performs a mathematical operation and returns the result, which is displayed in the interface.

Since formulas are loaded from the database in text form, their direct execution may be unsafe. For protection, the wrapper function safe_formula() is used, which ensures execution in a limited context, access to which is only available to the math module and the d dictionary. This allows flexible interpretation of dependencies, while preventing the execution of malicious code or critical commands (Figure 7).

Applies hereeval()in a strictly limited context where only the library is availablemathand a dictionary of variablesd. This approach allows for flexible interpretation of formulas and at the same time protects the system from failures: any error returns the value0.0, and the program continues to work.

The mechanism for selecting formulas for calculation takes into account:

- mandatory dependencies (mandatory_formula = 1);
- formulas associated with the selected drawing (via tableEb);
- formulas associated with the selected support (tableSupport_formula).

The combined formula list is used to build a list of variables (Formula Variables) and interface generation, its code is presented in Figure 7.

```
def update_active_formulas(self):
    """Обновление списка активных формул"""
    formulas = self.mandatory_formulas + self.eb_formulas + self.support_formulas
    self.active_formulas = []

    # Получаем ID формул для получения переменных
    formula_ids = [f[0] for f in formulas]

    # Получаем используемые переменные
    self.cursor.execute(f"""
        SELECT DISTINCT variable_name
        FROM FormulaVariables
        WHERE formula_id IN ({','.join('?'*len(formula_ids))})
    """, formula_ids)

    self.all_variables = [row[0] for row in self.cursor.fetchall()]
    self.create_input_fields()
```

Fig. 7. – Update code for formulas involved in calculations

Thus, the user sees on the screen only those fields that are necessary for calculations in a specific configuration, and the system processes only relevant formulas.

Before performing calculations, the application generates a data dictionary, which contains:

- values entered manually by the user;
- values substituted from the reference bookReference_data;
- values extracted from the tableVariables_dependent_on_material_processing_type.

Next, each formula from the active list is passed to the formula_wrapper wrapper, and the result is placed in data under the name of the target variable.

2.5 Ensuring fault tolerance and graceful shutdown

In real production conditions, it is impossible to completely eliminate operator errors, incomplete data, or disruptions in the sequence of operations. Therefore, the system was designed to handle any such situations without stopping the application.

One of the most common cases is when the user enters data that does not match the expected type - for example, text instead of a number or an empty value. Such situations are handled in the calculate_all() function (an example of implementation is shown in Figure 8).

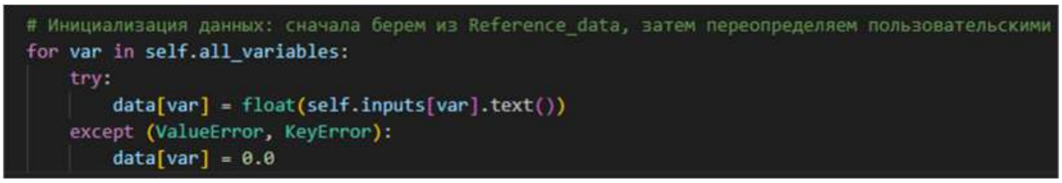

```python
# Инициализация данных: сначала берем из Reference_data, затем переопределяем пользовательскими
for var in self.all_variables:
    try:
        data[var] = float(self.inputs[var].text())
    except (ValueError, KeyError):
        data[var] = 0.0
```

Fig. 8. – Example of code implementation of fault tolerance

In case of incorrect input, the variable is automatically assigned the value 0.0, which prevents a crash. This mechanism is especially important considering that the end users are engineers and technologists who may not be aware of all the internal restrictions on the data format.

Since all calculation dependencies are stored in the database as strings and executed via the eval() mechanism, there is a risk of errors - division by zero, access to missing variables or syntax violations. To minimize these risks, a protective wrapper has been implemented, which in the event of a failure returns a safe value (0.0) and records the error in the console. Thanks to this, the program continues to work, maintaining the stability of the interface.

The project also provides for situations where certain parameters — variables, iterations, or formulas — may be missing from the database. Instead of stopping execution, the application checks for the required information and, if it is missing, simply does not display the corresponding elements. An example of implementation is shown in Figure 9.

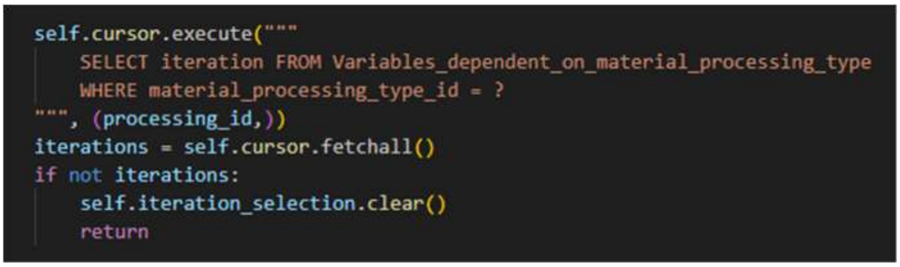

```python
self.cursor.execute("""
    SELECT iteration FROM Variables_dependent_on_material_processing_type
    WHERE material_processing_type_id = ?
""", (processing_id,))
iterations = self.cursor.fetchall()
if not iterations:
    self.iteration_selection.clear()
    return
```

Fig. 9. – Example of code when the required data is not found

This approach guarantees the correct operation of the system even with a partially filled database, which is especially important at the implementation stage, when not all information can be entered in advance.

Conclusion

Within the framework of this article, a software system was designed and implemented, intended for automated selection of mechanical processing parameters, corresponding to all established requirements. The main task of the development was to create an adaptive, reliable and convenient tool for engineers and technologists, providing autonomous operation and high accuracy of calculations.

The following key results were obtained during the work:

- a system was created that uses a local SQLite database to store all the necessary information - drawings, materials, processing methods, support types, calculation dependencies and reference variables. This made it possible to eliminate the fragmentation of information typical of traditional approaches using Excel tables or paper media, and to provide a single reliable source of data;
- a reactive interface based on PyQt5 has been implemented, forming a set of input fields depending on the current configuration (drawing, material, processing method, iteration). Calculations are performed almost instantly (less than 0.2 s), allowing the user to see the result of changing the input parameters in real time. This significantly speeds up the process of selecting optimal processing modes and increases the productivity of specialists;
- mechanisms for handling exceptional situations (division by zero, missing variables, incorrect input) have been implemented, which prevent abnormal termination of the program. When an error occurs, the system returns a safe value (0.0) and registers the event in the log, ensuring continuous operation. This approach is especially important for production environments, where software stability is a critical factor;
- the program architecture is built on a modular principle and includes three main areas - the interface (GUI), the database (DB) and the computing engine (Engine). This simplifies maintenance, modernization and adding new

functionality. For example, the integration of additional formulas, variables or materials is carried out by changing the contents of the database without editing the source code;

- to interpret formulas stored as strings, the eval() function is used in a strictly limited and secure environment, which allows for flexible specification of mathematical dependencies with complete protection from the execution of unwanted code;
- the software suite functions completely autonomously, does not require a connection to the network or external servers, and all necessary data and graphic files are stored locally. This makes the system especially convenient for production sites with limited access to the Internet.

Thus, the developed software demonstrates an effective solution to the current problem of automating the selection of mechanical processing parameters in mechanical engineering, combining the accuracy of calculations, ease of use and resistance to errors.

Funding. This research has been/was/is funded by the Science Committee of the Ministry of Science and Higher Education of the Republic of Kazakhstan (Grant No. AP26101943).

References

[1] Wang Z. The milling parameters of mechanical parts are optimized by NC machining technology //Frontiers in mechanical engineering, Volume 10, 2024,https://doi.org/10.3389/fmech.2024.1367009

[2] Nurzhanova O., Zharkevich O., Berg A., Zhukova A., Mussayev M, Buzauova T., Abdugaliyeva G.,
Shakhatova A Evaluation of the Structural Strength of a Prefabricated Milling Cutter with Replaceable inserts During Machining //Material and Mechanical Engineering Technology, No. 4, 2023. – P.10-17

[3[Klackova I., Ivanova T., Kuric I., Korshunov A., Koretckiy V. Application of progressive technologies based on digitalization in mechanical engineering //MM Science journal, December, 2022 DOI: 10.17973/MMSJ.2022_12_2022140

[4] Berg A., Nurzhanova O., Vytautas T., Vitushenko D. Improvement of Base Sets for Complex Configuration Parts when Assessing their Manufacturability within Industry 4.0 //Material and Mechanical Engineering Technology, 2, 2024. P. 25 - 35 DOI: 10.52209/2706-977X_2024_2_25

[5] Gupta D.P., Gopalakrishnan B., Chaudhari SA, Jalali S. Development of an integrated model for process planning and parameter selection for machining processes //International Journal of Production Research, Vol. 49, No. 21, 1 November 2011, 6301–6319 DOI: 10.1080/00207543.2010.523722

[6] Senapati A.K., Mohanty S. A Review on the Effect of Process Parameters on Different Output Parameters During Machining of Several Materials //International journal of engineering sciences & research technology, 3(3): March, 2014. – P.1 – 11

[7] Kumar A., Gori Y., Dutt N., Singla YK, Maurya A. Advanced Computational Methods in Mechanical and Materials Engineering. – NY: “Taylor & Francis Group”, LLC, 2022. – 71 p.

[8] Zhetessova G., Yurchenko V., Nikonova Y., Zharkevich O. The development of the computer-aided design system for production processes of component part machining for single-piece production and repair conditions //Journal of Applied Engineering Science, 17, 4, 651, 2019, P. 599 - 609 DOI: 10.5937/jaes17-21470

[9] Kozlova EP, Kuznetsova SN, Romanovskaya EV, Andryashina NS, Garina EP Automation of technological processes in mechanical engineering //IOP Conf. Series: Materials Science and Engineering 1111 (2021) 012030, doi:10.1088/1757-899X/1111/1/012030

[10] Trokhymchuk I., Svirzhevskyi K., Tkachuk A., Zabolotnyi O., Zablotskyi V. The Structure of Automated Control Systems for Precision Machining of Parts Bearing // Innovations in Mechatronics Engineering II21 June 2022, P. 182–192

[11] Savelyeva N., Nikonova T., Zhetessova G., Irina K., Yurchenko V., Cernašˇejus O., Zharkevich, O., ˙ Dandybaev E., Berg A.; Vassenkin S., Baimuldin M. Implementation of Simulation Modeling of Single and High-Volume Machine-Building Productions //Designs, 2024, 8, 24.https://doi.org/10.3390/designs8020024

[12] Zadeh AY, Shahbazy M. A Review into Data Science and Its Approaches in Mechanical Engineering //5th International conference in and engineering Applied research on science, 2, 2020, DOI: 10.48550/arXiv.2012.15358

[13] Xie, K. Research on the Application of Automatic Control System in Mechanical Engineering 3rd International Workshop on Materials Engineering and Computer Sciences (Advances in Computer Science Research, volume 78, 2018, P. 79 - 82

[14] Kamrani A., Abouel Nasr EA Computer-Based Design and Manufacturing Engineering //Design and Rapid Prototyping, 2009 DOI: 10.1007/978-0-387-95863-7_7

[15] Grabowik C., Kalinowski K., Kempa W., Paprocka I. A method of computer aided design with self-generative models in NX Siemens environment //IOP Conference Series Materials Science and Engineering, 2015, 95(1):012123 DOI: 10.1088/1757-899X/95/1/012123

[16] Song P.P., Qi Y.M., Cai D.C. Research and Application of Autodesk Fusion360 in Industrial Design //OP Conf. Series: Materials Science and Engineering 359, 2018 012037 doi:10.1088/1757-899X/359/1/012037

[17] Zbiciak M, Grabowik C., Janik W. An automation of design and modeling tasks in NX Siemens environment with original software – generator module //IOP Conf. Series: Materials Science and Engineering 95, 2015, 012117 doi:10.1088/1757-899X/95/1/012117

[18] Lysek K., Gwiazda A., Herbus K. Application of CAM systems to simulate a milling machine work IOP Conf. Series: Materials Science and Engineering 400, 2018, 042037 doi:10.1088/1757-899X/400/4/042037

[19] Zhang K., Xiao W., Fan X., Zhao G. CAM as a Service with dynamic toolpath generation ability for process optimization in STEP-NC compliant CNC machining Journal of Manufacturing Systems, Volume 80, 2025, P.294-308 https://doi.org/10.1016/j.jmsy.2025.03.004.

[20] Ghosh A.K., Fattahi S., Ura S. Towards Developing Big Data Analytics for Machining Decision Making. //J.Manuf. Mater. Process, 2023, 7, 159.https://doi.org/10.3390/jmmp7050159

[21] Radhakrishnan P., Subramanian S., Raju V. CAD/CAM/CIM. Edition third. – Deli: New Age International (P) Limited, Publishers, 2008. – 690 p.

[22] Sazonova A.O., Drozdov A.A. Classification and place of cam systems in computer-aided design systems //Vestnik Pstu, No. 2, 2014. P.34 – 42.

[23] Machado F., Malpica N., Borromeo S. Parametric CAD modeling for open source scientific hardware: Comparing OpenSCAD and FreeCAD Python scripts //PLOS ONE, December 5, 2019, https://doi.org/10.1371/journal.pone.0225795

[24] Ling-Lin C., Qi C., Jiacheng Z. Application of Delphi Software in the Teaching of Basics of Mechanical Design // LNEE, volume 112, 2011, P. 443–447
[25] Hibino H., Fukuda Y., Yura MA Study on Java Base Simulation System for Manufacturing System Designs //The proceedings of the JSME annual meeting, July 2000, 2000.3, P. 563-564 DOI: 10.1299/jsmemecjo.2000.3.0_563
[26] Kuryło P., Frankovský P., Malinowski M., Maciejewski T., Varga J., Kostka J., Adrian Ł., Szufa S., Rusnáková S. Data Exchange with Support for the Neutral Processing of Formats in Computer-Aided Design/Computer-Aided Manufacturing Systems //Appl. Sci. 2023, 13, 9811.https://doi.org/10.3390/app13179811

Information of authors

Nurzhanova Oxana Amangeldyevna, PhD, acting associate professor, Abylkas Saginov Karaganda Technical University
e-mail: nurzhanova_o@mail.ru

Berg Alexandra Sergeevna, PhD, Abylkas Saginov Karaganda Technical University
e-mail: kibeko_1995@mail.ru

Berg Andrey Alekseevich, senior lecturer, Abylkas Saginov Karaganda Technical University
e-mail: 22526633@mail.ru

Bakenov Adilkhan Amangeldievich, m.t.s., design engineer, "Maker" LLP
e-mail: bakenov.work@yandex.kz

Semerenko Ilya Andreevich, master student, Abylkas Saginov Karaganda Technical University
e-mail: i7776455656@gmail.com

DOI 10.52209/2706-977X_2025_3_41 **IRSTI 55.03.03** **UDC 69.331.438**

Tests and Analysis of the Rigidity of a Safety Fence

Banas P.[*]
Poznan University of Technology, Poland
*corresponding author

Abstract. Today's Industry 4.0 requirements, including production automation, necessitate the securing of production lines to ensure maximum safety for employees. This article presents a solution for fastening systems in safety fences used on production lines. The main objective of the research was to compare the rigidity of the entire fence, i.e., a set of different elements, depending on the fastening system used for the mesh panel and fence post, based on simulation tests. Both commercially available solutions and own solutions were compared. The parameter for evaluating the solutions is the maximum displacement value, which is derived from computer simulation and allows for an estimation, within a certain range, of the behavior of the system under real conditions. The maximum displacement values recorded during the simulation range from 14 to 20 mm. Achieving the appropriate level of fence rigidity is required to ensure safety on the production line, and the use of an appropriate solution allows for an increase in safety and working conditions. The analysis carried out allowed the behavior of the object as a result of the force to be estimated, but it completely ignores material aspects and factors such as heat distribution, vibrations or parameters that vary in reality, such as the condition of the material, temperature, or the environment in which the tested object is located.

Key words: safety fence, fastening systems, safety, MES, production, industry 4.0

Introduction

Nowadays, production activities are becoming more automated [1] and the presence of machines on production lines is commonplace [2]. Since not every production line can be fully automated, the human factor is still present in most plants [3]. The presence of machines and people in the same plant, on the same production line, poses a certain danger [4]. The work area for each group should be properly planned and designated within the plant in order to avoid undesirable incidents.

One method of securing the working area of industrial machinery is the use of safety fences [5], which allow the machine's working area to be separated from the human working area. This eliminates the accidental possibility of an unwanted element entering the machine's working area on the production line. This increases safety in the production plant and protects expensive machines from breakdown or damage. The main role of safety fences is to prevent the operator from contact with the machine during its operation, although they can also perform other tasks. Guards are designed to separate the safety zone and prevent access to the danger zone. Fences should be designed in a way that is reliable and does not allow unauthorized access to restricted areas when it is dangerous or unauthorized. There are also sensor-based solutions that are designed to detect human presence in the exclusion zone and can control the operation of devices in a designated area [6], although this solustion do not effectively protect against many physical hazards. There are also combinations of classic solutions with modern algorithms to increase safety [7].

When used in work areas where there is a risk of material, objects, or fragments being ejected, due to the nature of the work and the technological process, fence must ensure safety for the operator and other potentially endangered persons. The guard usually performs two main functions, which are to prevent personnel, objects, or other persons from accessing the danger zone and to stop parts of the machine, including workpieces, in the area protected by the guard [8]. Safety fences are characterized by several parameters [8] according to which their safety can be assessed. First of all, these are its dimensions, i.e., thickness and width, as well as the very important height. Another parameter that is important in terms of safety is the design of mesh panels, which, due to the environment of a production line, often cannot be full covers and must ensure good visibility. Therefore, fence panels are most often made of thin, welded bars. The density of the fence translates into the required distance of the fence from the danger zone and its strength. The rigidity of the fence is essential for the safety of the protected area and its surroundings, protecting the environment from sources of danger and the consequences of an undesirable event, such as flying debris.

The main objective of the research was to compare the rigidity of the entire fence, i.e., a set of various elements, depending on the fastening system used for the mesh panel and fence post, based on simulation tests. There is also a proposition of own concepts for fastening safety fences, which have the potential to streamline the fence installation process while maintaining all safety standards. The analysis was performed on the basis of computer simulation in Autodesk Inventor, where the displacement of materials after applying a force of 2000 N to the side surface of the mesh panels was evaluated. Performing this type of analysis is necessary in order to examine the ability of an object to perform its intended function [9–10]. The program itself is a proven and widely used tool that utilizes pre- and post-processors for graphical engineering interpretation, where the computational model can be described by solid and surface elements [11–12]. The main novelty presented in the article is our own concept of a fastening system, which is characterized by better parameters in terms of assembly and low production costs, giving it a significant advantage over competing solutions.

However, it should be remembered that achieving high strength parameters for a fence may involve high production costs related to the technological process of manufacturing the components, the necessary materials, and the method of processing. The solution should ensure high strength parameters at the lowest possible and reasonable production costs [13–16].

1. Materials and methods

Conducting an economic analysis allows for a preliminary estimate of the manufacturing costs of the tested safety fence model, which in itself should be optimized in terms of production price, have appropriately selected tolerances and surface treatment in order to achieve a favorable manufacturing cost [17]. The selected fastening concepts should also be tested for strength in order to determine the solution that will ensure the greatest rigidity of the fence. The rigidity of the fence is essential for the safety of the protected area and its surroundings, protecting them from sources of danger and the consequences of an undesirable event, such as flying debris from broken machine parts. The analysis was performed on the basis of a computer simulation in Autodesk Inventor, where the displacement of materials after applying a static force of 2000 N to the side surface of the mesh panels was evaluated. The model was recreated in a computer program, where a simulation was performed during which the assumed force was applied, taking into account the effect of gravity. All fastening system solutions are installed at the same height, i.e., 1904 mm from the base of the post and 1800 mm from the base of the mesh panel, which is ¾ of its height. The fence model (Fig. 1) is the same for all three considered solutions for fastening the mesh panel and fence post.

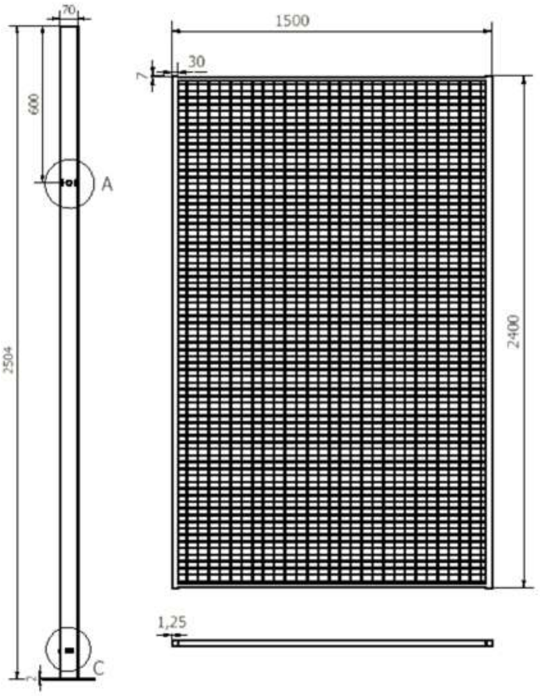

(a) (b)

(a) fence post; A – mounting system installation point, C – mesh panel mounting point on the post, (b) mesh panel

Fig. 1. Model of the tested safety fence

Safety fence should have a simple and economically justified design [15]. It is advantageous for the fence to be simple and quick to install and to require the smallest possible number of operators [16]. The paper presents three concepts for a mounting system: concept 1 is a solution commonly used in industry, while concepts 2 and 3 are original solutions.

1) Concept 1 – metal clamps

There are many ready-made solutions on the market, one of which is metal clamps (Fig. 2). This is one of the most commonly used solutions and involves the use of metal clamps that grip the mesh panel and are attached to the pole, using a screw connection between the clamp and the pole and between the clamp and the mesh panel. This solution is simple in design and manufacture, but requires specially designed screws and a lot of work during installation. A very advantageous feature of this solution is its low manufacturing cost, although separate structures for intermediate and angular connections must be taken into account (Fig. 2). The solution with a metal bracket is simple in design, but requires more steps during installation and increased labor during the preparation of elements for installation. There is also an increased number of parts, and the screws must be designed in such a way that the fasteners cannot be completely disconnected. The design of the system must not create a risk of losing any of the components of the fastening system.

(a) (b)

Fig. 2. Metal clamps available on the market; (a) clamp for indirect (parallel) connections, (b) clamp for angular (perpendicular) connections

2) Concept 2 – snap-on caps

The second concept, which is our own solution, is the use of a cap with a snap-on mechanism, mounted at the end of the mesh panel in contact with the post (Fig. 3). The cap utilizes the deformation of the material during pressing, which is caused by the overlapping geometry of the objects. When the cap is fixed at the correct height, the snap closes, fixing the position of the post and the mesh (Fig. 4.). Disassembly involves inserting a tool that allows the latch to be pulled away from the geometry on which it was locked.

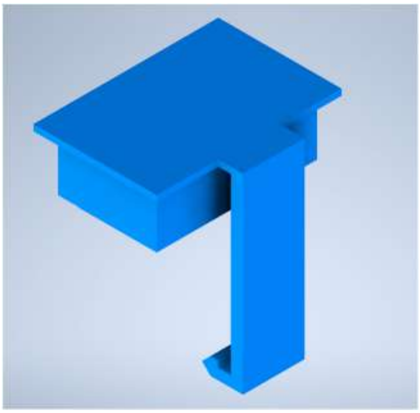

Fig. 3. Model of a snap-on cap used to connect a mesh panel to a post

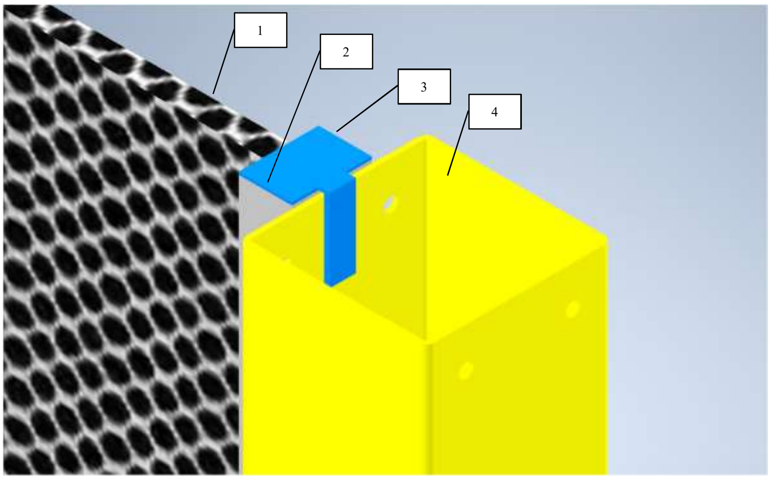

1 – mesh panel, 2 – mesh panel profile, 3 – snap-on cap, 4 – fence post

Fig. 4. The concept of using a snap-on cap as a fastening system in safety fences

3) Concept 3 – mounting pin

The third concept, also our own, is a connection using a fixing pin installed in the pole structure or mesh profile. It allows for a simple design and quick installation. The mesh panel support profile has a hole that allows the pin with a tool hole to be inserted and locked in place in order to release the lock during disassembly (Fig. 5).

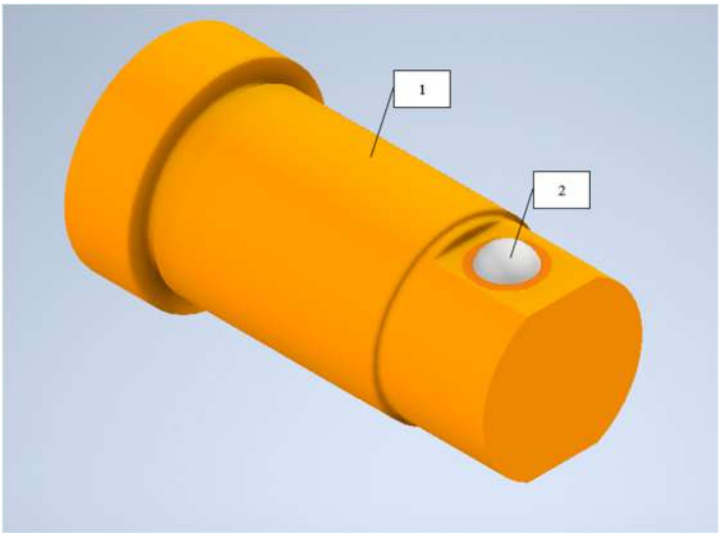

1 – pin, inserted into the installation hole, 2 – double-sided latch

Fig. 5. Mounting pin with latch

The solution using a mounting pin allows for quick installation, but requires a specially designed tool for removal. The pin itself must be permanently connected to the post by pressing it in. The pin must be installed in such a way that it can be removed from the inside of the protected area to allow for removal once the security fence is fully assembled. The pin, when installed in the socket, passes through the cutouts in the mesh profile and the fence post, resulting in a snap-in effect after passing through the last hole in the post. The advantage over metal clamps (Fig. 2) is that the element is less visible from the outside, which translates into better transparency of the mesh panels due to less visibility restriction (Fig. 6).

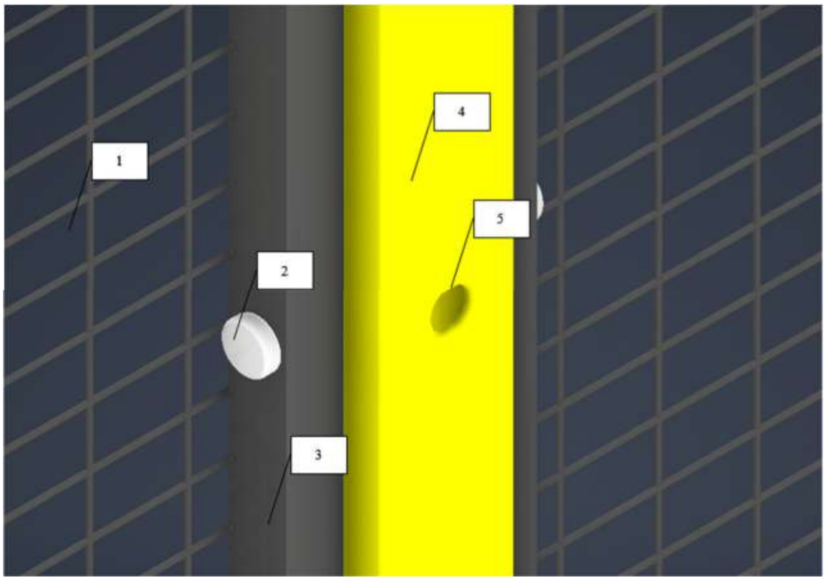

1 – mesh panel, 2 – mounting pin, 3 – mesh panel profile, 4 – fence post, 5 – cutout for mounting pin in the post

Fig. 6. Installation of mounting pins in a safety fence

Another advantage of this solution is the possibility of installing the mesh panel on either side of the pole, as the holes required for installation can be made on either side of the pole as needed. This translates into lower production costs, as only one type of pole, one type of mesh panel, and one type of pin are manufactured.

During the simulation, a fence model was prepared (Fig. 7), whose structural changes resulted solely from the fastening system used. Each model consisted of four fence posts, three mesh panels, and the number of fasteners required to connect the mesh panels and posts. In addition, each fence was subjected to the force of gravity to bring the simulation results closer to reality, and a static force of 2000 N was applied to the entire side surface of the panel profiles.

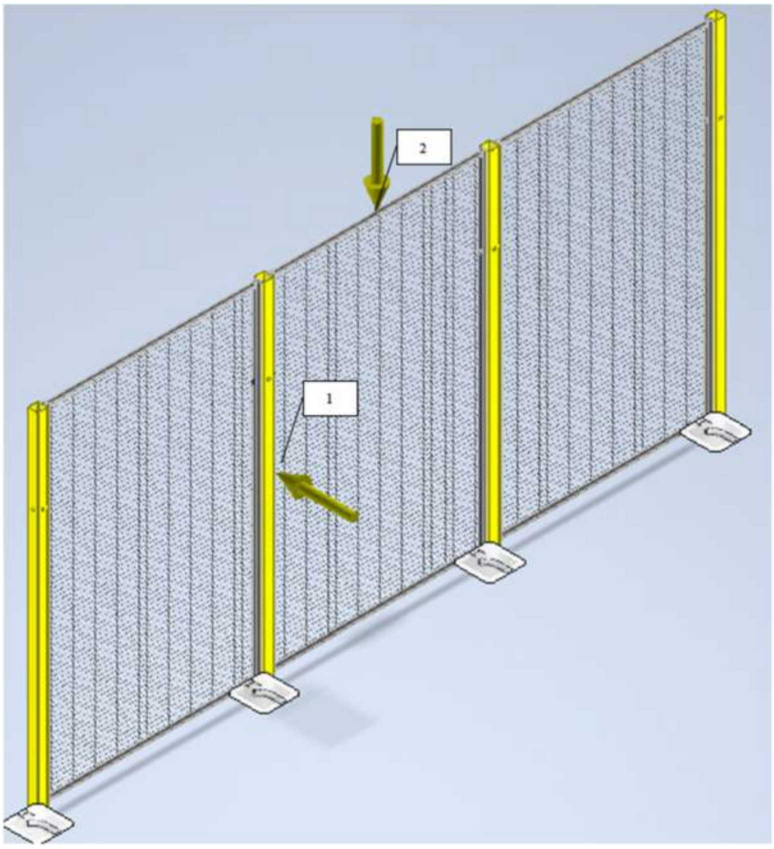

1 – force of 2000 N acting on the side profile of the panel, 2 – force of gravity loading the fence

Fig. 7. Model of a safety fence with forces acting on it

The main parameter assessed in the simulation was displacement, where the displacement of the point furthest from the initial position was evaluated and, on this basis, the stiffness of the fence was assessed. This value was read by the program used to model the fence and perform the simulation.

2. Simulation results

The first simulation (Fig. 8) was performed for concept 1 – intermediate and angular clamps. The fully reconstructed fence, which uses clamps as a system for attaching mesh panels to posts, results in a panel displacement of 17.427 mm when a force of 2000 N is applied to the surface of the mesh panel frame. However, the main advantage of this solution in terms of strength is the possibility of using an increased number of fasteners. This is more advantageous due to the increased rigidity of the structure, but it requires more time for installation and more work by the operator, and increases the cost of purchasing clamps. The simulation result using three pairs of clamps on each fence post (Fig. 9) shows a reduction in the maximum displacement of the fence by almost 3 mm compared to the first simulation tests for the solution with one pair of clamps.

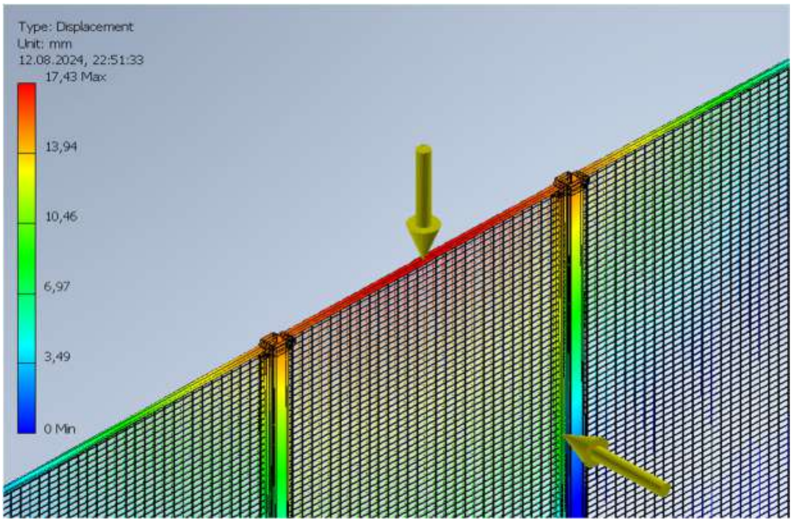

Fig. 8. The results of simulation strength tests for a fence fixed with one pair of clamps

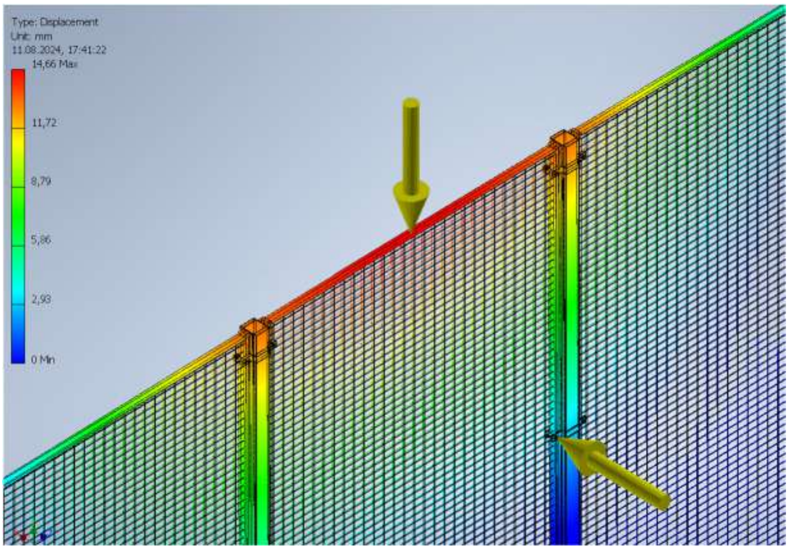

Fig. 9. Results of simulation strength tests for a fence fixed with three pairs of clamps

Based on simulation tests for fencing using caps (Fig. 10), i.e., the second concept, similar results were obtained as for clamps, but due to the method of installing the caps, it is not possible to use multiple caps to increase the rigidity of the fence.

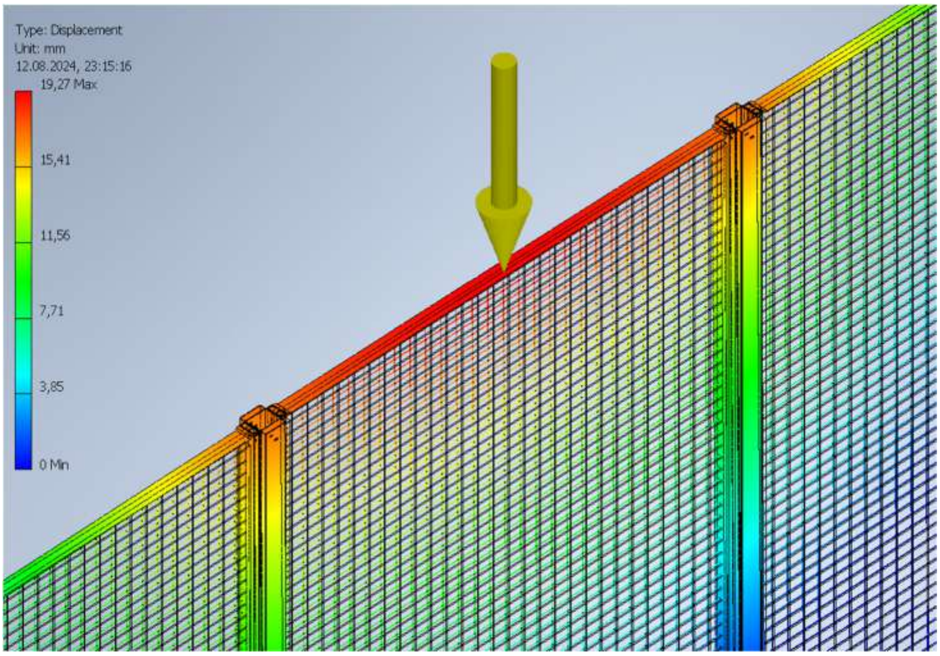

Fig. 10. Results of simulation strength tests for fencing secured with caps

After applying a force of 2000 N and gravitational force, the maximum displacement equal 19.27 mm was obtained. This is a displacement that is almost 2 mm greater than the previous solution, which was based on a single pair of clamps, and almost 5 mm greater than the solution with three pairs of clamps.

The fastening pins, which constitute the third concept of the fastening system solution, can be used multiple times to achieve higher fence rigidity. The results of the simulation (Fig. 11) carried out on a fence using this element show that the maximum displacement value is almost the same as for a single pair of fastening clamps and amounts to 17.432 mm. No simulation was performed for the solution with multiple fastening pins because the data collected so far allows us to predict its results. However, it is worth noting that although the maximum displacement value itself is comparable, the pin is a more advantageous solution in terms of strength, not because of the rigidity of the fence, but because of its inherent durability. Metal clamps are made of bent thin sheets of metal. The pin, on the other hand, is turned from a thick metal rod. Resistance to deformation and stress will therefore be significantly greater for the pin than for the clamps. Therefore, it is worth considering mounting pins as a more durable solution, while ensuring the same level of fence rigidity.

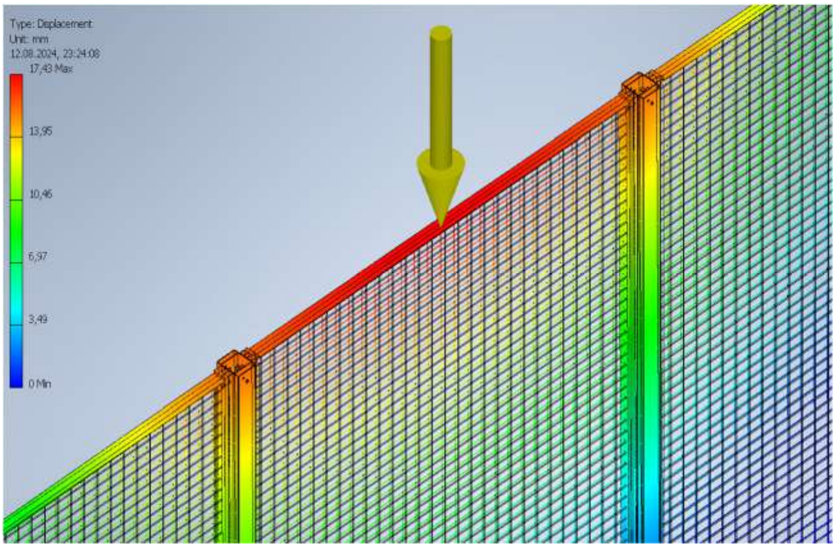

Fig. 11. Results of simulation strength tests for fencing fixed with pins

From the data collected (Fig. 12) from the strength simulation, the lowest maximum displacement value can be observed for three pairs of clamping collars. There is only a slight difference in maximum displacement between one pair of clamps and the fastening pins, with the clamps being significantly cheaper, but less advantageous in terms of the assembly process and strength considerations. The cap provided the least rigidity for the fence.

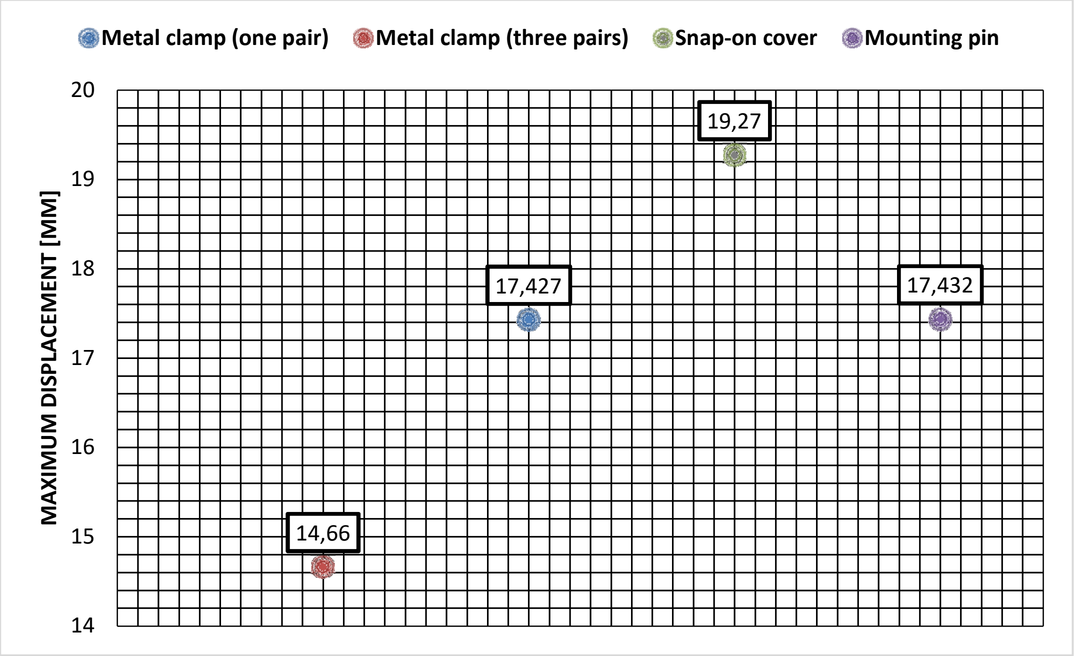

Fig. 12. Maximum displacement chart for simulation tests performed

3. Economic and ergonomic analysis

The fastening system solution in safety fencing should be economically justified while ensuring adequate strength and ergonomic installation, where one of the key features is the number of operators required for installation, installation time, and availability of installation components. Poor ergonomics, on the other hand, can cause musculoskeletal strain [17-19].

The metal clamps used in the first concept of the fastening system require the use of two or three types of clamps: intermediate, angular, and end clamps. Clamps are one of the most common solutions, which is why their purchase price is very low at wholesale prices. It is unlikely that starting your own production of these elements would result in lower or even the same costs of erecting a fence. Especially since three types of clamps may be required to build a fence, in-house production of these elements will almost certainly not be cost-effective for single or small-batch production. Therefore, it remains to purchase clamps from the market, which are affordable. It was assumed in the work that multiple clamps could be used. However, even when using single pairs for assembly, this is a solution that will probably require the most time during installation. This is due to the design of the clamp, which consists of two elements that must be permanently connected to each other. After placing the mesh panel between these elements, the clamp must be tightened properly to prevent the panel from shifting or becoming loose. Each clamp must be fixed at the correct height of the fence. If appropriate markings have been made on the posts or fixing holes, this will speed up the operation. However, one pair of threaded connections must be screwed onto each pair of intermediate or angle clamps. The operation would be much faster with the use of a suitable electric device, but this requires having it in your equipment. The fence can be installed by a single operator with proper planning of the operation and assembly activities, but this can be significantly more difficult. Mounting the mesh panel on a support element does not ensure that all degrees of freedom are eliminated. The panel may rotate and fall out of its axis, posing a risk of injury to the operator. In addition, intermediate and angle clamps should be installed with two adjacent mesh panels placed on the supporting elements. For this reason, a second operator may be required during installation for this fence model. Installing a fence using clamps may require specialized tools to speed up the process. This solution also does not offer the possibility of quick disassembly and will be as complex as installation. This is certainly the solution with the worst ergonomics; despite its low production cost and simplicity of construction, it does not offer the possibility of quick and easy installation.

The snap-on cap presented as the second fastening system concept has a complex design, and the material used must have elastic properties to ensure proper functioning of the fastening element. Depending on the technology used, its production can be very costly. Manufacturing the cap by injection molding involves significant costs in the form of purchasing the appropriate equipment and making the injection mold. For small-batch production, it is more advantageous to use the injection molding services of an external company, but this requires an injection mold, which is very expensive to manufacture. The price of the material itself is low compared to the costs associated with this technological process. Therefore, this solution could be used in mass production, where the cost of starting production is not so significant due to the planned sales horizon and production volume. Caps offer much faster installation, but their installation involves difficult access to the installation area. It is necessary to reach the upper end of the mesh panel profile in order to install the cap, which snaps into place. This can be done by a single operator, as they are able to install the mesh panel on the support element, climb onto a step or ladder, and install the cap. This is not the safest solution, but it is definitely possible. The installation of the cap itself consists only of inserting it into the mesh panel profile, after adjusting its angle relative to the post profile, lowering it, and snapping it onto the profile. A step or ladder will definitely be needed. This may not be necessary for safety fences of lower height. For the disassembly process, a ladder or step stool should again be used to provide access to the area for the disassembly tool, which must be inserted to knock the latch out of the post geometry before disassembling the mesh panel. This is a favorable solution in terms of installation, but the main disadvantage is the need to use a step stool or ladder for tall fences.

The third concept based on a mounting pin is a solution whose cost is comparable to that of metal clamps, and is slightly higher or almost identical to the cheapest solution on the market presented in the first concept. The cost of purchasing materials, processing, and all technological processes that must be carried out in order to obtain a finished component for assembly can be significantly reduced. As a result, the cost of production of the component is very similar to that of metal clamps, with the possibility of starting your own production, which will be justified even for small-batch production. This is due to the availability of the tools necessary to manufacture this element, mainly a hydraulic press and a CNC lathe, which, unlike the injection mold mentioned in the second concept, can be used for other projects or sold after production is completed. The installation of pins, i.e., the third concept, differs slightly from the installation of a cap, i.e., the second concept, and also requires at least one operator. It is still a relatively simple process that can be carried out fairly quickly. The only thing you need to do is insert the pin into the mounting holes after determining the position of the mesh panel. The disassembly process is similar to that described in the concept with a mounting cap and consists only of releasing the lock from the pin and sliding it out of the hole in the fence post. This solution is therefore the most advantageous in terms of the ergonomics of installation and removal. Like the other concepts, it requires the use of tools, but does not require a step ladder or ladder and allows for quick installation and removal.

Table 1 contains a multi-criteria comparison of the concepts under consideration, compiled on the basis of analyses and simulations. Each aspect is assessed on a scale of bad, good, and very good. A poor rating means that the solution has the worst rating for the selected parameter among the concepts under consideration; the opposite applies to a very good rating. A good rating places the solution in the middle or in the same position as other solutions with the same rating for the aspect under consideration. Based on this table, it is possible to quickly identify the solution that best reflects the consumer's needs depending on their situation.

Table 1. Multi-criteria comparison of solutions

Solution	Strength	Cost	Ergonomics
Concept 1	Good	Very good	Bad
Concept 2	Bad	Bad	Good
Concept 3	Very good	Good	Very good

Conclusion

The article presents the results of simulation strength tests for selected concepts of fastening systems in safety fences. Based on the tests conducted and the results obtained, the following conclusions can be drawn:

1. The use of one metal clamp allowed for a maximum displacement of 17.427 mm;
2. The use of multiple clamps allowed for the greatest reduction in displacement, bringing it down to 14.66 mm;
3. The mounting cap achieved the worst result of all, with a displacement of 19.27 mm;
4. The mounting pins allowed for a displacement value similar to that of a single pair of clamps, with a slight, barely noticeable difference in favor of strength considerations;

5. Mounting pins and clamps can be used in multiple quantities to significantly increase the rigidity of the entire fence, although this entails higher construction costs and requires more manpower during installation;
6. Pins are a more robust solution compared to clamps, as their construction is more durable and resistant, and the system consists of fewer components.

Based on the simulations and analysis carried out, mounting pins can be considered the most advantageous solution, both in terms of strength, economy, and ergonomics (Table 1). They ensure high fence rigidity, higher than all others considered in this study, and additionally have high inherent resistance to loads and stresses. What is more, their production method does not involve complex technological processes that require increased financial outlays. Although metal clamps are certainly a cheaper solution in economic terms, they require the design and production of three versions of the same element: intermediate clamps (parallel connection), angle clamps (perpendicular connection), and end clamps (located on the last post in the fence). The pin is manufactured as a single design solution for all types of connections. Caps are also not economically advantageous due to their complex shape and construction. They require injection molding, which is associated with high start-up costs and is completely unprofitable for small-batch production. For ergonomic reasons, no solution can match snap-on caps, which are the fastest to install, but properly prepared posts and panels can be connected just as quickly using pins.

The test results and analysis of solutions are sufficient to consider the mounting system solution using mounting pins to be inexpensive, robust, and easy to install. Based on this knowledge, a suitable design can be prepared for further testing. This design can also be left for further development without yet moving on to the production stage. The right direction for development would be to refine the pin design so that the latch release system is already inside it and only requires the use of a special tool to release it, which will allow unnecessary interference with the pole structure to be avoided. This is because the current solution provides for special holes to allow the pin to be removed. Therefore, it is worth optimizing the design in terms of assembly efficiency (DFA), reducing the number of assembly and disassembly operations and simplifying them. It is also possible to adapt the design of the fences themselves to different assembly methods, which do not necessarily require human involvement. Fence installation can be robotized to eliminate or reduce the need for human labor. The implementation of Lean Manufacturing should also be considered in order to continuously improve processes, eliminate material waste, and improve production efficiency.

References

[1] Optical Inspection Software for a Selected Product on the Smart Factory Production Line //Advanced Manufacturing Processes II : Selected Papers from the 2nd Grabchenko’s International Conference on Advanced Manufacturing Processes (InterPartner-2020), September 8-11, 2020, Odessa, Ukraine, p. 785-796.

[2] Sękala A., Kost G., Banas W., Gwiazda A., Grabowik C. Modelling and simulation of robotic production systems //Journal of Physics: Conference Series. 2198. 012065. 10.1088/1742-6596/2198/1/012065. 2022.

[3] Sgarbossa F., Grosse F.H., Neumann W.P., Battini D., Glock Ch.H., Human factors in production and logistics systems of the future //Annual Reviews in Control, Volume 49, 2020, p. 295-305, https://doi.org/10.1016/j.arcontrol.2020.04.007.

[4] Zhao J., Pang R., Zhang S., Human Reliability Evaluation of Assembly Production Line //Int J Performability Eng vol. 14, no. 12, December 2018, p. 3109-3117 DOI: 10.23940/ijpe.18.12.p20.31093117.

[5] Oberer-Treitz S., Dietz T., Verl A., "Safety in industrial applications: From fixed fences to direct interaction," IEEE ISR 2013, Seoul, Korea (South), 2013, p. 1-4, doi: 10.1109/ISR.2013.6695745.

[6] Zhang Ch. Dynamic virtual fences for improving workers safety using BIM and RTLS //Proceedings of the 14th International Conference on Computing in Civil and Building Engineering. 2012.

[7] Changfeng W., Kan Z., Yong L., Yichen C., Dongdong Z., Haoqiong Y. Exploration of the application of electronic fences driven by computer algorithms in industrial safety //Proc. SPIE 13692, Fourth International Conference on Electronics Technology and Artificial Intelligence (ETAI 2025), 136925M (24 July 2025); https://doi.org/10.1117/12.3068456.

[8] Gonet R. Skuteczność ogrodzeń ochronnych jako elementów bezpieczeństwa //Warszawa EcoMS Consulting Sp. z o.o, 9/2021, p. 88-91.

[9] Kilikevicius A., Bacinskas D., Selech J., Matijosius J., Kilikeviciene K., Vainorius D., Ulbrich D., Romek D.: The Influence of Different Loads on the Footbridge Dynamic Parameters //Symmetry. vol. 12, nr 4, 2020, p. 657-1 - 657-21.

[10] Pieniak D., Walczak A., Oszust M., Przystupa K., Kamocka-Bronisz R., Piec R., Dzień G., Selech J., Ulbrich D.: Influence of Thermal Shocks on Residual Static Strength, Impact Strength and Elasticity of Polymer-Composite Materials Used in Firefighting Helmets //Materials, 15(1), 57, 2022, p. 1-21.

[11] Selech J., Ulbrich D., Włodarczyk K., Kowalczyk J., Marcinkiewicz J., Opioła M.: Koncepcja i analiza konstrukcji uniwersalnego uchwytu narzędzi urządzenia do badania elementów pracujących w gruncie //Przegląd Mechaniczny, Wydawnictwo Sigma-Not, 6/2017, p. 42-44, doi 10.15199/148.2017.6.8.

[12] Włodarczyk K., Ulbrich D., Selech J., Kowalczyk J., Marcinkiewicz J., Płotecki K.: Opracowanie modelu 3D i analiza konstrukcji kanału glebowego //Mechanik, 7, 2017, p. 600-602, doi.org/10.17814/mechanik.2017.7.85.

[13] Smith A.L., Reliability of engineering materials. 1st Edition, Elsevier, 2013 October 22.

[14] Selech J., Ulbrich D., Włodarczyk K., Kowalczyk J., Adamkiewicz J. //The prototype of stream amplifier used in transport of polydisperse medium. Procedia Engineering. Vol 192, 2017, p. 777-781.

[15] Kim Y.J., Byung R.Ch. Economic integration of design optimization //Quality Engineering, 2000, 12.4, 561-567.

[16] Warguła Ł., Rosiak S., Gierz, L., Gavrilin A., Bykadorov S. The concept of a wood chopping machine with a mechanical overload system ensuring continuity of work //Mater. Mech. Eng. Technol, 2021, 3, 21-26. DOI 10.52209/2706-977X_2021_3_22.
[17] Stanton N.A., Mark S.Y. Guide to methodology in ergonomics: Designing for human use. CRC Press, 2002.
[18] Warguła Ł., Wieczorek B., Giedrowicz M., Kukla M., Nati, C. Wood Chippers: Influence of Feed Channel Geometry on Possibility of Musculoskeletal System Overload. Croatian Journal of Forest Engineering //Journal for Theory and Application of Forestry Engineering, 2025, 46(1), 59-76 doi: https://doi.org/10.5552/crojfe.2025.2501.
[19] Wieczorek B., Kukla M., Warguła Ł., Giedrowicz M., Ergonomic guidelines for the design interfaces of additive modules for manual wheelchairs: sagittal plane //Scientific Reports 13, 1199, 32023. https://doi.org/10.1038/s41598-023-39085-7.

Information of the author

Banas Piotr, Eng., M.Sc student, Poznan University of Technology
e-mail: piotr.banas@student.put.poznan.pl

DOI 10.52209/2706-977X_2025_3_51 IRSTI 81.09.01 UDC 621.9.047

Analysis of Operating Conditions for Parts in the Metallurgical and Machine-Building Industries and Justification for the Choice of Protective Coating

Kulikov V.Yu.*, Kvon Sv.S., Issagulov A.Z., Kovalyova T.V., Olzhatayev O.
Abylkas Saginov Karaganda Technical University, Karaganda, Kazakhstan
*corresponding author

Abstract. Aggressive operating conditions, such as high temperatures, chemical environments, abrasive wear, and corrosion, lead to premature wear and failure of parts in the metallurgical and machine-building industries. To solve this problem, protective coatings are used, but traditional methods (galvanic, chemical treatment) often do not provide sufficient reliability in extreme conditions. One of the most effective solutions is gas thermal spraying, which allows coatings with unique properties such as high hardness, wear resistance, corrosion resistance, and strong adhesion to the substrate to be applied. This article is devoted to the analysis of the operating conditions of parts in aggressive environments and the justification for choosing gas thermal spraying as the optimal protection method. Particular attention is paid to the selection of powder materials, such as WC/Co, Cr_3C_2-NiCr, Cr_2O_3, and Al_2O_3, depending on the type of wear (corrosive, abrasive, adhesive). Various types of gas thermal spraying and their advantages are considered. The correct choice of material and spraying method can significantly increase the service life of equipment, reduce repair costs, and increase overall production efficiency.

Keywords: corrosion, wear, adhesion, hardness, protective coating.

Introduction

Modern industry, particularly the metallurgical and machine-building sectors, faces the problem of premature wear and tear and destruction of machine parts and equipment [1]. The reasons for this are aggressive operating conditions, including exposure to high temperatures, aggressive chemical environments, abrasive wear, corrosion, and erosion [2]. These factors lead to a reduction in the service life of parts, increased repair and replacement costs, and production downtime [3].

This problem is global in nature, causing significant economic damage estimated at billions of dollars annually. According to research, losses associated with corrosion and wear amount to 4-5% of the GDP of developed countries, with a significant share of these losses attributable to industrial equipment [4]. In the context of the metallurgical and machine-building industries, where parts operate under extreme temperatures, high mechanical loads, and aggressive chemical environments, the problem of wear becomes particularly acute [5].

The key types of wear leading to premature failure of parts are corrosion, mechanical (adhesive, abrasive), and fatigue wear [6]. Each of these mechanisms has its own specific characteristics and requires an individual approach to protection.

In the metallurgical and machine-building industries, parts are regularly exposed to aggressive environments. In metallurgical furnaces, casting and heat treatment equipment, parts are exposed to hot gases, melts, and slags [7]. For example, in continuous steel casting plants, parts that come into contact with molten metal are subject to intense corrosion, which reduces their service life to a few weeks [8]. In mechanical engineering, especially in the manufacture of chemical equipment, parts work in contact with solutions of acids, alkalis, salts, and other aggressive reagents [9]. For example, in pumps for pumping sulfuric or nitric acid, in valves and pipelines, corrosion can lead to complete destruction of parts within a few months, creating a threat of accidents [10].

Parts operating in the open air are exposed to atmospheric precipitation, industrial emissions, and salts, and are subject to corrosion and mechanical wear, significantly reducing their service life [11]. According to research [12], even in a temperate climate, the corrosion rate of unprotected steel can reach 0.1-0.2 mm per year, and in aggressive industrial atmospheres, this figure increases several times.

The solution to this problem lies in the use of protective coatings, which significantly extend the service life of parts and increase their reliability [13]. They often have thickness limitations, are brittle, have low adhesion, or are insufficiently resistant to combined effects [14].

Among the many existing coating methods, gas-thermal technologies occupy a special place. Gas-thermal coatings have a unique combination of properties, such as high hardness, wear resistance, corrosion resistance, and adhesion to the substrate [15].

To ensure the physical and mechanical properties of the coating, it is necessary to select the right material for gas thermal spraying. Powders used for gas thermal spraying can be classified according to their chemical composition and purpose [16]:

1) Powders based on metals and alloys;
2) Powders based on carbides, borides, and nitrides;
3) Powders based on oxides;
4) Composite powders (cermets);

Powders based on metals and alloys are the most extensive group, including materials based on iron, nickel, cobalt, copper, and their alloys. They are used to restore the dimensions of parts, increase wear resistance, and improve corrosion resistance [17]. Powders based on carbides, borides, and nitrides, often referred to as hard alloys, have exceptional hardness and wear resistance. The most common are tungsten and chromium carbides [18]. Oxide-based powders, such as aluminum oxide (Al_2O_3), zirconium dioxide (ZrO_2), and chromium oxide (Cr_2O_3), are used to create coatings with high hardness, wear resistance, and heat resistance [19]. Composite powders are a mixture of a metal matrix and a solid phase (e.g., carbides or oxides). They combine the plasticity of metal and the hardness of ceramics, making them ideal for conditions of abrasive wear and impact loads [20].

The assessment of the operating conditions of parts in the machine-building and metallurgical industries that operate in aggressive environments and the selection of materials for gas thermal spraying are key to improving the reliability, durability, and cost-effectiveness of equipment as a whole.

In this regard, the purpose of this article is to analyze the operating conditions of parts in the metallurgical and machine-building industries that operate in aggressive environments and to justify the use of gas-thermal coating as the most effective and universal solution for their protection. Particular attention will be paid to the selection of optimal chemical compositions for coatings capable of withstanding specific types of aggressive exposure.

1. Working conditions for parts in the metallurgical and machine-building industries

Machine and equipment parts in the metallurgical and machine-building industries are exposed to various aggressive environments, which can be divided into several groups, as shown in Table 1.

Table 1. Aggressive environments and components in the metallurgical and machine-building industries

Environment	Part	Consequence of interaction between a part and its environment
Diluted solutions of nitric acid, solutions of salts with oxidizing properties	Fastening parts, rollers, bushings for machines and vessels (Figure 1a)	Nitric acid causes intense corrosion of most metals, especially carbon and low-alloy steels. Salt solutions cause active corrosion, especially in areas of stress concentration.
Atmospheric precipitation, aqueous solutions of organic acid salts at room temperature, shock loads	Parts with increased plasticity that are subject to impact loads – hydraulic press valves (Figure 1b) Parts that come into contact with atmospheric precipitation – pipes (Figure 1c)	Corrosion is exacerbated by mechanical stresses, leading to corrosion-mechanical wear. These stresses can cause damage to coatings and substrates.
Temperatures up to 1200 °C in air and hydrocarbon atmospheres	Sheet metal parts for furnace rollers (Figure 1d), hangers and supports in boilers, furnace screens (Figure 1e)	Accelerate corrosion processes and can cause thermal destruction of the part surface.
Temperature up to 780°C	Rotors, discs, blades (Figure 1f)	Leads to thermal stresses, which can cause the coating to peel off.
Conditions of abrasive wear	Plungers, rods (Figure 1g), guide rollers, grippers	Destruction of the part's surface
Conditions for adhesive wear	Piston rings (Figure 1 h), hydraulic cylinder rods, plain bearings (Figure 1i), bushings	Scuffing, scratches, micro-welding on the surface of the part

Mating parts of machines and equipment in the metallurgical industry operate under extreme conditions, which leads to the appearance of various surface defects that accelerate wear and tear and can lead to breakdowns. These defects can be classified according to their origin and nature. Abrasive wear caused by the impact of solid particles (dust, dirt, wear products) entering the friction zone. This leads to the formation of scratches, grooves, and scuffs on the surface of parts, which increases friction and temperature. Fatigue wear occurs under the influence of high alternating loads, which leads to the formation of microcracks on the surface [21]. Over time, these cracks grow, and metal particles separate from the surface, forming spalling. The causes of fatigue wear are often defects in the structure of coatings, such as pores, cracks, and oxide films. To prevent this, dense coatings are necessary. Adhesive wear occurs when working without lubrication or when there is a lack of it. In this case, areas of rubbing surfaces adhere at the molecular level and then break down, leading to the formation of deep scratches and grooves.

In order to avoid the consequences of surface damage to parts operating in aggressive environments, protective coatings must be used. One promising direction for applying protective coatings is gas thermal spraying. Gas thermal spraying is a process of heating, dispersing, and transferring condensed particles of the sprayed material by a gas or plasma flow to form a layer of the desired material on the substrate [22].

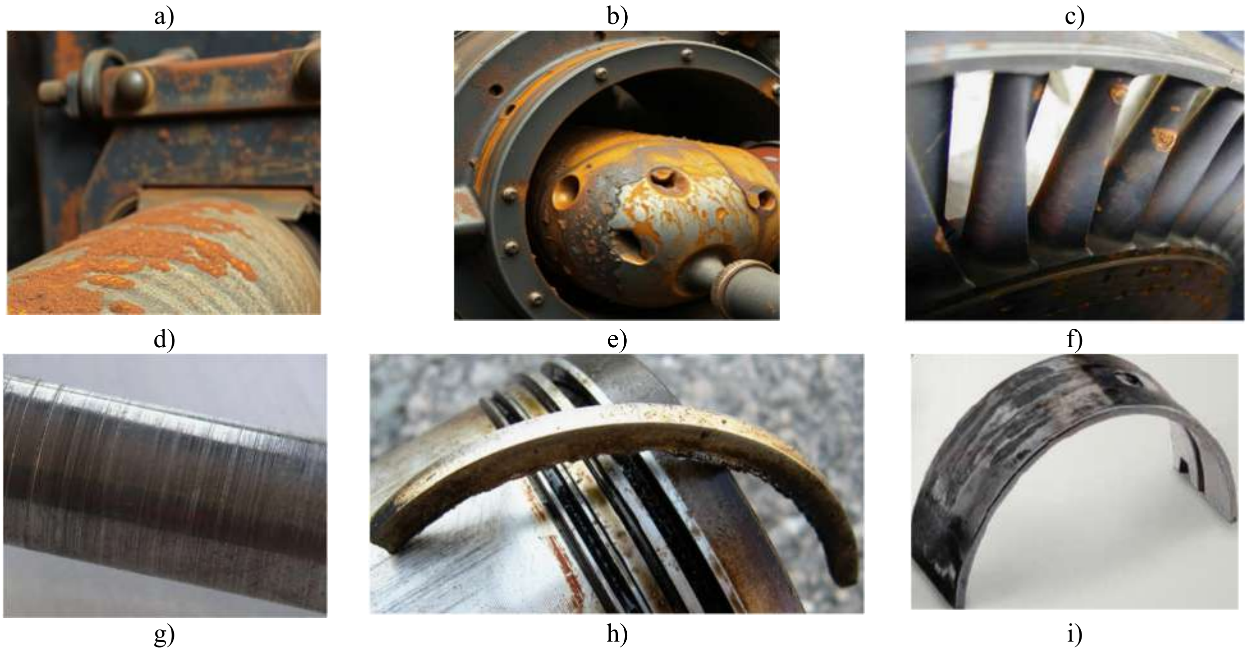

Fig. 1. – Effects of aggressive environments on parts in the metallurgical and machine-building industries

The following types of gas-thermal spraying are most commonly used to increase the wear resistance of parts: high-velocity oxygen fuel (HVOF) spraying / high-velocity (supersonic) spraying (HVAF); plasma spraying, detonation spraying [23].

There are several methods of gas-flame spraying, depending on the energy that acts on the sprayed material (Figure 2).

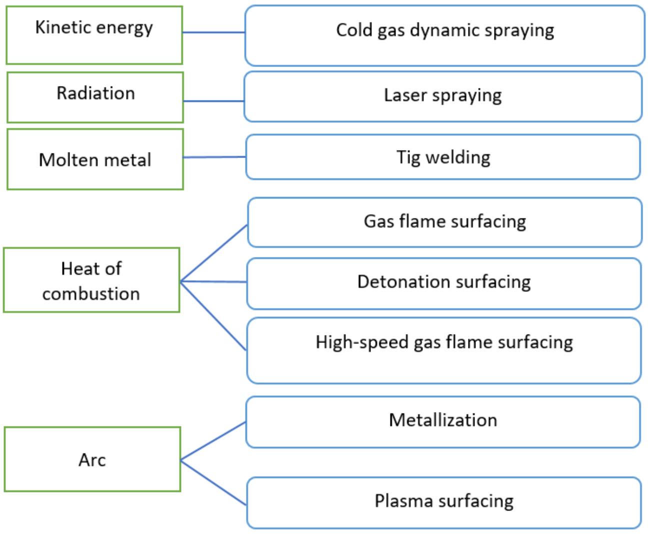

Fig. 2. – Classification of gas-thermal spraying methods based on the energy source

The use of gas-thermal coating application has a number of significant advantages [24]:

1) Gas-thermal methods allow coatings to be applied from a wide range of materials: metals, alloys, cermets. This makes it possible to select the optimal coating composition for any aggressive environment and operating conditions;

2) During gas thermal spraying, coating particles in a plastic state collide with the substrate at high speed, forming a strong mechanical bond and, in some cases, a diffusion bond;

3) Gas-thermal coatings can have a thickness ranging from tens of microns to several millimeters, which allows for the creation of reliable protection against corrosion wear;

4) During the spraying process, the substrate temperature usually does not exceed 150-250 °C, which eliminates thermal deformation, structural changes, and softening of the part;

5) Gas thermal spraying can be used not only to protect new parts, but also to restore worn ones, which significantly reduces repair costs.

6) Many gas thermal processes are more environmentally friendly than galvanic processes, as they do not use toxic chemicals.

2. Materials for improving the wear resistance of parts in the metallurgical and machine-building industries

The choice of powder for gas thermal coating depends on the service properties of the part (relative wear resistance, friction coefficient, heat resistance, corrosion resistance, heat resistance, contact endurance).

Taking into account the types of wear during the operation of parts in the metallurgical and machine-building industries, materials for gas thermal spraying can be classified (Table 2).

Table 2. Materials for gas thermal spraying for a specific type of wear

Type of wear	Material for gas thermal spraying
Corrosion wear	Co-, Ni-alloys or Cr_2O_3 and Al_2O_3 impregnated oxide/ceramic coatings
Abrasive wear	WC/Co and mixture NiCrBSi + WC/Co
Adhesive wear	Mo + NiCrBSi

Corrosion wear is successfully countered by:
1) Cermets:
– tungsten carbide (WC-Co 88-12, WC-Co-Cr 86-10-4);
– chromium carbide (Cr_3C_2-NiCr 75-25);
2) Metal oxides (Cr_2O_3, Al_2O_3).
The hardness of typical wear-resistant coatings is shown in Figure 3.

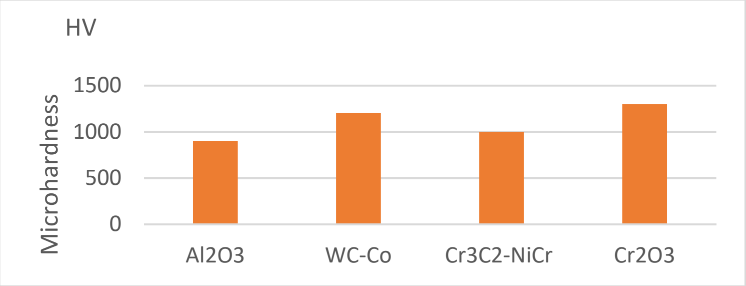

Fig. 3. – Hardness of wear-resistant coatings

Aluminum oxide (Al_2O_3) is a very hard but brittle material. Aluminum oxide spraying creates coatings with high hardness and excellent dielectric properties [25]. The coating has good wear resistance to abrasion. Aluminum oxide coatings are used on parts operating under abrasive wear conditions where high impact strength is not required. It is used for insulating coatings on pump shafts where electrical insulation and wear resistance are required. In metallurgy, it is used on guide rollers operating at high temperatures.

Tungsten carbide in a cobalt matrix (WC-Co) is the most well-known and widely used cermet for gas thermal spraying [26]. Tungsten carbide (WC) particles provide exceptional hardness and wear resistance, while the cobalt matrix (Co) binds them together, providing the necessary ductility and strength. The ratio of WC to Co can vary (e.g., WC-12Co, WC-17Co) depending on the required properties. WC-Co coatings are used to protect against abrasive wear and erosion. They are applied to rods, pump sleeves, plungers, seals, and wear surfaces in the metallurgical industry (e.g., guide rollers, grippers). The coating has high compressive strength and excellent erosion resistance.

The main advantage of Cr_3C_2-NiCr lies in the synergy (complementary action) of its components [27]. Cr_3C_2 provides exceptional hardness and wear resistance. NiCr (the binding matrix) provides ductility, adhesion strength, as well as corrosion and heat resistance. The coating is applied to ball valves, valve seats, and pump impellers to increase their wear resistance in aggressive environments. Cr_3C_2-NiCr coating is also applied to shafts operating under conditions of friction and wear, such as pressure rollers in the metallurgical industry. As a replacement for hard chrome, Cr_3C_2-NiCr coating is applied to hydraulic cylinder rods. This provides high wear resistance, corrosion protection, and better environmental performance compared to chrome plating.

The Cr_2O_3 coating is a hard, dense, and chemically inert ceramic. It is this coating that determines the key properties of the coating [28]. The Cr_2O_3-based coating has high microhardness, which makes it extremely resistant to abrasive wear and erosion. This property is its main advantage. The coating has natural lubricating (tribological) properties, which reduces friction between mating surfaces. This is especially important in conditions of dry friction or insufficient lubrication. Chromium oxide is a stable compound and does not react with most chemically aggressive environments, providing excellent corrosion resistance. Cr_2O_3 is also stable at high temperatures and does not lose its properties, allowing the coating to be used in conditions where metals can soften or oxidize. This coating is applied to protect parts from abrasive wear and corrosion, especially when pumping aggressive liquids (for example, for pump rods and plungers in the chemical industry or at treatment plants).

To protect against high-temperature corrosion, the schemes shown in Figures 4 and 5 are used.

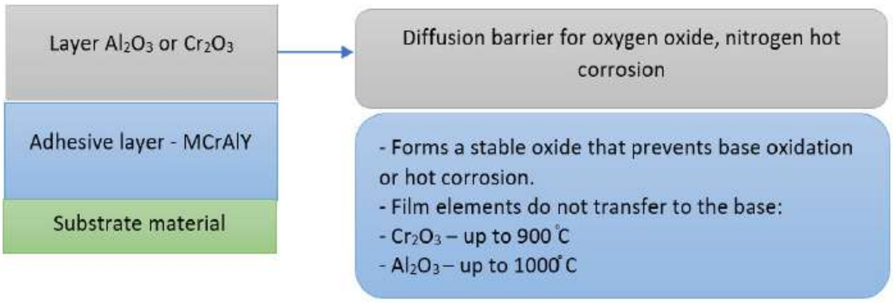

Fig. 4. - Corrosion coatings operating at temperatures up to 1000 °C

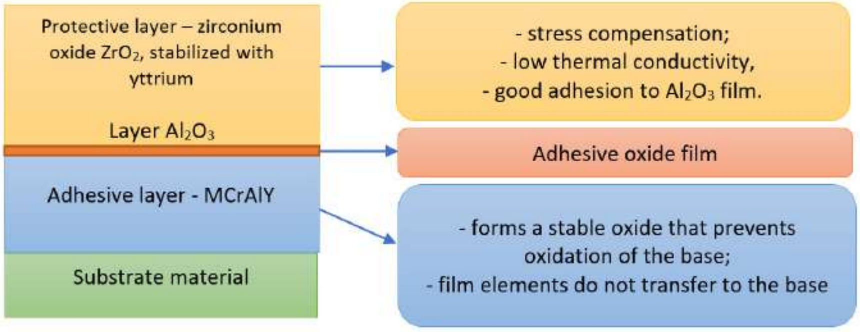

Fig. 5. - Thermal barrier coatings for turbine blades (up to 1,200 °C)

To increase wear resistance, WC/Co or NiCrBSi+WC/Co mixtures are used in cases where the part is subject to abrasive wear [29]. At the same time, to achieve high and uniform hardness, as well as a homogeneous and dense coating structure, it is best to use high-velocity oxy-fuel spraying (HVOF/HVAF) for mating surfaces.

To avoid adhesive wear, it is necessary to prevent metallurgical interaction between surfaces, which leads to micro-welding. For example, in engine cylinders, this is achieved using a special porous coating. It is applied using plasma spraying (a mixture of molybdenum and NiCrBSi), and the pores retain the lubricant. Ni-Cr-B-Si is a self-fluxing powder widely used for spraying and melting [30]. The nickel base provides good corrosion resistance and strength. Chromium (Cr) increases corrosion and erosion resistance, while boron (B) and silicon (Si) lower the melting point and promote the formation of a glassy phase during melting, which ensures a dense and non-porous coating.

The use of specialized powder materials in gas thermal spraying technology opens up wide opportunities for improving the wear resistance, corrosion resistance, and strength of parts in the machine-building and metallurgical industries. The right choice of material, taking into account the operating conditions of the part and the required properties of the coating, can significantly extend the service life of equipment, reduce repair costs, and increase overall production efficiency. Each material has its own area of application, from metal-ceramic powders that provide exceptional hardness to ceramic materials that create heat-shielding barriers.

In summary, in order to select the optimal material for gas thermal coating, it is necessary to know:

- the operating conditions of the part - abrasive wear, erosion, corrosion, impact loads, high temperatures;
- the required properties of the coating - hardness, strength, corrosion resistance, thermal insulation properties;
- the spraying method - high-velocity oxygen fuel (HVOF) spraying, plasma spraying, detonation spraying, etc.

This makes gas-thermal coating a versatile and indispensable tool in modern industry.

Conclusion

Parts used in the machine-building and metallurgical industries are subjected to intense aggressive influences, such as high temperatures, abrasive wear, and corrosion, which leads to their rapid wear and destruction. Traditional protection methods, such as electroplating, do not always cope with extreme conditions, as they have limitations in terms of thickness, brittleness, and low adhesion. In this regard, gas thermal spraying has proven itself to be a highly effective and versatile method for protecting and restoring parts.

A key aspect of the success of gas thermal spraying is the correct choice of powder material. Materials intended for spraying are divided into several groups: metals and alloys, carbides, borides, nitrides, oxides, and composite powders (cermets). For example, Co- and Ni-alloys, as well as ceramic coatings based on chromium oxides and aluminum oxide, are used for parts subject to corrosion wear.

Under conditions of abrasive wear, carbide-based materials such as WC/Co and their mixtures with NiCrBSi show the best results. To protect against adhesive wear, which causes micro-welding and scoring, coatings based on molybdenum and NiCrBSi are used.

Gas thermal spraying technology has a number of advantages, including the ability to create a strong mechanical and diffusion bond between the coating and the substrate, no thermal deformation of the part due to low heating temperatures, and the ability to apply coatings of varying thicknesses. This makes gas thermal spraying a versatile tool that can not only protect new parts but also effectively restore worn ones. In general, a thorough analysis of operating conditions, the correct choice of powder material and spraying method (e.g., HVOF for high-velocity spraying or plasma spraying for porous coatings) can significantly increase the durability and reliability of equipment, reduce maintenance costs, and increase overall production efficiency.

The next area of research will be the selection of the composition ratio of powders for gas-thermal spraying with damping properties using the high-speed gas-flame spraying method.

Acknowledgments. This research was conducted as part of grant AP 26199877 from the Science Committee of the Ministry of Education and Science of the Republic of Kazakhstan, entitled “Development of technology for applying composite protective coatings to equipment parts in the metallurgical and machine-building industries.”

References

[1] Artiukh V., Mazur V., Sahirov Yu., Kapustina N. Protection of Metallurgical Machines from Breakdowns at Iron and Steel Works //Advances in Intelligent Systems and Computing, 1, 2020 DOI: 10.1007/978-3-030-37916-2_94

[2] Bhardwaj D. Introduction to Surface Engineering for Corrosion and Wear Resistance. - Netherlands: ASM International, 2001. – 345 p.

[3] Rakesh Lt. Dr. Santosh KumarLt. Dr. Santosh Kumar Overview of Corrosion and its Control: A Critical Review //Proceedings on Engineering Sciences Proceedings on Engineering Sciences, 3(1), 2021, DOI: 10.24874/PES03.01.002

[4] Mazumder M.A.J. Global Impact of Corrosion: Occurrence, Cost and Mitigation // Global Journal of Engineering Sciences 5(4), 2020, DOI: 10.33552/GJES.2020.05.000618

[5] Winkelmann H., Badisch E., Kirchgaßner M., Danninger H. Wear Mechanisms at High Temperatures. Part 1: Wear Mechanisms of Different Fe-Based Alloys at Elevated Temperatures //Tribology Letters, 34(3), 2009, 155-166 DOI: 10.1007/s11249-009-9421

[6] Dodiya V. K., Parmar J. P. A Study of Various Wear Mechanism and its Reduction Method // IJIRST –International Journal for Innovative Research in Science & Technology, Volume 2, Issue 09, February 2016

[7] Okorie O. High Temperature Rheological Characteristics of Iron and Steel Making Slag and its Waste Heat Recovery-A Review //Advances in Metallurgical and Material Engineering, Volume 3, Issue 1, 2020 DOI: 10.36959/508/401

[8] Aneziris C. G., Biermann H. Numerical Simulation of Continuous Steel Casting Regarding the Enhancement of the Cleanliness of Molten Steel .Multifunctional Ceramic Filter Systems for Metal Melt Filtration, Springer Series in Materials Science 337, pp 769–785 https://doi.org/10.1007/978-3-031-40930-1_30

[9] Avdeev Ya.G., Kuznetsov Yu.I. Effect of iron (III) salts on steel corrosion in acid solutions. A review //Int. J. Corros. Scale Inhib., 2021, 10, no. 3, 1069–1109

[10] Pracht G., Perschnick N. A material challenge – Pumps in sulphuric acid application // Procedia Engineering 138, 2016, 421 – 426

[11] Kusmierek E., Chrzescijanska E. Atmospheric corrosion of metals in industrial city environment //Data in Brief 51(C), 2015. P. 23-30 DOI: 10.1016/j.dib.2015.02.017

[12] Konovalova V. The effect of temperature on the corrosion rate of iron-carbon alloys //Materials Today Proceedings, 38(5), 2020 DOI: 10.1016/j.matpr.2020.08.094

[13] Islam M.S., Hasan M.J., Poroma P., Sakter S. A review on the environment friendly electroplating of Cr (III) & Cr (VI) //Journal of Science and Engineering Papers, 01(01), 2024 DOI: 10.62275/josep.24.1000006

[14] Aljibori H.S., Al-Amiery A.A.H., Kadhum A.A.H Advances in corrosion protection coatings: A comprehensive review International Journal of Corrosion and Scale Inhibition 12(4), 2023,1476-1520 DOI: 10.17675/2305-6894-2023-12-4-6

[15] Zhetessova G., Zharkevich O., Pleshakova, Ye., Yurchenko V., Platonova Ye., Buzauova T. Building mathematical model for gas-thermal process of coating evaporation //Metalurgija 55(1), 2016, 63-66

[16] Łatka L., Pawłowski L, Winnicki M., Sokołowski P., Małachowska A., Kozerski S.Review of Functionally Graded Thermal Sprayed Coatings //Applied Science, 2020, 10(15), 5153; https://doi.org/10.3390/app10155153

[17] Skyba M.Ye., Stechyshyn M.S., Oleksandrenko V.P., Mashovets N.S., Bilyk Yu.M. Wear resistance of composite electrolytic coatings //Problems of tribology 27(1/103), 2022, 6-13 DOI: 10.31891/2079-1372-2022-103-1-6-14

[18] Matikainen V, Peregrina S.R., Ojala N., Koivuluoto H., Shubert J., Houdková Š., Vuoristo P. Erosion wear performance of WC-10Co4Cr and Cr_3C_2-25NiCr coatings sprayed with high-velocity thermal spray processes //Surface and Coatings Technology, 370, 2019 DOI: 10.1016/j.surfcoat.2019.04.067

[19] Agarwal S., Singh S. Evaluation of Dry Sliding Wear Characteristics in Al5052/TiB_2/ZrO_2 Composites Against EN-31 Steel Counterbody //Material and mechanical engineering technology, 4, 2024, P.44 – 50 DOI 10.52209/2706-977X_2024_4_44

[20] Zharkevich O., Zhunuspekov D., Sherov K., Abayeva N., Akhmetov K., Taimanova G., Naboko Ye., Nurzhanova O. Mathematical modeling of the process of applying a gas-thermal coating to long rods of quarry special equipment //Journal of Applied Engineering Science,Volume 23, Number 2, 2025, No 1268, P. 236-242

[21] Morshed-Behbahani K., Farhat Z., Nasiri A. Effect of Surface Nanocrystallization on Wear Behavior of Steels: A Review Materials (Basel), 2024, 17(7), 1618. DOI: 10.3390/ma17071618

[22] Dolmatov A., Gulyaev I., KuzminV.I., Lyskov E. A., Ermakov K. A. Analysis and optimization of gas-thermal spray process in terms of condensed phase velocity and temperature //Thermophysics and Aeromechanics, 24(1), 2017, 83-94 DOI: 10.1134/S0869864317010097

[23]Amin S., Panchal H. A Review on Thermal Spray Coating Processes International Journal of Current Trends in Engineering & Research, Volume 2 Issue 4, 2016, P. 556 - 563

[24] Gerasimova A. A., Gorbatyuk S. M., Devyatiarova V. V. Application of Gas-Thermal Coatings on Low-Alloyed Steel Surfaces //Solid State Phenomena, 2018, 284, 1284-1290 DOI: 10.4028/www.scientific.net/SSP.284.1284

[25] Sirota V.V., Zaitsev S.V., Limarenko M.V., Prokhorenkov D.S., Churikov A.S. Effect of powder morphology on the structure and properties of Al_2O_3 based coatings obtained by detonation spraying. Construction Materials and Products. 2024. 7 (5). 7. DOI: 10.58224/2618-7183- 2024-7-5-7

[26] Ferrer M.Y., Peña G., Rodríguez L.F. Obtaining and characterizing of WC-Co coatings obtained from thermal spray by flame //Journal of Physics Conference Series, 1386(1), 2019, 012023 DOI: 10.1088/1742-6596/1386/1/012023

[27] Ksiazek M., Boron L., Radecka M., Richert M., Tchorz A. Mechanical and Tribological Properties of HVOF-Sprayed (Cr_3C_2-NiCr+Ni) Composite Coating on Ductile Cast Iron //Journal of Materials Engineering and Performance, Volume 25(8), 2016, 3185–3193 DOI: 10.1007/s11665-016-2226-x
[28] Pang X., Gao Dr. K., Yang Dr. H., Qiao Dr. L, Wang Dr. Y. The Cr_2O_3 coating is a hard, dense, and chemically inert ceramic. It is this coating that determines the key properties of the coating //Advanced engineering materials 2007, 9, No. 7, P. 594-599 DOI: 10.1002/adem.200700057
[29] Nikonova T., Gierz Ł., Berg A., Turla, V., Warguła Ł., Yurchenko V., Abdugaliyeva G., Zhunuspekov D., Wieczorek B., Robakowska M. Comparative Analysis of Strength Fatigue Properties and Abrasive Wear Resistance for a New Composition of Polymer Concrete Coated with Metal Alloy Powders //Coatings 2023, 13, 586.
[30] Tang L., Kang J., He P., Ding S., Chen S., Liu M., Xiong Yu., Ma G., Wang H. Effects of spraying conditions on the microstructure and properties of NiCrBSi coatings prepared by internal rotating plasma spraying //Surface and Coatings Technology, 374, 019 DOI: 10.1016/j.surfcoat.2019.06.056

Information of the authors

Kulikov Vitaly Yuryevich, c.t.s., professor, Abylkas Saginov Karaganda Technical University
e-mail: v.kulikov@ktu.edu.kz

Kvon Svetlana Sergeevna, c.t.s., professor, Abylkas Saginov Karaganda Technical University
e-mail: s.kvon@ktu.edu.kz

Issagulov Aristotel Zeinullinovich, d.t.s., professor, Abylkas Saginov Karaganda Technical University
e-mail: a.isagulov@ktu.edu.kz

Kovaleva Tatyana Viktorovna, PhD, tutor, Abylkas Saginov Karaganda Technical University
e-mail: t.kovalyova@ktu.edu.kz

Olzhatayev Olzhas Kanatovich, doctoral student, Abylkas Saginov Karaganda Technical University
e-mail: olzhasmailru7@gmail.com

DOI 10.52209/2706-977X_2025_3_58 IRSTI 81.09.03 UDC 539.37:620.17:531.7

Enhancement of Mechanical and Dynamic Properties of Elastomeric Nanocomposites for Structural Vibration Isolation: A Review of Materials, Mechanisms, and Applications

Al-Abboodi T.M.M.[1], Alaiwi Y.[1], Al-Khafaji Z. [2, 3] *, Falah M.[4]
[1]Altinbas University, Istanbul, Turkey
[2]Universiti Kebangsaan Malaysia, Bangi, Selangor, Malaysia
[3]Scientific Research Centre, Al-Ayen University, Thi-Qar, Iraq
[4]Al-Mustaqbal University, Hillah, Babil, Iraq
*corresponding author

Abstract. Elastomeric materials, particularly natural rubber (NR), exhibit exceptional mechanical resilience, energy absorption, and damping characteristics, making them vital in various engineering applications involving dynamic loading and vibration control. However, inherent limitations such as poor ozone resistance, thermal instability, and insufficient mechanical stiffness necessitate material modification to meet the demands of advanced structural systems. This review presents a comprehensive examination of recent advancements in the reinforcement of elastomeric matrices with nanostructured fillers, focusing primarily on zinc oxide (ZnO), multi-walled carbon nanotubes (MWCNTs), and sodium bicarbonate ($NaHCO_3$). The effects of these additives on the tensile strength, elongation at break, tear resistance, fatigue life, dynamic stiffness, and damping capacity of rubber-based composites are critically analyzed. Additionally, the study explores the integration of optimized rubber formulations into viscoelastic foundations for structural elements such as plates subjected to free and transient vibration loading. Emphasis is placed on the interplay between molecular chain structure, cross-linking mechanisms, filler dispersion, and their collective impact on the macroscopic behavior of the composite system. Numerical simulation approaches, including finite element modeling using SOLIDWORKS, are also reviewed to highlight their role in predicting the structural response of plate-foundation systems. The article consolidates experimental findings and theoretical models to guide future research and development of high-performance elastomeric systems in vibration mitigation and structural damping applications.

Keywords: natural rubber (NR), nano-composites, structural vibration isolation.

Introduction

The capacity to describe the mechanical response of elastomeric materials is a significant technological issue that needs to be fully comprehended, so it should be highlighted in detail [1]. Even though elastomers can be manufactured from diverse organic materials, all elastomers are polymers composed of extremely long-drawn molecular chains [2].

Elastomers are both synthetic and natural rubber. These elastomers are amorphous polymers with numerous combined components to form a rubber compound. The heating process and the chemical reaction of the elastomers called is vulcanization, which transforms the raw elastomeric materials into solid and elastic rubber materials [3]. As a result, elastomers are commonly referred to as rubber, and when subjected to stress, they have a high capacity for great deformation, distinguishing them from plastics. Put another way, they can be extended to one hundred percent of their original length without permanently deforming. Deformation is allowed through the polymer chain's arrangement and molecular structure of the elastomer. At rest, the polymer chain is incredibly warped and entangled, while the chain becomes linear when stress is applied [4–7]. These chains return to the normal, unstressed state after being released from stress. To ensure the chain is unstructured at rest, the elastomer's molecular structure should not be permitted to align itself and form a crystalline structure. Adding groups to polymer chains or utilizing more than one kind of monomer is the most common method of avoiding crystallization and regulating the aligned chains. Thus, the final product chain of an elastomer is cross-linking [8–11].

Cross-linking is the process of combining polymer chains and joining them with chemical bonds. These connections of chains limit motion while the strength is also increased [12]. Due to the inexpensive and availability of elastomeric components, they have a wide range of applications in real life and especially in engineering, such as tires, engine mounts, vibration isolators, gaskets, biomechanics, medical/dental, and solid propellants. They are also widely used due to their energy absorption and exceptional damping properties, as well as their flexibility, rebound, long-term use, and capability to resist humidity, high temperatures, and stress. Also, non-toxic. Elastomers are one-of-a-kind materials. It often behaves like a very viscous fluid through processing and molding. Elastomers can be subjected to substantial reversible elastic deformation when their polymer chains are bonded by the curing (or vulcanization) process. It will return to its former shape after removing the effective force, except if a failure occurs. The elastomer's one-a-kind properties, such as [13,14]:

i. Large deformations under the influence of load, and the elongation may reach five hundred percent in engineering applications.
ii. The stress-strain relation is noticeably non-linear.
iii. Exhibits substantial damping properties because of viscoelastic behaviors.
iv. Temperature and time-dependent behaviors.

v. Incompressible or incompressible, which indicates that its volume changes significantly under the action of stress, with the Poison's ratio being near or equal to 0.5.

The effects of high levels of vibration and noise are among the most common reasons that lead to the failure of the structures. As a result, rubber is used as a foundation for these structures in most applications to reduce these effects. In addition, Structure systems of a viscoelastic foundation are widely used in actual life for engineering applications such as decks of ships used as helipads for helicopters, runways of airports [14], railways vehicles, or any structure provided by the viscoelastic foundation. The viscoelastic foundation adds exterior damping to these structures, which is vital to the dynamic response. The viscoelastic foundation showed a time- time-frequency-dependent mechanical property. Therefore, the viscoelastic foundation is a mechanical component that is very important in the design process of the structure [15].

Relying on the above application's structure-foundation system can be represented as a thin plate sitting on the viscoelastic foundation. As a result, categorized the present works into two parts. Part one: studying the effects of adding the different percentages of ZnO and filler reinforcement (different percentages of MWCNT) to the natural rubber experimentally to obtain a suitable recipe characterized by good damping, good dynamic stiffness, and good fatigue life. Part two: Using the properties of the suitable recipe extracted from part one which recipe has good damping properties and good dynamic stiffness as a foundation for a thin plate to study the effects of various boundary conditions of plate edges, plate aspect ratio, and type of load on the dynamic response of a plate-foundation system analytically and numerically (by SOLIDWORKS software) [16].

Natural Rubber (NR)

Natural rubber is a fundamental elastomer and continues to play a vital role in the industry. It is one type of rubber from the heave tree as latex that grows in tropical regions and numerous countries. Indonesia, Malaysia, and Thailand are the largest producers, accounting for 80% of global consumption. Collect the latex in cups, then pour into containers before being transferred to the rubber factor. To generate technically specified, consistent viscosity grades of natural rubber, the latex is treated with stabilizers such as sodium sulfite, formaldehyde, and ammonia, as well as hydroxylamine, which may also add to enhance coagulation. Milled the rubber into sheets, cleaned, dried, smoked, and finally categorized to make smoked sheets [13].

Natural rubber is composed of carbon and hydrogen and has the empirical formula (CHs). The structure of natural rubber is a cis-1,4-polyisoprene (2-methyl-1,3-butadiene), as shown in Figure (1), and it has a glass transition temperature of about -70 °C [15,16]. It has a flexible nature, particularly if it has a high grade of (cis.) due to the existence of methyl groups following one of the chains that prevent the natural rubber from sufficiently arranging itself. As a result, gaps will arise between particles that dissipate the energy of the vibration wave. On the other hand, the uniformity of the molecular structure enables natural rubber to crystalline at low temperatures and increases hysteresis [17].

Furthermore, natural rubber has excellent low-temperature resistance, even down to -57 °C, where its stiffness can increase significantly [18]. Springs, bearings, vibration isolators, and heavy-duty tires are among the products made from natural rubber. It is utilized in seals, hoses, belts, conveyors, and other items for a specific function [19]. Table (1) lists the characteristics of Natural rubber.

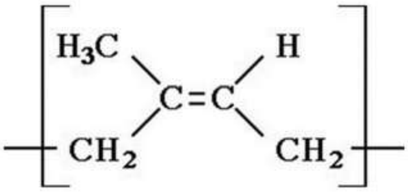

Fig. 1. - Natural Rubber Structure.

Table 1. Advantages and disadvantages of NR [20].

Advantages	Disadvantages
Tear Strength	Uniformly of Quality
Wear Resistance	Aging Resistance
Impact Resilience	Fatigue Resistance
Low Heat Generation	Ozone Resistance

Sodium Bicarbonate ($NaHCO_3$)

The structure of sodium bicarbonate $NaHCO_3$ or sodium hydrogen carbonate is represented by the monoclinic crystalline form. This salt is composed of sodium ions and bicarbonate ions, where ($NaHCO_3$) is its molecular formula. It is commonly called baking soda. It has a weak base and is used in cooking. The pH value is about 8.31. Figure (2) shows that structure.

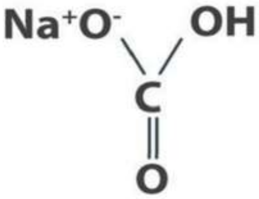

Fig. 2. - Carbon Nano-tubes (CNTs).

Ijimain Japan discovered CNTs in 1991 [21]. CNTs are among the most investigated nanomaterials owing to their unique features, for instance, high ratio of length to diameter, extraordinary strength, remarkable visuals, and conductivity experiences, making them attractive options for a diverse range of different applications [22]. A CNT is a graphene sheet (with carbon atoms arranged in a hexagonal pattern similar to the honeycomb) wrapped up to produce a hollow cylinder with diameters typically measured in a nanometere.

A nanometer is one-billionth of a meter, or around ten thousand times smaller than a human hair [23]. In other words, a graphene sheet shows a rolled-up chicken wire with a continued intact hexagonal lattice and carbon molecules at the vertexes of the hexagons [24,25].

Carbon nanotubes (CNTs) come in three types: MWCNTs, double-walled CNTs (DWCNTs), and Single-walled carbon nanotubes (SWCNTs). Because of the high aspect ratio (length-to-diameter ratio) and small diameter, the (SWCNTs) are 1D (meaning one-dimensional) substantial allotropes of carbon atoms. SWCNT has a hollow cylindrical shape produced by rolling a single layer of graphene sheets. Two or multiple rolling sheets of concentric graphene nano-tubes inside other nano-tubes give DWCNTs and MWCNTs respectively. Figure (3) shows the three types of CNTs mentioned earlier [26].

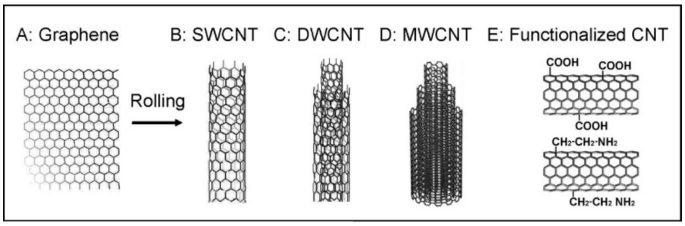

Fig. 3. - Types of CNTs.

Russian doll and Parchment structures are the two types of MWCNTs. In the Russian doll structure, numerous concentric CNTs that, the structure has a small and large diameter). Meanwhile, in the parchment structure, a single graphene sheet is wrapped around itself many times, similar to a rolled-up paper scroll, as seen in Figure (4) [27].

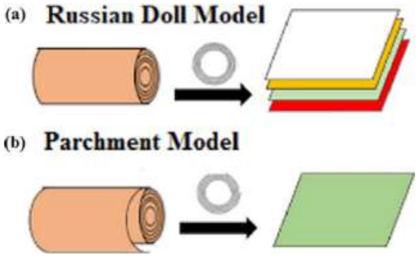

Fig.4. - Structures of MWCNTs.

Chemical vapor deposition are discharge, and laser ablation are three ways of producing CNTs. Most of these operations are carried out in emptiness or using gases for treatment. In chemical vapor deposition, the CNTs may be developed in airless or air pressure. All of these techniques can produce high-quality nanotubes in large amounts [28,29].

The arc discharge method generates CNTs by containing a chamber with two opposite electrodes (anode and cathode) constructed of graphite poles. These electrodes are placed in inactive gas (argon or Helium at 500 TORR), and a potential difference is used between them to produce an arc-resulted plasma. As a result, the carbon atoms are evaporated and deposited on the cathode pole, illustrated in Figure (5) [30,31].

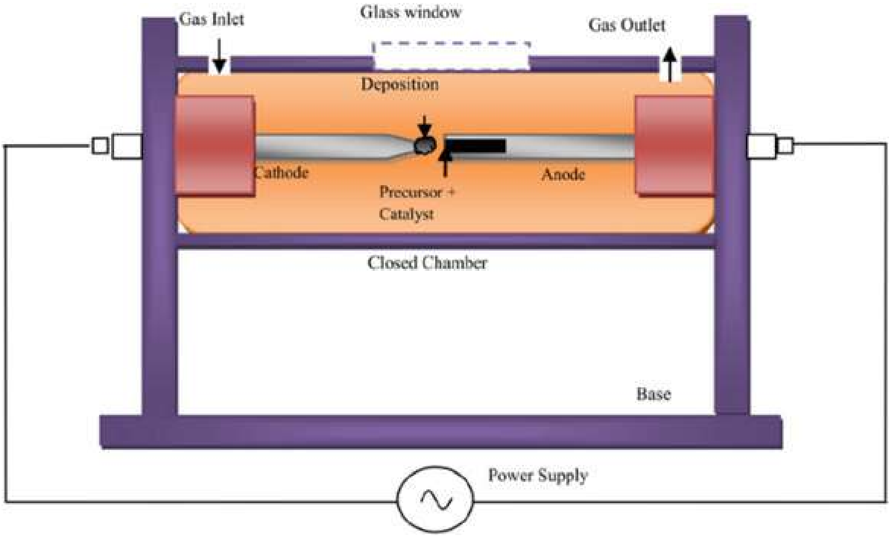

Fig. 5. - Arc discharge device.

In the laser ablation method, CNTs are produced by applying a laser beam to a solid graphite target instilled in a quartz tube within an inactive environment and subjected to a temperature of about 1200 °C, as seen in Figure (6). As a result, the graphite target evaporates, and then the carbon tubes are deposited on a copper collector that is cooled by water [32,33].

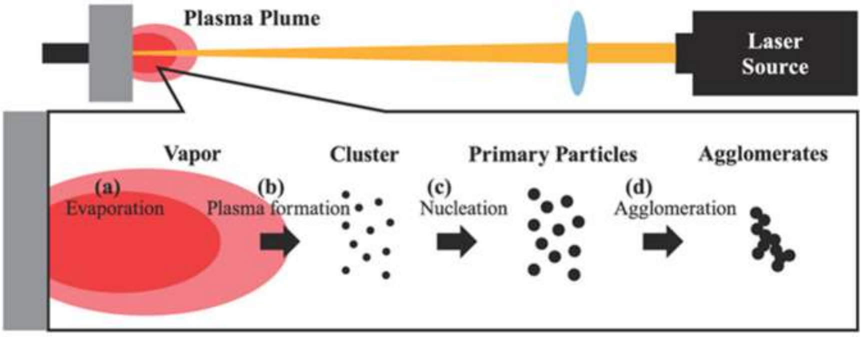

Fig.6. - Laser ablation method.

Injected the reaction compartment with a combination of hydrocarbons such as (ethylene ethanol, propylene, acetylene, CO, and methane), a metal catalyst such as (CO, Fe, and Ni), and inert gas, as shown in Figure (7). After injection, the reaction compartment is heated to temperatures between (500-1000 ℃ at the air pressure), and nano-tubes are formed on the device's base due to fractured hydrocarbon [34,35].

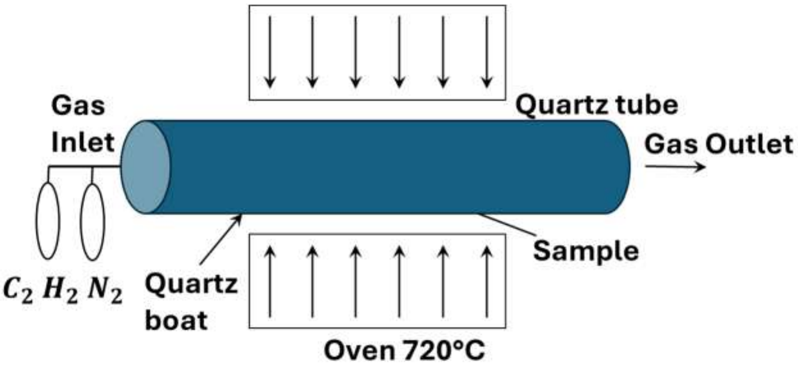

Fig. 7. - Chemical vapor deposition method.

Natural rubber is extensively used in many engineering applications because of its advantages, such as flexibility. However, some properties, like ozone resistance, oil resistance, damping, fatigue, and dynamic stiffness, are unsuitable for some applications. So, rubber blends, that is, natural rubber mixed with one or more types of synthetic rubber, are considered an appropriate way to change the efficiency of rubber materials to obtain the desired properties.

Carbon black remains the most common and extensively used reinforcing filler. Furthermore, its properties, such as particle size, surface activity, structure, and surface area, influence the basic properties of polymers.

CNTs are used as reinforcing fillers added to rubber compounds to enhance their electrical, mechanical, and dynamic properties. The enhancement of these properties by adding CNTs in different proportions to the rubber compounds can be achieved when there is sufficiently better interaction between the rubber compounds and the CNT particles and when the CNT particles are well distributed within the polymer matrix. The viscoelastic foundations represent a part of the structure widely used in many engineering applications. This structure can be modeled as a plate, beam, or pipe sitting on viscoelastic foundations according to the application to be studied.

The mechanical, physical, and dynamical properties of elastomers have gained extensive attention from researchers. Those researchers are focused on the improvement of different properties of elastomers such as tensile strength, elongation, compression, curing characteristics, resilience, fatigue, dynamic stiffness, damping, and swelling under the effects of many factors like vulcanization agents, thermal agents, blends type, and type of reinforcement fillers.

The feasibility of making epoxidized natural rubber (ENR)-alumina nanoparticles composites (ENRAN) was studied using melt compounding followed by Sulphur curing. To examine the impact of filler loading on the cure characteristics and mechanical qualities, alumina nanoparticles were incorporated into the compounding recipes at concentrations of 10, 20, 30, 40, 50, and 60 parts per hundred rubbers (phr). SEM analysis was used to examine the distribution of alumina nanoparticles (SEM). Compared to empty ENRs, curing times were cut by as much as 40 percent when alumina nanoparticles were added to the matrix. As the cross-link density rose in the presence of alumina nanoparticles, so did the minimum torque (ML), the maximum torque (MH), and the torque difference (MH-ML). The ENR compound's tensile strength, elongation at break (EB), and impact strength dropped as the proportion of alumina nanoparticles to the total increased. However, the results showed better hardness and tensile modulus than unfilled ENRs. Increasing the ENRANs' MH, ML, tensile modulus, and hardness resulted from the matrix's evenly dispersed alumina particles [36].

The research was published concerning the creation of reinforced elastomer composite by adding reinforcing fillers Al_2O_3 and SiO_2 individually to the styrene butadiene rubber (SBR) with a range of loading stages (0-5-10-15-20 and 25 pp-hr). It has been demonstrated that mechanical properties, except for robustness, can be improved by adding reinforcing fillers and raising their loading level. In particular, silica fillers were superior to alumina fillers in terms of increasing these properties. In terms of ultimate strength tensile (67 MPa), with the elasticity of modulus at 100% elongation (13MPa) and percentage of elongation at break, the alloy SBR reinforced with silica fillers 25 pp-hr displayed the most significant values (172%). The silica reinforcement in the styrene-butadiene rubber decreased its minimum resilience to 65.59 percent. The figures for its hardness and abrasion resistance were also the highest and the lowest, respectively. The loading amount of reinforcing fillers had a notable impact on the physical characteristics, which meant that the liquid's action (swelling) was unique to that factor. By incorporating the strengthening of fillers and an increase in in terms of thermal conductivity, the filler loading was also improved. Fillers made of alumina rather than silica tend to significantly impact heat conductivity. Due to the increasing volume of reinforcing fillers, rubber composites' specific gravity must be increased [37].

The NR nano-composites were prepared using pure attapulgite (PAT) or modified attapulgite (MAT) in a double-roller plasticator mixer (PAT-450 and PAT-850, respectively), both of which were heated to 450 and 850 degrees Celsius for two hours. Modified attapulgite was distinguished by its immaculate crystal structures, which were clear by FTIR, TEM, XRD, and BET analysis. The findings suggested that the attapulgite's structure shifted when the temperature was raised. The mechanical characteristics of the NR nano composites were also studied to see how they were affected by the PAT treatment and composition. The data demonstrated that AT facilitated the natural rubber curing process. Nano composites containing various kinds of attapulgite outperformed pure NR samples in terms of tensile strength, wear ability, and solvent resistance. Scanning electron micrographs revealed that the filler was localized at the interface, which caused compatibilization with otherwise immiscible mixes. A thermo gravimetric study showed that the NR/PAT nanocomposites significantly increased thermal stability [38].

The nano fillers reinforced natural/synthetic rubber were studied, and the production of synthetic composites with micro and nano-$CaCO_3$ as filler material was also studied for comparison purposes. It has been discussed how fillers may change rubber's mechanical strength, thermal conductivity, and permittivity, among other qualities. However, the nanoparticles' high surface energy makes them prone to climbing together, which has proven to be a challenge. Nano-sized calcium carbonate ($CaCO_3$) is used as a reinforcing agent in various sports equipment compositions (laminated sheets for inflated balls, for example). $CaCO_3$ particles are impermeable; therefore, the permeability to gases and vapors becomes lower when added to flexible polymeric membranes. Permeation values were reduced because the nano-$CaCO_3$ filler in NBR formed a more convoluted route against gas penetration than traditional fillers [39].

Work on the fabrication of Matrix composites was achieved Using curauá fiber and a nanoparticulate mineral (montmorillonite clay - MMT) as reinforcing agents were, made from Styrene-Butadiene-Styrene (SBS) (SBS). Composites with 5, 10, and 20 percent cure Fiber and a maleic anhydride grafted styrene (ethylenic butylene)-styrene triblock copolymer underwent testing for tensile strength, grip strength, rebound resilience, flex fatigue life, abrasion loss, hardness, and water absorption (MA-g-SEBS) coupling agent. The best mechanical properties were found in the hybrid SBS composite containing 2% MMT and 5% curauá fiber. Increases in All mechanical parameters were negatively affected by fiber content up to 20 wt.%, and tensile strength was negatively affected by the addition of 5 wt.% MMT. The poor mechanical performance of composites with increasing concentrations of curauá fiber and MMT nanoparticles may be due to poorly distributed clay agglomerates (tactoids) in the hybrid composites. Using plasticizer further decreased the tensile strength of all SBS composites, whereas incorporating MMT nanoparticles decreased their water absorption [40].

Researchers worked on the calendaring procedure for reinforcing synthetic compounds of styrene-butadiene rubber (SBR) and natural rubber (NR) with Al_2O_3 and SiO_2 fillers. Adding alumina and silica particles at different ratios has changed the tensile characteristics of both styrene butadiene rubber (SBR) and natural rubber (NR) (5, 10, 15, 20, and 25 pphr). Increasing the loading amount of both reinforcing particles improved the tensile properties. Natural rubber's tensile qualities were superior to styrene-butadiene rubber's, and silica particles were more efficient in reinforcing the material than alumina ones. Maximum tensile strength at break (70MPa), modulus of elasticity (18 MPa), and elongation percentage at break (350%) were measured for natural rubber reinforced with (25 pphr) of Silicon dioxide [41].

Natural rubber vulcanizates with varying concentrations of titanium dioxide particles were produced and characterized. Rubber samples were vulcanized in a hydraulic press after being processed in a two-roll mill used in the lab. Our prior research served as the basis for creating the rubber combination and the rubber-processing technology. Titanium dioxide loadings of 15, 25, 45, and Vulcanizates with a range of TiO_2 particle sizes were found to perform well across the board. A study using Fourier transform infrared spectroscopy revealed that the chemical structure of the resulting natural-based composites was unaffected by the addition of titanium dioxide particles85 wt % per 100 wt % of natural rubber were used to obtain the samples. This research aimed to identify the effects of varying titanium oxide particle loadings on the chemical composition and morphological, mechanical, and thermo-mechanical characteristics of natural rubber-based composites. It was clear from the SEM micrographs that the TiO_2 particles were evenly distributed throughout the natural rubber matrix. At more significant concentrations of TiO_2 in the matrix, the filler began to aggregate. The resulting natural rubber composites exhibited somewhat varied thermal stability, as determined by thermo gravimetric analysis. A dynamic mechanical and thermal examination found that the glass transition temperatures of the produced materials are close to one another. However, more significant energy loss occurred during mechanical work on the materials, and higher cross-link density was achieved by increasing titanium dioxide concentration in the produced materials [42].

It was found that nitrile rubber (NBR) enhanced with hybridized Graphene oxide (GO) and silicon dioxide (SiO_2) nanoparticles increased mechanical and dynamic mechanical capabilities. The newly produced hybrid nanoparticles (GO/SiO_2) were more thermally stable than GO due to the uniform dispersion of SiO_2 nanoparticles on the surface and between GO layers. Soluble blending and mechanical solution procedures were used to generate $GO/SiO_2/NBR$ nano-composites, which were then tested for their mechanical characteristics. It was found that the tensile strength of $GO/SiO_2/NBR$ nano-composites grew more gradually than that of GO/NBR and SiO_2 nano-composites. In contrast, the elongation at break varied only gradually. In addition, dynamical tests revealed that incorporating GO/SiO_2 hybrid nanoparticles into NBR improved the material's elasticity. Morphological studies of $GO/SiO_2/NBR$ and GO/NBR nanocomposites led researchers to infer that the hybridization of the GO/SiO_2 was the crucial factor in reinforcing the mechanical characteristics and elasticity of the NBR [43].

The traditional ZnO was replaced with nano-ZnO as an activator, and its impact on the tensile characteristics of natural rubber composites was studied. Traditional ZnO was used as the activator in one compound at a concentration of 8 p hr (part per hundred rubber), whereas Nano-ZnO was used in eight other compounds at values of (0.2), (0.6), (1.0), (1.4), (1.8), (2.2), (2.6), and 4% phr. We used a Monsanto T10 Tensometer to conduct the tensile test. The results indicated that at 1.8 phr, Nano zinc strength under tension and modulus of elasticity were higher for oxide, at 300%. The cost of the compounds was reduced by 77.5% when traditional ZnO was replaced with Nano ZnO. Moreover, its tensile strength was increased by 38.14%, and its impact on the environment was diminished by 62% [44].

Preparation methods, characterization methods, and developed nano-composites mechanical and thermal characteristics and their most recent applications were all presented. Rubber nano-composites (RNCs) have found commercial homes in the tire and sports sectors thanks to their benefits in terms of product weight, energy loss, and air retention [45].

Investigation was carried out on how using a novel reinforcing material differs from using carbon black or other traditional reinforcement materials in various applications. This research demonstrates the use of white cement as a carbon black substitute in construction applications, adding a new material, sediment dust, to recipes that traditionally call for carbon black as a reinforcement, all to examine the materials' mechanical properties. Samples were tested for properties, including tensile strength, tear resistance, hardness, and compressibility, and the reinforcement formulas that included carbon black came out on top in every case. The practical test also showed that using white cement and Nanoparticles of sediment dust (new reinforcing material) produced acceptable results in comparison to the traditional recipes reinforced by carbon black, particularly when using percentages between (2-8%) [46].

Detailed processes involved in making nano-scale carbonaceous reinforcements in rubber nano-composites include graphene, expanded graphite, SWCNTs and MWCNTs, graphite oxide, graphene oxide, and hybrid fillers made up of combinations of individual fillers. After that, we looked at the thermomechanical characteristics (glass transition temperature, crystallization temperature, and melting point) and static mechanical parameters (parameters for fracture toughness, tensile strength, elongation at break, and Young modulus) of these nanocomposites of rubber. Finally, the results found by Payne and Mullin in rubber-containing carbon nanofillers were discussed [47].

Some investigators looked at how rubber's mechanical characteristics and creep behavior may be altered by reinforcement using carbon multi-wall Nanoparticle composites. The mechanical characteristics (rubber's strength) and mechanical creep behavior weight fraction impacts of Nanoparticle materials are being evaluated as part of the study. Experimental methods created many rubber samples with varying concentrations of Nanoparticles. The mechanical characteristics and behavior of the materials were then evaluated using tensile and creep testing equipment. Nanoparticles were utilized at 0%, 2%, 4%, 6%, 8%, and 1% by weight, respectively. The creep behavior is also studied numerically, employing the finite element method within the ANSYS software, and the findings are compared to those obtained by experimental calculations. The comparison indicates that the inaccuracy is less than or equal to (8.36%). The research concluded that rubber's mechanical characteristics and creep behavior were influenced by roughly (65%) with reinforcement by (1%wt) for multi-wall carbon Nanomaterial [48].

Comprehensive research was presented on nanofillers in natural rubber, including carbon nanostructures, clays, and spherical silica particles made using the sol-gel technique. It was shown that various parameters, including processing conditions, filler dispersion state, polymer-filler interactions, and filler morphological characteristics, influence the mechanical response of NR. Mechanical reinforcement using rod-shaped particles, such as those found in clay, carbon fibers, or CNTs, is much more effective owing to the particles' anisotropic nature and ability to align themselves in the direction of stretch, even if the sol-gel technique is used. vulcanized rubber yields almost ideal distributions. Distribution (exfoliation) in the rubber is crucial for performing multilayer fillers like clays and graphitic structures. Still, peeling off an entire layer of clay or graphite is difficult, limiting the huge nano-reinforcement that could otherwise be achieved. Due to strain amplification effects, crystallization always began at a lower strain value than in the empty matrix [49].

The investigation of how nano ZnO differed from traditional ZnO was carried out in its effects on natural rubber composites' curing characteristics and mechanical qualities. Nano ZnO (particle size = 10-30 nm, surface area = 30-60 m2/g), added at concentrations of 0, 0.4, 0.8, 1.2, 1.6, and 2 pphr, was used to create six different rubber composites. ZnO was mixed with rubber at the standard concentrations of 0, 2, 4, 5, 6, and 8 parts per million to create six different compounds. The torque differential increased by 4.77 percent, while the cure rate index increased by 48.29 percent. There was a 7.37 percent increase in tensile strength, a 3.27 percent increase in modulus at 300%, and a 5.73 percent drop in hardness. There was a 75% decrease in ZnO content in rubber composites when nano ZnO was used instead of regular ZnO [50].

It was shown that nanomaterials and particles have been found to positively affect how composite materials act in context, which has been investigated. This influence was found to extend to factors such as the material's size, shape, dispersal method, adherence, and compatibility with other phases taken into account throughout the production process. So, they looked at how various nanomaterials performed depending on loading circumstances and adhesion sizes in the designated fillers class. Moreover, it demonstrated the optimum filler quantity for increasing mechanical characteristics and fracture toughness from interlaminar and intralaminar viewpoints. In addition, a system was developed to categorize the impacts of soft, complex, and hybrid fillers, demonstrating how some fillers had spectacular benefits for improving specific properties. In addition, the optimal nanomaterial application in terms of loading circumstances was elucidated. The review concluded with hints about how nanofillers and particles impact the beginning of damage and the behavior of fiber-reinforced plastic composites [44].

The reinforced polymer mix (silicone rubber: 5% PMMA) with two distinct types of natural nano-powders is used to create nanocomposite composites. Loading levels (0%, 0.1%, 0.2%, 0.3%, and 0.4%) of Pomegranate peel powder (PPP) and seed powder of dates ajwa (SPDA) were tested. Mechanical parameters, including tensile strength, hardness, compressive strength, and surface roughness, were evaluated, and FTIR, DSC, and SEM analyses were performed on the produced sample. Based on the data, a combination of 2% PPP and 3% Ajwa Seed Powder yields the best possible qualities [51].

To restore the functionality and enhance the aesthetics of maxillofacial prostheses, looked at the enhanced characteristics of hybrid nanocomposite materials. 95% styrene-butadiene-methacrylate (SR)/5% poly(methyl methacrylate (PMMA) and (PPP) polymer mix composite was modified by adding ultra-high-molecular-weight polyethylene (UHMWPE) fiber of varying lengths (0%, 2%, and 1%) to improve the characteristics of silicone rubber for maxillofacial prosthesis applications. Based on the findings, the ideal component ratio of the hybrid composite sample is 95% SR, 5% PMMA, PPP at 0.2%, and UHMWPE at 0.5% in a continuous state fiber added. Consequently, the mixture may be a contender for reaching the qualities needed for the applications of maxillofacial prostheses [52].

Some researchers have investigated how combining SiO_2 nanoparticles into a styrene-butadiene rubber and natural rubber (NR) affects the latter's mechanical and physical properties (SBR). Nanoparticles were added at concentrations of 0, 0.2, 0.4, 0.8, 1, 1.5, 2, 2.5, and 3 pp hr to the rubber blend (30% NR/ 70% SBR) in an experimental two-roll mill with molds and a thermal piston; the pressure, temperature, and time difference test conditions were standard; and the rubber blend was prepared with vulcanization factors, accelerators, and activators. Mechanical properties (hardness, fatigue, and compression set) improved in the lab with increasing percentage load (pphr) up to 0.8 pphr, when a little decrease occurred. Increases in SiO_2 concentration in the rubber formula increase viscosity and decrease torque, scorch, and cure times [53].

Some investigators did a look at how nano-silica particles affected the properties of SiO_2-doped ethylene propylene diene monomer (EPDM) and styrene butadiene rubber (SBR). The composite EPDM/SBR was processed with and without a silane coupling agent in an open mill mixer. The composites' curing behavior, mechanical properties, hardness, rebound resilience, swelling resistance, abrasion resistance, and compression set were all studied. Components were tested for various characteristics, including curing speed, hardness, rebound resilience, swelling resistance, abrasion resistance, and compression collection. Mechanical characteristics, including swelling resistance, hardness, abrasion, and compression set, were enhanced in EPDM/SBR rubber composites when introducing nano silica particles [54].

A thorough analysis was provided for plant-based filler rubber biocomposites. The matrix (natural or synthetic rubber) and lignocellulosic fillers (cellulose from plants) determined the structure's divisions (natural fiber, microcrystalline cellulose, lignin, and nitrocellulose) [55]. Curing behavior and static and dynamic mechanical properties of the resultant rubber bio-composites were investigated. In addition, a comparison was made of the attributes of these rubber bio-composites after taking into account the impact of hybrid filler systems, surface modification of lignocellulosic filler, and the rubber matrix [56].

The qualities of the Nanotube rubber material were investigated using inverse FE modeling and indentation tensile testing. NR rubber's mechanical properties were improved by adding nano-tubes of carbon varying ratios of multiple-walled CNTs subjected to high tensile stress. All- Recently, CNTs have begun to appear in natural rubber. To generate nano-composites, a solvent casting method, toluene, was employed. 0.2%, 0.4%, 0.6%, 0.8%, and 1%. The mechanical characteristics of NR CNTs have been investigated. Parametric FE models were used to simulate and validate indentation tensile tests on rubber samples. The rubber samples' hyperelastic properties under uniaxial tension were identified using an inverse materials parameter identification strategy. The data on material properties and force-displacement relationships may be automatically updated and extracted. with ABAQUS FE software. We will use these curve-fitting parameters and display equations to draw a mathematical connection between and. curve coefficients. Material attributes were shown to streamline the inverse FE modeling process [20].

A study of recycled rubber composites was produced with different reinforcements in the literature through toughening methods, mechanical and physical qualities, and microstructural and fracture surface research. Microscale reinforcements (glass bubbles and alumina fiber) and nano-scale reinforcements (nano-silica and graphene nano-platelets) exploited as reinforcements in rubber composites were comprehensively examined. Most research into recycled rubber composites has found that using micro-scale particles to strengthen the material improves the structural, physical, and mechanical qualities while making the composites cheap and lightweight. High toughness and impact resistance are two qualities that may make composites made from recycled rubber a good fit for specific uses [57].

The epoxy and epoxy-based carbon fiber-reinforced polymer tensile characteristics were investigated to determine the fracture toughness and glass transition temperature. (CFRP). The experiment included three CSR nanoparticle-containing additives, with the filler fraction in the epoxy resin ranging from 2% to 6% by weight. The maximum filler percentage of CSR nanoparticles resulted in a decrease in tensile strength and elastic modulus of 10–20% and an increase in fracture toughness of 60–108%, as shown by experimental data. A maximum of 53% increase in CFRP interlaminar fracture toughness was recorded for ACE MX 960 at 4 wt.% CSR content. The glass transition temperature of the epoxy increased by 10–20 degrees Celsius for every doubling of the number of CSR nanoparticles in each addition. In some cases, a combination of stiff and soft particles may be preferable to employing only one kind of particle to provide the desired tensile properties and fracture toughness [58].

Conclusion

This review has critically examined the enhancement of mechanical and dynamic properties of elastomeric materials - particularly natural rubber - through the incorporation of nanostructured reinforcements such as ZnO, MWCNTs, and $NaHCO_3$. The integration of these fillers has demonstrated significant improvements in tensile strength, elongation at break, tear resistance, dynamic stiffness, and damping behavior, thereby extending the functional performance of elastomers under complex loading conditions.

The literature reveals that the performance enhancement is primarily governed by filler morphology, dispersion quality, interfacial bonding with the polymer matrix, and the cross-linking density achieved during vulcanization. MWCNTs exhibit exceptional reinforcing efficiency among the reviewed nanofillers due to their high aspect ratio and mechanical robustness, while ZnO and $NaHCO_3$ contribute to curing kinetics and microstructural stability.

Furthermore, applying these optimized elastomeric formulations as viscoelastic foundations in structural systems, such as thin plates subjected to free and transient vibrations, has shown promise in controlling structural dynamics and mitigating vibration-induced stresses. Finite element modeling has proven to be an essential tool for predicting the behavior of such systems and validating experimental findings.

The convergence of material innovation and structural dynamics modeling underscores the strategic role of nano-composite rubber in next-generation vibration isolation and damping systems. Future research should focus on optimizing filler content, improving dispersion techniques, and exploring multifunctional filler systems to further advance the capabilities of elastomeric composites in mechanical and civil engineering applications.

References

[1] Nam T.H., Petríková I., Marvalová B. Effects of applied strain, magnetic field, and temperature on the compressive stress relaxation behavior of magneto-sensitive elastomers. Mech Time-Dependent Mater 2024;28:917–36. https://doi.org/10.1007/s11043-023-09654-4.

[2] Wei P, Yan X, Huang F. Supramolecular polymers constructed by orthogonal self-assembly based on host–guest and metal–ligand interactions. Chem Soc Rev 2015;44:815–32.

[3] Kareaga Laka Z. Dynamic stiffness and damping prediction on rubber material parts, FEA and experimental correlation 2016.

[4] Sallal HA, Radhi MS, Mahboba MH, Al-Khafaji Z. Impact of embedded sol-gel synthesized triple composites on polymer's mechanical properties. Egypt J Chem 2022. https://doi.org/10.21608/ejchem.2022.154630.6684.

[5] Falah M, Al-khafaji Z. Behaviour Of Reactive Powder Concrete Hollow Core Columns Strengthened With Carbon Fiber Reinforced Polymer Under Eccentric Loading. Electron J Struct Eng 2022;22:28–38.

[6] Sallal HA, Mahboba MH, Radhi MS, Hanif A, Al-Khafaji ZS, Ahmad S, et al. Effect of adding (ZrO2-ZnO) nanopowder on the polymer blend (lamination and methyl vinyl silicone) in a hybrid nanocomposite material. J King Saud Univ 2024;36:103061.

[7] Al-Abboodi T, Yaser A, Al-Khafaji; Z. Reducing vibration and noise in the oil sector using nanoparticle-reinforced polymers. Acad J Manuf Eng 2024;2024.

[8] Radhi NS, Salman AJ, Al-Khafaji Z. Investigation of in vitro behavior of composite coating hydroxyapatite-nano silver on 316L stainless steel substrate by electrophoretic technic for biomedical tools. Open Eng 2024;14:20240017.

[9] Radhi N.S., Al-Khafaji Z., Mareai B.M., Radhi S., Alsaegh AM. Reducing oil pipes corrosion by (zn-ni) alloy coating on low carbon steel substrate by sustainable process //J Eng Sci Technol 2023;18:1624–38.

[10] Aldawoudi K., Nattah A.M., Radhi N.S., Al-khafaji Z.S., Ibrahim M.K. Identify Microstructure and Mechanical Behavior of Aluminum Hybrid Nano Composite Prepared by Casting Technique. Jordan J Mech Ind Eng 2025;19:163–70.

[11] Salman A.J., Radhi N.S., Al-Khafaji Z. Identify in Vitro behavior of composite coating Hydroxyapatite-Nano Silver on Titanium substrate by Electrophoretic Technic for Biomedical Applications //Open Eng 2024.

[12] Chen J., Garcia E.S., Zimmerman S.C. Intramolecularly cross-linked polymers: from structure to function with applications as artificial antibodies and artificial enzymes //Acc Chem Res 2020;53:1244–56.

[13] Mullins L. Softening of rubber by deformation //Rubber Chem Technol 1969;42:339–62.

[14] Holden G. Thermoplastic elastomers //Appl. Plast. Eng. Handb., Elsevier; 2024, p. 97–113.

[15] Dinsmore RP. Rubber Chemistry //Ind Eng Chem 1951;43:795–803.

[16] Junoh MABM. Studies on the Properties of Conductive Particulate Fillers Filled Rubber Composite 2008.

[17] Carter LJ. Industrial minerals: New study of how to avoid a supply crisis. Science (80-) 1970;170:147–8.

[18] Ciesielski A. An introduction to rubber technology. iSmithers Rapra publishing; 1999.

[19] Sisanth KS, Thomas MG, Abraham J, Thomas S. General introduction to rubber compounding. InProgress in rubber nanocomposites (pp. 1-39). India Elsevier Inc. Available from Http//Www Sci Com/Science/Book/9780081004098 2017;10:1016.

[20] Jweeg M.J., Alazawi D.A., Jebur Q.H., Al-Waily M., Yasin N.J. Hyperelastic modelling of rubber with multi-walled carbon nanotubes subjected to tensile loading //Arch Mater Sci Eng 2022;114:69–85.

[21] Iijima S. Helical microtubules of graphitic carbon //Nature 1991;354:56–8.

[22] Pal G., Kumar S. Modeling of carbon nanotubes and carbon nanotube–polymer composites //Prog Aerosp Sci 2016;80:33–58.

[23] Marinković S.N. Carbon nanotubes //J Serbian Chem Soc 2008;73:891–913. https://doi.org/10.2298/JSC0809891M.

[24] Rothon R. Particulate fillers in thermoset plastics //Fill Polym Appl 2017:111.

[25] Dai H. Carbon nanotubes: opportunities and challenges //Surf Sci 2002;500:218–41.

[26] Mensah B, Kim HG, Lee J-H, Arepalli S, Nah C. Carbon nanotube-reinforced elastomeric nanocomposites: a review. Int J Smart Nano Mater 2015;6:211–38.

[27] Gupta N, Gupta SM, Sharma SK. Carbon nanotubes: Synthesis, properties and engineering applications. Carbon Lett 2019;29:419–47.

[28] Rao CNR, Voggu R, Govindaraj A. Selective generation of single-walled carbon nanotubes with metallic, semiconducting and other unique electronic properties //Nanoscale 2009;1:96–105.

[29] Sharma R, Sharma AK, Sharma V. Synthesis of carbon nanotubes by arc-discharge and chemical vapor deposition method with analysis of its morphology, dispersion and functionalization characteristics //Cogent Eng 2015;2:1094017.

[30] Kundrapu M, Li J, Shashurin A, Keidar M. A model of carbon nanotube synthesis in arc discharge plasmas //J Phys D Appl Phys 2012;45:315305.

[31] Arora N, Sharma NN. Arc discharge synthesis of carbon nanotubes: Comprehensive review //Diam Relat Mater 2014;50:135–50.

[32] Szabó A, Perri C, Csató A, Giordano G, Vuono D, Nagy JB. Synthesis methods of carbon nanotubes and related materials //Materials (Basel) 2010;3:3092–140.

[33] Lu Z, Raad R, Safaei F, Xi J, Liu Z, Foroughi J. Carbon nanotube based fiber supercapacitor as wearable energy storage //Front Mater 2019;6:138.

[34] Sirisinha C, Prayoonchatphan N. Study of carbon black distribution in BR/NBR blends based on damping properties: influences of carbon black particle size, filler, and rubber polarity //J Appl Polym Sci 2001;81:3198–203.

[35] Filchakova M, Saik V. Single-walled carbon nanotubes: structure, properties, applications, and health & safety. Tuball 2021.

[36] Mohamad N, Muchtar A, Ghazali MJ, Mohd DH, Azhari CH. The effect of filler on epoxidised natural rubber-alumina nanoparticles composites. Eur J Sci Res 2008;24:538–47.

[37] Oleiwi JK, Hamza MS, Abed MS. Improving the properties of the tire tread by adding SiO_2 and $Al2O_3$ to SBR rubber. Int J Appl Eng Res 2010;5:1637–52.

[38] Wang J, Chen D. Mechanical properties of natural rubber nanocomposites filled with thermally treated attapulgite. J Nanomater 2013;2013:496584.

[39] Khan I, Bhat AH. Micro and nano calcium carbonate filled natural rubber composites and nanocomposites 2013.

[40] Borba PM, Tedesco A, Lenz DM. Effect of reinforcement nanoparticles addition on mechanical properties of SBS/Curauá fiber composites. Mater Res 2014;17:412–9.

[41] Oleiwi JK, Hamza MS, Abed MS. Study the tensile characteristics of elastomer composites reinforced with alumina and precipitated silica particles. Eng Tech J 2015;33:1079–94.

[42] Datta J, Kosiorek P, Włoch M. Effect of high loading of titanium dioxide particles on the morphology, mechanical and thermo-mechanical properties of the natural rubber-based composites. Iran Polym J 2016;25:1021–35.

[43] Zhang Z, He X, Wang X, Rodrigues AM, Zhang R. Reinforcement of the mechanical properties in nitrile rubber by adding graphene oxide/silicon dioxide hybrid nanoparticles. J Appl Polym Sci 2018;135:46091.

[44] Hadi FA, Kadhim RG. A study of the effect of nano zinc oxide on cure characteristics and mechanical properties of rubber composites. J. Phys. Conf. Ser., vol. 1234, IOP Publishing; 2019, p. 12043.

[45] Jawaid M, Salit MS, Alothman OY. Green biocomposites: design and applications. Springer; 2017.

[46] Abd Ali NK. A new reinforcement material for rubber compounds (Sediment dust nanoparticles and white ceminte). 2018 1st Int. Sci. Conf. Eng. Sci. Sci. Conf. Eng. Sci., IEEE; 2018, p. 163–8.

[47] Srivastava SK, Mishra YK. Nanocarbon reinforced rubber nanocomposites: detailed insights about mechanical, dynamical mechanical properties, payne, and mullin effects //Nanomaterials 2018;8:945.

[48] Mohamed M, Fahad N, Al-Waily M, Resan K. Rubber Creep Behavior Investigation with Multi Wall Tube Carbon Nano Particle Material Effect //Int J Mech Eng Technol 2018;09:729–46.

[49] Bokobza L. Natural rubber nanocomposites: A review. Nanomaterials 2018;9:12.

[50] Chen G.H., Li Y, Wu S.X., Li D., Yang S.S. Nano-particle's effect on silicone rubber inhibitor //IOP Conf. Ser. Mater. Sci. Eng., vol. 479, IOP Publishing; 2019, p. 12115.

[51] Woldemariam MH, Belingardi G, Koricho EG, Reda DT. Effects of nanomaterials and particles on mechanical properties and fracture toughness of composite materials: A short review //AIMS Mater Sci 2019;6:1191–212.
[52] Salih S, Oleiwi J, Kadhim H. Investigation the Properties of Silicone Rubber Blend Reinforced by Natural Nanoparticles and UHMWPE fiber //Int J Mech Eng Technol 2019.
[53] Subeh AA, Al-Maamori MH, Hamzah AF. The effect of the nanoparticle SiO_2 on the mechanical and physical properties of rubber composites //IOP Conf. Ser. Mater. Sci. Eng., vol. 987, IOP Publishing; 2020, p. 12015.
[54] Vishvanathperumal S, Anand G. Effect of nanosilica on the mechanical properties, compression set, morphology, abrasion and swelling resistance of sulphur cured EPDM/SBR composites //Silicon 2022;14:3523–34.
[55] Hussein SA, Al-Khafaji Z, Alfatlawi TJM, Abbood A-KN. Improvement of Permeable Asphalt Pavement by adding Crumb Rubber. Open Eng 2022;inpress:1–12.
[56] Kazemi H, Mighri F, Rodrigue D. A review of rubber biocomposites reinforced with lignocellulosic fillers. //J Compos Sci 2022;6:183.
[57] Kabakçi GC, Aslan O, Bayraktar E. A review on analysis of reinforced recycled rubber composites //J Compos Sci 2022;6:225.
[58] Glaskova-Kuzmina T, Stankevics L, Tarasovs S, Sevcenko J, Špaček V, Sarakovskis A, et al. Effect of core–shell rubber nanoparticles on the mechanical properties of epoxy and epoxy-based CFRP //Materials (Basel) 2022;15:7502.

Information of the authors

Al-Abboodi T.M.M., msc., lecturer assistant, Department of Mechanical Engineering, Altinbas University
e-mail: yaser.alaiwi@altinbas.edu.tr

Alaiwi Y., PhD, professor, Department of Mechanical Engineering, Altinbas University
e-mail: yaser.alaiwi@altinbas.edu.tr

Zainab Al-Khafaji, Department of Civil Engineering, Faculty of Engineering and Built Environment, Universiti Kebangsaan Malaysia; Scientific Research Centre, Al-Ayen University
e-mail: p123005@siswa.ukm.edu.my

Mayadah Falah, Building and Construction Techniques Engineering Department, Al-Mustaqbal University
e-mail: mayadah.waheed@uomus.edu.iq.

DOI 10.52209/2706-977X_2025_3_68 **IRSTI 55.43.29** **UDC 631.117**

Method of Ultrasonic Cleaning of Internal Combustion Engine Radiator Tubes by Transverse Exposure

Sinelnikov K. A., Moldabaev B. G., Zhunusbekova Zh. Zh.*
Abylkas Saginov Karaganda Technical University Karaganda, Kazakhstan
*corresponding author

Abstract. This article is dedicated to the study of the ultrasonic cleaning method for vehicle cooling system radiators using transverse exposure to ultrasonic waves. The conducted experiment confirmed the high efficiency of the method based on water cavitation inside the radiator tubes. During the study, key liquid parameters were measured, including density, mass, outflow velocity, and scale content. The results demonstrated that ultrasonic cleaning with transverse exposure effectively removes scale without damaging the radiator structure, thereby improving heat exchange efficiency. An analysis of the dynamic changes in the mass of the removed scale showed that transverse ultrasonic exposure ensures a more uniform energy distribution across the entire radiator surface, increasing the degree of cleaning compared to the longitudinal method. This approach enhances the operational characteristics of the cooling system, extends its service life, and reduces maintenance costs, while also providing an additional environmental benefit by eliminating the need for aggressive chemical reagents.

Keywords: Transport machinery, radiator, cavitation, ultrasound, dispersing, ultrasonic generator, emitter.

Introduction

Contamination of the radiator and cooling system of an internal combustion engine (ICE) significantly affects the performance, durability, environmental impact, and cost-efficiency of vehicle operation. The radiator and cooling system play a crucial role in maintaining the engine's optimal temperature. When these components become contaminated, heat exchange efficiency decreases substantially, leading to engine overheating, accelerated wear of its components, and a reduced service life [1-2].

Engine overheating is one of the most common and dangerous issues caused by cooling system contamination. The primary problem of contamination is the formation of corrosion and scale inside the radiator tubes, thermostat, water pump, and engine channels. These deposits not only obstruct the free flow of coolant but can also damage system components, causing leaks or complete cooling system failure. As a result, the temperature in the combustion chambers rises, negatively affecting all engine processes [3]. The oil used for lubricating moving parts begins to degrade faster, losing its protective properties. This, in turn, increases friction between components, accelerates their wear, and may lead to severe damage, such as cylinder deformation or piston failure [4]. In cases of significant contamination, the engine may overheat to the point where thermal destruction of critical components, including the cylinder head, occurs, necessitating costly repairs or complete engine replacement.

Additionally, overheating leads to increased fuel consumption. When an engine operates under unfavorable temperature conditions, the combustion efficiency of the fuel mixture decreases. Consequently, more unburned hydrocarbons are released into the atmosphere. These substances, along with carbon dioxide (CO_2), carbon monoxide (CO), and nitrogen oxides (NO_x), significantly contribute to environmental pollution. A vehicle with a contaminated cooling system becomes a major source of harmful emissions, negatively impacting the environment and reducing air quality in urban areas [5-8].

The economic losses associated with radiator and cooling system contamination cannot be ignored. Increased fuel consumption, frequent overheating, and the need for more frequent repairs or component replacements lead to significant operational costs. Furthermore, coolant leaks, which often contain toxic chemicals, can contaminate soil and water bodies, creating additional environmental risks [9-10].

From a reliability and safety perspective, cooling system contamination increases the likelihood of sudden failures while driving. This can lead to hazardous situations, especially if engine overheating occurs in heavy traffic or far from service centers.

To prevent these issues, regular diagnostics, maintenance, and repairs of the cooling system are recommended, as they play a key role in extending engine life and reducing environmental impact. Flushing the radiator, using high-quality coolants, and following maintenance schedules help keep the system in optimal condition [11].

Regular maintenance not only protects the engine from overheating and extends its lifespan but also helps save fuel, reduce harmful emissions, and lower operational costs. Thus, maintaining the cleanliness of the radiator and cooling system not only prolongs the vehicle’s lifespan but also improves environmental conditions, making transportation safer and more cost-effective.

In modern conditions, two main methods are used to clean radiator tubes—mechanical and chemical. The mechanical method involves inserting a probe into the radiator tubes to remove contaminants. However, this method can damage the radiator, leaving scratches and chips on its surface, which weaken the structure and promote future corrosion. Chemical cleaning, on the other hand, involves using alkalis for copper radiators and acids for aluminum ones. Despite the high efficiency of this method, it also carries certain risks. Chemical agents can cause corrosion of other materials in the radiator structure and lead to the formation of microcracks and leaks, negatively impacting the device’s durability [12].

Modern engineering technologies are focused on developing safer and more effective cleaning methods, including those for diagnostics, geographic studies, and gas and liquid purification. One promising technology is ultrasonic cleaning, which is already widely used in various industries, including exhaust gas purification [13-15]. Ultrasonic waves can break down contaminant particles, significantly reducing harmful emissions into the atmosphere and improving overall environmental conditions [16-21]. The advantages of the ultrasonic method include its high efficiency and safety, as it does not cause material damage and does not require aggressive chemicals [22-23].

Given the increasing environmental and safety requirements in the automotive industry, we propose a new method for cleaning radiator scale using ultrasonic exposure to the water inside the radiator tubes. This method offers significant advantages over traditional mechanical and chemical cleaning methods. It eliminates the risk of radiator structure damage and minimizes the need for chemical reagents, making it safer and more environmentally friendly.

The goal of our experiment was to confirm the effectiveness of the transverse ultrasonic wave exposure method for radiator cleaning and to demonstrate its practical value.

The scientific novelty of this study lies in the development of dependencies that determine the effectiveness of radiator cleaning using transverse ultrasonic exposure.

1. Materials and methods

The ultrasonic radiator cleaning method is based on the phenomenon of water cavitation inside the radiator tubes under the influence of ultrasonic waves. Cavitation is the process of forming and subsequently collapsing microscopic gas bubbles in a liquid, releasing a significant amount of energy. This leads to a localized increase in temperature and pressure, which has a destructive effect on deposits such as scale and other contaminants. This process effectively cleans the internal surface of radiator tubes without the need for mechanical or chemical agents, eliminating the risk of material damage and preserving the structural integrity of the radiator. Thus, ultrasonic cleaning is an innovative and promising technology that ensures high cleaning efficiency while maintaining environmental safety [24-25].

Preliminary research included experimental studies that confirmed the feasibility of using ultrasound for cleaning vehicle radiators. The results demonstrated the high efficiency of the ultrasonic radiator cleaning method [26]. Special attention in the experiment was given to the direction of ultrasonic waves relative to the radiator tubes. Longitudinal ultrasonic wave exposure was examined, where the wave propagates along the axis of the tubes, minimizing energy losses at medium boundaries. In the preliminary experiment, a low-viscosity liquid was used. The choice of this liquid was based on theoretical and practical considerations: low viscosity promotes more intense cavitation bubble formation under ultrasound exposure, enhancing the destruction of deposits [27-28]. The research results showed that ultrasonic cavitation significantly increases cleaning efficiency without negatively affecting the radiator structure, ensuring high process safety.

The authors also considered transverse ultrasonic wave exposure, where waves must pass through the tube walls twice, causing significant energy attenuation and reducing overall cleaning efficiency. However, in this case, the ultrasonic emitter was installed in a fixed position without movement across the radiator surface [29-30].

Transverse ultrasonic wave exposure for radiator cleaning was conducted with the emitter moving across the radiator surface. The experimental study on cleaning the cooling system radiator was performed on an Opel Vectra B 1.6-liter engine cooling radiator, as shown in Figures 1 and 2.

Fig. 1 – Opel Vectra B car

Fig. 2 – Opel Vectra B radiator

The setup for heating, supplying, and filtering the liquid was manufactured based on preliminary studies and is shown in Figure 3.

Fig. 3 – Assembled setup for radiator cleaning

Ultrasonic exposure was applied transversely with the movement of the ultrasonic emitter across the entire surface of the radiator, as shown in Figures 4 and 5.

Fig. 4 – Installation of the ultrasonic emitter on the radiator

Fig. 5 – Ultrasonic impact on the radiator

During the experiment, key liquid characteristics were measured, including its density, volume, and mass, to assess the influence of these parameters on the efficiency of ultrasonic radiator cleaning. High-precision equipment was used for the measurements, ensuring maximum accuracy and reliability of the obtained data.

To determine the liquid mass, MH-500 electronic precision scales with a measurement accuracy of up to 0.01 grams were used. The liquid volume was measured using two types of measuring containers: a 100 ml graduated cylinder for precise measurements of small volumes and a 1000 ml measuring jug for handling larger quantities of liquid [31]. This approach allowed for flexibility in adapting to different experimental requirements and ensured the necessary data accuracy.

2. Experiment

In the experiment, distilled water was used as the flushing liquid due to its lowest dynamic viscosity. The water was heated to a temperature of 60°C. The selected liquid parameters provided optimal conditions for the rapid and effective manifestation of cavitation processes and scale dispersion in the radiator.

The experimental study was conducted as follows: distilled water was poured into the assembled setup and heated to a specified temperature, followed by the determination of mass, volume, density, and outflow velocity of the water through the radiator, as shown in Figures 6–8.

Fig. 6 – Determination of liquid temperature

Fig. 7 – Determination of liquid volume

Fig. 8 – Determination of liquid mass

In the first stage, the ultrasonic generator was activated for 60 seconds at each point, and the ultrasonic emitter was moved across the radiator surface, as shown in Figure 9.

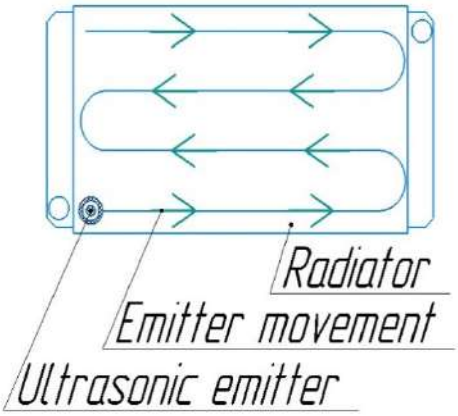

Fig. 9 – Ultrasonic impact scheme on the radiator

The total duration of the first stage was 1200 seconds, and the experiment consisted of three stages. After each stage, the liquid parameters were determined, and the liquid was weighed to obtain precise quantitative data on its mass and density. The mass of scale was determined by subtracting the mass of clean water from the total mass of the resulting pulp, allowing for an accurate measurement of the removed scale.

The pulp is a mixture of liquid and solid scale particles that detached from the radiator tubes due to ultrasonic exposure during the cleaning process. Scale, in turn, consists of solid mineral deposits that form on the surfaces of heat exchange elements due to the heating or cooling of the liquid. Over time, these deposits significantly reduce the efficiency of the cooling system by obstructing normal heat exchange.

During the experiment, the pulp was used as an indicator of cleaning efficiency. Key parameters were measured, such as the mass of removed scale, its concentration in the liquid, and the volume of removed contaminants. The collected data allowed for an assessment of the effectiveness of ultrasonic exposure. The difference between the mass of the pulp before and after cleaning was used for the quantitative determination of the method's efficiency.

3. Results and discussion

An analysis of the collected data was conducted, revealing key patterns and establishing dependencies between the different measured parameters. Based on these dependencies, graphs were constructed to visually represent and better understand the research results.

Measured parameters, including the mass of removed scale, concentration of solid particles in the liquid, pulp density, outflow velocity of the liquid from the tubes, and temperature changes, were presented in Table 1.

Table 1. Measured parameters under ultrasonic exposure

№	Ultrasonic exposure time (seconds)	| Liquid mass (grams)	Liquid density (g/cm³)	Liquid outflow time (seconds)	Liquid temperature (°C)	Liquid outflow velocity (ml/s)
1	0	99,13	0,9913	5,64	60	177,30
2	1200	99,47	0,9947	5,31	60	188,32
3	2400	99,98	0,9998	5,02	60	199,20
4	3600	100,21	1,0021	4,78	60	209,21

The analysis of the obtained experimental data revealed a correlation between the liquid density and its outflow velocity through the radiator tubes, depending on the duration of ultrasonic exposure. These dependencies were visualized in the form of graphs, presented in Figure 6, which allowed for a clear representation of the dynamic changes and a deeper understanding of the cleaning process characteristics.

Thanks to the identified relationships, it became possible to determine the most effective operating modes of the ultrasonic equipment, enabling the maximum intensity of radiator tube cleaning. These results not only provide a theoretical understanding of the ultrasonic mechanism but also offer valuable recommendations for the practical application of the method.

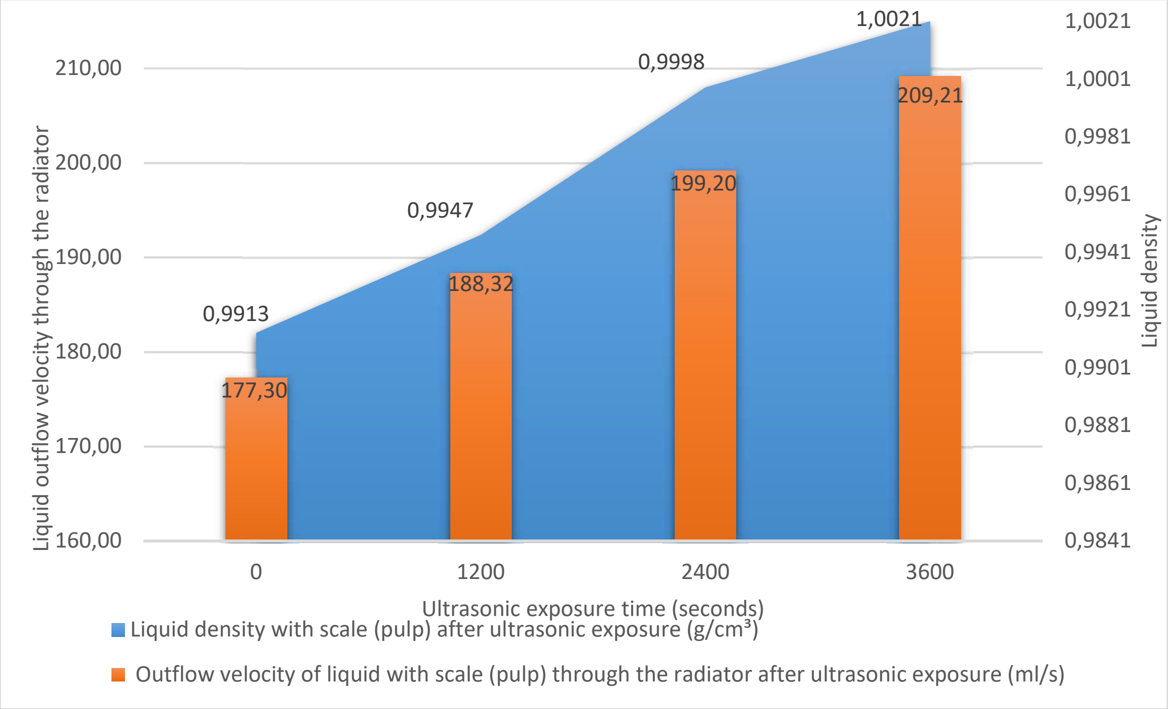

Fig. 10 – Changes in liquid density and outflow velocity through the radiator depending on ultrasonic exposure time

The obtained graphical dependencies demonstrate how the intensity of ultrasonic wave exposure affects the efficiency of contamination removal. Increasing the processing time gradually led to an increase in liquid density due to the washing out of solid scale particles, which, in turn, influenced the outflow velocity. This indicates that ultrasonic exposure has a more pronounced effect on pulp outflow compared to clean water as processing time increases.

Table 2 presents the dynamic changes in pulp mass depending on the ultrasonic treatment duration, with corresponding graphs shown in Figure 11. These data reflect the weight of the pulp and scale content over time during ultrasonic exposure. By subtracting the mass of clean water from the total pulp mass, the mass of removed scale was determined.

This approach provides a quantitative assessment of the efficiency of the ultrasonic cleaning process and highlights the impact of ultrasonic exposure on the removal of scale from the internal cavities of the radiator.

Table 2. Mass of liquid and scale after exposure

Ultrasonic wave exposure time on the radiator (seconds)	Liquid mass (grams)	Scale mass after ultrasonic exposure (grams)
0	99,13	0
1200	99,47	0,34
2400	99,98	0,85
3600	100,21	1,08

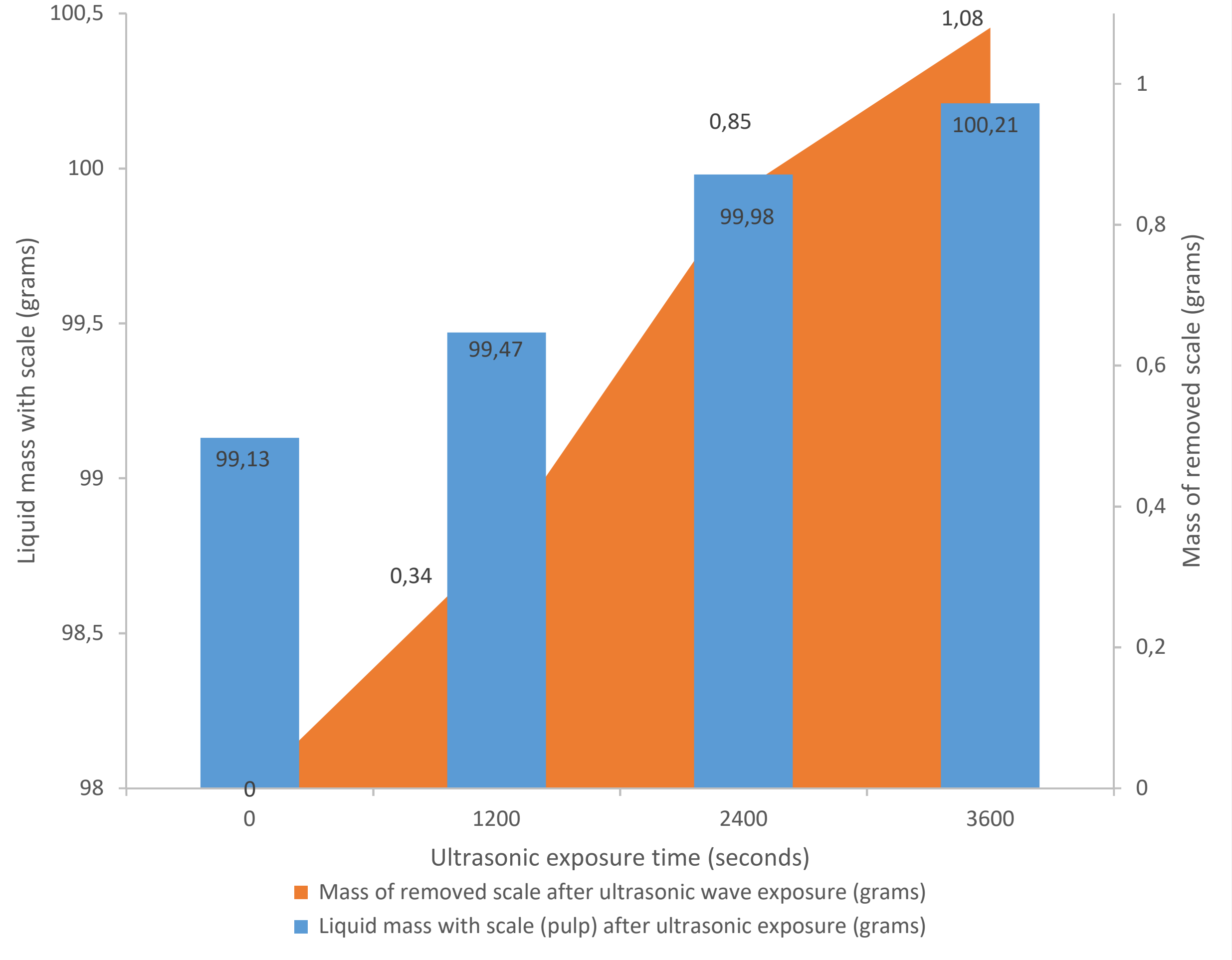

Fig. 11 – Obtained pulp and scale mass depending on ultrasonic exposure time

The analysis of these changes allows us to track the dynamics of the scale removal process from the radiator. As the ultrasonic exposure time on the vehicle radiator increases, the concentration of scale in the liquid rises. The obtained data confirm the impact of ultrasonic cleaning on the efficiency of deposit removal, supporting the initial assumption about the effectiveness of this method in the maintenance of vehicle cooling systems.

Conclusions

The conducted study confirmed that transverse ultrasonic wave exposure is an effective and safe method for removing contaminants compared to longitudinal exposure. The obtained results demonstrated that the use of transverse ultrasonic waves outperforms longitudinal exposure. Unlike longitudinal exposure, the transverse method ensures an even distribution of cavitation processes across the entire radiator surface, contributing to a more intensive scale removal process.

Experimental data confirmed that an increase in transverse ultrasonic exposure time leads to a significant increase in the mass of removed scale. The analysis of dynamic liquid parameters showed an improvement in outflow velocity, indicating an effective restoration of the radiator tube’s flow capacity.

The transverse ultrasonic exposure technology is based on the principle of cavitation, which occurs inside the liquid contained within the radiator. During the experiment, the ultrasonic emitter was moved across the entire radiator surface, ensuring a uniform distribution of waves and active breakdown of deposits. This approach minimized energy losses at medium boundaries, which are characteristic of the longitudinal method, where ultrasonic waves propagate along the tube axis and partially dissipate.

Thus, the proposed method not only enables the elimination of contaminants without the risk of damaging the structure but also significantly increases the lifespan of the cooling system. This makes ultrasonic cleaning a promising technology for integration into vehicle maintenance practices, providing both economic and environmental benefits.

References

[1] Savich E.L. Automobile Structure. Engines: Textbook. – Minsk: Higher School, 2019. – 334 p.

[2] Kravchenko V.A., Butkov R.I. Maintenance and Repair of Motor Vehicles. – Zernograd, 2015. – 339 p.

[3] Rutenburg G.B. Operation and Repair of Automobile Radiators. – Moscow, 1955. – 81 p.

[4] Tokarev A.O., Mironenko I.G. Failures of Machine Parts. Analysis of Causes, Technical Diagnostics, and Prevention. — Moscow; Vologda: Infra-Engineering, 2020. — 220 p.

[5] Larichkin V.V., Gusev K.P. Industrial Ecology. Laboratory Workshop. – Novosibirsk: Publishing House of NSTU, 2011. – 56 p.

[5] Ospanov O., Yeleuov G., Kadyrova I., Bekmurzinova F. The Life Expectancy of Patients with Metabolic Syndrome After Weight Loss: Study Protocol for a Randomized Clinical Trial (LIFEXPE-RT). // Trials, Vol. 20, 2019 – p. 1-7.

[6] Mindubayeva F., Niyazova Y., Nigmatullina R., Sadykova D., Akhmaltdinova L., Salikhova Y., Kadyrova I., Akhmetova M., Sabirova D. Membrane Serotonin Transporter as a Biomarker of Pulmonary Arterial Hypertension in Children with Congenital Heart Defect. // Research Journal of Pharmacy and Technology. Vol. 13, Issue 5, 2020. – p. 2435-2438. doi: http://dx.doi.org/10.5958/0974-360X.2020.00436.9.

[7] Akhmaltdinova L., Kolesnichenko S., Lavrinenko A., Kadyrova I., Avdienko O., Panibratec L. Influence of Pathogen Type on Neonatal Sepsis Biomarkers. // Wiley, International Journal of Inflammation. Vol. 2021, Issue 2. – p. 1-7. doi: http://dx.doi.org/10.1155/2021/1009231.

[8] Ibatov M.K., Kadyrov A.S., Pak I.A., Kadyrova I.A., Askarov B.Sh. Results of Experimental Studies on the Performance of Ultrasonic Cleaning Equipment for Automotive Exhaust Gases //Ugol, 2020, (2 (1127)), 73-78.

[9] Ivanov V.P., Yaroshevich V.K., Savich A.S. Automobile Repair. – Minsk: Higher School, 2009. – 383 p.

[10] TM 10-450 Sheet Metal Work, Body, Fender, and Radiator Repairs / War Department. – Washington, 1941. – 119 p.

[11] Ilyin M.S. Bodywork. Straightening, Welding, Painting, Anti-corrosion Treatment. – Moscow, 2009. – 480 p.

[12] Kadyrov A., Sarsembekov B., Ganyukov A., Suyunbaev S., Sinelnikov K. Ultrasonic Unit for Reducing the Toxicity of Diesel Vehicle Exhaust Gases. // Communications - Scientific Letters of the University of Zilina. – 2022. – Vol. 24, No. 3. – p. B189-B198. – https://doi.org/10.26552/com.C.2022.3.B189-B198

[13] Kadyrov A.S., Amangeldiev E.A. New Specifications of the Theory of Ground Cutting. // Periodico Tche Quimica. Vol. 166, Issue 31, 2019 – p. 922-936.

[14] Kadyrov A., Kryuchkov Y., Kukesheva A., Pak I., Kurmasheva B., Kabikenov S. Development of Calculation Methodology for Optimizing the Operating Mode of an Electric Pulse Unit for Cleaning Exhaust Gases. // Communications - Scientific Letters of the University of Zilina. – 2024. – Vol. 26, No. 1. – p. B41-B53. - https://doi.org/10.26552/com.C.2024.011

[15] Sarsembekov B.K., Kadyrov A.S., Kunayev V.A., Issabayev M.S., Kukesheva A.B. Experimental Comparison of Methods for Cleaning Car Exhaust Gas by Exposure Using Ultrasound and Laser Radiation. // Material and Mechanical Engineering Technology, 2024, Vol. 3, 2024 – p. 44–53.

[16] Kadyrov A.S., Kunaev V.A., Georgiadi I.V. Prospects for Processing of Ferrous Metallurgical Waste Based on ArcelorMittal Temirtau Experience. // Metallurgist, Vol. 62, Issue 1-2, p. 22–28.

[17] Kadyrov A., Kryuchkov Y., Sinelnikov K., Ganyukov A., Sakhapov R., Kukesheva A. Studying the Process of the Internal Combustion Engine Exhaust Gas Purification by an Electric Pulse. // Communications - Scientific Letters of the University of Zilina. – 2022. – Vol. 24, No. 4. – p. B275-B287. - https://doi.org/10.26552/com.C.2022.4.B275-B287

[18] Kukesheva A., Kadyrov A., Kryuchkov Y. Establishing the Parameters of the Operation Mode of the Electric Pulse Automobile Muffler. // Journal of Applied Engineering Science. Vol. 22, Issue 1, 2024. – p. 89–99. doi: 10.5937/jaes0-45196

[19] Pak I. Experimental Study of the Ultrasonic Muffler Efficiency for Improving the Exhaust Gas Cleaning System of Internal Combustion Engines of Automobiles. // Material and Mechanical Engineering Technology, No. 2, 2024 – p. B53-B63. - DOI 10.52209/2706-977X_2024_2_53

[20] Makhambetov E. N., Baisanov A. S., Isagulov A. Z., Grigorovich K. V., Timirbayeva N. R. Production of Complex Calcium-Containing Ferrous Alloys of Waste Smelter Slags and High-Ash Coals // Steel in Translation, Volume 49 (10), 2019 p. 698–702, DOI:10.3103/S0967091219100085

[21] Moldabaev B., Sinelnikov K., Kukesheva A. Justification of the Method of Vehicle Engine Radiator Ultrasonic Cleaning //Communications - Scientific Letters of the University of Zilina, Vol. 27, Issue 1, 2025. – p. 75-84, doi: https://doi.org/10.26552/com.C.2025.015.

[22] Sakhapov R.L. Method of Cleaning Internal Combustion Engine Radiator Tubes with Ultrasound. // Material and Mechanical Engineering Technology, No. 2, 2024 – p. B18-B24. - DOI 10.52209/2706-977X_2024_2_18

[23] Kardashev G.A. Physical Methods of Intensification of Chemical Technology Processes. – Moscow: Chemistry, 1990. – 205 p.

[24] Golyamina I.P. Ultrasound: A Small Encyclopedia. – Moscow: Soviet Encyclopedia, 1979. – 400 p.

[25] Kozyrev S.P. Hydroabrasive Wear of Metals under Cavitation. – Moscow: Mashinostroenie, 1971. – 240 p.

[26] Magomedov U.B., Magomedov M.M.-Sh., Alkhasov A.B. Handbook on Thermal Conductivity and Dynamic Viscosity of Water and Aqueous Salt Solutions. – Moscow: Fizmatlit, 2013. – 219 p.

[27] Fetisova G.P. Materials Science and Material Technology: In 2 Parts. – 8th Edition, Revised and Expanded. – Moscow: Yurayt, 2018. – Part 2. – 389 p.

[28] Kadyrov A., Sinelnikov K., Sakhapov R., Ganyukov A., Kurmasheva B., Suyunbaev S. Studying the Process of Transport Equipment Cooling System Ultrasonic Cleaning. // Communications - Scientific Letters of the University of Zilina. – 2022. – Vol. 24, No. 4. – p. B288-B300. - https://doi.org/10.26552/com.C.2022.4.B288-B300

[29] Sinelnikov K.A. Development and Research of Technical Maintenance and Operation Methods for Automobiles Using Ultrasound: PhD Dissertation (8D071). – Karaganda, 2023. – 142 p.

[30] Afonsky A.A., Dyakonov V.P. Measuring Instruments and Mass Electronic Measurements. Engineer's Library Series. – Moscow: SOLON-PRESS, 2010. – 544 p.

Information of the authors

Sinelnikov Kirill Anatolyevich, PhD, Abylkas Saginov Karaganda Technical University
e-mail: coolzero7777@gmail.com

Moldabaev Baurzhan Galymovich, doctoral student, Abylkas Saginov Karaganda Technical University
e-mail: baurmoldabaev62@mail.ru

Zhunusbekova Zhanara Zhumashevna, PhD, Abylkas Saginov Karaganda Technical University
e-mail: zhzhzh_84@mail.ru

DOI 10.52209/2706-977X_2025_3_77 IRSTI 55.63.29 UDC 621.574

Heat Recovery Based Thermodynamic Analysis of Adsorption Refrigeration

Ashok V.*, Sachdeva G.
National Institute of Technology Kurukshetra, Haryana, India
*corresponding author

Abstract: The increasing entropy of the universe is a fundamental driver accelerating the rise in Earth's temperature, thereby significantly intensifying the global demand for cooling technologies. Heat-driven adsorption refrigeration systems have emerged as a promising solution, effectively utilizing low-grade thermal energy to meet this growing demand. This study presents a numerical analysis of a two-bed adsorption refrigeration system employing 208C activated carbon and monolithic carbon composite as adsorbents, with R32 serving as the adsorbate. The performance of the system was evaluated in terms of the Coefficient of Performance (COP), considering variations in condenser pressure, evaporator pressure, and maximum desorption temperature across different adsorbent–adsorbate pairs. The results indicate that the monolithic carbon composite–R32 pair exhibits a superior COP compared to the 208C–R32 combination. To further enhance system efficiency, a novel heat recovery-based adsorption refrigeration cycle was developed, wherein the heat rejected during the cooling and adsorption processes is effectively reutilized for the heating phase. The monolithic carbon composite–R32 pair achieved the highest COP within the heat recovery-based cycle, demonstrating its strong potential for application in efficient, sustainable cooling systems.

Keywords: COP, adsorption, desorption, activated carbon.

Introduction

As industrialization increases, entropy generation also rises, leading to a temperature increase on Earth [1]. Consequently, there is a significant surge in the demand for cooling. The conventional vapor compression refrigeration system utilizes high-grade energy, such as mechanical power or electricity, to operate. Additionally, the use of refrigerants like CFC, HFC, and HCFC contributes to ozone layer depletion [2].

To address these issues, researchers are actively working on solid sorption refrigeration using composite adsorbent. The significance of adsorption refrigeration has grown tremendously because it utilizes low-grade energy, specifically waste heat, for its operation and low-cost composite adsorbent. Moreover, it employs environmentally friendly refrigerants like ammonia, methanol, and water. Adsorption refrigeration and air-conditioning technology involve negligible moving parts, resulting in the absence of noise and vibrations. Numerous combinations of adsorbates and adsorbent composites exhibit broad working temperature ranges, spanning from 50 to 420°C. For instance, activated carbon paired with NH_3 or CH_3OH, as well as zeolite-water and silica gel-water combinations are among the available options. These pairings offer versatility across a wide temperature spectrum.

Several investigations [3] have explored the utilization of low-grade energy sources, such as industrial waste heat or solar heat, within the field of adsorption technology for various applications, including desalination or the generation of cooling and refrigeration effects. A notable illustration is the study conducted by Wang et al. [4], where they developed an adsorption air conditioner for a locomotive driver cabin. This system, powered by exhaust gases with temperatures ranging from 350°C to 450°C, exhibited a cooling power of 5 kW and a COP of 0.25. Operating with an exhaust temperature of 450°C, cooling air temperature of 40°C, and chilled water temperature of 10°C, the setup achieved a cycle time of 1060 seconds. Additionally, Zejli et al. [5] proposed a theoretical model for a multi-effect desalination system employing adsorption heat pump technology with zeolite composite as the solid vapor adsorbent. Despite these advancements, it is crucial to recognize that several researchers have observed that the simple adsorption refrigeration cycle often yields low COP values, typically ranging from 0.1 to 0.6.

Researchers have actively tackled the challenge of improving the COP in adsorption refrigeration systems [6], acknowledging its historically low values by using various adsorbent composites. A noteworthy contribution by Akahira et al. [7] involved the exploration of a two-bed adsorption refrigeration cycle utilizing silica gel and activated carbon composites. They incorporated mass recovery to leverage pressure differentials and enhance refrigerant mass circulation, specifically with the silica gel-water pair. The study concluded that the mass recovery-based cycle, particularly when supplied with hot and cooling water, outperformed the basic cycle in terms of both Cooling Capacity (CC) and COP. Expanding on this work, Wang et al. [8] demonstrated various adsorption refrigeration cycles with adsorbent composites, including continuous heat recovery, mass recovery, thermal wave, convective thermal wave, cascade multi-effect, and hybrid heating and cooling cycles. In another innovative approach, Sapienza et al. [9] introduced an adsorptive chiller based on three hybrid adsorbers, conducting their initial testing campaign under real HVAC operating conditions.

In a different avenue, Krzywanski et al. [10] analyzed a tri-bed twin-evaporators-based adsorption chiller model using genetic algorithms (GA) and artificial neural networks (ANN) to optimize cooling capacity. However, it's worth noting that the operational complexity of the different adsorbent composites with tri-bed twin-evaporator adsorption chiller increased. Additionally, Saha et al. [11] designed a dual-mode silica gel–water-based adsorption chiller that effectively utilizes waste heat (40°C to 95°C). This dual-mode system showcases versatility in adapting to different heat sources for improved efficiency.

After the 1973 oil crisis, researchers [12], [13], initiated a quest for alternative energy sources, with a particular emphasis on renewable energy to meet global energy demands by using various adsorbent composites[14], [15], [16] .

Solar energy emerged as a favored option, especially for refrigeration and cooling applications, where Vapor Compression Refrigeration Systems (VCRS) could potentially be replaced by solar-operated adsorption refrigeration systems, thereby reducing reliance on electricity. Berdja et al. [14] explored solar adsorption refrigeration in the Algerian climate using ANSYS for temperature distribution analysis over the adsorption plate. Their analysis extended to different components of solar adsorption systems, including the adsorption plate and the evaporative chamber, with considerations for various arrangements and adsorbent composites. Anyanwu et al. [17] contributed to the field by establishing a thermodynamic design procedure for solar adsorption refrigeration, and conducting performance analyses with different adsorbent composite and adsorbate pairs.

An adsorption-based air-conditioner has been designed and fabricated [18] utilizing a silica gel-water working pair. In their experimental investigation, they observed significant cost benefits and proposed the residential application of the adsorption-based air-conditioner for cooling and heating. The application of compound parabolic concentrators in conducting comparative experiments within adsorption refrigeration systems has been explored [19]. To enhance system performance across various operating modes, they implemented an improved mass transfer method. With enhanced mass transfer a solar adsorption refrigeration prototype has been developed [20] which concluded an average enhancement of 35.9% in refrigeration capacity with adsorbent composites.

The effectiveness significantly hinges on the careful selection of adsorbent composite [21] and adsorbate pairs during the design phase, necessitating thorough research [22], [23], [24]. In an investigation conducted by Ahmed et al. [25], various adsorbate pairs used in solar adsorption systems were explored, revealing that Silica gel and chlorides with water exhibited the highest Coefficient of Performance (COP), while zeolite with water demonstrated inferior performance under similar conditions. Additionally, Zhang et al. [26] reviewed novel adsorbent-absorbate working pairs for adsorption refrigeration, assessing their impact on performance parameters such as COP and specific cooling power. Essential properties of adsorbent-adsorbate pairs influencing performance include the adsorbent's particle size, composites, micropore size, total porosity, and stability. Li et al. In summarizing the above research on adsorbent-adsorbate properties, it is evident that further research is imperative to meet the growing demands for enhanced adsorption refrigeration performance.

1. Working principle

1.1 Basic Intermittent Cycle

The basic cycle consists of essential components, including an adsorber bed, an evaporator, a condenser, an expansion device, various valves, and heating and cooling systems, as depicted in Figure 1. The adsorption refrigeration process comprises four stages: sensible heating, desorption and condensation, sensible cooling, and adsorption and evaporation.

During the sensible heating process, the concentration of refrigerant within the adsorber bed remains constant (isosteric), while the temperature increases from T_1 to T_2, and the pressure reaches P_c. After sensible heating, the desorption process initiates, and the adsorbate enters the condenser at P_c. Throughout desorption, the temperature of the bed rises from T_2 to T_3. Upon completing the desorption process, the cooling and depressurization of the adsorber bed commence, resulting in a temperature reduction fromT_3 to T_4. As the adsorber bed reaches T_4 and the pressure aligns with P_e, the adsorption process begins, during which the temperature decreases from T_4 to T_1.

This paper analyzed the thermodynamic performance of the basic and heat recovery type adsorption refrigeration cycle. Four performance parameters; T_1, T_3, P_e and P_c were used to obtain the COP relation for comparing different adsorbent-adsorbate pairs at different operating conditions.

1.2 Continuous Cycle

The intermittent nature of the basic single-bed adsorption refrigeration cycle stems from the alternating occurrence of adsorption and desorption processes. To ensure continuous production of the refrigeration effect, a minimum of two adsorber beds is required [Ojha et al. [13]].

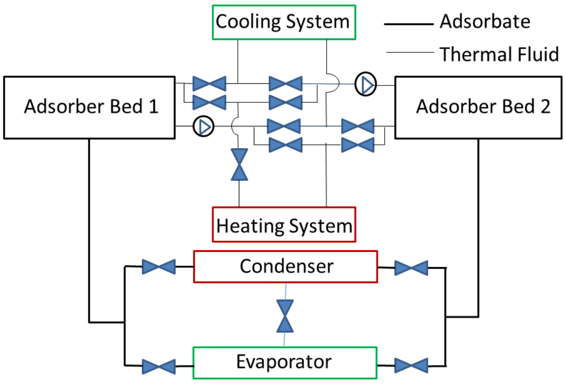

Fig. 1. - Heat recovery-based adsorption refrigeration system. The thick line represents the flow of adsorbate, while the thin represents the flow of thermal fluid.

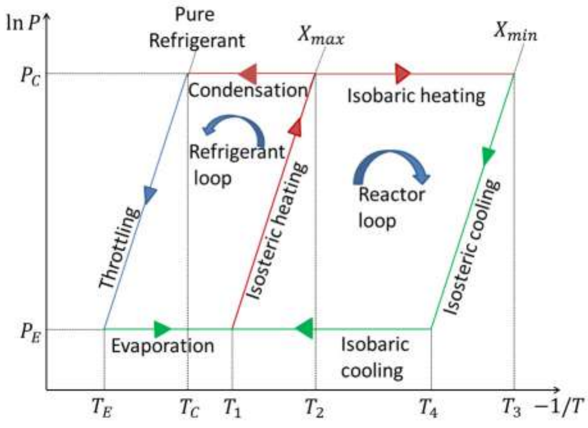

Fig. 2. - Clapeyron diagram of adsorption refrigeration cycle.

1.3 Regenerative Cycle

After the completion of the desorption of refrigerant from the bed there will be a lot of heat in the bed, a substantial amount of heat remains within the bed. This residual heat presents an opportunity for utilization in heating applications during the subsequent bed heating phase. To boost the efficiency of the adsorption refrigeration cycle, optimizing the harnessing of this released heat is essential. By incorporating this rejected heat into the sensible heating process, we can effectively reduce the overall demand for external heat input, thereby enhancing the overall performance of the cycle.

2 Mathematical modeling

2.1 Adsorption Equilibrium

The adsorption of the adsorbate in the adsorption bed has been estimated through the D-A (Dubinin-Astakhov) equation:

$$x = x_o \ \exp\left[-K\left\{ \frac{T}{Tsat} - 1 \right\}^n \right] \tag{1}$$

The latent heat of sorption has been calculated for any temperature and pressure using Eq. (2), where R represents the gas constant:

$$\frac{d}{dT}\left(\ln P\right) = \frac{h}{RT^2} \tag{2}$$

2.2 Heat Equation for Sensible Heating

The heat required for heating the bed and the adsorbed refrigerant from evaporator pressure to condenser pressure has been calculated using Eq. (3). Eq. (4) delineates the relationship between the mass of the adsorbed refrigerant and the maximum concentration, along with the mass of the activated carbon:

$$\left(Q_h\right) = \int_{T_1}^{T_2} C_{v,ac(T)} m_{ac} dT + \int_{T_1}^{T_2} C_{va(T)} m_a dT \tag{3}$$

$$m_a = x_{conc} m_{ac} \tag{4}$$

2.3 Desorption Heat

The heat required for desorption, necessary to release the refrigerant from the bed at a constant condenser pressure, has been calculated using Eq. (5). Subsequently, the desorbed refrigerant enters the condenser, where the refrigerant undergoes the condensation process:

$$Q_g = \int_{T_2}^{T_3} C_{pac(T)} m_{ac} dT + \int_{T_2}^{T_3} C_{pa(T)} m_a dT + \int_{T_2}^{T_3} m_a h_a \frac{\partial x\left(T, T_c\right)}{\partial T} dT \tag{5}$$

2.4 Cooling of Adsorber bed

The cooling heat for the adsorber bed after the desorption phase is computed by Eq. (6), which is taken from the cooling effect generated by the system. During this stage, the pressure within the adsorber bed decreases from the condenser P_c to P_e, while the temperature concurrently drops from T_3 to the T_4:

$$Q_c = \int_{T_4}^{T_3} C_{pac(T)} m_{ac} dT + x_{dil} \int_{T_4}^{T_3} C_{va(T)} m_{ac} dT \tag{6}$$

2.5 Adsorption Heat

The adsorption of the refrigerant from its gaseous phase onto the surface of the adsorbent composite occurs in the liquid form, necessitating the rejection of latent heat from the adsorber bed and has been calculated using Eq. (7):

$$Q_{ad} = \int_{T_4}^{T_1} C_{p,ac(T)} m_{ac} dT + \int_{T_4}^{T_1} m_a h_a \frac{\partial x\left(T, T_e\right)}{\partial T} dT + \int_{T_4}^{T_1} C_{p,a(T)} m_a dT - \int_{T_4}^{T_1} C_{p,ag(T)} m_{ac} \Delta x d\left(T - T_e\right) \tag{7}$$

The second term in Eq. (7) accounts for adsorption heat, while the last term has been included to accommodate any cooling effect generated by the refrigerant. After the refrigerant undergoes condensation in the condenser, a combination of liquid and vapor refrigerant is present as it expands from P_c to P_e . As a result, the cooling needed for the vapor refrigerant is calculated using Eq. (8):

$$Q_{co} = \int_{Te}^{Tc} C_{v,f(T)} \left(x_{conc} - x_{dil}\right) m_{ac} dT \tag{8}$$

The refrigeration effect produced by the system has been calculated using Eq. (9). The latent heat of evaporation has been determined at the evaporator pressure corresponding to the respective refrigerant:

2.6 System Performance Equations

$$Q_{ref} = L_e \left(x_{conc} - x_{dil}\right) m_{ac} \tag{9}$$

The system's performance, expressed as the COP), is established through Eq. (10):

$$COP = \frac{Q_{ref} - Q_c - Q_{ad} - Q_{co}}{Q_g + Q_h} \tag{10}$$

2.7 Equations for Heat Recovery

The fraction of heat rejected during the adsorption process and cooling of the bed has been utilized for the heating process, thereby reducing the amount of heat required for a sensible heating process:

$$Q_r = e\left(Q_{ad} + Q_c\right) \tag{11}$$

The recovered heat has been calculated using Eq. (11), where 'e' represents the effectiveness of the regenerator and has been assumed to be 0.8 in this investigation:

$$COP_r = \frac{Q_{ref} - Q_c - Q_{ad} - Q_{co}}{Q_g + Q_h + Q_r} \tag{12}$$

The performance of the heat recovery-based cycle has been evaluated using Eq. (12).

Table 1. D-A equation's parameter for adsorbent-adsorbate pairs

Activated Carbon	Refrigerant	x_0	K	n
208C	R32	0.476	2.4634	1.3880
Monolithic	R32	0.461	2.6729	1.3326

3 Results and discussion

3.1 Variation of P_e and P_c

From Fig. 3 it is clear that as the condenser pressure increases the heat requirement for the desorption of the refrigerant increases hence the COP decreases while with the increase in evaporator pressure (P_e), as shown in Fig. 4, the COP increases for both the basic and heat recovery-based cycles increases because the heat requirement for the desorption process decreases.

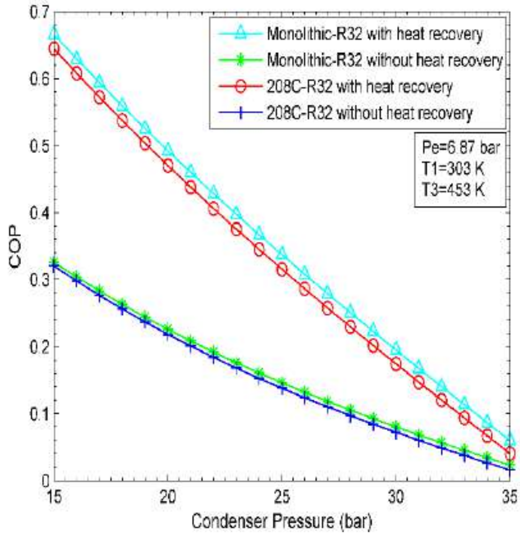

Fig. 3. - COP for R32 with P_c

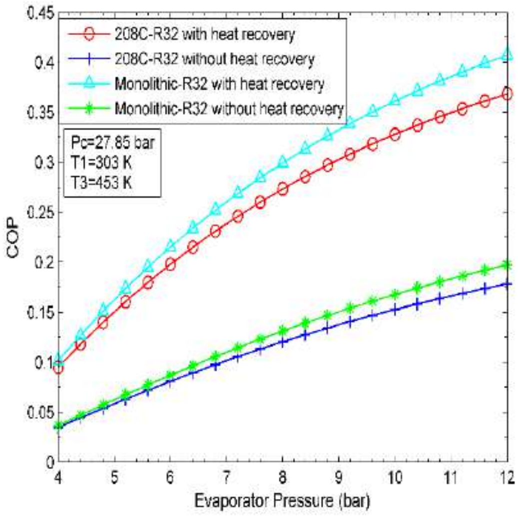

Fig. 4. - COP for R32 with P_e

As the desorption temperature increasing the desorption of the refrigerant from the adsorber bed increases but after a certain time the desorption rate from the bed decreases because the concentration of adsorbate on the bed decreases and at the same time the heat input decreases so it results in the decrease the COP of the system (Fig. 5).

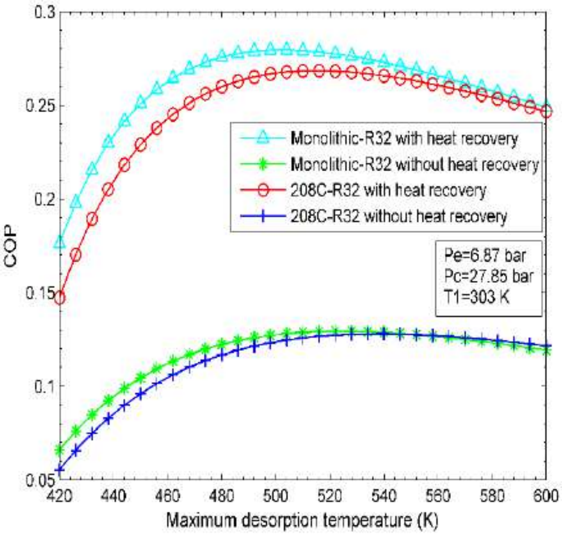

Fig. 5. - COP for R32 with maximum desorption temperature

The specific heat capacities, enthalpy and characteristic gas constant are given in Table 2 for the calculation of the different heat equations.

Table 2. Thermo-physical properties

Property name	R32	Activated Carbon
$C_p\left(kJ/kgK\right)$	2.27	$0.175+2.245\times10^{-3}\times T$
$C_v\left(kJ/kgK\right)$	0.93	$0.175+2.245\times10^{-3}\times T$
$C_p\left(gas\right)\left(kJ/kgK\right)$	1.2	-
$C_{v,a,avg}\left(kJ/kgK\right)$	0.99	-
$h_{fg,eva}\left(kJ/kgK\right)$	323.16	-
$R\left(kJ/kgK\right)$	0.16	-

Conclusions

A thermodynamic model has been methodically created and examined for both basic and heat recovery-based adsorption refrigeration cycles, considering diverse combinations of adsorbates and adsorbent composites. The study involves the systematic tuning of essential operating parameters such as evaporator pressure, condenser pressure, and maximum desorption temperature. From the analysis, it has been analyzed that COP decreases with an increase in the condenser pressure and increases with an increase in the evaporator pressure. By increasing maximum desorption temperature the COP first increases and then decreases. From the above analysis, it has been also analyzed that reducing the size of the system adsorbent composite plays an important role in adsorbing the adsorbate.

Acknowledgment

The support from the NIT Kurukshetra, Haryana (India) was appreciated.

Nomenclature

$C_{p,}$	Specific heat of adsorbate at constant pressure [J/kg K]	Q_{ref}	Condensation energy [J]
$C_{p,}$	Specific heat of activated carbon at constant pressure [J/kg K]	R	Gas constant for adsorbate [J/molK]
$C_{p,}$	Specific heat of adsorbate gas at constant pressure [J/kg K]	T_1	Minimum adsorption temperature [K]
$C_{v,}$	Specific heat of activated carbon at constant volume [J/kg K]	T_2	Minimum desorption temperature [K]
C_{vj}	Specific heat of saturated liquid adsorbate at constant volume [J/kg K]	T_3	Maximum desorption temperature [K]
H	Heat of adsorption	T_4	Maximum adsorption temperature [K]
H_{f}	Latent heat of vaporization [J/kg]	e	Effectiveness of regenerator
K	Dubinin coefficient	T_c	Condensation temperature [K]
m_a	Mass of adsorbed adsorbate [kg]	T_{sat}	Saturation temperature [K]
m_a	Mass of activated carbon [kg]	x_0	Saturation concentration of adsorbate [kg/kg]
n	Coefficient in D-A equation	x_{conc}	Maximum conc. of adsorbed adsorbate [kg/kg]
P_c	Condensing pressure [Pa]	x_{dil}	Adsorbate conc. after desorption [kg/kg]
Q_g	Desorption energy [J]	Δx	Amount of desorbed adsorbate

References

[1] Tiratsoo J. Incidentand TPI detection: A new solution? Glob Pipeline Mon 2009;5:1–29. https://doi.org/10.1029/2010RG000345.

[2] Savitha DC, Ranjith PK, Talawar B, Rana Pratap Reddy N. Refrigerants for sustainable environment–a literature review. Int J Sustain Energy 2022;41:235–56. https://doi.org/10.1080/14786451.2021.1928129.

[3] El-Sharkawy II, Abdelmeguid H, Saha BB. Towards an optimal performance of adsorption chillers: Reallocation of adsorption/desorption cycle times. Int J Heat Mass Transf 2013;63:171–82. https://doi.org/10.1016/j.ijheatmasstransfer.2013.03.076.

[4] Wang DC, Xia ZZ, Wu JY. Design and performance prediction of a novel zeolite-water adsorption air conditioner. Energy Convers Manag 2006;47:590–610. https://doi.org/10.1016/j.enconman.2005.05.011.

[5] Zejli D, Benchrifa R, Bennouna A, Bouhelal OK. A solar adsorption desalination device: First simulation results. Desalination 2004;168:127–35. https://doi.org/10.1016/j.desal.2004.06.178.

[6] Li XH, Hou XH, Zhang X, Yuan ZX. A review on development of adsorption cooling - Novel beds and advanced cycles. Energy Convers Manag 2015;94:221–32. https://doi.org/10.1016/j.enconman.2015.01.076.

[7] Akahira A, Alam KCA, Hamamoto Y, Akisawa A, Kashiwagi T. Mass recovery adsorption refrigeration cycle - Improving cooling capicity. Int J Refrig 2004;27:225–34. https://doi.org/10.1016/j.ijrefrig.2003.10.004.

[8] Wang X, Chakarborty A, Ng KC, Saha BB. How heat and mass recovery strategies impact the performance of adsorption desalination plant: Theory and experiments. Heat Transf Eng 2007;28:147–53. https://doi.org/10.1080/01457630601023625.

[9] Sapienza A, Gullì G, Calabrese L, Palomba V, Frazzica A, Brancato V, et al. An innovative adsorptive chiller prototype based on 3 hybrid coated/granular adsorbers. Appl Energy 2016;179:929–38. https://doi.org/10.1016/j.apenergy.2016.07.056.

[10] Krzywanski J, Grabowska K, Herman F, Pyrka P, Sosnowski M, Prauzner T, et al. Optimization of a three-bed adsorption chiller by genetic algorithms and neural networks. Energy Convers Manag 2017;153:313–22. https://doi.org/10.1016/j.enconman.2017.09.069.

[11] Saha BB, Koyama S, Kashiwagi T, Akisawa A, Ng KC, Chua HT. Waste heat driven dual-mode, multi-stage, multi-bed regenerative adsorption system. Int J Refrig 2003;26:749–57. https://doi.org/10.1016/S0140-7007(03)00074-4.

[12] Dusane BM, Ghuge C. A Review On Solar Adsorption Refrigeration System // IOSR J Eng WwwIosrjenOrg ISSN 2016;06:1–07.

[13] Khattab NM. A novel solar-powered adsorption refrigeration module. Appl Therm Eng 2004;24:2747–60. https://doi.org/10.1016/j.applthermaleng.2004.04.001.

[14] Berdja M, Abbad B, Yahi F, Bouzefour F, Ouali M. Design and realization of a solar adsorption refrigeration machine powered by solar energy //Energy Procedia 2014;48:1226–35. https://doi.org/10.1016/j.egypro.2014.02.139.

[15] Sumathy K, Yeung KH, Yong L. Technology development in the solar adsorption refrigeration systems. Prog Energy Combust Sci 2003;29:301–27. https://doi.org/10.1016/S0360-1285(03)00028-5.

[16] Louajari M, Mimet A, Ouammi A. Study of the effect of finned tube adsorber on the performance of solar driven adsorption cooling machine using activated carbon-ammonia pair. Appl Energy 2011;88:690–8. https://doi.org/10.1016/j.apenergy.2010.08.032.

[17] Anyanwu EE, Ogueke N V. Thermodynamic design procedure for solid adsorption solar refrigerator. Renew Energy 2005;30:81–96. https://doi.org/10.1016/j.renene.2004.05.005.

[18] Pan Q, Peng J, Wang H, Sun H, Wang R. Experimental investigation of an adsorption air-conditioner using silica gel-water working pair. Sol Energy 2019;185:64–71. https://doi.org/10.1016/j.solener.2019.04.054.

[19] Zhao C, Wang Y, Li M, Zhao W, Li X, Yu Q, et al. Impact of three different enhancing mass transfer operating characteristics on a solar adsorption refrigeration system with compound parabolic concentrator. Renew Energy 2020;152:1354–66. https://doi.org/10.1016/j.renene.2020.01.110.

[20] Wang Y, Li M, Ji X, Yu Q, Li G, Ma X. Experimental study of the effect of enhanced mass transfer on the performance improvement of a solar-driven adsorption refrigeration system. Appl Energy 2018;224:417–25. https://doi.org/10.1016/j.apenergy.2018.05.017.

[21] Younes MM, El-Sharkawy II, Kabeel AE, Saha BB. A review on adsorbent-adsorbate pairs for cooling applications. Appl Therm Eng 2017;114:394–414. https://doi.org/10.1016/j.applthermaleng.2016.11.138.

[22] Askalany AA, Salem M, Ismail IM, Ali AHH, Morsy MG. A review on adsorption cooling systems with adsorbent carbon. Renew Sustain Energy Rev 2012;16:493–500. https://doi.org/10.1016/j.rser.2011.08.013.

[23] Thu K, Chakraborty A, Saha BB, Ng KC. Thermo-physical properties of silica gel for adsorption desalination cycle. Appl Therm Eng 2013;50:1596–602. https://doi.org/10.1016/j.applthermaleng.2011.09.038.

[24] Ismail A Bin, Li A, Thu K, Ng KC, Chun W. Pressurized adsorption cooling cycles driven by solar/waste heat. Appl Therm Eng 2014;67:106–13. https://doi.org/10.1016/j.applthermaleng.2014.02.063.

[25] Ahmed MS, Shehata AABDE, Abd A, Shehata E-K. A review: future of the adsorption working pairs in cooling 2007.

[26] Zhang X, Wang F, Lei X, Wang Y, Zhang Q, Wu X, et al. Influential factors and optimization analysis of adsorption refrigeration system performance. AIP Adv 2020;10. https://doi.org/10.1063/5.0026131.

Information of the authors

Ashok Verma, m.tech, research scholar, Department of Mechanical Engineering, NIT Kurukshetra
e-mail: ashok_61900050@nitkkr.ac.in

Sachdeva Gulshan, PhD,assistant professor, Department of Mechanical Engineering, NIT Kurukshetra
e-mail: gulshansachdeva@nitkkr.ac.in

DOI 10.52209/2706-977X_2025_3_84 IRSTI 55.13.17 UDC 621.73

Method for Optimizing the Parameters of Mechanical Processing of Holes to Ensure Cutting Tool Stability and Cost-Effective Machining

Zhetessova G.S.[1], Zharkevich O.M.[1]*, Kozhanov M.G.[1], Khrustaleva I.N.[2]
[1] Abylkas Saginov Karaganda Technical University, Karaganda, Kazakhstan
[2] Peter the Great St. Petersburg Polytechnic University, St. Petersburg, Russia
*corresponding author

Abstract. This article describes a new approach to optimizing the parameters of mechanical hole machining, which solves the problem of compromise between various criteria, such as machining time, tool durability, and surface quality. Traditional optimization methods, as shown in the study, usually focus on a single parameter, which inevitably leads to deterioration in others. For example, increasing the cutting speed to reduce machining time causes rapid tool wear, while reducing parameters to improve surface quality significantly increases time and production costs. To overcome these shortcomings, a methodology based on weighted multi-criteria analysis was developed. The methodology includes several stages: data collection, formation of objective functions, definition of constraints, normalization of criteria, and selection of an optimization method. A key element is the use of weighting coefficients, which allow the methodology to be adapted to specific production priorities. The study was conducted using a specific example of optimizing hole drilling in 45 steel. Weighting coefficients were set, with the greatest weight given to processing time (0.5), followed by roughness (0.3) and tool resistance (0.2). As a result, the following parameters were recognized as optimal: cutting speed v_c = 22 m/min and feed f_z = 0.2 mm/rev. With these values, the processing time was reduced from 37.9 to 28.7 seconds, while tool durability decreased from 275.2 to 176.4 μm. This clearly demonstrates that the method has found a compromise solution that allows reducing the time without critically compromising tool durability.

Keywords: optimization, cutting speed, feed rate, tool resistance, processing time

Introduction

Modern mechanical engineering faces the need to reduce costs, increase productivity, and improve product quality [1]. In the context of hole machining, which is one of the most common and important operations in mechanical engineering, this task is particularly relevant [2]. The technological process of hole machining is a complex operation that can include several stages: drilling, boring, countersinking, and reaming [3]. Each of these stages has its own characteristics and requires a careful approach to the selection of machining parameters. Traditional methods based on optimizing a single parameter (e.g., minimizing machining time) often lead to deterioration in others, such as tool durability or surface roughness [4]. This makes it relevant to use a multi-criteria approach that allows finding a compromise solution that takes into account all important aspects of the technological process.

Traditional optimization methods have typically focused on maximizing a single specific criterion. For example, in drilling, the goal was often to reduce processing time, as this directly affects productivity [5]. To achieve this, the cutting speed (vc) and feed rate (fz) were typically increased. However, as studies [6] show, this approach leads to rapid drill wear and deterioration in the surface quality of the hole. This trade-off between high productivity and tool durability is one of the key problems with the traditional approach.

Boring is an operation used to increase the diameter and improve the accuracy of an existing hole [7]. In traditional boring optimization, the focus can be either on minimizing time or on achieving high accuracy. Time optimization, as with drilling, involves the use of high speeds and feeds, which in turn can cause vibrations, lead to poor surface quality, and premature wear of the boring tool [8]. If accuracy is the priority, then the machining parameters are reduced, which leads to a significant increase in machining time and, as a result, to an increase in production costs [9].

Countersinking is an intermediate stage used to increase the diameter of a hole and prepare it for subsequent reaming or thread cutting. In the traditional approach, countersinking optimization often boiled down to selecting parameters that would ensure minimum surface roughness [10]. This was achieved by reducing the cutting speed and feed rate, which in turn led to an increase in the operation time. Such a unidirectional approach does not take into account economic aspects and may be ineffective in mass production conditions.

Reaming is the final operation used to produce holes with high precision and low roughness. Here, traditional optimization methods are almost always aimed at achieving the highest possible surface quality. This is achieved by very low feed rates and cutting speeds, making reaming one of the slowest operations in the hole machining process [11]. While surface quality is a key criterion for reaming, completely ignoring machining time can lead to significant delays in the production cycle.

Particular attention should be paid to the drilling operation, as it is one of the first in the technological process and the success of subsequent stages largely depends on it. With traditional drilling optimization methods, parameters such as cutting speed (vc), feed rate (fz), and cutting depth (ap) vary [12]. These parameters directly affect the machining time (Tpro), tool life (Tc), and surface quality (Ra) [13]. For example, increasing the cutting speed and feed rate to reduce machining time leads to faster tool wear and potential deterioration of surface quality [14]. On the other hand, reducing these parameters to increase tool life or improve surface quality leads to a significant increase in machining time [15]. Thus, the traditional approach, focused on a single criterion, does not allow finding the optimal balance between all important indicators, which creates a contradiction between them.

Thus, traditional optimization methods based on improving one parameter lead to deterioration of others, creating a trade-off between processing time, tool life, and surface quality. This problem is exacerbated by the fact that at each stage of hole machining (drilling, boring, countersinking, reaming), parameters such as cutting speed (vc), feed rate (fz), and cutting depth (ap) can be varied, which directly affect all three criteria [16]. This contradiction makes it relevant to use a multi-criteria approach, which allows finding a compromise solution that takes into account all important aspects of the technological process.

The application of a multi-criteria approach in technological processes is not only desirable but also vital for achieving competitive advantages. Unlike traditional methods, multi-criteria optimization allows several objectives to be taken into account simultaneously, such as minimizing processing time, maximizing tool durability, and achieving the required surface quality. The use of methods such as hierarchy analysis, weighted sum methods, or genetic algorithms allows for the construction of a mathematical model that reflects the relationship between processing parameters and key performance indicators. This enables engineers to make informed decisions based not only on production factors, but also on economic factors. Ultimately, comprehensive analysis allows not only to find the best compromise, but also to predict how a change in one parameter will affect the entire system, which significantly reduces risks and increases the stability of the production process. Multi-criteria analysis is becoming a key tool for improving production efficiency in a highly competitive market. This approach allows us to move from empirical parameter selection to scientifically based design of technological processes, ensuring sustainable development and innovative leadership.

The purpose of this study is to develop a methodology for improving the efficiency of the production process by optimizing key parameters such as processing time, surface quality, and tool wear based on multi-criteria analysis. The subject of this study is the development of a methodology for optimizing material flow parameters in mechanical engineering production.

A specific example is the technological operation of hole machining, which is one of the most common and important in mechanical engineering. As part of this work, an analysis of existing approaches to the optimization of technological processes was carried out, their shortcomings were identified, and a new methodology based on weighted multi-criteria analysis was proposed.

1. Research methodology

1.1 Selection of criteria

To solve this problem, a method based on multi-criteria analysis was developed. The essence of the method is to find the optimal solution that will be the best in terms of several criteria simultaneously.

The following criteria were selected for this study:

1. Minimizing processing time (Tpro):

$$Tpro = n\cdot f_z\cdot L\cdot i \tag{1}$$

where L - length of the surface being processed;
i - number of passes;
n - spindle rotation speed;
f_z - feed.

2. Minimizing surface roughness (Ra):

$$Ra = C\cdot f_{zx}\cdot v_{cy} \tag{2}$$

where C,x,y - empirical coefficients;
v_c – cutting speed.

3. Maximizing tool resistance (Tc):

$$Tc = v_{cm}\cdot f_{zn}\cdot Cv \tag{3}$$

where Cv,m,n - коэффициенты, зависящие от материала инструмента и заготовки.

The goal is to find a combination of parameters (vc, fz, ap) that will be optimal according to all three criteria.

1.2 Stages of the parameter optimization methodology

The methodology includes the following stages, as shown in Figure 1.

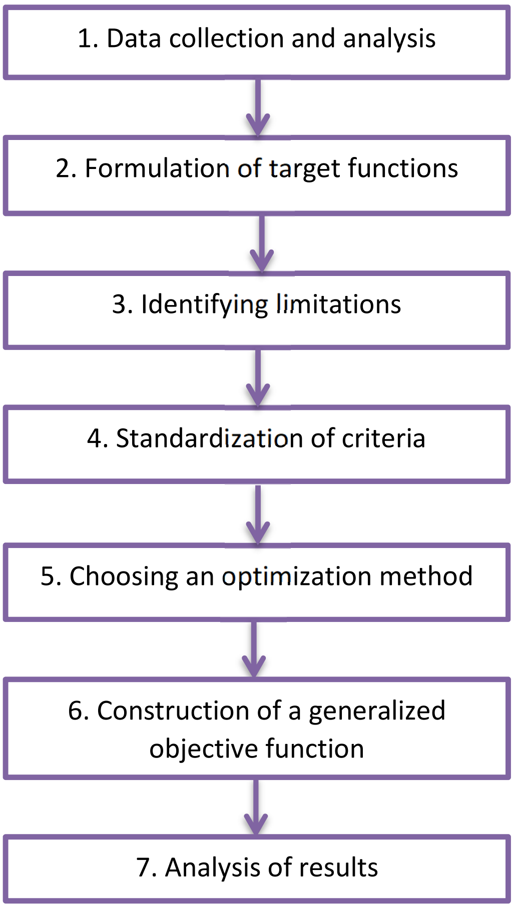

Fig. 1. – Stages of the methodology for optimizing mechanical processing parameters

During the data collection and analysis stage, information is gathered on materials, tools, equipment, and quality requirements. When forming target functions, mathematical models are created for each of the three criteria. It is also important to impose restrictions on variable parameters (vc, fz, ap) based on the technical characteristics of the equipment and tools [17]. For example, maximum spindle speed, maximum feed rate, etc. At the criterion normalization stage, all criteria must be converted to a dimensionless form, since they have different dimensions and ranges of values [18]. This allows them to be compared with each other. After standardizing the criteria, it is necessary to select an optimization method. To solve the problem of multi-criteria optimization of hole processing, the weight coefficient method was chosen [19]. This method allows each criterion to be assigned a certain weight (significance) depending on production priorities. For example, if speed is most important, the weight coefficient for processing time (Tpro) will be higher.

When constructing the generalized objective function, the normalized criteria were combined into a single function, taking into account the weighting coefficients:

$$F_{gen} = w_1 \cdot \frac{T_{pro}}{pro} + w_2 \cdot \frac{Ra}{Ra_{min}} + w_3 \cdot \left(1 - \frac{T_c}{T_{cmax}}\right) \tag{4}$$

where w_1,w_2,w_3 - weight coefficients, the sum of which equals 1;

T_{pro} – processing time;
T_{promin} – minimum processing time;
Ra – roughness;
Ra_{min} – minimum roughness.

At the stage of solving the optimization problem, the minimum of the generalized objective function was sought using the gradient descent method [20].

2. Results and discussion

A specific example was chosen to demonstrate how the method works: drilling a hole with a diameter of 10 mm and a length of 65 mm in a 45 steel part. P6M5 high-speed steel drill bit was used for mechanical processing of the holes. The resulting roughness of the machined surface was Ra 1.6.

The initial data for the calculation are given in Table 1.

Table 1. Initial data for optimizing the mechanical processing of holes

Parametr	Value
Cutting speed, v_c	from 10 to 30 m/min
Feed rate, f_z	from 0.1 to 0.3 mm/rev
Cutting depth, a_p	from 1 to 5 mm
Weight coefficients: w_1 (time) w_2 (roughness) w_3 (resistance)	 0.5 0.3 0.2

Based on empirical formulas and constraints, dependency graphs were constructed and an optimal solution was found that minimizes the generalized objective function. The optimization process for the mechanical processing of holes by drilling is shown in Figure 2.

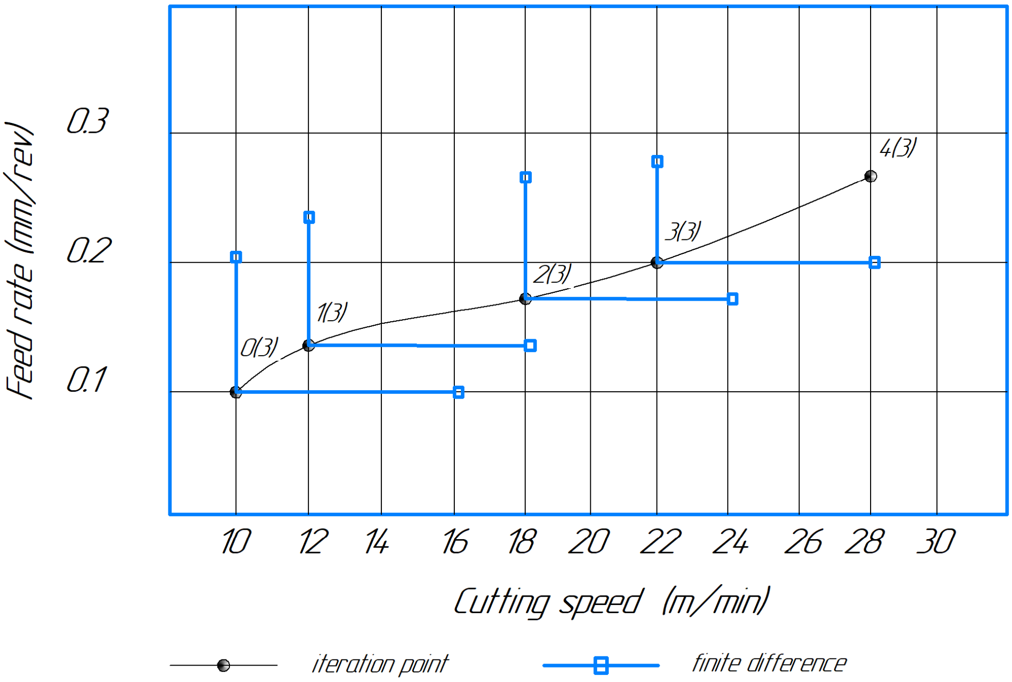

Fig. 2. Optimization of cutting parameters during mechanical processing of a hole

Based on the graph presented, which illustrates the optimization of drilling parameters, it is possible to trace the relationship between cutting speed (vc) and feed rate (fz) at each iteration.

The graph shows how the system searches for the best combination of parameters during the optimization process. The starting point, designated as iteration 0, corresponds to a cutting speed of 10 m/min and a feed rate of 0.1 mm/rev. Then, at each subsequent iteration (1, 2, 3, and 4), the parameters gradually change.

As a result, the optimal parameters were achieved in the fourth iteration, since the final difference between the parameters under consideration is minimal. This point corresponds to the following values: the cutting speed (vc) is 22 m/min, and the feed rate (fz) is 0.2 mm/rev.

The graph (Figure 3) shows that with each iteration, the processing time (green line) decreases. For example, at iteration 0, the time was 37.9 seconds, and at iteration 4, it was 28.7 seconds. This confirms that the optimization process succeeded in reducing the time, which is one of the goals of the methodology.

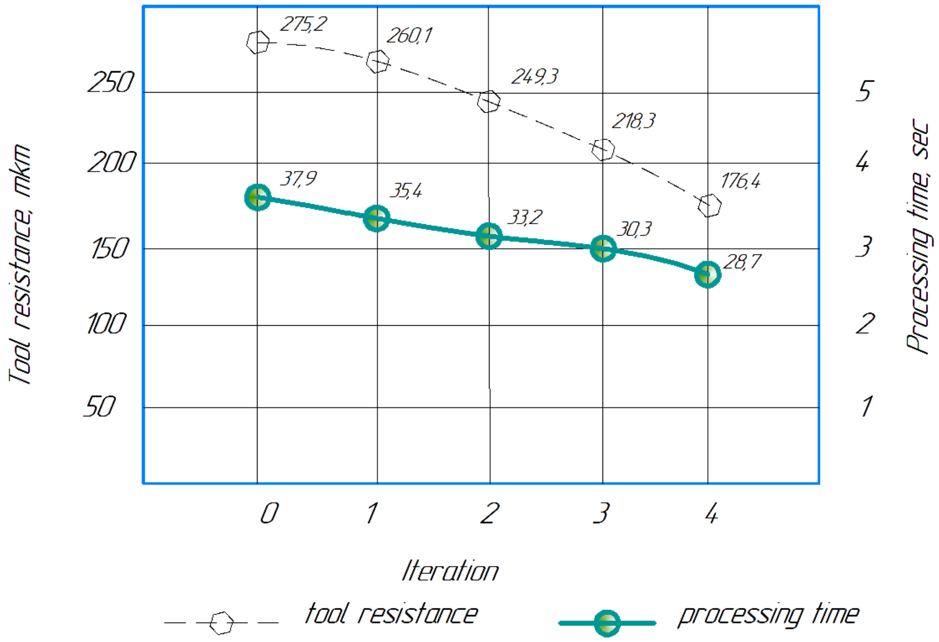

Fig. 3. Dependence of tool resistance and processing time in each iteration

At the same time, the tool's durability (dashed line) also decreases, but not as much as if the optimization had been performed only in terms of time. At iteration 0, the durability was 275.2 µm, and at iteration 4, it was 176.4 µm. This result demonstrates that the methodology has found a compromise solution that reduces processing time without completely sacrificing tool durability.

The following parameters were recognized as optimal:

- v_c = 22 m/min;
- f_z = 0.2 mm/rev;
- a_p = 4 mm.

These parameters achieve a compromise between processing time, tool durability, and surface quality, which is the best solution for these conditions.

The results showed that the proposed method allows finding optimal cutting parameters that differ significantly from those that would be selected when optimizing according to a single criterion. For example, when optimizing only for time, the cutting speed would be maximum, which would lead to rapid tool wear. When optimizing only for quality, the speed would be minimum, which would lead to a significant increase in processing time. Thus, a multi-criteria approach allows finding a balanced and effective solution.

Conclusions

The study showed that traditional optimization methods focused on a single criterion lead to compromises that worsen other important indicators. For example, increasing the cutting speed to reduce processing time leads to rapid tool wear. Conversely, lowering parameters to improve surface quality significantly increases processing time and production costs. The proposed approach solves this problem by finding a balanced and effective solution.

The developed method for optimizing material flow parameters based on multi-criteria analysis has proven its effectiveness in the example of a technological operation for machining holes. It allows finding the optimal cutting parameters that take into account not only the processing time, but also the surface quality and tool durability.

Main conclusions:

- multi-criteria analysis is an effective tool for solving complex optimization problems in mechanical engineering;
- the use of weighting coefficients allows adapting the methodology to specific production priorities;
- the methodology can be scaled to optimize more complex technological processes, including turning, milling, and grinding.

The next step in the research will be to develop software to automate calculations and implement the methodology in real production.

Acknowledgements

This research is funded by the Committee of Science of the Ministry of Science and Higher Education of the Republic of Kazakhstan (grant under the theme IRN AP23490796 “Development of digital models of the production process based on multi-criteria analysis of BigData management within the framework of technological preparation of production of machine-building enterprises” (2024 - 2026).

References

[1] Nurzhanova O., Zharkevich O., Berg A., Zhukova A., Mussayev M, Buzauova T., Abdugaliyeva G., Shakhatova A. Evaluation of the Structural Strength of a Prefabricated Milling Cutter with Replaceable inserts During Machining // Material and Mechanical Engineering Technology, №4, 2023. – P. 10 - 17
[2] Sikhimbaev, M.R., Sherov, K.T., Zharkevich, O.M., Sherov, A.K., Tkachyova, Y.O. Experimental studies of stabilization of boring cutter form - building top oscillation //Journal of Vibroengineering, 2012, 14(2), P. 661–670.
[3] Fundamentals of Manufacturing Engineering Using Digital Visualization. Chapter: Machining Methods. - 2024 – 234 p.
[4] Erçetin A., Aslantas K., Özgün Ö., Perçin M., Patel G. C. M. Optimization of Machining Parameters to Minimize Cutting Forces and Surface Roughness in Micro-Milling of Mg13Sn Alloy //Micromachines 14(8), 1590, 2023
[5] Pollák M., Kočiško M., Petrus J., Grozav S.D., Ceclan V. Research into the Impact of Spindle Speed and Feed Rate Changes on the Life of a Deep-Drilling Technology Tool //Machines, 10(4), 268, 2022
[6] Bondor P., Rusu D.O., Voina I. D., Contiu G., Popa M. S. Influence of Variation of Cutting Speed on Wear, Cutting Forces and Tool Temperature during Performance Drilling //Technical Gazette 30, 1, 2023, 354-360
[7] Sedlak J., Zouhar J., Kolomy S., Slany M., Necesanek E. Effect of high-speed steel screw drill geometry on cutting performance when machining austenitic stainless steel //Scientific Reports, volume 13, 9233, 2023
[8] Kali´nski K.J., Galewski M.A., Mazur M.R., Morawska S. N. An Improved Method of Minimizing Tool Vibration during Boring Holes in Large-Size Structures //Materials, 2021, 14, 4491
[9] Qehaja N., Jakupi K., Bunjaku A., Bruçi M., Osmani H. Effect of Machining Parameters and Machining Time on Surface Roughness in Dry Turning Process //Procedia Engineering, 100, 2015. – P. 135 – 140
[10] Hassen M., Jallouli I. Krichen A. Advanced analysis for the countersinking process, International Journal of Advanced Manufacturing Technology, Volume 90, 2017. - P.3473–3481
[11] Rosa V. A. O., Silva M.B., Arantes L. J. Investigation of the Reaming Operation of Holes Machined in Sintered Carbon-Iron Pistons //World Tribology Congress, 2013, Torino, Italy, September 8 – 13, 2013. – P.1-4
[12] Alagarsamy V., Sagayaraj S. A.V., Raveendran P. International Journal of Engineering Research and General Science Volume 4, Issue 2, March-April, 2016
[13] Senthil K.S., Selva K.V.K, Rohinth.J, Renga R.S R. Optimization of drilling parameters //International Journal of Engineering, Science and Mathematics, Vol. 7 Issue4, April 2018, P.196 - 211
[14] Deepak S. S. K. Cutting Speed and Feed Rate Optimization for Minimizing Production Time of Turning Process //International Journal of Modern Engineering Research, Vol.2, Issue.5, 2012, P.3398-3401
[15] Naife A. Talib Studying the effect of cutting speed and feedrate on tool life in the turning processes //Diyala Journal of Engineering Sciences, 22-23 December, 2010, P. 181-194
[16] Sherov K., Mussayev M., Usserbayev M., .Bekzhanov Y., Myrzakhmet, B. Investigation of the method of thermal friction turn-milling of high strength materials // Journal of Applied Engineering Science, 2022, 20(1), P. 13–18
[17] Guiotoko E.H., Aoyama H., Sano N. Optimization of hole making processes considering machining time and machining accuracy // Journal of Advanced Mechanical Design, Systems, and Manufacturing, 2017, Volume 11, Issue 4. P. 1 - 13
[18] Vafaei N., Ribeiro R.A, Camarinha-Matos L.M. Importance of Data Normalization in Decision Making: case study with TOPSIS method //Nazanin Vafaei, Rita A Ribeiro, Luis M. Camarinha-Matos, Serbia, May 27-29, 2015
[19] Zhetessova G.S., Zharkevich O.M., Shakhatova A.T., Khrustaleva I.N., Shkodyrev V.P. Additive Optimization Method for Choosing CNC Machines for Technological Preparation of Machine-Building Production // Material and Mechanical Engineering Technology, №3, 2024. – P.32 – 37
[20] Tapkir A. A Comprehensive Overview of Gradient Descent and its Optimization Algorithms //IARJSET, 10(11), 2023

Information of the authors

Zhetessova Gulnara Santayevna, d.t.s., professor, Abylkas Saginov Karaganda Technical University
e-mail: zhetesova@mail.ru

Zharkevich Olga Mikhailovna, c.t.s., professor, Abylkas Saginov Karaganda Technical University
e-mail: zharkevich82@mail.ru

Kozhanov Murat Galiaskarovich, m.t.s, head of department, Abylkas Saginov Karaganda Technical University
e-mail: spark.2011@mail.ru

Khrustaleva Irina Nikolayevna, c.t.s., docent, Peter the Great St. Petersburg Polytechnic University
e-mail: irina.khrustaleva@mail.ru

DOI 10.52209/2706-977X_2025_3_90 IRSTI 81.09.03 UDC 537.226

Structures, Dielectric Constant, Impedance and Electrical Conductivity of Carbon/Cu_2O Nanowire (C/CONW) Composite Electrode Derived from Self-Adhesive Carbon Grain from Pre-Carbonized Date Palm leaves (Phoenix Dactylifera L.), Carbon Black and Cu Powder

Abbas F.M.[1*], Khalofa A.[2], Abbas H.M.[3], Al-Ahamd Z.A.[3], Abdelrahman A. E.[4]
[1*]King Khalid University, Abha, Saudi Arabia
[2]Ministry of Science Higher Education and Scientific Research, Saudi Arabia
[3]National for Research Remote Sensing Authority, Khartoum, Sudan
[4]Act Center for Research, Singa, Sudan
*corresponding author

Abstract. Composite electrodes, especially carbon-metal oxide composites, hold promising potential in numerous industrial applications such as supercapacitors and electrochemical energy storage. This study focuses on developing high-performance composite electrodes utilizing pre-carbonized date palm leaves, carbon black and copper powder. The main objective of this research is to enhance the mechanical and electrical properties of composite electrodes while exploring the potential of agricultural waste utilization. The methodology involves ball-milling pre-carbonized date palm leaves (PCDPLs), followed by manual mixing with carbon black (CB) and copper (Cu) powder, pressing into pellets, and carbonization at 1000°C in a nitrogen environment. X-ray diffraction (XRD) analysis confirmed the polycrystalline structure of the composite electrode with EDXD confirming the presence of Cu_2O nanowires. Frequency-dependent dielectric parameters, impedance and electrical conductivity were analyzed utilizing the Cole–Cole plot in a range of (0-8) MHz. Results demonstrate improved crystallinity and performance of the composite electrodes, emphasizing the potential of utilizing agricultural waste for sustainable, high-performance electrode materials. This research highlights the importance of utilizing agricultural waste for developing advanced composite electrodes with enhanced performance capabilities, contributing to sustainable waste management and industrial applications in energy storage technologies.

Keywords: carbon/copper oxide composites, X-ray diffraction, pre-carbonized date palm leaves, Cu_2O nanowires, Cole-Cole plot.

Introduction

Composite electrodes or carbon-metal oxide electrodes are extensively developed employing distinct methodologies to improve industrial applications. For instance, carbon/metal oxide is a class of composite electrodes that has improved electrical properties and mechanical performances by incorporating a metal oxide compound. These types of composite electrodes have been utilized for transmission and distribution of electric power such as super capacitors [1] and electrochemical energy storage [2]. These are further developed by incorporating nanostructure fillers such as nanoparticles, nanowires and nanotube compounds to enhance the composite electrode mechanical performance and chemical stability [3]. It has also been revealed that the nano-structuring of the electrode materials has a positive effect on the electrode performance [4].

Currently, most commercial supercapacitor electrodes are manufactured from carbon due to its low cost, excellent corrosion resistance, superior cyclic stability and long service life, as the electrode does not undergo chemical alteration during charge/discharge cycles [5]. However, the maximum capacitance is restricted by the active electrode surface area and the pore size distribution [6].

Copper oxide (Cu2O) nanowires are widely utilized as p-type semiconductor compounds in numerous applications, including the degradation of methyl orange [7], super capacitors [8], heterojunction solar cells [9], biomedical fields [10] and surface coatings [11]. Depending on the preparation method and the proportions of constituents utilized, the copper oxide CuO phase may be accompanied by other complex structures, primarily Cu_2O and Cu4O3. Among these, CuO and Cu_2O are the most stable compounds. The synthesis method for Cu_2O nanostructure has been extensively reviewed in numerous researches which cover both physical and chemical methodologies [12-14].

Moreover, the carbon material in these types of composites can be prepared from numerous carbonaceous substances such as biomass material and agricultural waste material such as oil palm empty fruit bunch [15], olive stone [16], lignocellulose [17] and date palm leaves [18, 19]. In the present work, the raw carbon precursor is date palm leaves. Due to its high carbon content, low cost and low ash. Date palm leaves has been examined to produce solid carbon and activated carbon material with a high surface area and good electrical and mechanical properties [19]. Additionally, it has been revealed that pre-carbonized at low heat treatment and the milling process is very important to enhance the self-adhesive properties of the carbon produced.

Furthermore, the Cole–Cole plot proposed by Havriliak, Negami's and Debye is an analytical method utilized to characterize composite electrode. It illustrates the frequency dependence of impedance, dielectric parameters and conductivity. The Havriliak, Negami's and Debye explained the skewed and arcuate shape observed in graphical configuration of composite materials [20]. For instance, the dielectric constant (both real and imaginary parts) and the dielectric loss tangent are established methodologies for evaluating the conductivity behavior of electrode materials. A dielectric loss tangent greater than 1 indicates high conductivity whereas a tangent less than 1 indicates non-conductive behavior [21]. It has been observed that the Cole–Cole plots of various electrodes, metal oxide and polymer materials tend to exhibit similar shapes [22].

Despite extensive development in the synthesis of composite electrodes, there remains an urgent need for optimizing the mechanical performance, chemical stability and electrical properties of these materials. This research emphasizes on the potential of incorporating nanostructure fillers to enhance electrode properties and explore the benefits of utilizing carbon derived from agricultural waste such as date palm leaves. The main objective is to synthesize composite electrode utilizing self-adhesive carbon grains from pre-carbonized date palm leaves, carbon black and copper powder. This research primarily focuses on the characterization of the crystalline structures and frequency-dependent properties such as dielectric constant, impedance and electrical conductivity of the composite electrode and to explore its potential applications thereby contributing to the field of advanced composite electrodes with improved performance capabilities.

The significance of this research lies in its innovative strategy of developing composite electrodes by utilizing self-adhesive carbon grains derived from pre-carbonized date palm leaves, carbon black and copper powder. By exploring the underutilized potential of agricultural waste, this research not only improves the mechanical and electrical properties of composite electrodes but also offers a sustainable solution to waste management. The incorporation of nanostructure fillers such as Cu_2O nanowires is expected to significantly improve the dielectric constant, impedance and electrical conductivity of the electrodes, thereby advancing their performance in industrial applications such as super capacitors and electrochemical energy storage [23]. This research also characterizes the frequency-dependent properties of these novel composite materials, providing valuable insights for further development and application in advanced material sciences.

1. Methodology

1.1 Pre-carbonized Date Palm leaves (PCDPLs)

The raw material that is the date palm leaves (Phoenix dactylifera L) were sectioned into small pieces and thoroughly washed with hot water. These pieces were subsequently dried at 100°C for two hours. The dried leaves then underwent pre-carbonization in a vacuum chamber at 280°C for 4 hours, leading to shrinkage and mass loss due to the expulsion of tars, oxygen, carbon monoxide and other volatiles components [24]. The pre-carbonized date palm leaves (PCDPL) were then ball-milled into fine carbon grain powder to enhance their self-adhesive properties.

1.2 Composite Electrode Preparation

The C/Cu_2O nanowire composite electrodes were synthesized by combining PCDPLs at concentrations of 50%, 60%, 70%, 80% and 90% with commercial carbon black at concentrations of 6%, 12%, 18%, 24% and 30% and copper powder (99.6% purity) at concentrations of 4%, 8%, 12%, 16% and 20%. The components were manually mixed and then stored in a plastic container. One gram of the resulting mixture was pressed into pellets by applying 12 metric tons of pressure without the addition of any binder. All grain pellets exhibited excellent self-adhesive properties before being carbonized at 1000°C in a nitrogen environment employing a multistep heating process, as described by [18].

Following carbonization, the composite electrode produced were thoroughly washed with hot distilled water to remove impurities until a pH of 6 was achieved, then dried in an oven at 100ºC for four hours. Measurement of the pellet dimension was carried out utilizing a micrometer screw gauge and the bulk density was determined by dividing the mass of the sample by its volume with results averaged over five replicates for each sample.

1.3 X-Ray Diffraction (XRD)

An X-ray diffraction (XRD) experiment was conducted on carbon composite pellets by utilizing Rigaku D/Max-X-ray diffractometer with Cu-Kα radiation. The scanning was conducted at a rate 5 seconds per 0.1° step size, covering a diffraction angle (2θ) range from 20° to 70°.

1.4 Energy Dispersions X-ray Diffraction (EDXD)

Energy dispersion X-ray diffraction (EDXD) was employed on selected sample to identify the structure of Cu_2O nanowire.

1.5 Dielectric Constants

The frequency dependent dielectric parameters, specifically the Real part (*Er*) and imaginary part (*Ei*) were analyzed utilizing the Cole–Cole plot. The real and the imaginary parts were determined as stated by [21, 25]

$$Er(\omega) = E_o + r^{\frac{-A}{2}}(E_o - E_\infty)\, cosA\theta \tag{1}$$

$$Ei(\omega) = r^{\frac{-A}{2}}(E_o - E_\infty)\, SinA\theta \tag{2}$$

$$TanA\theta = \frac{Ei(\omega)}{Er(\omega) - E_o} \tag{3}$$

$$\text{Phase } (\theta) = \frac{1}{A} Tan^{-1}\left(\frac{Ei(\omega)}{(Er(\omega)-Eo)}\right) \quad (4)$$

$$\text{Dielectric loss Tangent} = \frac{Ei(\omega)}{Er(\omega)} \quad (5)$$

where r is the constant and A is the angular frequency.

1.6 Impedance (Z)

The frequency dependence of impedance and conductivity both the real part and the imaginary part was measured employing an e-Agilent E4980A precision LRC meter (inductance [L], capacitance [C], and resistance [R]) cell devise. This analysis utilized the Cole-Cole plot to refer to Debye behaviours as done in previous researches [21, 26]. The measurements were performed utilizing option 001 (DC Measurements) by applying voltages from 0 to 5 V with a frequency range of 103MHz to 8x 10^5 Hz to characterize the impedance and conductivity behavior of the composite electrode. Impedance which depends on the frequency (ω) of the source, is described as the combination of the real part (Z') and the imaginary part (Z") as stated by [27].

$$Z = Z' + iZ'' \quad (6)$$

$$Z' = \frac{R_p}{1+(\omega R_p C_p)^2} \quad (7)$$

$$Z'' = \frac{\omega R^2_p C_p}{1+(\omega R_p C_p)^2} \quad (8)$$

The value of the Cp can be given from equations (2) and (3) at medium and lower frequency range as

$$C_p = \frac{Z''}{Z' R_p} \quad (9)$$

1.7 Electrical Conductivity (EC)

The frequency-dependent analysis of conductivity, including the real part (EC(r)) and imaginary part (EC(i)) was conducted utilizing the Cole-Cole plot to refer to Debye behaviors, following the approach outlined by [21]. An electrical component with option 001 (DC Measurements) was employed, applying voltages ranging from 0–5 volts and frequencies ranging from 0 MHz –6.5 MHz to analyze the conductivity behavior of the produced electrode. The AC conductivity is defined as

$$EC(AC) = Ec(DC) + A(\omega)^s \quad (10)$$

where DC is the direct current, $\omega = 2\pi f$, f is the frequency and A is a constant.

2.Result and Discussion

2.1 Composite Electrode Properties

Table 1 demonstrates data on the average weight and bulk density of composite electrode (C/Cu_2O) nanowire. The bulk density exhibits a slight increase from 1.303 g/cm^3 to 2.26 g/cm^3 with the augmentation CB+Cu % content. The density of the carbon composite pellets is approximately 50% of that of pure-graphite structure and falls within the range of densities for carbon filament electrodes (1.77 g/cm^3) and glassy carbon (Sigradur K) (1.540 g/cm^3), indicating that the composite has achieved substantial density. Additionally, the table also reveals that the yield of the composite electrode improves with increasing CB+Cu % content. This improvement is attributed to a reduction in non-carbon content and volatile components which contributes to the enhanced bulk density of the product.

Table 2. The raw composition concentrations data before and after carbonization

Raw Data Before Carbonization				Data After Carbonization		
PCDPLs %	CB %	Cu %	Weigh	Weight	Electrode	Black Density
			(g)	(g)	Yield	(g/cm^3)
90%	6%	4%	1.00	0.48±0.01	48%	1.30±0.03
80%	12%	8%	1.00	0.53±0.03	53%	1.38±0.02
70%	18%	12%	1.00	0.56±0.00	56%	1.86±0.05
60%	24%	16%	1.00	0.59±0.01	59%	2.02±0.11
50%	30%	20%	1.00	0.62±0.01	62%	2.25±0.01
Carbon filament electrode	-	-	-	-	-	1.77
Graphite	-	-	-	-	-	2.26
Sigradur K	-	-	-	-	-	1.540
			(g)	(g)	Yield	(g/cm^3)
90%	6%	4%	1.00	0.48±0.01	48%	1.30±0.03
80%	12%	8%	1.00	0.53±0.03	53%	1.38±0.02
70%	18%	12%	1.00	0.56±0.00	56%	1.86±0.05
60%	24%	16%	1.00	0.59±0.01	59%	2.02±0.11
50%	30%	20%	1.00	0.62±0.01	62%	2.25±0.01
Carbon filament electrode	-	-	-	-	-	1.77
Graphite	-	-	-	-	-	2.26
Sigradur K	-	-	-	-	-	1.540

2.2 X-ray Diffraction

Figure 1 illustrates the X-ray diffraction pattern for composite electrode pellets exhibiting strong peaks at reflection planes (002), (110), (111), (100), (200) and (111) corresponding to diffraction angles (2θ) of 25.9°, 28.7°, 36.4, 39.69°, 43.9, 50°.32 and 53.25° respectively. This pattern indicates a polycrystalline structure. It is evidently proven from figure 1 that the composite electrode produced enhances the crystalline structure as distinguished by three prominent sharp peaks at (002), (100) and (111) characteristic of a graphitic-like structure. Additionally, strong diffraction peaks (110), (111), (200) and (211) represent the dominant structure of Cu_2O in the composite.

Moreover, the X-ray spectrum analysis indicates that an increase in the percentage of (CB+Cu) % content leads to the enhancement in the crystalline structure of the produced composite electrode. This effect is especially pronounced in the composite electrode sample prepared with a 50% concentration which exhibits a structure of pure-graphitic as evidenced by the X-ray diffraction spectrum depicted in Figure 1. Furthermore, these findings correspond with the bulk density measurement as demonstrated in Table 1, which shows equivalence to that of pure graphite.

These observations support the concept that the combination of (Cu+ CB) with PCDPLs promotes a more graphitic structure, reducing the graphitization temperature up to 1000°C by employing multiple heating profiles in nitrogen environments. This reduction in graphitization temperature is expected to yield economic benefits and provides an alternative approach to minimize graphite production costs.

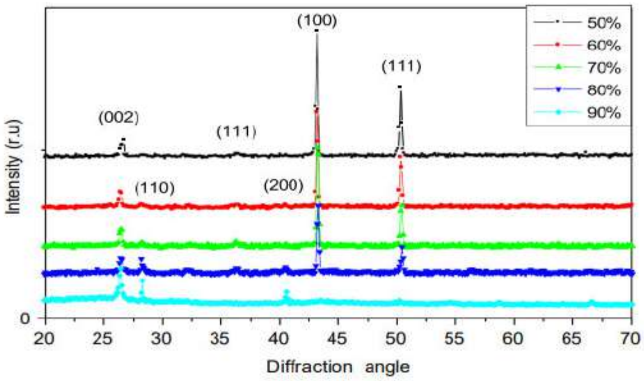

Fig. 8. - X-ray diffraction profiles of the C/Cu_2O nanowire composite electrode.

2.3 EDXD

Figure 2 illustrates the visual representation of the EDXD electron image exhibiting a specific composite electrode treated with 70% PCDPLs. It reveals the vertical growth of Cu_2O nanowires on the Cu/Cu_2O cluster substrate synthesized through a pyrolysis mechanism, exhibiting varying orientations.

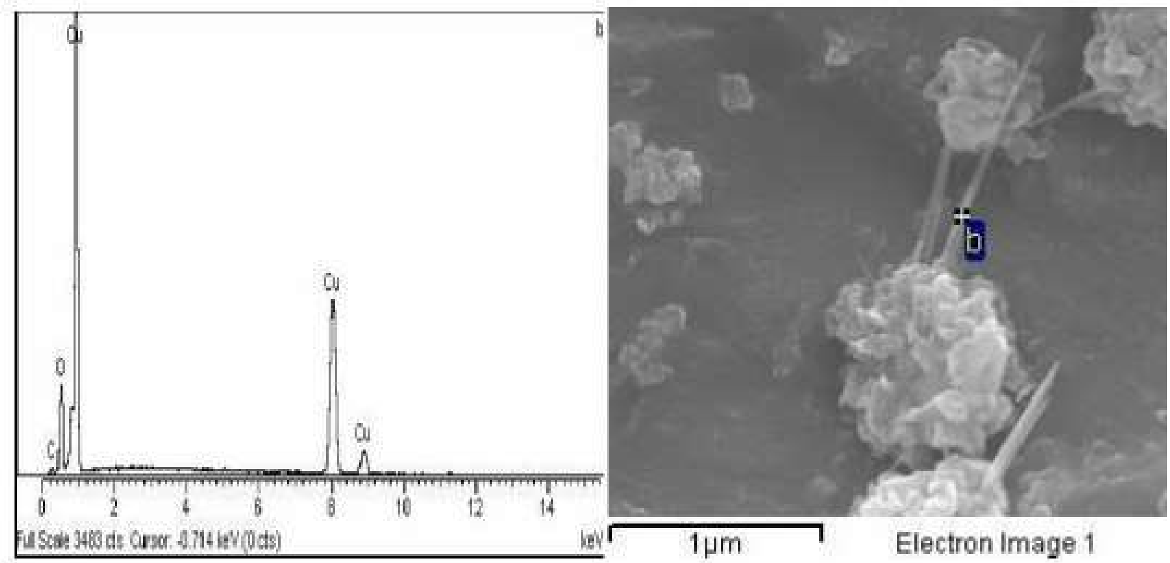

Fig. 2. - EDXD electron image of the selected composite electrode

2.4 Impedance

The widely recognized Cole–Cole plot originally proposed by Havriliak and Negami's through analytical methods explained the graphical configuration and arcuate shape observed in the medium and low frequency range (103MHz – 8x105Hz) of the composite electrode. However, the presence of a semicircular sketch was not detected within this frequency range as illustrated in Figure 3. It is expected that the frequency ranges utilized are insufficient to fully capture the threshold dominance of the Havriliak and Negami's analytical behavior.

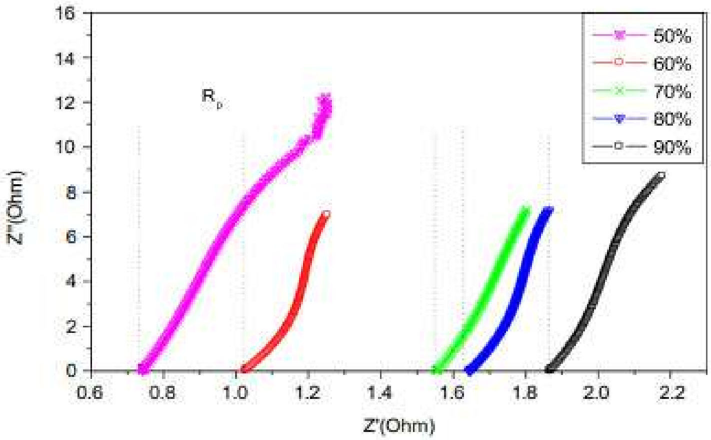

Fig. 9. - Cole-Cole Plots illustrating the frequency-dependent impedance, with the imaginary part (Z") plotted against the real part (Z') for composite samples ranging in concentration from 50% to 90%.

Additionally, the impedance bridge data demonstrated in Table 2 highlights the values of Rp (polarization resistance) and the maximum Z" (imaginary part) and Z' (real part) at medium and lower frequencies. The data from the table 2 also reveals that the Z" value for the 90% concentration and Z' value for the 50% concentration are higher as compared to other electrode compositions, suggesting an enhancement in Z' with an increase in (CB+Cu) % content.

Table 3. Impedance results plotted in a Cole-Cole plot as a function of frequency

Composite Electrode Cell	Rp (Ohm)	Z"(max) (Ohm)	Z'(max) (Ohm)
90%	0.735	12.30	1.250
80%	1.021	7.00	1.250
70%	1.550	7.33	1.800
60%	1.630	7.19	1.870
50%	1.860	8.80	2.175

Furthermore, it is evident from the data that the Cole–Cole plots observed in numerous carbon electrodes and metal oxide exhibited that all these plots have approximately similar shape as reported by [28].

2.5 Electrical Conductivity (EC)

Figures 4 and 5 illustrates the frequency-dependent variation of electrical conductivity represented by the real part (EC(r)) and imaginary part (EC(i)) respectively, composite electrode samples treated with different percentages of PCDPLs (50%, 60%, 70% and 80%) (298 K). Notably, the real part exhibits a marked increase at lower frequencies followed by a decrease at higher frequencies, indicating a characteristic behavior. The intercept on the y-axis represents the DC resistance as noted by [29]. On the Contrary, the imaginary part exhibits a significant increase at lower frequencies and a subsequent decrease at higher frequencies.

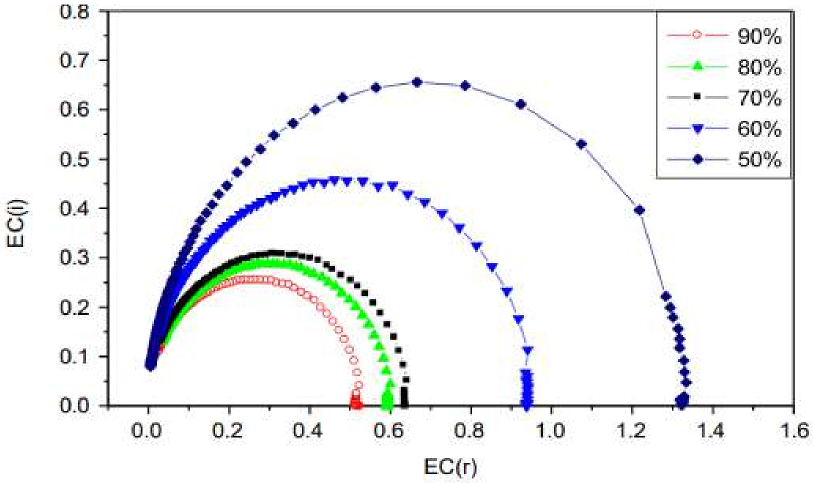

Fig. 10. - The Cole-Cole plots of frequency dependence impedance (imaginary part Z'' versus the real part Z') for composite samples treated with varying percentages of PCDPL, ranging from 50% to 90%.

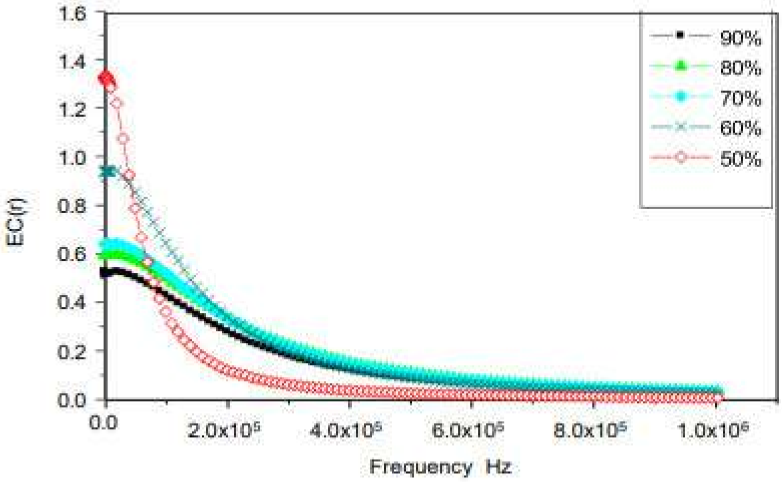

Fig. 11. - Frequency-dependent variation of electrical conductivity represented by the real part (EC(r)) of composite electrode samples treated with varying percentages of PCDPL, ranging from 50% to 90%.

Additionally, the Cole-Cole graphical plot of the imaginary part (EC(i)) is plotted against the real part at (EC(r)) as a function of frequency [30]. This plot reveals the semi-circular patterns with a narrow threshold range from 0 to 1.32 as observed in Figure 6 and demonstrated in Table 2. Figure 6 explains the theoretical behavior predicted by the Debye method as discussed by [21]. Furthermore, it is observed that the semicircular sketch patterns increase with higher percentages of (CB+Cu), indicating a rise in electrical conductivity with increasing (CB+Cu) content although the conductivity values remain relatively low.

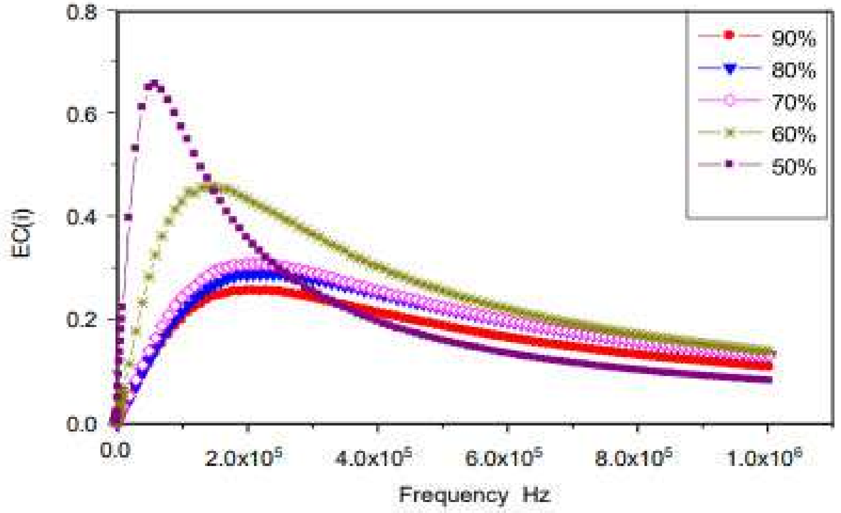

Fig. 12. - Frequency-dependent variation of electrical conductivity represented by the imaginary part (EC(i)) of composite electrode samples treated with varying percentages of PCDPL, ranging from 50% to 90%.

These effects are expected to the vertical growth of Cu_2O nanowires in varying orientations on the surface of the composite electrode, as illustrated in Figure 2. This vertical growth is expected to hinder the transfer of mobility carriers, consequently reducing the electrical conductivity behavior of the produced composite electrode, as suggested by [26]. Most Probably, this behavior is due to the addition of CB and Cu as rigid fillers to the PCDPLs, leading to enhanced electrical properties of the composite product and also by enhancing occupational mobility carrier in the electrode contact points.

Moreover, table 3 demonstrates the relationship between the percentage of composite electrode cell and the Cole-Cole plot of conductivity behavior as a function of frequency. It reveals the range of frequencies over which the imaginary electrical conductivity (EC(i)) increases then decreases for different composite electrode cell percentages. The table suggests that the frequency range over which this behavior is observed increases as the percentage of composite electrode cell increases.

Table 4. Cole-Cole plot of Conductivity Behavior as a Function of Frequency

Composite electrode cell	Semi-circular sketch dominos (EC (r))	EC(i) max
90%	(0 - 0.520)	0.255
80%	(0 - 0.591)	0.287
70%	(0 - 0.642)	0.303
60%	(0 - 0.938)	0.453
50%	(0 - 1.32)	0.644

Conclusion

A Carbon/Cu_2O nanowire composite electrode has been successfully developed utilizing pre-carbonized date palm leaves, carbon black and Cu powder, exhibiting improved mechanical and electrical properties. XRD analysis revealed that all CCOC pellets possess a polycrystalline structure while EDXD results confirmed the Cu_2O structure as nanowire. The combination of three materials, i.e. biomass PCDPLs + CB and Cu results in nanoparticle-composite carbon with significantly improved crystallinity. The incorporation of Cu_2O nanowires enhanced the dielectric constant, impedance and conductivity. Cole-Cole plots revealed consistent frequency-dependent behavior across distinct composite compositions. This research emphasizes on the potential of utilizing agricultural waste for developing advanced, high-performance composite electrodes for industrial applications, particularly in supercapacitors and electrochemical energy storage.

The study's limitations include a narrow frequency range for impedance analysis, potentially insufficient to fully capture the Havriliak and Negami’s behavior and the relatively low conductivity values due to the vertical growth of Cu_2O nanowires may hinder carrier mobility in the composite electrode. Additionally, the research also does not extensively explore the benefits of other metal oxides compared to Cu2O. Furthermore, the specific impact of each constituent (PCDPLs, CB, Cu) on the mechanical and electrical properties was not fully studied.

This study opens pathways for broader applications in renewable energy technologies, such as solar cells and fuel cells. The sustainable approach of utilizing agricultural waste could inspire further researches into other biomass-derived materials, promoting circular economy principles and cost-effective electrode manufacturing. Additionally, the improved dielectric properties and impedance behaviors of these composites may lead to advancements in electronic devices and sensors, providing a versatile platform for future innovations in various high-performance technological sectors.

Data Availability Statement: The datasets generated and/or analyzed during the current study are available from the corresponding author, Fatima Musbah Abbas, upon reasonable request.

Competing Interests: The authors have no relevant financial or non-financial interests to disclose.

Funding: The authors declare that no funds, grants, or other support were received during the preparation of this manuscript.

Author Contributions: All authors contributed to the study conception and design. Material preparation, data collection and analysis were performed by [Fatima Musbah Abbas], [Selma Elsheikh Abdelrahman] and [Abubaker Elsheikh Abdelrahman]. The first draft of the manuscript was written by [Fatima Musbah Abbas] and all authors commented on previous versions of the manuscript. All authors read and approved the final manuscript.

Acknowledgements: The authors extend their appreciation to Deanship of Scientific Research at King Khalid University for funding this research through General Research Project under grant number (RGP.1/127/44-1444).

References

[1] S. Saini, P. Chand, and A. Joshi, "Biomass derived carbon for supercapacitor applications," *Journal of Energy Storage,* vol. 39, p. 102646, 2021.

[2] R. Liu *et al.*, "Carbon coating on metal oxide materials for electrochemical energy storage," *Nanotechnology,* vol. 32, no. 50, p. 502004, 2021.

[3] A. Barra, C. Nunes, E. Ruiz-Hitzky, and P. Ferreira, "Green carbon nanostructures for functional composite materials," *International Journal of Molecular Sciences,* vol. 23, no. 3, p. 1848, 2022.

[4] R. Xu *et al.*, "Well-defined nanostructures for electrochemical energy conversion and storage," *Advanced Energy Materials,* vol. 11, no. 15, p. 2001537, 2021.

[5] Y. Wang *et al.*, "Recent progress in carbon-based materials for supercapacitor electrodes: a review," *Journal of Materials Science,* vol. 56, pp. 173-200, 2021.

[6] A. Elmouwahidi, E. Bailón-García, J. Castelo-Quibén, A. Pérez-Cadenas, F. Maldonado-Hódar, and F. Carrasco-Marín, "Carbon–TiO 2 composites as high-performance supercapacitor electrodes: synergistic effect between carbon and metal oxide phases," *Journal of Materials Chemistry A,* vol. 6, no. 2, pp. 633-644, 2018.

[7] Z. Xie *et al.*, "Effect of impurity in Cu 2 O nanowires on the degradation of methyl orange," *Journal of Materials Science: Materials in Electronics,* vol. 31, pp. 3817-3824, 2020.

[8] D. Majumdar and S. Ghosh, "Recent advancements of copper oxide based nanomaterials for supercapacitor applications," *Journal of Energy Storage,* vol. 34, p. 101995, 2021.

[9] C. Dumitru, V.-F. Muscurel, and L. Fara, "Cu2O layer analysis and optimization based on a metal-oxide tandem heterojunction solar cell," *Materials Today: Proceedings,* vol. 5, no. 8, pp. 15895-15901, 2018.

[10] N. Verma and N. Kumar, Synthesis and biomedical applications of copper oxide nanoparticles: an expanding horizon," *ACS biomaterials science & engineering,* vol. 5, no. 3, pp. 1170-1188, 2019.

[11] S. Masroor, "Basics of metal oxides: properties and applications," *Inorganic Anticorrosive Materials,* pp. 85-94, 2022.

[12] T. H. Tran *et al.*, Effect of annealing temperature on morphology and structure of CuO nanowires grown by thermal oxidation method, *Journal of Crystal Growth,* vol. 505, pp. 33-37, 2019.

[13] Z. Starowicz *et al.*, Materials studies of copper oxides obtained by low temperature oxidation of copper sheets," *Materials Science in Semiconductor Processing,* vol. 121, p. 105368, 2021.

[14] M. Košiček, J. Zavašnik, O. Baranov, B. Šetina Batič, and U. Cvelbar, "Understanding the growth of copper oxide nanowires and layers by thermal oxidation over a broad temperature range at atmospheric pressure," *Crystal Growth & Design,* vol. 22, no. 11, pp. 6656-6666, 2022.

[15] M. Ikhsan and R. Ramli, "Measurements and analysis of crystal structures of activated carbon of empty fruit bunch from oil palm biomass waste," in *Journal of Physics: Conference Series*, 2020, vol. 1528, no. 1: IOP Publishing, p. 012031.

[16] P. Ibeh, F. García-Mateos, J. Rosas, J. Rodríguez-Mirasol, and T. Cordero, "Activated carbon monoliths from lignocellulosic biomass waste for electrochemical applications," *Journal of the Taiwan Institute of Chemical Engineers,* vol. 97, pp. 480-488, 2019.

[17] V. Dhyani and T. Bhaskar, "A comprehensive review on the pyrolysis of lignocellulosic biomass," *Renewable energy,* vol. 129, pp. 695-716, 2018.

[18] F. M. Abbas, Z. A. Al Ahmad, R. O. E. Elgezouly, and A. E. Abdelrahman, "Characterization of carbon pellets prepared from date palm leaves (Phoenix dactylifera L.) by compression pressure: X-ray diffraction measurements and applications," 2022.

[19] A. E. Abdelrahman, F. M. Abbas, and A. K. Arof, "Crystallite Parameters, Amorphous Contents and Surface Functional Groups, Contents of Activated Carbon Prepared from KOH Treated Pre-Carbonized Date Palm Leaves (Phoenix dactylifera L.)," 2023.

[20] S. Bhattacharjee, A. Banerjee, N. Mazumder, K. Chanda, S. Sarkar, and K. K. Chattopadhyay, "Negative capacitance switching in size-modulated Fe_3O_4 nanoparticles with spontaneous non-stoichiometry: confronting its generalized origin in non-ferroelectric materials," *Nanoscale,* vol. 12, no. 3, pp. 1528-1540, 2020.

[21] R. Han, Y. Liu, J. Shi, G.-X. Chen, and Q. Li, "Enhanced dielectric properties and breakdown strength of polymer/carbon nanotube composites by coating an SrTiO3 layer," *e-Polymers,* vol. 21, no. 1, pp. 272-278, 2021.

[22] G. A. Khouqeer, B. A. El-Badry, and M. Zaki, "Improvement of the optical properties, dielectric behaviors and Cole-Cole plot of gamma-irradiated polyvinyl alcohol filled by nanostructured aluminum metal oxide," *Journal of Radiation Research and Applied Sciences,* vol. 17, no. 2, p. 100871, 2024.

[23] M. Harilal *et al.*, "Environment-modulated crystallization of Cu2O and CuO nanowires by electrospinning and their charge storage properties," *Langmuir,* vol. 34, no. 5, pp. 1873-1882, 2018.

[24] V. D. Vaibhav Dhyani and T. B. Thallada Bhaskar, "A comprehensive review on the pyrolysis of lignocellulosic biomass," 2018.

[25] K. Wilczyński, A. Wróblewska, A. Daniszewska, J. Krupka, M. Mrozowski, and M. Zdrojek, "Modulation of dielectric properties in low-loss polypropylene-based composites at GHz frequencies: theory and experiment," *Scientific Reports,* vol. 12, no. 1, p. 13104, 2022.

[26] N. Aguilo-Aguayo, T. Drozdzik, and T. Bechtold, "Impedance analysis of electrodes made of continuous carbon filaments in a 20 cm2 redox flow cell," *Journal of Electroanalytical Chemistry,* vol. 926, p. 116954, 2022.

[27] S. Demirezen and S. A. Yerişkin, "Frequency and voltage-dependent dielectric spectroscopy characterization of Al/(Coumarin-PVA)/p-Si structures," *Journal of Materials Science: Materials in Electronics,* vol. 32, pp. 25339-25349, 2021.

[28] K. Samatha, H. Vijeth, and R. Sagar, "Electrical and electrochemical properties of nanostructured Ni and Zn substituted Co_3O_4 spinels for thermistors and supercapacitor applications," *Journal of Energy Storage,* vol. 52, p. 104871, 2022.

[29] Y. Jiang, J. Huang, H. Ji, B. Wang, Z. Huang, and M. Soleimani, "Study on dual-frequency imaging of capacitively coupled electrical impedance tomography: Frequency optimization," *IEEE Transactions on Instrumentation and Measurement,* vol. 71, pp. 1-18, 2022.

[30] C. Y. Tan, N. Farhana, N. M. Saidi, S. Ramesh, and K. Ramesh, "Conductivity, dielectric studies and structural properties of P (VA-co-PE) and its application in dye sensitized solar cell," *Organic Electronics,* vol. 56, pp. 116-124, 2018.

Information of the authors

Abbas Fatima Musbah, PhD, professor, King Khalid University
e-mail: FatimaM.Abbas1@researchergroup.co

Khalofa Ahlam, professor, Ministry of Science Higher Education and Scientific Research
e-mail: ahlam_khalofa12@outlook.com

Abbas Hanan Musbah, PhD, professor, National for Research Remote Sensing Authority, Khartoum, Sudan
e-mail: hanan_musbah12@outlook.com

Al-Ahamd Zehbh Ali, PhD, professor, National for Research Remote Sensing Authority
e-mail: zehbh-al-ahamd@outlook.com

Abdelrahman Abubaker Elsheikh, PhD, associate professor, director, Act center for research
e-mail: 3elsheikh98@outlook.com

DOI 10.52209/2706-977X_2025_3_99 IRSTI 55.43.13 UDC 629.3

Environmental and Economic Feasibility of Implementing Electro-Impulse Mufflers on Motor Vehicles

Kabibollayev B.B., Kukesheva A.B.*, Kadyrov A.S., Kryuchkov E.Y., Karsakova A.Zh.
Abylkas Saginov Karaganda Technical University, Karaganda, Kazakhstan
*** corresponding author**

Abstract. The article addresses the issue of atmospheric pollution caused by motor vehicles and proposes a solution in the form of implementing electro-impulse mufflers for diesel engines. It presents the results of experimental studies confirming a reduction in CO_2 concentration and smoke levels, as well as an increase in oxygen content in exhaust gases. A methodology for calculating the economic efficiency of introducing electro-impulse mufflers has been developed, taking into account emission taxes and the prevention of environmental damage. Calculations specific to Kazakhstan show that the implementation of this technology leads to a 42% reduction in emissions, up to 25% fuel savings, a decrease in emission payments by 11 billion tenge annually, and the prevention of environmental damage amounting to over 1.25 trillion tenge. The results obtained demonstrate the environmental and economic feasibility of integrating electro-impulse mufflers into the national exhaust gas purification system.

Keywords: electro-impulse muffler, diesel engine, emissions, smoke level, economic effect, transport.

Introduction

Mechanical and automotive engineering play a key role in the modern economy by driving industrial development, creating jobs, advancing technological progress, and improving the population's standard of living. These industries contribute to increased mobility, enhanced efficiency in technical and logistical processes, and greater competitiveness of national production. However, the intensification of transportation flows, the growing number of motor vehicles, the expansion of urban agglomerations, and the rise in freight transport both within and outside cities are increasing the environmental burden on the natural environment. This is reflected in the rise of harmful emissions, air pollution, increased noise levels, and a decline in the quality of urban life. Therefore, the development and implementation of environmentally friendly and resource-efficient technologies in the transport sector have become particularly relevant.

One of the most significant negative consequences of the transport sector is the emission of exhaust gases, especially carbon dioxide (CO_2), which contributes to global warming and climate change. According to international studies, the transport sector is one of the largest sources of CO_2 emissions worldwide, with road transport accounting for 71.7% of these emissions. This highlights the urgent need for effective measures to reduce the carbon footprint [1, 2].

In addition, air pollution caused by nitrogen oxides, sulfur compounds, and soot particles has a serious impact on public health, provoking respiratory and cardiovascular diseases [3]. According to data from the World Health Organization (WHO), around 7 million people die prematurely each year due to the effects of air pollution (Figure 1).

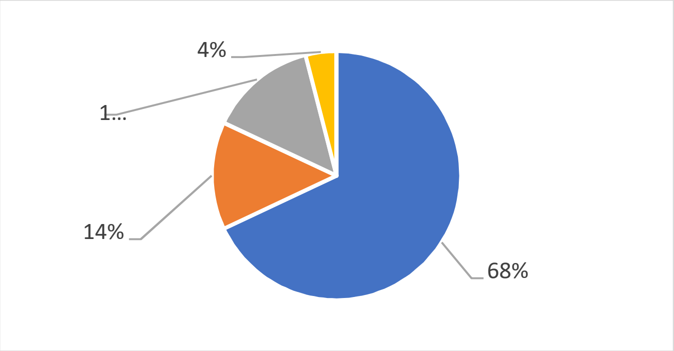

Fig. 1 – Indicators of the World Health Organization (WHO)

Approximately 68% of these cases are linked to ischemic heart disease and stroke, 14% to chronic obstructive pulmonary disease (COPD), 14% to acute lower respiratory infections, and 4% to lung cancer [4,5].

In Kazakhstan, air pollution is also a pressing issue. According to the World Bank's 2022 report, the country sees more than 10,000 premature deaths annually due to air pollution, resulting in economic losses of over 10.5 billion USD each year.

Several cities in Kazakhstan regularly experience concentrations of harmful substances in ambient air that exceed the maximum allowable limits (MAL). According to data from the Ministry of Ecology, Geology and Natural Resources, the most polluted cities include Astana, Almaty, Karaganda, Temirtau, and Aktobe (Table 1).

Table 1. The most polluted cities in Kazakhstan

№	City	Indicators
1	Astana	Over 1,300 cases of exceeding the MAL for harmful substances, especially near Babatayuly Street.
2	Almaty	1,940 cases of exceeding the MAL, particularly in the areas of the Almaty Arena Ice Palace and nearby residential districts.
3	Karaganda	56 cases of severe air pollution, mainly due to suspended particles (PM2.5 and PM10).
4	Temirtau	54 cases of high pollution, primarily from nitrogen dioxide.
5	Aktobe	Exceedances of the MAL for nitrogen dioxide and hydrogen sulfide were recorded [6,7].

Moreover, in dense urban traffic conditions, vehicles often operate at low engine speeds, are forced to stop frequently at traffic lights, idle in traffic jams, and move in a pattern of constant acceleration and braking. As a result:

– The level of harmful emissions increases, as fuel combustion becomes less efficient, leading to significantly higher emissions of nitrogen oxides (NO_x), carbon monoxide (CO), and particulate matter (PM2.5, PM10);

– The exhaust system operates sub-optimally, reducing the effectiveness of catalytic converters and diesel particulate filters (DPFs);

– Fuel consumption rises, adding further environmental impact and increasing operating costs;

– Engine lifespan decreases, as frequent stops and low-speed driving contribute to greater wear and tear of engine components.

To reduce the negative environmental impact of transportation under urban conditions, various technologies and methods are used worldwide. However, each has its own advantages and disadvantages.

One common solution is the use of electric and hybrid vehicles, which do not emit CO_2 or particulates during operation. However, widespread adoption is hindered by high costs, limited driving range, and insufficient charging infrastructure. Additionally, battery production requires rare earth metals, placing further strain on the environment and increasing dependence on finite natural resources. Mining and processing of rare earth elements are associated with significant environmental pollution, high energy consumption, and socio-economic risks - especially in countries where the major deposits are concentrated. Thus, despite their environmental benefits in operation, electric vehicles are not a fully "green" alternative and require a comprehensive life cycle impact assessment, from raw material extraction to battery disposal.

Another option is the use of biofuels, such as biodiesel and bioethanol, which can reduce carbon monoxide and particulate emissions. However, their use tends to increase nitrogen oxide emissions, and their production requires vast agricultural areas, often leading to deforestation and rising food crop prices.

To reduce emissions in diesel and gasoline vehicles, catalytic converters and diesel particulate filters (DPFs) are widely used. These effectively reduce harmful substances in exhaust gases but require regular maintenance and replacement. In city driving, where engines often run at low speeds, the effectiveness of these systems decreases, and their failure can result in costly repairs [8,9].

Another solution is the use of natural gas (compressed or liquefied). Gas-powered vehicles emit significantly fewer pollutants than traditional diesel or gasoline vehicles. However, modifications to the engine are required, and the lack of fueling infrastructure limits the widespread adoption of this technology [10,11].

A simple method for reducing emissions in urban driving is the implementation of start-stop systems, which automatically turn off the engine during stops at traffic lights or in traffic. This helps save fuel and reduce emissions, but frequent engine restarts increase the load on the starter and battery, potentially causing premature wear [12,13].

Based on the identified pros and cons of current methods and technologies, their practical implementation efficiency has been evaluated according to the following criteria: emission reduction effectiveness, economic feasibility, and implementation risks (Table 2).

Table 2. Evaluation of the Practical Effectiveness of Existing Emission Reduction Methods

Method	Emission Reduction Effectiveness	Economic Feasibility	Implementation Risks
Electric Vehicles	High (no emissions during operation)	Low (high purchase cost and infrastructure requirements)	High (underdeveloped infrastructure, expensive batteries)
Gas-powered Transport (CNG/LNG)	Medium (reduced NO_x and CO emissions)	Medium (costly equipment and fueling stations)	Medium (lack of refueling stations, vehicle conversion required)
Catalytic Converters and Diesel Filters	Medium (effective only at high temperatures)	Medium (high replacement and maintenance costs)	Medium (ineffective in urban conditions, risk of filter clogging)
Start-Stop System	Low (only saves fuel during idling)	High (simple and inexpensive to install)	Low (increased wear on battery and starter)

There are also domestic solutions aimed at neutralizing harmful emissions from vehicles. In particular, researchers from the Abylkas Saginov Karaganda Technical University, at the Department of "Transport Engineering and Logistics Systems," are developing electro-impulse, ultrasonic, and laser mufflers for vehicles [14,15]. These devices are based on the physical principles of the impact of electro-impulses, ultrasound, and lasers on the exhaust gas flow, which leads to processes such as electrical ionization, ultrasonic coagulation, and laser dissociation — all of which contribute to reducing harmful substance content [16].

Preliminary experimental studies have already confirmed the effectiveness of the proposed methods, demonstrating a reduction in carbon dioxide levels, decreased smoke density, and increased oxygen concentration in exhaust gases [17,18]. However, the technologies are still in the testing phase and require further research to optimize their design and adapt them to various operating conditions.

Despite this, the proposed direction is considered promising because integrating electro-impulse, ultrasonic, and laser devices into vehicle exhaust systems does not require significant modifications to the exhaust system design, making it possible to implement them without substantial cost increases [19,20].

Electro-impulse mufflers are the most suitable for diesel engines since, compared to ultrasonic and laser mufflers, they offer stable influence on both smoke levels and gas composition. Additionally, electro-impulse mufflers have the following advantages:

First, electro-impulse technology maintains its effectiveness at low engine speeds, which is especially important for vehicles operating in conditions of frequent stops and acceleration in urban traffic. Unlike ultrasonic mufflers, which require a stable gas flow to effectively trigger coagulation processes, electro-impulse discharges act directly on soot particles and nitrogen oxides, breaking them down even during unstable engine operation.

Second, electro-impulse mufflers consume less energy than laser systems, making them a more economical and practical solution for vehicles where additional loads on the onboard power supply must be minimized. Laser systems require complex optical equipment and precise tuning to effectively decompose harmful substances, complicating their operation under conditions of high vibration and dustiness, which are typical for freight transport.

Moreover, electro-impulse mufflers can be easily integrated into standard exhaust gas systems without requiring significant structural changes. This allows for their use in both new vehicle models and as part of retrofitting already operating fleets, making them the most realistic and accessible solution for practical implementation.

Thus, electro-impulse mufflers represent the most optimal option for diesel engines, providing effective emission reduction, cost-efficiency, and reliability under demanding operating conditions.

However, the economic feasibility of large-scale implementation of electro-impulse mufflers has not yet been proven. Without proper economic justification, market introduction, commercialization, and the organization of mass production at machine-building plants could face difficulties. Therefore, the development of a calculation methodology proving the cost-effectiveness of implementing electro-impulse mufflers is a relevant task.

The objective of this study is to develop a methodology for calculating the effectiveness of implementing electro-impulse mufflers for diesel vehicles.

To achieve this objective, the following tasks were solved:

– the physical principles of electro-impulse muffler operation were examined;

– an analysis of experimental test bench results was conducted;

– a methodology for calculating the economic efficiency of electro-impulse muffler implementation was developed;

– the prospects for integrating electro-impulse mufflers into vehicle systems were assessed.

The scientific novelty of the research lies in obtaining new dependencies that confirm the effectiveness of the electro-impulse muffler implementation.

The practical significance of the research is as follows:
The results of the study can be applied in the modernization of exhaust gas treatment systems for diesel vehicles. This will help reduce air pollution, lower tax payments for harmful emissions, and improve the economic efficiency of logistics operations.

The developed calculation methodology can serve as a primary tool for assessing the potential of introducing electro-impulse mufflers into industrial production.

Thus, the study aims not only to scientifically justify the efficiency of electro-impulse mufflers but also to prove their economic and market feasibility, paving the way for mass production and commercial application.

1. Materials and Methods

The gas purification process in the electro-impulse muffler is based on the formation of a corona discharge between the electrodes [21]. A corona discharge is a glow that appears around the tips of electrodes when high voltage is applied, subsequently leading to the ionization process (Figure 2).

Fig. 2 – Corona discharge

Gas ionization is a process in which gas atoms or molecules lose or gain electrons under the influence of an electrical discharge. As a result of ionization, electrically charged particles are formed: positive ions if an atom loses an electron, and negative ions if it gains an electron [22].

The charged particles, while moving through the muffler, are attracted to the neutral gas particles, forming large aggregates that settle at the bottom of the housing due to electrocoagulation [23].

Experiments conducted on test benches with the electro-impulse muffler, and comparisons with the results from tests using ultrasonic and laser mufflers, confirmed the effectiveness of gas purification using electro-impulse technology (Figure 3).

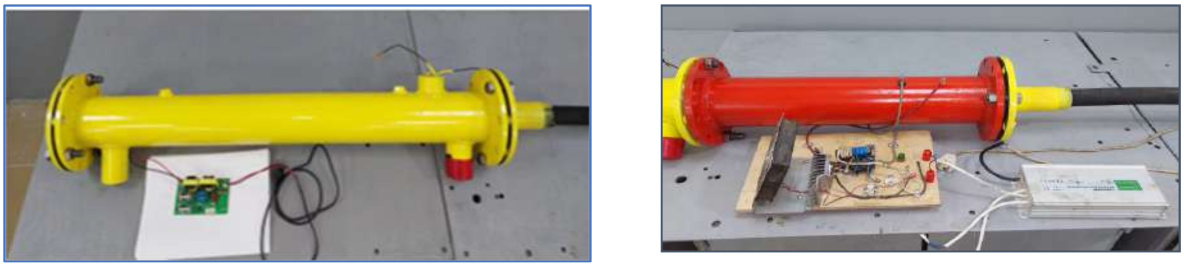

a) ultrasonic muffler

b) electro-impulse muffler

c) laser muffler

Fig. 3 – Experimental test benches for electro-impulse, ultrasonic, and laser mufflers.

Changes in carbon dioxide (CO_2) and oxygen (O_2) concentrations at various engine speeds were used as evaluation indicators. The experimental results for CO_2 and O_2 levels obtained from the three muffler test benches are presented in Table 3.

Table 3. Results of experimental research

№	Engine speed, rpm	Before exposure	750-1000	1000-1400	1400-1550
	Impact		after	after	after
1	CO_2 (Electro-impulse)	2,38	2,35	2,27	2,1
2	O_2 (Electro-impulse)	17,18	17,27	17,46	17,66
3	CO_2 (Ultrasound)	2,26	2,25	2,23	2,18
4	O_2 (Ultrasound)	17,34	17,36	17,46	17,5
5	CO_2 (Laser)	1,4	1,35	1,35	1,38
6	O_2 (Laser)	18,97	18,87	19,01	18,43

Based on the experimental data presented in Table 3, comparative graphs were created to show the effectiveness of the three types of exhaust gas treatment (electro-impulse, ultrasonic, and laser) in terms of CO_2 and O_2 indicators for diesel engines (Figures 3 and 4).

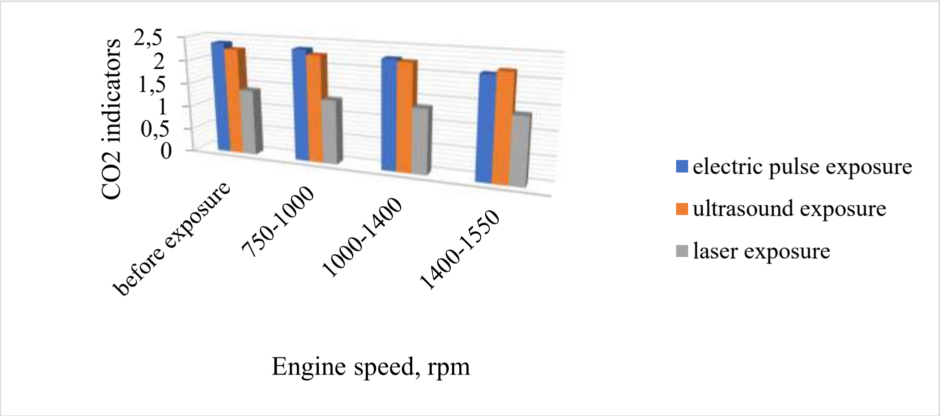

Fig. 3 – Comparison of the efficiency of three types of treatment on CO_2 indicators

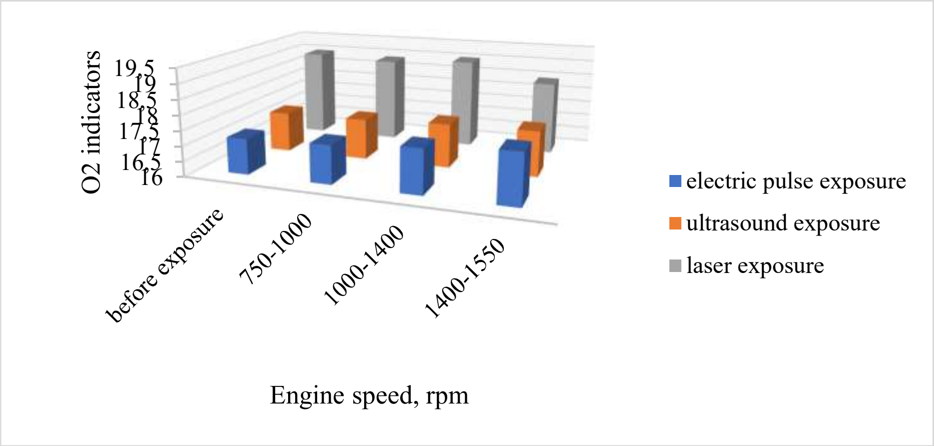

Fig. 4 – Comparison of the efficiency of three types of treatment on O_2 indicators

The results showed that electro-impulse treatment ensures a stable reduction in CO_2 concentration – from 2.38% to 2.10% as engine speed increases, indicating a decrease in the amount of incompletely burned products. At the same time, there is a positive trend in the increase of O_2 concentration – from 17.18% to 17.66%, which indicates more complete combustion of the fuel mixture.

Ultrasonic treatment demonstrated a similar but slightly less pronounced efficiency: CO_2 concentration decreased to 2.18%, and O_2 content increased to 17.50%. Thus, ultrasound has a positive effect, but its impact is inferior to electro-impulse treatment.

Laser treatment showed the highest oxygen content in the exhaust gases – up to 19.01%, which indicates a high level of combustion completeness. However, CO_2 concentration remains at a low level without significant reduction as the engine speed increases, with values stabilizing in the range of 1.35–1.38%. This may indicate an initially cleaner combustion process, but lower sensitivity to changing engine operating conditions.

Additionally, the smoke indicators of exhaust gases were studied as a result of experiments conducted on three test stands. The results of the experiments are presented in Table 4 and in Figure 5.

Table 4. Results of exhaust gas smoke indicators

№	Engine speed	Before (%)	750-1000	1000-1400	1400-1550
			after (%)	after (%)	after (%)
1	Electro-impulse	50	45	36	29
2	Ultrasound	54	35	44	46
3	Laser	80	60	80	60

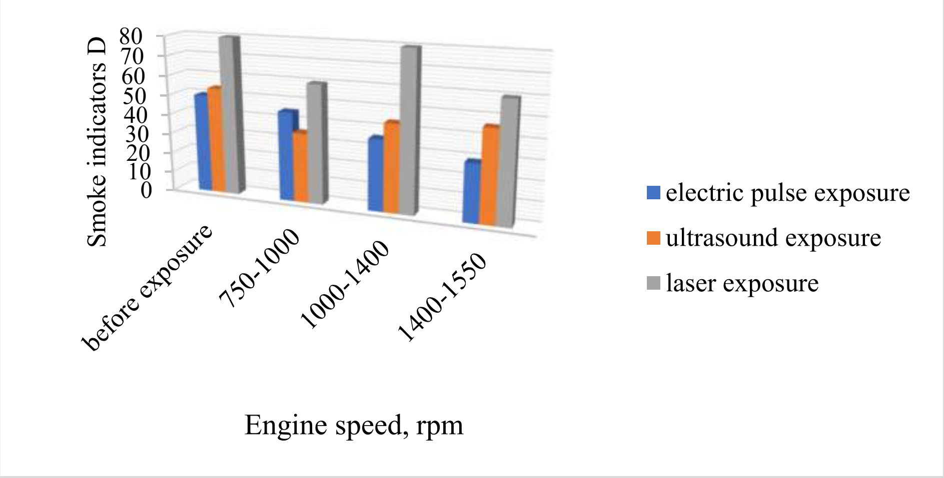

Fig. 5 – Comparison of the effectiveness of three types of treatment on smoke density (D)

The results showed that electro-impulse treatment ensures stable and consistent reduction of pollutant levels as engine speed increases. The value decreased from 50% to 29%, indicating high efficiency of the technology under dynamic engine operating conditions. This suggests good adaptability of the method to varying loads and speeds.

Ultrasonic treatment showed effective pollutant reduction at low engine speeds (down to 35%). However, as the engine speed increased, the smoke level rose again - up to 46% at 1400 - 1550 rpm. This indicates the method's instability under increased loads and a limited effective operating range.

Laser treatment demonstrated an initial reduction in pollution (down to 60% at 750–1000 rpm), but in the mid-speed range (1000–1400 rpm), the effect was neutralized - the smoke level returned to its original value (80%), then dropped again at higher rpm. These fluctuations indicate the method's sensitivity to engine operating modes and the possible need for fine-tuning of the equipment for specific conditions.

Based on the conducted analysis of the experimental results, it can be concluded that the electro-impulse method is the most efficient and stable method for reducing harmful emissions across all considered engine operating modes. It provides the greatest and most consistent reduction in indicators, especially at higher rpm.

Thus, electro-impulse treatment can be recommended as a priority method for integration into diesel engine exhaust gas purification systems.

Based on the conducted research, the design and technical specifications of the electro-impulse muffler were developed. The following recommendations were also made:

– the electrode diameter should not exceed 0.27 m, and the optimal distance between them is 0.32 m;

– to address issues such as electrode burn-out and discharge into the casing, it is recommended to replace the electrodes with automotive spark plugs and to manufacture the muffler casing from dielectric material;

– to increase gas purification efficiency, it is recommended to install two to six spark plugs with electrodes at varying distances inside the muffler;

– the optimal electrode spacing and frequency of electrical impulses were determined for different engine speeds:

– 750 rpm (78.5 rad/s) – 0.008 m, 23.04 Hz;

– 1280 rpm (130.9 rad/s) – 0.004 m, 20.42 Hz;

– 4500 rpm (471 rad/s) – 0.002 m, 46.57 Hz.

The general layout of the proposed electro-impulse muffler, based on the data above, is shown in Figure 6.

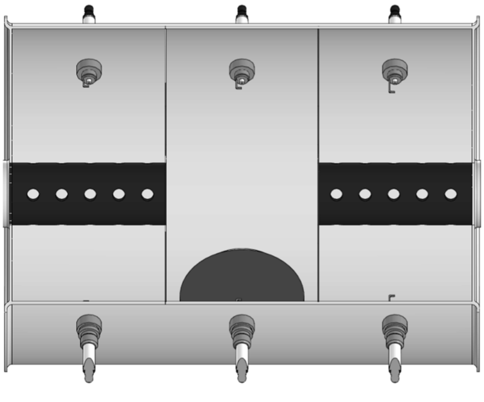

Fig. 6 – Design scheme of the electro-impulse muffler

The obtained results and recommendations require the development of a prototype of an electric pulse muffler and its installation on vehicles for testing in real conditions.

Further development and serial production of electric pulse mufflers will require not only the refinement of their design, but also additional testing in real conditions. Also, the introduction of this technology in the transport industry requires a comprehensive assessment of its financial and environmental efficiency.

The development of a methodology for calculating the economic efficiency of introducing electric pulse mufflers will allow an objective assessment of their competitiveness compared to traditional exhaust gas cleaning systems. This analysis includes a reduction in taxes paid for environmentally harmful emissions, a reduction in fuel consumption due to its complete combustion, as well as environmental benefits.

Thus, for the further development and improvement of the production of electric pulse mufflers, not only engineering and technological aspects are needed, but also a comprehensive economic analysis proving the real commercial feasibility of their mass implementation.

2. Results and discussion

A methodology for calculating the efficiency of implementing an electric pulse muffler has been developed. The presented calculation methodology compared the emission rates of pollutants before and after installing the electric pulse. The possibility of installing them on 540.8 thousand trucks in Kazakhstan is being considered (according to data from the Bureau of National Statistics of Kazakhstan for 2023-2024). The calculation methodology is presented below:

Emission mass before installation of the electric pulse muffler:

$$M_b = \frac{Q \cdot \rho \cdot D_{\text{b}} \cdot T_y \cdot N}{1000} \tag{1}$$

$$M_b = \frac{10 \cdot 0{,}84 \cdot 0{,}5 \cdot 2628 \cdot 540800}{1000} = 5969134{,}08$$

where Q - fuel consumption per vehicle, l/h;
ρ - density of diesel fuel, kg/l (0.84 kg/l);
D_b - the level of gas smoke before installing an electric pulse muffler (0.5);
T_y - annual work of the car, hours;
N - Number of trucks (540800 units)

Fuel consumption before installing an electric pulse muffler:

$$Q = \frac{R \cdot \vartheta}{100} \tag{2}$$

$$Q = \frac{25 \cdot 40}{100} = 10$$

where R - average fuel consumption per 100 km, l/100 km (25 l/100 km);
ϑ- average vehicle speed, km/h (40 km/h).

Annual operating time of the vehicle:

$$T_y = T_d \cdot Д_{w.y.} \cdot K_u \tag{3}$$

$$T_y = 8 \cdot 365 \cdot 0{,}9 = 2628$$

where T_d - daily operating time of the vehicle, hours (8 hours);
$Д_{w.y.}$ - number of working days per year (250-365 days);
K_u - actual utilization factor (0.9).

Emission mass after installation of an electric pulse muffler:

$$M_a = \frac{Q \cdot \rho \cdot Д_a \cdot Ty \cdot N}{1000} \tag{4}$$

$$M_a = \frac{10 \cdot 0{,}84 \cdot 0{,}29 \cdot 2628 \cdot 540800}{1000} = 3462097{,}76$$

where D_a - Pollution level after system installation (0.29 g/kg).

Reduction of emissions after installation of an electric pulse muffler:

$$\Delta M = M_b - M_a \tag{5}$$

$$\Delta M = 5969134{,}08 - 3462097{,}76 = 2507036{,}32$$

Emissions fee before installing an electric pulse muffler:

$$P_b = M_b \cdot H_{tr} \cdot K \tag{6}$$

$$P_b = 5969134{,}08 \cdot 3538{,}80 \cdot 1{,}26 = 26615700319{,}7$$

where H_{tr} - emission tax rate, tenge/t (109 MCI per 1 ton of the specified fuel - 3538.80 tenge);
K - total coefficient.

Total coefficient:

$$K = K_{tf} \cdot K_e \cdot K_{na} \tag{7}$$

where K_{tf} - coefficient for the type of fuel (diesel - 0.9);
K_e - coefficient up to the economic limit (1.2);
K_{na} - coefficient (1.1–1.5) depending on the presence of a specially protected natural area.

$$K = 0{,}9 \cdot 1{,}2 \cdot 1{,}17 = 1{,}26$$

Emissions Fee After Installing an Electric Pulse Muffler:

$$P_a = M_a \cdot H_{tr} \cdot K \tag{8}$$

$$P_a = 3462097{,}76 * 3538{,}80*1{,}26 = 15\ 437\ 106\ 156{,}9$$

Reduction of emission fees after installation of an electric pulse muffler:

$$\Delta P = P_b - P_a \tag{9}$$

$$\Delta P = 26615700319{,}7 - 15437106156{,}9 = 11\ 178\ 594\ 162{,}8$$

Reducing environmental damage:

$$C_d = \frac{Э_d}{M} \tag{10}$$

where C_d - economic losses from 1 ton of emissions (according to WHO and World Bank data). Economic damage from air pollution in Kazakhstan is 10 billion US dollars ≈ 5 trillion tenge;

M – the mass of pollutants emitted into the atmosphere. Every year, 10 million tons of pollutants are emitted into the atmosphere.

$$C_d = \frac{5\ 000\ 000\ 000\ 000}{10\ 000\ 000} = 500\ 000$$

$$E_d = \Delta M \cdot C_d \tag{11}$$

Reducing economic damage:

$$E_d = 2\ 507\ 036{,}32 \cdot 500\ 000 = 1\ 253\ 518\ 160\ 000$$

Fuel economy:

$$E_f = \frac{Q \cdot \Delta \cdot T_y \cdot N \cdot C_{di}}{1000} \tag{12}$$

Smoke reduction percentage ΔD:

$$\Delta D = \frac{D_b - D_a}{D_b} \cdot 100\% \tag{13}$$

$$\Delta D = \frac{(0{,}5\ -\ 0{,}29)}{0{,}5} \cdot 100\% = 42\%$$

Fuel efficiency:

$$\Delta = \Delta D \cdot K \tag{14}$$

where K – conversion factor ≈ 0.5–0.7

$$\Delta = 42\% \cdot 0{,}6 = 25{,}2\%$$

$$E_f = \frac{10\ \cdot\ 25{,}2\ \cdot\ 2628\ \cdot\ 540\ 800\ \cdot\ 260}{1000} = 93\ 118\ 491\ 648$$

Calculation of costs for implementation of the system:

$$C_{integ} = P_{inst} \cdot N + C_{ser} \cdot N$$

$$C_{integ} = 80\ 000 \cdot 540\ 800 + 10\ 000 \cdot 540\ 800 = 48\ 672\ 000\ 000$$

where P_{ins} – cost of installing one muffler (80,000 tenge);

N - number of vehicles;

C_{ser} – annual service cost (10,000 tenge).

Overall economic effect:

$$E_e = \Delta P + Э_d + E_f - C_{integ} \tag{15}$$

$$Э_d = 11\ 178\ 594\ 162{,}8 + 1\ 253\ 518\ 160\ 000 + 93\ 118\ 491\ 648 - 48\ 672\ 000 = 1{,}357{,}766{,}573{,}810.8$$

Efficiency Ratio:

$$K = Э_e / C_{integ} \tag{16}$$

$$K_e = 1\ 357\ 766\ 573\ 810{,}8/48{,}672{,}000{,}000 = 27{,}9$$

Relative reduction in emissions:

$$k_1 = \frac{\Delta M}{M_b} \tag{17}$$

$$k_1 = \frac{2507036{,}32}{5969134{,}08} = 0{,}42$$

Efficiency and profitability of implementation from an environmental point of view:

$$k_2 = \frac{Э_d}{C_{integ}} \tag{18}$$

$$k_2 = \frac{1253518160000}{48672000000} = 25{,}75$$

Fuel Economy Indicator:

$$k_3 = \frac{O_{2(b)} - O_{2(a)}}{O_{2(b)}} \tag{20}$$

$$k_3 = \frac{17{,}66\ -\ 17{,}18}{17{,}18} = 0{,}03$$

Based on the calculations carried out, a graph of changes in the main indicators was drawn up, confirming the feasibility of introducing electric pulse mufflers (Figure 7).

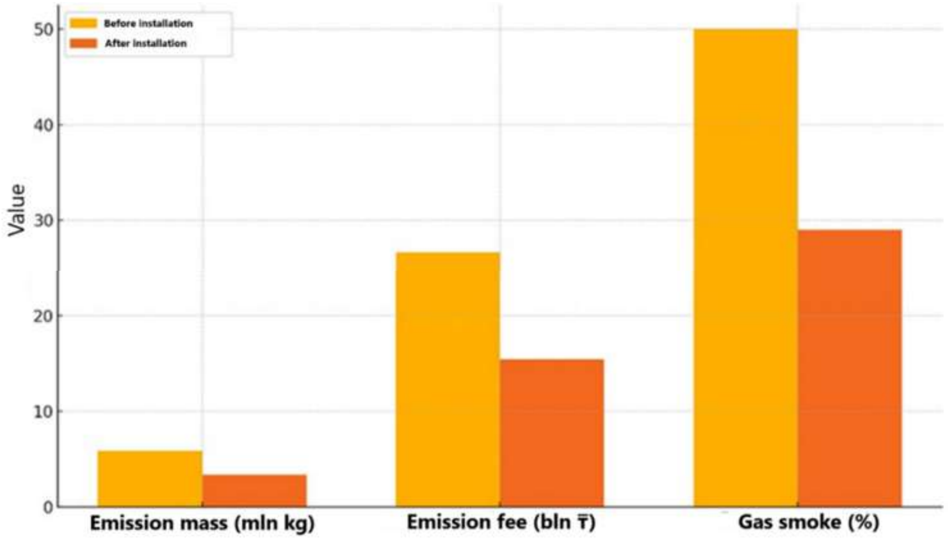

Fig.7. – Graph of changes in indicators before and after installation of an electric pulse muffler

The developed methodology for the implementation of the electric pulse muffler demonstrated its high efficiency in all key indicators, both in the environmental and economic aspects. Calculations showed that the mass of pollutant emissions before the installation of the device was 5969134.08 kg, and after the implementation it decreased to 3462097.76 kg. Thus, it was possible to reduce the volume of emissions by 2507036.32 kg, which is equivalent to a decrease of 42%. This confirms the environmental performance of the proposed solution and its compliance with modern requirements for reducing the negative impact on the environment. At the same time, significant savings were achieved due to the reduction of the emission fee: before the implementation of the muffler, the fee was 26.62 billion tenge per year, and after - 15.44 billion tenge, which made it possible to save 11.18 billion tenge annually. This is a weighty argument in favor of reducing the tax burden on transport enterprises. In addition, according to the World Bank and WHO, the economic damage from air pollution is 500,000 tenge per ton of emissions. Therefore, the prevented environmental damage is estimated at 1.25 trillion tenge per year, which is a significant contribution to environmental protection.

In addition, a 42% reduction in exhaust smoke improved the completeness of fuel combustion, which made it possible to achieve fuel savings of 93.12 billion tenge per year. In total, this formed a total economic effect of 1,357.77 billion tenge. With installation costs of 48.67 billion tenge, the implementation efficiency ratio was 27.9. This means that for every 1 tenge invested in the implementation of mufflers, there is almost 28 tenge of total benefit. This is an indicator of high economic efficiency, proving that the implementation proposal will bring significant returns. Additional evaluation factors also confirm the effectiveness of the technology implementation: the relative reduction in emissions was 42%, the environmental profitability was 25.75, and the fuel economy indicator for oxygen content was 3%. Each tenge invested in mufflers prevents environmental damage by 25.75 tenge. This indicates a high environmental effect and payback even without taking into account fuel savings and taxes. All this allows us to conclude that it is highly feasible to use an electric pulse muffler for modernizing the vehicle fleet and scaling the solution within the framework of the state environmental policy of the Republic of Kazakhstan. Due to the simplicity of the design and reliability of operation, the introduction of electric pulse mufflers into serial production of machine-building plants is promising, especially relevant in the period of limited resources and the transition to "green" technologies.При проектировании электроимпульсного глушителя важно учитывать стоимость материалов, чтобы обеспечить экономичность и доступность устройства. Ниже приведена приблизительная оценка материалов, необходимых для изготовления электроимпульсного глушителя на основе комплектующих для автомобиля ГАЗ-3302 Next с двигателем Evotech 2.7 Евро-5:

Table 5. Estimated cost of materials required for manufacturing electric pulse mufflers

Components	Description	Estimated price (tenge)
Coil	Original models	5000 – 8000
Spark plugs	Original models	7000 – 10000
Insulation materials	Ceramic or heat-resistant plastic insulators	3000 – 5000
Switch housing	Steel or aluminum housing	15 000 – 20 000
Fasteners	Clamps, brackets, rubber supports	3000 – 5000
Electronic control unit	Pulse generator, control electronics	10 000 – 15 000
Wire and connecting elements	High-voltage cables, switches	2000 – 4000
Additional materials	Coatings, sealants, anti-corrosion coatings	2000 – 3000
All		70,000

Catalytic converters cost an average of 500,000 tenge and are widely used, but are limited to partial neutralization. Electric vehicles, completely eliminating carbon emissions, are expensive (about 10 million tenge) and require infrastructure. Thus, based on the above, the introduction of electro-pulse mufflers is the optimal solution.

Conclusion

The conducted study confirmed the high efficiency of electric pulse mufflers for reducing harmful emissions and improving the environmental performance of diesel engines. It was found that the installation of the device provides a reduction in the mass of emissions by up to 42%, a reduction in the fee for emissions by 11.18 billion tenge and the prevention of environmental damage by more than 1.25 trillion tenge per year. Additionally, fuel savings are achieved by increasing the completeness of combustion.

In addition, a comparison with the experimental results obtained on stands with ultrasonic and laser mufflers showed that the electric pulse version is a more energy-efficient, structurally simple and economically feasible solution. It can be adapted to the existing fleet of vehicles without significant design changes.

Also, according to calculations, the efficiency coefficient was 27.9, which demonstrates a high level of profitability of the project. Localization of muffler production at machine-building enterprises of Kazakhstan will stimulate the development of industry, create new jobs and reduce import dependence. Thus, the developed technology has not only scientific and applied, but also strategic significance for the sustainable development of the country's transport sector.

References

[1] Aminzadegan, S., Shahriari, M., Mehranfar, F., Abramović, B. Factors affecting the emission of pollutants in different types of transportation: A literature review. // Energy Reports, Vol. 8 Issue 1, 2022 – p. 2508-2529.

[2] Sinelnikov K.A., Moldabaev B.G., Zhunusbekova Z.Z., Kukesheva A.B. Theoretical and Experimental Analysis of Ultrasonic Cleaning of Internal Combustion Engine Radiators with the Development of Practical RecommendationsMaterial and Mechanical Engineering Technology // *Material and Mechanical Engineering Technology*, Vol., 7, Issue 1, 2025. - p. 87 – 95.

[3] Kadyrova I.A., Mindubaeva F.A., Grjibovski A.M. Prediction of outcomes after stroke: A systematic review. //Human Ecology (Russian Federation), Vol. 4, Issue 10, 2015 – p. 55 – 64

[4] Akhmaltdinova L., Sirota V., Babenko D., Zhumaliyeva V., Kadyrova I., Maratkyzy M., Ibrayeva A., Avdienko O. Proinflammatory cytokines and colorectal cancer – the impact of the stage. *Wspolczesna Onkologia*, Vol. 24, Issue 4, 2021. – p. 207-210.
[5] Yessenbayeva A., Kadyrova I, Aukenov N., Shaimardanov N. Apsalikov B., Massabayeva M., Kazymov M., Shakhanova A., Mussazhanova Zh., Biomarkers of immunothrombosis and polymorphisms of IL2, IL6, and IL10 genes as predictors of the severity of COVID-19 in a Kazakh population //PLoS ONE, Vol. 18, Issue 6, 2023. – p. 61-67.
[6] Kozhagulov S., Adambekova A. A., Quadrado J. C., Salnikov V., Rysmagambetova A., Tanybayeva A. Trends in Atmospheric Emissions in Central Asian Countries Since 1990 in the Context of Regional Development. 2025 – p. 1-44.
[7] Kovalev P.V., Popova S.D., Issagulov A.Z., Kulikov V.Y., Kvon S.S. Investigation of the effect of high strength strips steel modification with rare-earth metal (REM). // Metalurgija, Vol. 56, Issue 3-4, 2017. – p. 393 – 395.
[8] Doucette R. T., McCulloch M. D. Modeling the prospects of plug-in hybrid electric vehicles to reduce CO_2 emissions //Applied Energy. Vol. 88, Issue 7. 2011. – p. 2315-2323.
[9] Sherov K.T., Absadykov B.N., Sikhimbayev M.R., Togizbayeva B.B., Esirkepov A. Investigation of the stress-strain state of components of a hydraulic impact device. // News of the National Academy of Sciences of the Republic of Kazakhstan. Series of geology and technical science, Vol. 1, Issue 457, 2023 - 260-269.
[10] Khan M. I., Yasmin T., Shakoor A. International experience with compressed natural gas (CNG) as environmental friendly fuel //Energy Systems. Vol. 6, Issue 4. 2015.– p. 507-531.
[11] Moldabaev B., Sinelnikov K., Kukesheva A. Justification Of The Method Of Vehicle Engine Radiator Ultrasonic Cleaning. // Communications - Scientific Letters of the University of Zilina, Vol. 27, Issue 1, 2025. – p. 75-84.
[12] Cieślik W., Pielecha I., Borowski P. Effects of start–stop system on the operation of drive system in urban traffic conditions //Journal of mechanical and transport engineering, Vol. 67, Issue 2, 2015. – p. 15-26.
[13]. Kadyrov A., Kurmasheva B., Suyunbaev Sh., Sinelnikov K., Sakhapov R., Ganyukov A. Studying the process of transport equipment cooling system ultrasonic cleaning //Communications - Scientific Letters of the University of Zilina, Vol. 24, Issue 4, 2022. – p. 288-300
[14] Sarsembekov B.K., Kadyrov A.S., Kunayev V.A., Issabayev M.S., Kukesheva A.B. Experimental Comparison of Methods for Cleaning Car Exhaust Gas by Exposure Using Ultrasound and Laser Radiation //Material and Mechanical Engineering Technology, Vol. 6, Issue 3, 2024. – p. 44-54.
[15] Kukesheva A., Kadyrov A., Kryuchkov Y. Establishing the parameters of the operation mode of the electric pulse automobile muffler //Journal of Applied Engineering Science. Vol. 22, Issue 1, 2024. – p. 89–99.
[16] Kadyrov A., Bembenek M., Sarsembekov B., Kukesheva A., Nurkusheva S. The Influence of the Frequency of Ultrasound on the Exhaust Gas Purification Process in a Diesel Car Muffler //Appl. Sci. Vol.14, Issue 12, 2024. – P. 1-19.
[17] Pak I., Kadyrov A., Askarov B., Suleyev B., Karsakova A. Developing and Studying the Method of Ultrasonic Purification and Utilization of Internal Combustion Engine Exhaust Gases. // Communications-Scientific Letters of the University of Zilina, Vol. 25, Issue 3, 2023. – p. 245-258.
[18] Ibatov M.K., Kadyrov A.S., Pak I.A., Kadyrova I.A., Askarov B.S. The results of experimental studies of the capacitive equipment of ultrasonic cleaning of exhaust gases of vehicles. // Ugol, Vol. 21, Issue 2, 2020. – p. 73 – 78
[19] Pak I. Experimental study of the ultrasonic muffler efficiency for improving the exhaust gas cleaning system of internal combustion engines of automobiles. // Material and Mechanical Engineering Technology, Vol. 6, Issue 2, 2024. - p. 53 – 63
[20] Ilesaliev D.I. Design of Ultrasonic Technology to Improve the Efficiency of Car Exhaust Gas Cleaning System. // Material and Mechanical Engineering Technology, Vol. 6, Issue 2, 2024. – p. 3 – 7.
[21] Kadyrov A., Sarsembekov B., Kukesheva A., Sinelnikov K. Application of electric pulse and ultrasonic mufflers for increasing the degree of exhaust gas purification in car engines. // International Journal of Innovative Research and Scientific Studies, Vol. 8, Issue 1, 2025 – p. 33 – 40.
[22] Kadyrov A., Kryuchkov Ye., Sinelnikov K, Ganyukov A., Sakhapov R., Kukesheva A. Studying the process of the internal combustion engine exhaust gas purification by an electric pulse // Communications - Scientific Letters of the University of Zilina, Vol. 24, Issue 4, 2022. – P. 275-287
[23] Kadyrov A., Kukesheva A., Kryuchkov Ye., Pak I., Kurmasheva B, Kabikenov S. Development of Calculation Methodology for Optimizing the Operating Mode of an Electric Pulse Unit for Cleaning Exhaust Gases //Communications - Scientific Letters of the University of Zilina, Vol. 26, Issue 1, 2024. – P. 41-53

Information of the authors

Kabibollayev Bekarys, student, Abylkas Saginov Karaganda Technical University
e-mail: bekakabibollaev@mail.ru

Kukesheva Aliya, PhD, Abylkas Saginov Karaganda Technical University
e-mail: aliya.kukesheva@bk.ru

Kadyrov Adil, d.t.s., Abylkas Saginov Karaganda Technical University
e-mail: adil.suratovich@mail.ru

Kryuchkov, Yevgeniy, PhD, Abylkas Saginov Karaganda Technical University
e-mail: kryuchkov.yevgeniy94@gmail.com

Karsakova Akbope, PhD, Abylkas Saginov Karaganda Technical University
e-mail: karsakova84@mail.ru

DOI 10.52209/2706-977X_2025_3_111 **IRSTI 55.47.07** **UDC 623.746**

Study of FLC, PID, and LQR Control Methods for Precise Drone Landing in Wind Conditions

Ormanov A.N.1,[*], Dyusekeev K.A.[2], Shidlovskiy S.V.[3]
Astana IT University, Astana, Kazakhstan
L.N. Gumilyov Eurasian National University, Astana, Kazakhstan
National Research Tomsk State University, Tomsk, Russia
*corresponding author

Abstract. The article presents a comparative analysis of three controllers — FLC, PID, and LQR — for precise drone landing under external disturbances such as wind. The simulation was performed in MATLAB/SIMULINK with 3D animated models. The controllers were tested under identical initial conditions, evaluating landing accuracy and execution time. The results showed that the FLC demonstrated robustness to uncertainties (85.47% accuracy, 9.2 s), but required more computational resources. The PID controller provided 90.37% accuracy in 4.5 s, remaining simple and effective. The LQR achieved the best results — 98.98% accuracy in 4.5 s, demonstrating optimality and stability. The choice of controller depends on the conditions: FLC for complex uncertain situations, PID for simple tasks, and LQR for maximum accuracy and stability. The obtained data can be used in the development of drone control systems.

Keywords: drone, quadcopter, fuzzy logic controller (FLC), PID Controller, linear-quadratic regulator (LQR), precise drone landing, external disturbances, MATLAB/SIMULINK, drone control.

Introduction

Unmanned Aerial Vehicles (UAVs), commonly referred to as drones, have become increasingly significant in various sectors such as agriculture, logistics, infrastructure monitoring, and emergency response [9]. Their ability to operate in environments that are hazardous or inaccessible to humans has made them essential tools for automation and real-time data collection [8]. In particular, the problem of autonomous landing has gained considerable attention, as it is a critical phase for ensuring the safety, endurance, and efficiency of UAV operations [11]. Precise landing is especially important for scenarios such as docking on charging stations, landing on moving platforms, or performing missions in urban and confined environments [13].

The task of autonomous landing poses several challenges. UAVs are often subjected to external disturbances such as wind, turbulence, and sudden payload variations, which may lead to instability or positional inaccuracy [4]. Moreover, conventional control strategies may not be sufficient when dealing with uncertainties, nonlinearities, and rapidly changing operating conditions. As a result, robust and adaptive control algorithms are needed to guarantee stable and accurate landings [10].

Among the most commonly applied methods, the Proportional-Integral-Derivative (PID) controller remains popular due to its simplicity and ease of implementation [10], [16]. However, its performance is limited under nonlinear and highly dynamic conditions. The Fuzzy Logic Controller (FLC) has been introduced to handle uncertainty and approximate reasoning, offering better adaptability compared to classical methods [1], [3]. On the other hand, the Linear Quadratic Regulator (LQR), derived from optimal control theory, provides mathematically grounded solutions that minimize control effort while maintaining system stability [11], [12]. Several studies have demonstrated the successful application of these controllers in UAV path tracking, altitude stabilization, and trajectory control [13], [14], yet their comparative performance in precision landing remains underexplored.

Therefore, this study aims to fill this research gap by conducting a comparative analysis of FLC, PID, and LQR controllers for precise drone landing under external disturbances such as wind. Through simulation in MATLAB/Simulink, the effectiveness of each control method is evaluated in terms of accuracy and stability. The findings of this research are expected to contribute to the development of more reliable UAV landing systems, thereby enhancing their applicability in real-world missions.

1. Methodology

This section discusses the development of a drone control system using Fuzzy Logic Controller (FLC), Proportional-Integral-Derivative (PID) controller, and Linear-Quadratic Regulator (LQR). Each controller has unique features, advantages, and limitations, making them suitable for different scenarios. Mathematical models were developed in MATLAB/SIMULINK, considering the drone's motion dynamics and wind effects, to demonstrate and compare the effectiveness of each controller. The following subsections provide detailed approaches to designing and testing FLC, PID, and LQR under real-world conditions.

For the development of the model in MATLAB/SIMULINK, identical initial conditions were set for all controllers:

- X error — 2 m.
- Y error — 1.5 m.
- Z error — 5 m.
- Rotation angle — 10°.
- Wind speed — 2 m/s.

- Wind direction — 45°.
- Drone weight — 2 kg.

These parameters allow for a proper comparison of the controllers' effectiveness during drone landing, and they can be adjusted to analyze different scenarios.

Fuzzy Logic Controller (FLC)

In this subsection, we will develop fuzzy control algorithms for drone landing.

The advantages of using a fuzzy logic system lie in the ability to apply intuitive data and expert knowledge about the controlled object, as well as in the absence of the need for an exact mathematical model [4].

For the development of the FLC, MATLAB with the FuzzyLogicDesigner library will be used [2], [15]. The Mamdani fuzzy logic system, one of the most popular models, has been chosen. In this system, rules are described in an "if-then" format, which allows for flexible consideration of parameters affecting landing [3]. For example, a rule could be: "If the drone's altitude is high (Z = HIGH), then the descent speed is low (Uz = DOWN_HIGH)."

The system will use 6 input variables: errors along the X (Ex) and Y (Ey) axes, altitude errors (Z), yaw angle (θ), and wind parameters — wind speed (WindForce) and wind direction (WindDir). The output will consist of 4 control variables: along the X (Ux) and Y (Uy) axes, altitude (Uz), and rotation angle (Utheta). The system diagram is presented in Fig. 1.

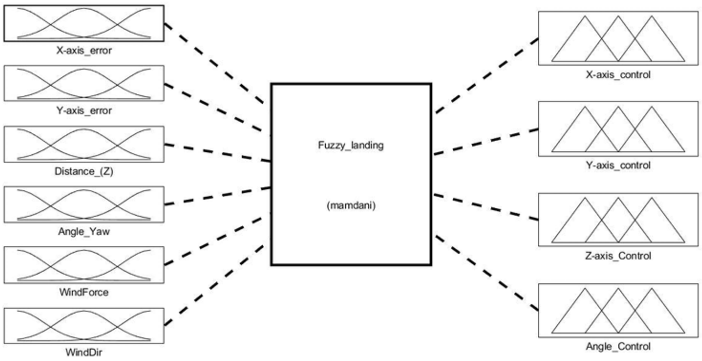

Fig. 1. - Fuzzy logic system diagram for drone landing control

Next, for convenience and to simplify the rule base, we performed fuzzy logic grouping. Dividing the system into logical blocks (such as input and output variables, membership functions, and rules) allows for efficient management of individual components and enables changes to be made without the need to revise the entire control logic [3], [2].

As a result, the system was divided into three groups:

Positioning errors (X, Y).
Errors in altitude and angle.
Compensation for wind influence.

This approach allows for more flexible tuning of the control system and adapting it to different operating conditions. The grouped components of the system are shown in Fig. 2.

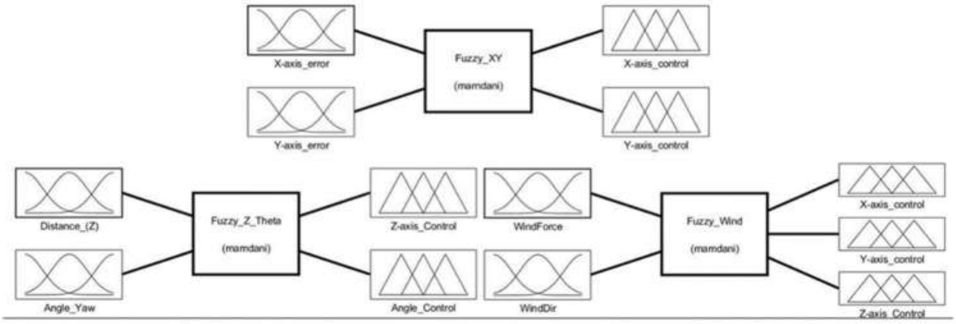

Fig. 2. - Grouping of fuzzy control system components

Positioning Errors (X, Y): The Fuzzy_XY FLC, shown in Figure 1, adjusts the drone’s position in the horizontal plane (X and Y axes) [5], minimizing deviations from the target coordinates. During landing, the drone may shift due to navigation errors, wind disturbances, or control characteristics. To ensure precise landing, the system analyzes the current position and generates corrective control actions to eliminate horizontal coordinate errors.

Input Variables:

- Error along the X-axis (Ex): Determines the drone’s left or right displacement relative to the landing point (range from -2 to 2 meters) [1].
- Error along the Y-axis (Ey): Similar to Ex but indicates forward or backward deviation.

Output Variables:

- Control signals for the X-axis (Ux) and Y-axis (Uy): Normalized within the range [−1, 1]. The system generates corrective actions to return the drone to the designated point. Control along the X-axis compensates for deviations along X, while control along the Y-axis regulates movement along Y.

Triangular Membership Functions (MFs): Defined as follows, following a similar approach as in [12]:

$$\mu_{BigLeft} = \begin{cases} 1, & x \leq -1.5 \\ \dfrac{-x-1}{0.5}, & -1.5 < x < -1.0 \\ 0, & x \geq -1.0 \end{cases} \tag{1}$$

Similar functions are defined for other linguistic variables: SmallLeft, Zero, SmallRight, and **BigRight**. Detailed membership functions are shown in Fig. 3.

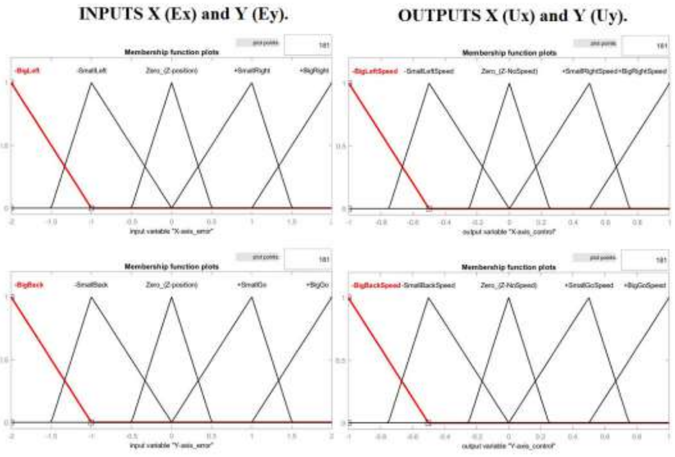

INPUTS X (Ex) and Y (Ey).

OUTPUTS X (Ux) and Y (Uy).

Fig. 3. - Membership Functions for X(Ex), Y(Ey), X(Ux), and Y(Uy)

A key stage is the creation of a rule base for correcting errors along the X and Y axes, establishing the relationship between input and output variables.

For each group of variables, a rule base is developed to define the relationships between input and output variables. The centroid method is used for defuzzification [3].

$$U = \frac{\Sigma_i \mu_i x U_i}{\Sigma_i \mu_i} \tag{2}$$

where *μi* - is the degree of membership of the output variable *Ui* in the given rule.

Table 1. Rule base for correcting X and Y errors

#	Input (Ex)	Input (Ey)	Output (Ux)	Output (Uy)
1	BigLeft	BigLeft	BigRight	BigRight
2	BigLeft	SmallLeft	BigRight	SmallRight
3	BigLeft	Zero	BigRight	Zero
25	…	…	…	…

Errors in height (Z) and angle (Theta): The Fuzzy_Z_Theta block, shown in Figure 1, controls the drone's height and orientation during landing, ensuring smooth and safe descent. The drone adjusts its horizontal position, regulates the height to avoid hitting the surface, and, if necessary, corrects the yaw angle [6].

Input Variables:

- Distance to the marker (Z): The drone's height (0–10 meters)
- Yaw angle (Theta): The orientation angle relative to the landing pad (-30° to 30°)

Output Variables:

- Height control (Uz): The descent speed (-1 to 1)
- Angle control (Utheta): Correction of the yaw angle for alignment.

Membership functions (MF) for Z:

$$\mu_{FAR} = \begin{cases} 1, & z \geq 5 \\ \dfrac{z-2}{3}, & 2 \leq z \leq 5 \\ 0, & z < 2 \end{cases} \tag{3}$$

Similar membership functions are defined for the linguistic variables **LANDED**, **CLOSE**, and **MID**. For the yaw angle, the membership functions are similar to those used for the positioning errors along the X and Y axes.

Table 2. Rule base for height and yaw angle

#	**Input (Z)**	**Input** (Theta)	**Output (Uz)**	**Output (Utheta)**
1	FAR	-Large	Down_High	+Large
2	MID	Zero	Down_Low	+Large
3	CLOSE	+Small	Zero	-Small
20	…	…	…	…

Wind Effect Compensation: The Fuzzy_Wind block, shown in Figure 1, compensates for the wind's effect on the drone during landing, minimizing its impact on the flight path.

In this block, 28 rules were formulated to ensure effective control and decision-making based on fuzzy logic. These rules allow the system to account for various conditions and adapt to changes in the surrounding environment.

Input Variables:

- Wind Force (WindForce) directly affects the adjustment of yaw angles and control signals [7]. Value range: [0, 10] m/s.
- Wind Direction (WindDir) this parameter describes the wind's direction relative to the drone's movement. It is measured in degrees (0° - 360°). The system accounts for eight primary directions.

Output Variables:

- (Ux, Uy, Uz) remain consistent with the functions from groups 1 and 2.

The membership function equation is defined similarly to equations (1) and (2).

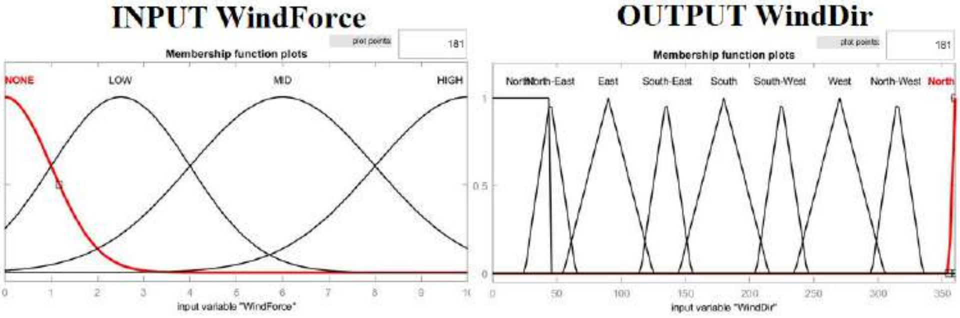

Fig. 4. - Membership Functions of WindForce and WindDir

Fig 6. Surface plot showing the relationship between WindForce, WindDir, and control signals. For example, with a strong wind (around 10 m/s) and a direction of 90 degrees, the control signal can reach a value of -0.5, indicating the need for a leftward adjustment. The graph demonstrates the operation of the fuzzy controller, considering wind strength and direction to generate control signals.

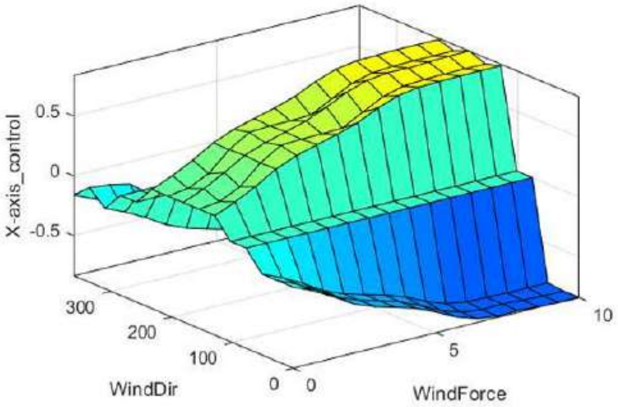

Fig. 5. - Surface plot of wind effect (WindForce and WindDir)

1) ***MATLAB/SIMULINK:*** As noted in [8], FLC is a complex system requiring significant computational resources due to the processing of multiple input parameters and logical rules. The dynamics of the drone's movement are described by mathematical models, including differential equations presented below:

2)

$$\frac{dX}{dt} = \frac{F_x}{M}, \frac{dY}{dt} = \frac{F_y}{M}, \frac{dZ}{dt} = \frac{F_z}{M} \tag{4}$$

The control signals calculated by fuzzy controllers update the drone's coordinates; however, wind creates additional forces that require compensation. To address this, a separate controller adjusts the trajectory by calculating the correction signals U_{x_cor}, U_{z_cor}, U_{z_cor}based on wind speed and direction, improving landing accuracy. The drone's movement is described by equations that account for both primary and correction signals, for example, for the X-axis:

$$X(i) = X(i-1) + \frac{U_x + U_{x\_cor}}{Mass} * dt \tag{5}$$

where $X(i)$ is the current coordinate, U_x is the control signal, U_{x_cor} is the correction signal, $Mass$ is the drone's mass, and dt is the time step. Similar equations are applied for the Y, Z axes, and the yaw angle.

Based on these equations and initial conditions, a model was built, as shown in Fig. 9.

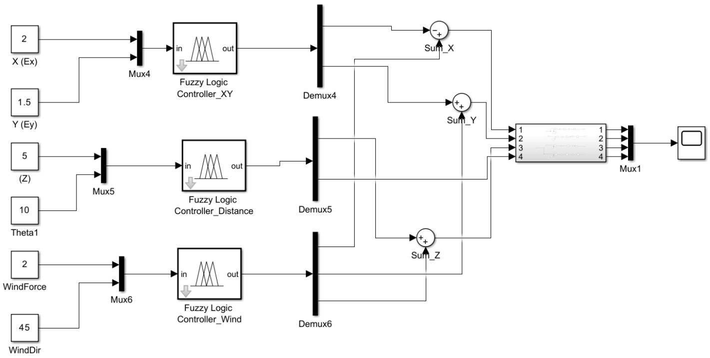

Fig. 6. - Structure of the Fuzzy Controller for Drone Landing

Fig. 6 shows three FLC blocks, each playing a key role in ensuring the drone's stability during landing, effectively compensating for the wind's influence. By considering the wind's strength and direction, as well as adjusting control signals along the X, Y, and Z axes, the drone maintains stability and landing accuracy even in challenging weather conditions. In each block, the rule bases from top to bottom are 25, 20, and 28.

Proportional–Integral–Derivative (PID)

The second stage of the work presents a drone control system model based on a PID controller, ensuring stable and accurate landing. In the presence of wind, the control becomes more complex due to the external forces impacting the trajectory.

The PID controller, widely used in various systems [9], [16], was integrated into the quadcopter system for precise landing. A separate controller is used for each axis (X, Y, Z) and the yaw angle (θ), with carefully selected proportional (Kp), integral (Ki), and derivative (Kd) coefficients, ensuring stability and accuracy of control.

Table 3. PID Controller Coefficients for Drone

Axis	Proportional Coefficient (Kp)	Integral Coefficient (Ki)	Derivative Coefficient (Kd)
X-Axis	1.8	0.01	0.1
Y-Axis	1.8	0.01	0.1
Z-Axis	0.9	0.145	0.1
Angle θ	1.0	0.01	0.1

The PID controller coefficients are selected to minimize the error between the current drone position and the target point, ensuring stability and accuracy. Kp quickly responds to deviations, Ki compensates for errors, and Kd reduces oscillations, improving the smoothness of control. This approach is described in [10], [9].

The drone's motion equations for the X, Y, and Z axes and changes in yaw angle, considering inertia, are similar to equation (5). A larger moment of inertia complicates the change in angular velocity.

The control input is calculated using the following equation:

$$U_x = K_{p\_X} * ex + K_{i\_X} * \int eXdt + K_{d\_X} * \frac{deX}{dt} \tag{6}$$

where $K_{p\_X} * ex$ is the proportional component that responds to the current error, $K_{i\_X} * \int eXdt$ is the integral component that accounts for the accumulated error over time, and $K_{d\_X} * deX/dt$ is the derivative component that responds to the rate of change of the error.

The control inputs are applied similarly for the Y, Z axes, and the yaw angle. Then, taking into account the initial conditions and coefficients, a PID controller is created in SIMULINK. The PID controller model for the X-axis is shown in Fig. 7. The same process is applied for the other axes and the yaw angle.

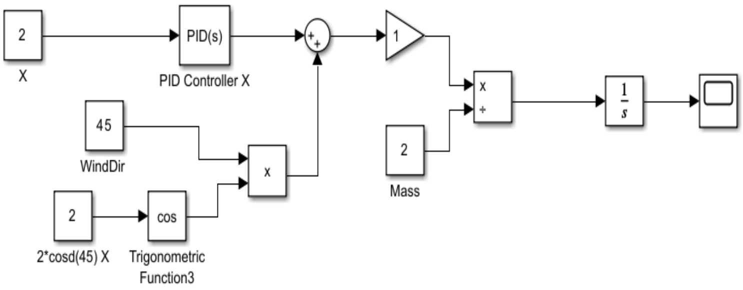

Fig. 7. - PID model in SIMULINK for the X-axis

creates an additional effect on the drone's movement, which is decomposed into components along the X, Y, and Z axes, as well as the yaw angle, depending on the direction.

$$F_{wind\_X} = F_{wind} * \cos(\theta_{wind}) \tag{7}$$

where F_{wind} is the total wind force, and $\cos(\theta_{\text{wind}})$ is the wind direction in degrees.

Linear–Quadratic Regulator (LQR)

This section presents the algorithm for precise drone landing on a specified marker under windy conditions using a Linear-Quadratic Regulator (LQR). The mathematical foundations of the method are discussed, including the system's dynamic equations, the solution to the Riccati equation, and the consideration of external disturbances.

The advantages of using LQR for drones lie in its ability to provide optimal control by minimizing deviations from the desired trajectory and accelerating system stabilization. This allows for high accuracy and efficiency in controlling the drone's movement, particularly in dynamic and changing conditions [4], [14].

The mathematical model equations are essential for analyzing the optimal control system, as these equations will later represent the system's performance [11].

The quadcopter model is described by a system of differential equations, with the drone's movement along the X, Y, and Z axes, as well as the yaw angle, defined by the state equations [11], [12]:

$$x^{\cdot} = A\_x + B\_u \tag{8}$$

where *x* is the state vector of the system, *A* is the system matrix describing the dynamics of the drone, and *B* is the control matrix.

The matrix *A* describes the change in the system's state (position and velocity) without considering control inputs. The motion along each axis is given as follows [13]:

$$\begin{bmatrix} \dot{x} \\ \dot{v} \end{bmatrix} = \begin{bmatrix} 0 & 1 \\ 0 & 0 \end{bmatrix} \begin{bmatrix} x \\ v \end{bmatrix} \tag{9}$$

The first row of matrix *A* shows that velocity *v* is the derivative of position *x*. The second row describes acceleration *a* as the derivative of velocity *v*, which is zero in the absence of external forces.

Matrix *B* defines the influence of the control input *u* (applied force) on the state changes of the drone:

$$\begin{bmatrix} \dot{x} \\ \dot{v} \end{bmatrix} = \begin{bmatrix} 0 \\ 1/m \end{bmatrix} u \tag{10}$$

The control input *u* affects only the acceleration, as per Newton's second law: *F=ma,* from which *a = F/m*.

LQR minimizes the quadratic cost function:

$$J = \int_0^{\infty} (x^T Q_x + u^T R_u) dt \tag{11}$$

where *Q* is the state weight matrix, determining the priorities for control accuracy, and *R* is the control effort penalty matrix (*R=1*).

$$Q = \begin{bmatrix} 800 & 0 \\ 0 & 800 \end{bmatrix} \tag{12}$$

In this case, the state weight matrix Q minimizes state deviations (e.g., position and velocity), while R penalizes excessive control effort. A higher value in Q prioritizes minimizing state error, and a value of 1 in R indicates the importance of control effort in the optimization.

The solution to the Riccati equation [13]:

$$A^T P + PA - PBR^{-1}B^T P + Q = 0 \tag{13}$$

The matrix P obtained from the solution is used to compute the feedback gain matrix:

$$K = R^{-1}B^T P \tag{14}$$

This approach optimizes control by minimizing the cost function J, as confirmed by MATLAB/Simulink simulations. Fig. 8 shows the X-axis model, with similar models for the other axes and yaw angle. Input data includes initial conditions, parameters, and wind effects per equation (6).

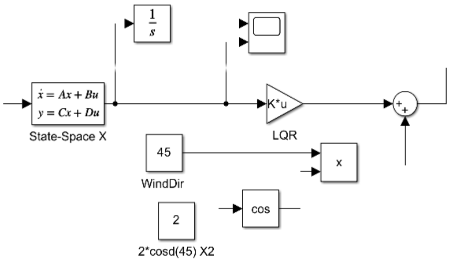

Fig. 8. - LQR Model in SIMULINK for the X-axis

2. Results and discussion

This section of the study presents the results of a drone landing simulation on a target point with coordinates (X=0, Y=0, Z=0) using three different types of controllers: Fuzzy, LQR (Linear-Quadratic Regulator), and PID (Proportional-Integral-Derivative). The results, shown in Fig. 9, demonstrate that all controllers effectively compensate for external factors such as wind, ensuring stable drone control.

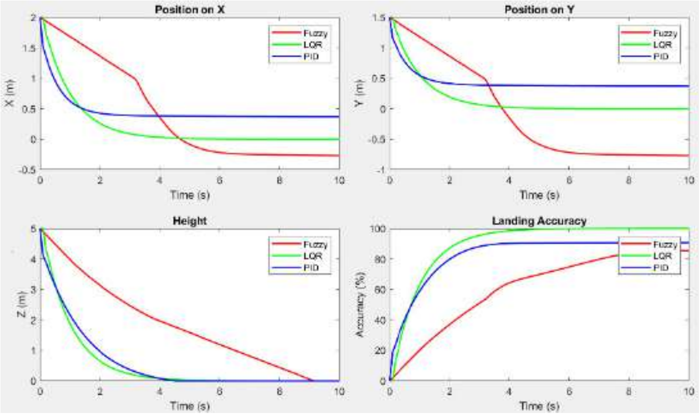

Fig. 9. - Simulation Results of FLC, LQR, and PID Controllers

Table 4. Accuracy and Landing Time Results

#	Accuracy %	Landing *t*
FLC	85.41%	9.20 seconds
LQR	98.86	4.50 seconds
PID	90.37%	4.50 seconds

$$Accuracy(i) = \left(1 - \frac{current\_er}{initial\_er}\right) * 100\% \tag{15}$$

The landing time is defined as the moment when the drone's altitude reaches the target altitude:

$$Landing_{Time} = \ t \ when \ Z(t) \leq \ Z_{target} \tag{16}$$

The FLC controller ensures a smooth position decrease with minor oscillations. The landing accuracy increases to 85.41%, while the landing time of 9.20 seconds is the longest among the three controllers, due to its adaptive nature adjusting control signals based on conditions.

The LQR controller offers the best performance in accuracy and landing time. With a landing accuracy of 98.86% and a landing time of 4.50 seconds, it ensures a fast, precise descent, making it the most efficient for this task.
The PID controller ensures a faster, more stable descent, with landing accuracy reaching 90.37%. The landing time is 4.50 seconds, significantly less than the Fuzzy controllers.

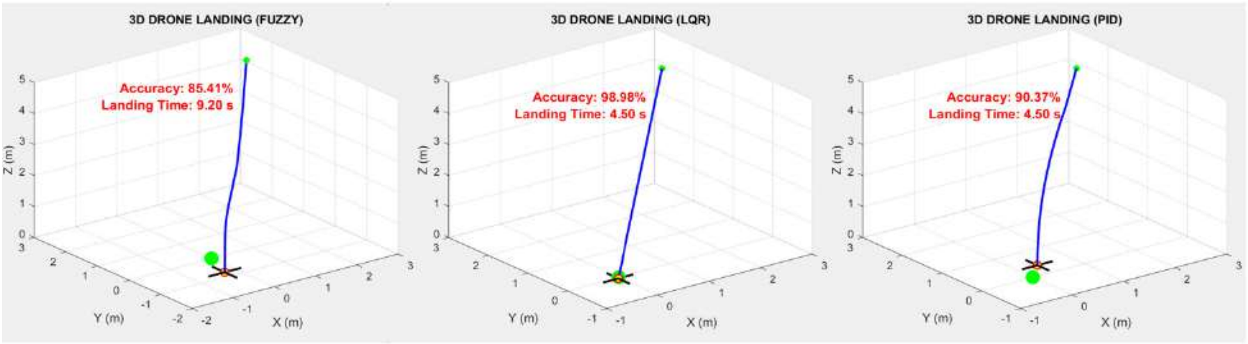

Fig.10. - 3D Animation of the Drone Landing Process Using FLC, LQR, and PID Controllers

Conclusion

The study presents a comparative analysis of three controllers—Fuzzy Logic Controller (FLC), Proportional–Integral–Derivative (PID), and Linear–Quadratic Regulator (LQR)—for precise drone landing in the presence of external disturbances, such as wind. Simulation in MATLAB/SIMULINK with 3D visualization allowed for the evaluation of landing accuracy and time under identical initial conditions.

The FLC demonstrated high adaptability to uncertainties and external disturbances, such as wind, and performs well with nonlinear systems and imprecise data, making it suitable for complex conditions. However, it lags behind other controllers in terms of accuracy and landing time, and its computational complexity may limit its use in real-world applications.

The PID controller provided balanced performance, improving landing time and accuracy compared to FLC. Its simplicity and efficiency make it a reliable choice for tasks where computational efficiency and ease of implementation are important. However, in conditions of high dynamics or uncertainty, the PID may struggle due to its fixed tuning parameters.

The LQR outperformed both FLC and PID in landing accuracy, achieving nearly perfect precision. Its optimal control strategy, with minimal oscillations and fast convergence to the target point, makes it the most effective for tasks requiring high landing accuracy. However, its implementation requires an accurate system model and may be more challenging to tune.

Directions for Future Research:

- The research into combining FLC, PID, and LQR. could lead to the development of more robust and accurate controllers;
- Testing controllers in real-world conditions on physical drones;
- Enhancing disturbance rejection to improve controller performance in the presence of complex external factors.

In conclusion, the choice of controller for drone landing depends on the specific task requirements, including the desired level of accuracy, the complexity of the environment, and available computational resources. The results of this study provide a solid foundation for selecting and optimizing controllers for various drone applications, ensuring safe and accurate landings even in challenging conditions.

References

[1] V. Indrawati, A. Prayitno, and T. A. Kusuma, "Waypoint navigation of AR.Drone quadrotor using fuzzy logic controller," Telkomnika, vol. 13, no. 3, pp. 381–38x, Sep. 2015. DOI: 10.12928/TELKOMNIKA.v13i3.xxxx.

[2] V. S. Fnu and K. Cohen, "Intelligent fuzzy flight control of an autonomous quadrotor UAV," in Proc. 52nd Aerospace Sciences Meeting, National Harbor, MD, USA, Jan. 2014, pp. 1–12. DOI: 10.2514/6.2014-0992.

[3] O. Rodríguez-Abreo, J. Rodríguez-Reséndiz, A. García-Cerezo, and J. R. García-Martínez, "Fuzzy logic controller for UAV with gains optimized via genetic algorithm," Heliyon, vol. 10, p. e26363, Feb. 2024. DOI: 10.1016/j.heliyon.2024.e26363.

[4] D. A. Beloglazov, I. S. Kobersi, E. Y. Kosenko, V. V. Solovyev, and V. V. Shadrina, "Analysis of practical aspects of using controllers in automatic control systems of quadcopters," Engineering Bulletin of the Don, no. 3, 2015. [Online]. Available: http://ivdon.ru/ru/magazine/archive/n3y2015/3078.

[5] V. Indrawati, A. Prayitno, and G. Utomo, "Comparison of two fuzzy logic controller schemes for position control of AR.Drone," in Proc. 2015 7th Int. Conf. Inf. Technol. Electr. Eng. (ICITEE), Chiang Mai, Thailand, Oct. 29–30, 2015. DOI: 10.1109/ICITEED.2015.7408972.

[6] P. Vadakkepat, T. C. Chong, W. A. Arokiasami, and X. Weinan, "Fuzzy logic controllers for navigation and control of AR.Drone using Microsoft Kinect," in *Proc. 2016 IEEE Int. Conf. Fuzzy Syst. (FUZZ-IEEE)*, Vancouver, BC, Canada, Jul. 24–29, 2016. DOI: 10.1109/FUZZ-IEEE.2016.7737778.

[7] B. Rached, M. Elharoussi, and E. Abdelmounim, "Fuzzy logic control for wind energy conversion system based on DFIG," in *Proc. 2019 Int. Conf. Wireless Technol., Embedded Intell. Syst. (WITS)*, Fez, Morocco, Apr. 3–4, 2019. DOI: 10.1109/WITS.2019.8723722.
[8] M. Rabah, A. Rohan, M. Talha, and others, "Autonomous vision-based target detection and safe landing for UAV," Int. J. Control Autom. Syst., vol. 16, no. 5, pp. 2375–2387, Oct. 2018. DOI: 10.1007/s12555-018-0071-x.
[9] M. Rinaldi, S. Primatesta, and G. Guglieri, "A comparative study for control of quadrotor UAVs," *Appl. Sci.*, vol. 13, no. 6, pp. 3464, Mar. 2023. DOI: 10.3390/app13063464.
[10] O. Polat and A. Sezgin, "Position control of a quadcopter with PID and fuzzy-PID controller," *J. Eng. Sci. Design*, vol. 12, no. 1, pp. 34–48, 2024. DOI: 10.21923/jesd.1223998.
[11] G. E. Setyawan, W. Kurniawan, and A. C. Lumban Gaol, "Linear quadratic regulator controller (LQR) for AR. Drone's safe landing," in *Proc. 2019 Int. Conf. Sustainable Inf. Eng. Technol. (SIET)*, Lombok, Indonesia, Sep. 2019, pp. 1–6. DOI: 10.1109/SIET48054.2019.8986078.
[12] T. K. Priyambodo, O. A. Dhewa, and T. Susanto, "Model of Linear Quadratic Regulator (LQR) control system in waypoint flight mission of flying wing UAV," *Journal of Telecommunication, Electronic and Computer Engineering (JTEC)*, vol. 12, no. 4, pp. 43–49, Oct.-Dec. 2020. [Online]. Available: https://jtec.utem.edu.my/jtec/article/view/5696.
[13] F. Ahmad, P. Kumar, and P. Patil, "Simulation of the quadcopter dynamics with LQR based control," *Materials Today Proceedings*, vol. 25, pp. 2066–2071, Jan. 2020, doi: 10.1016/j.matpr.2020.04.282.
[14] M. Rinaldi, S. Primatesta, and G. Guglieri, "A comparative study for control of quadrotor UAVs," Appl. Sci., vol. 13, no. 6, pp. 3464, Mar. 2023. DOI: 10.3390/app13063464.
[15] T.-L. Le, N. V. Quynh, N. K. Long, and S. K. Hong, "Multilayer interval type-2 fuzzy controller design for quadcopter unmanned aerial vehicles using Jaya algorithm," IEEE Access, vol. 8, pp. 163539-163548, Oct. 2020, doi: 10.1109/ACCESS.2020.3028617.
[16] A. Eltayeb, M. F. Rahmat, M. A. M. Eltoum, M. H. S. Ibrahim, and M. A. M. Basri, "Trajectory tracking for the quadcopter UAV utilizing fuzzy PID control approach," 2020 International Conference on Computer, Control, Electrical, and Electronics Engineering (ICCCEEE), Khartoum, Sudan, Feb. 26 - Mar. 1, 2021, doi: 10.1109/ICCCEEE49695.2021.9429636.

Information of the authors

Adilet Ormanov, PhD student, L.N. Gumilyov Eurasian National University, Lecturer, Astana IT University
e-mail: ormanov16@bk.ru

Kanagat Dyusekeev, PhD, L.N. Gumilyov Eurasian National University, Head of the Department of "Computer and Software Engineering"
e-mail: dyussekeyev_ka@enu.kz

Stanislav Shidlovskiy, Doctor of Technical Sciences, Dean of the Faculty of Innovative Technologies
National Research Tomsk State University
e-mail: shidlovskiysv@mail.ru